Behavior of Bentonite and Kaolin Clays at different Particle Interactions Under Chemical, Hydraulic, and Mechanical Loadings

Thesis

as a requirement for the degree of

Doctor of philosophy

at the Department of Civil Engineering
Indian Institute of Technology Guwahati

By

Dhanesh Sing Das
Roll No 156104025

Under the supervision of
Prof. TV Bharat

Guwahati, March 2022

Abstract

Volume change behavior of clays under mechanical, hydraulic, and chemical loadings is of great importance in various applications in the field of Geotechnical and Geoenvironmental engineering. The presence of a rich percentage of clay minerals such as montmorillonite and kaolinite in the clay soils results in heaving and subsidence problems, respectively. On the other hand, compressibility behavior and swelling pressure of bentonites is a significant concern in the geoenvironmental applications viz., landfills, low-high-level nuclear waste repositories, and impounding facilities. Equilibrium sediment volume is often used as a surrogate compatibility test for assessing the expansiveness of clays and the identification of different clay minerals. In this study, a theoretical model was proposed based on the diffuse double layer theory to estimate the equilibrium sediment volume of clays. Further, a simple technique for routine estimation of the surface area of plastic clays was proposed based on the developed theoretical framework for sediment volume. The method utilized equilibrium sediment volume measurement of clay soil in 0.1 N NaCl solution and used the theoretical equation for the surface area estimation. A generalized semi-empirical model was proposed for predicting the compressibility behavior of clayey soils of different plasticity over a wide range of consolidation pressures. The proposed model has validated over 114 compressibility datasets from 88 clayey soils and bentonites with different inundation fluids from the literature and the present study. Further, the Stern diffuse double layer model for the constant charge condition was developed for the first time to study the compressibility behavior of clays theoretically. The influence of compaction density and bentonite plasticity on the temporal swelling pressure evolution was analyzed using microstructural analysis. Further, the volume change behavior of air-dry kaolin due to wetting was studied at various compaction densities and under different applied loadings. Surface forces were evaluated at various pore scales at the air-dry and fully saturated state to explain the observed kaolin behavior.

Acknowledgment

First and foremost, I thank MHRD and IIT Guwahati for providing the fund to carry out my research work. Without financial assistance, it would have not been possible to carry out the research work.

1. I extend my heartfelt gratitude to the examiners of the thesis for their valuable suggestions and comments on improving the thesis quality. I will remain grateful to Lt. Narayan Reddy sir, Mechanical Department, IIT Guwahati for his kind support, guidance, and suggestions during the initial phase of my Ph.D.
2. I express my sincere gratitude to my Ph.D. supervisor (Prof. T.V. Bharat) for his constant support, guidance, encouragement, advice, and valuable discussions throughout. I must acknowledge him for providing the unconditional freedom to work, think and express whatever I have done in my research work by keeping faith in my capabilities.
3. I am highly thankful to my doctoral committee members, Prof. Rajan Choudhary (Chairman), Dr. Archana Nair from the department of civil engineering, and Prof. Sukayna Sharma from the Department of Humanities and Social Science, for their constant support, guidance, and suggestions during my work progress and seminars. Their valuable discussions and suggestions always motivated me to work better and deeper for the improvement of the quality of my research work.
4. I am also thankful to all Geotechnical Engineering faculty members, especially Prof. A. Murali Krishna from IIT Tirupati (formerly IIT Guwahati), Dr. Arindam Dey, and Prof. Sreedeep S. from the department of Civil Engineering, IIT Guwahati for their encouragement and suggestions.
5. I also acknowledge the support and technical assistance received from the staff namely Hariram Upadhaya from Geotech lab, Pranab Hazarika from Structure lab, C. Medhi, and P. Pathak from Env. lab, Department of Civil Engineering, IIT Guwahati.
6. I also extend my sincere gratitude to Prof. D. Kulkarni, Sanjib Sharma, Saibal, and Soumya from the Department of Mechanical Engineering, IIT Guwahati for providing the laboratory facility and assistance. I am thankful to Dr. Bula Choudhary from Biotech Park, IIT Guwahati for providing laboratory facility for freeze-drying the soil samples.
7. I am grateful to Prof. Manu Santhanu and Yuvraj from IIT Madras for MIP testing facility.

8. I express my acknowledgment to Prof Sukayna Sharma and Dr. Pankaj Singh from the department of humanities and Social Science, IIT Guwahati for their valuable suggestions and discussions.
9. I must acknowledge the immediate help and support received from Workshop, IIT Guwahati staff namely N. K. Das, Upen Gohain, D. Khaklary.
10. I am thankful to the co-founders of Yantrabot Technology- Arun Buragohain and Ayushman Gogoi for their technical assistance in my thesis work.
11. I acknowledge Dr. Sidananda Sarma, Scientific Officer, Dept. of Physics, IIT Guwahati for providing the XRD facility, Lukumoni, Harsha, Jayanta from the Chemical engineering department for providing the particle size analyzer, AAS facilities.
12. I am thankful to my fellow research scholar friends and seniors namely Karabi, Anwesha, Gourav, Manish from the Dept. of Bioscience and Bioengineering, P. Bakkal, Gopi, Narendra from Centthe re for Environmental Technology, Raj from the Dept. of Chemistry, Piyal Mondal, Devipriya, Pyare Mohan, Prerona from Dept. of Chemical Engineering, Ram, Deep, Shashi, Susmita from Dept. of Physics, IIT Guwahati for their help and assistance for various experimental test setups.
13. I am also grateful to my labmates – Chinumoni, Rakesh, Seema, Suresh, Himanshu, Ishan, Shivshant, Ankit, Partha, Akhila, Bedabhrata, Vishnu and Bhanu for sharing their knowledge and useful discussions along with healthy working environment and all other lab members for always being there whenever it is required and made me feel like family. Especially I extend my heartfelt acknowledgment to Rakesh, Himanshu, Seema, Suresh, Ishan, Shivshant, Rohit, and Kapish for their assistance in conducting various experiments during my Ph.D. work.
14. I would like to thank my best friends at IIT Guwahati, Jagadish, Nilutpal, Saurav, Pranab, Jimmy da, Bishu, Bhaskar, Bastav, Shilpa, Bidisha, Sweety, Himali, Anupama, and Rabha for creating a friendly and homely atmosphere.
15. Finally, I would like to express my deepest gratitude to my parents and brother who gave me blessings, moral support, and continuous encouragement to pursue my dreams.

Guwahati, March 2022 Dhanesh Sing Das

Table of contents

List of figures

List of Tables

1 Introduction

1.1 Background

The presence of clay soils often poses threat to infrastructure development and causes significant challenges to Geotechnical engineers. The presence of rich percentages of common clay minerals such as montmorillonite and kaolinite in the clay soils results in heaving and subsidence problems, respectively. On the other hand, bentonite clays, which are rich in montmorillonite minerals, find wide applications in the construction of landfills (Lee *et al.*, 2005; Tadikonda, Sivapullaiah and Allam, 2009, 2013; Das P., and Tadikonda, 2017; Manassero, Benson, and Bouazza, 2018), Low-high-level nuclear waste repositories (Grindrod et al., 1999; Gens et al., 2002; Pusch and Yong, 2006; Ye et al. 2010; Zheng et al., 2011; Tadikonda et al., 2021), and impounding facilities (Fall et al., 2009). The applications of natural clays such as kaolin are currently explored for landfill applications due to the virtues of their osmotic ability and reduction in hydraulic conductivity under the salt environment (Das and Tadikonda, 2021; Das P., 2021). The clays are subjected to different hydraulic, chemical, and mechanical loading conditions in the field during the infrastructure development and in the Geoenvironmental engineering applications. A comprehensive understanding and prediction of the volume change behavior of clays under different loading conditions, therefore, is of prime importance in the field of Geotechnical and Geoenvironmental engineering.

Equilibrium sediment volume (ESV) represents the lowest-level of particle-particle interaction of clays and is often used as a surrogate compatibility test used for assessing the expansiveness of clays for several decades (Sridharan and Prakash, 1999) (American Colloid Co., 1945; Rollings, 1969; Prakash and Sridharan, 2002). Further, the ESV data are used for the identification of different clay minerals (Wiklander and Andersson; 1955; Kariuki and Meer, 2004), classifying expansive soils (Sridharan and Prakash, 2000), qualitative understanding of the swelling behavior of clays (Deng et al., 2011), and correlating with different Geotechnical engineering properties of clays (Lee *et al.*, 2005) (Prakash and Sridharan, 2002; Lee et al., 2005). Theoretical understanding of the ESV behavior of clays under the influence of various physicochemical factors is important for a fundamental understanding of the behavior of clays under different chemical, hydraulic, and mechanical loading conditions. Specific surface area (S_a) is one of the essential surface properties of the clays to understand the clay behavior. It is defined as the surface area per unit mass of the

soil and is expressed in m^2/g. Both the internal and external surfaces contribute to the specific surface area in the expanding silicates layers. The clay surface properties control many soil physical processes such as swelling, shrinkage, adsorption, diffusion of ions, heat loss, water retention, and water movement (Muhunthan 1991; Petersen et al. 1996; Dolinar et al. 2007; Bharat et al. 2013; Revil and Lu 2013; Khorshidi et al. 2016; Gapak et al. 2017; Khorshidi and Lu 2017; Bharat and Gapak 2021). The estimation of S_a is, therefore, of paramount importance as these physical processes govern the design of engineered facilities such as landfills, nuclear waste repositories, and tunnels (Aubertin et al. 2003; Tripathy et al. 2004; Bharat 2004; Bharat et al. 2013). The surface area estimation is also essential for the theoretical evaluation of swelling pressure, compressibility behavior, and hydraulic conductivity of clay soils (Bolt 1956; Mitchell 2005; Tripathy et al. 2004; Bharat et al. 2013; Bharat and Sridharan 2015a). Several methods viz., EGME adsorption, MB sorption, water adsorption, and N_2 gas adsorption (BET) are being utilized to estimate the surface area of soils. Discrepancies exist among the methods as the underlying mechanisms are different for these methods. Further, the existing methods are either very time-consuming or require sophisticated equipment for the estimation of the surface area of clays. An alternative technique that provides a simple and quick way of estimation of surface area for clays is the need of the hour.

Volume change behavior of clays such as compressibility and swelling is controlled by the strong particle-particle interactions. Clays exhibit volume change behavior under mechanical, chemical, and hydraulic loads (wetting). The compressibility behavior of saturated clays is important for various engineering applications such as landfills, tailing impoundments, nuclear waste repositories, and construction activity on reclaimed land. Compacted bentonites are extensively used in landfills due to the presence of a high percentage of montmorillonite mineral content for controlling the diffusion rates of degraded waste (Lee *et al.*, 2005; Bharat et al., 2009, 2013; Das and Bharat, 2017; Manassero et al., 2018), for controlling the seepage rates from surrounding rock mass in high – low-level nuclear waste repositories (Pusch, 2006; Pusch, 2015), and for improving the stability of excavations under water-logged conditions such as harbors (Pusch, 2015). Different bentonites namely, MX80, FEBEX, Montigel, Gaomiaozi (GMZ), Kutch, Barmer, Yellow bentonite, Kunigel-V1, Ponza, etc. are widely used as landfill liners and are also the likely candidate material in nuclear waste repositories in different countries (Carlson, 2004; Karnland, 2010; Pusch, 2015; Das & Bharat, 2017; Gapak et al., 2017). Their plasticity (i.e., quality) varies

depending on the presence of different minerals, clay content, and percentage of different exchangeable cations. The volume change behavior of such bentonites under mechanical pressure is important in the presence of different saline environments in these applications. The maximum consolidation pressures up to which the compressibility data is required, in these applications, depends on the design considerations. The expected maximum vertical pressure on compacted liner systems in the landfills and tailing impoundments may range between 360 – 6,000 kPa (Peirce et al., 1986; Timmons et al., 2012) depending on the mound height and type of waste expected. On the other hand, the mechanical behavior of the bentonites are studied in the range of 3,000 – 42,000 kPa for various applications in high-level nuclear waste repositories as the stress level at the location of the waste disposal repositories are expected to be similar (Marcial, Delage, and Cui, 2002; Tripathy, Sridharan, and Schanz, 2004; Tripathy and Schanz, 2007; Baille, Tripathy and Schanz, 2010; Bharat, Sivapullaiah and Allam, 2013) (Pusch et al., 2011; Ye et al., 2014). Similarly, the compressibility behavior of various clayey soils at high mechanical loads is also important for building the infrastructure on reclaimed land (Mesri & Funk, 2014). However, the maximum applied normal pressure in conventional oedometers for studying the compressibility data is limited. Conversely, laboratory estimation of compressibility data beyond certain consolidation pressures using advanced set-ups is laborious, time-consuming, and expensive (Ng et al., 2006). The prediction of compressibility data using theoretical and empirical analysis has been of key interest to researchers.

Bentonite clays exhibit significant swelling pressure due to wetting under confined conditions. Swelling pressure is an important parameter for the design of nuclear waste repositories (NWRs), where pre-compacted bentonite blocks at air-dry water contents and high compaction densities are used as buffer material between waste canisters and surrounding saturated rock mass (Pusch and Yong 2006, Zheng et al. 2011, Tadikonda et al. 2021). The stress state of the repository is appropriately maintained from the swelling pressure development of the compacted bentonite blocks during the saturation process, apart from sealing the construction joints (Grindrod et al. 1999, Gens et al. 2002, Ye et al. 2010). The evolution of swelling pressure with time is important for understanding the stress development in the repository during the bentonite saturation process and bentonite hydration process up to saturation (Vaunat and Gens 2005).

Ground subsidence problems due to the collapse of the loess soil have been reported in most literature (Derbyshire, 2001; Houston et al., 2001; Peng et al., 2006; Delage et al., 2008; Li et al., 2016). Ground subsidence problems have been encountered in the ongoing infrastructural development projects in the North-Eastern region of India where significant kaolin deposits are present. Kaolin deposits are widely spread over various regions of South Asia; across China and various parts of India (Indian Bureau of Mines, 2018; Nakagawa et al., 2006), especially in the North-eastern part (Saikia et al., 2003; Saikia and Parthasarathy, 2010; Sengupta et. al., 2008). The kaolin deposits exist up to several meters of depth from the ground surface and naturally exists in dry condition. The wetting-induced collapse potential of kaolin is also reported in a recent laboratory study (Choudhury and Bharat, 2018). The influence of the natural density of kaolin and the stress state on the collapse behavior is important as the depth of the deposit and mechanical stresses vary in the field.

1.2 Motivation and Scope

The ESV of clays is controlled by the surface forces as the mechanical stresses are negligible at such a weak particle-particle interaction. Theories based on the surface forces, therefore, provide useful insights into the free swell volume of the clays. However, the theoretical study for understanding the free swell volume of the clays is scarce. The available models and experimental data report only the qualitative changes in ESV with pore-fluid parameters. Theoretical methodology for quantitative analysis of equilibrium volume of the clay sediments and ESV prediction using surface characteristics of the clays remains to be completed.

The available methods for surface area estimation of clay soils are based on the sorption of the probe molecules either at the dry-end state or the fully saturated state. The major limitation of the 'dry-end'-based methods such as the Ethylene glycol monoethyl ether (EGME) and the N_2-gas adsorption technique is that the accessibility of the internal surface area of clays is not guaranteed by the probe molecules. While water molecules have better accessibility to the internal surface area of clays, water sorption at the dry-end state is significantly influenced by the type and size of exchangeable cations on the clay surface, the extent of interlayer swelling, and the extent of capillary condensation occurring on particle surfaces and interfaces. Thus, the existing water sorption models are not suitable for the expansive clays. The methylene blue (MB) sorption technique, on the other hand, utilizes the fully saturated state of the clay particle. However, there

are some serious concerns associated with this method. Firstly, the dependency of MB sorption on the type of exchangeable cations of the clay surface, and secondly, the uncertainty in the surface area computation due to different possible orientations of the MB molecules in the adsorbed state. The ESV test can facilitate better accessibility for the water molecules into the internal surface area of clays in a fully swollen state dominated by the DDL repulsive forces where the influence of other surface forces is negligible.

Prediction of the compressibility behavior of montmorillonite-rich clays is often made based on the Gouy-Chapman DDL theory. However, the theoretical compressibility predictions are accurate only for very high quality (i.e., plasticity) clays such as sodium bentonites, but severely differ for low-medium quality clays containing calcium in the exchangeable state, and for illite clays. A generalized predictive model for the compressibility behavior of clays over a wide range of plasticity, saline conditions and consolidation pressure is the need of the hour.

The Gouy-Chapman DDL theory is often criticized for considering the ions as point charges, which is quite unrealistic. The theory often predicts much smaller void ratios than the measured data at higher pressures due to the overlooking of the specific effect of the size of cations. The DDL model proposed by Stern (1924), known as the Stern-DDL model, incorporates the effect of the size of the cation into the theory through consideration of a compact inner layer near the clay surface. Prediction of the compressibility behavior based on the Stern DDL model at constant surface charge case as applicable for clay soils, however, is not available yet.

A significant number of studies has been carried out on the swelling pressure behavior of several bentonites under the influence of compaction density and pore-fluids chemistry, in the recent past. A wide variety of swelling pressure evolution curves under the isochoric conditions have been reported for different bentonites at various compaction densities and in the presence of different pore fluids. The underlying mechanism responsible for the variable nature of SPEC with compaction density and bentonite plasticity is not well understood so far. Further, limited studies are available concerning the influence of the individual cation type and alkaline conditions in the pore-fluid on the swelling pressure evolution of bentonites.

The volume change behavior of kaolin soil compacted to MDD and OMC has been extensively studied in the past (Wheeler and Shivakumar, 1995, 2000; Shivakumar et al., 2010). The study on

the wetting-induced volume change behavior of kaolin at air-dried state, however, is very limited (Choudhuri and Bharat, 2018; Pedrotti and Tarantino, 2018, Sun et al., 2007). The wetting-induced volume change behavior of kaolin initially at air-dry state, therefore, is necessary to be investigated at different compaction densities and inundation pressure.

In this study, extensive experimental work has been carried out to understand the behavior of clays at weak particle interactions to strong particle interactions, where physicochemical forces are predominant. Further, a theoretical framework was developed based on the Gouy-Chapman DDL theory for saturated clays at a very low particle interaction to analyze the ESV of clays. A new method was developed to estimate the surface area of plastic clays based on the measured ESV and the developed theory. The stern DDL model was considered to incorporate the effect of cations size in the theoretical prediction of compressibility behavior at high pressures. Further, a generalized semi-empirical model was proposed for predicting the compressibility behavior of bentonites and natural clayey soils at high consolidation pressures. The effect of compaction density, bentonite plasticity, and pore-fluid chemistry on the swelling pressure evolution characteristics of compacted bentonites was studied. Microstructural analysis was carried out to bring out the underlying mechanisms responsible for the observed SPEC characteristics under the influence of compaction density and bentonite plasticity. The wetting-induced volume change characteristics of kaolin clays at various compaction densities were studied under different inundation pressures. An effort was made to understand the role of various pore-scale forces on the observed kaolin behavior through a detailed microstructural analysis.

1.3 Objectives

The aim of the work was to

- To develop a theoretical formulation using DDL theory for the saturated clay-water system at a very low interaction and understand the ESV behavior under different pore-fluid environments.
- To investigate various influencing parameters on the compressibility behavior of clays based on the literature data on a wide range of clayey soils and develop a generalized predictive model.

- To establish the potential distance relationship for the Stern DDL model to incorporate the effect of cation size for better prediction of saturated clay behavior at strong particle interactions.
- To carry out microstructural analysis to understand the influence of compaction density and plasticity on the SPEC characteristics.
- To study the effect of pore-fluid chemistry and the presence of sand content on the swelling pressure of compacted bentonites.
- To study the wetting-induced volume change behavior of "potentially" collapsible kaolin under different compaction densities and different normal loading conditions.
- To study the pore-scale forces responsible for the observed wetting-induced kaolin behavior through microstructural analysis.

1.4 Organization of the thesis

The thesis consists of ten chapters including five contributing chapters. **Chapter 1** presents the general introduction to the problem, the motivation behind the research work, and the objectives of the present study.

Chapter 2 presents the theoretical background of the physicochemical behavior of clays. A description of the basic unit structures of the primary clay minerals and their surface characteristics is presented, which is followed by the mechanisms involved in the clay-water interactions. The relevant surface forces in clay particle-particle interaction at different moisture states are presented next. The theoretical formulation of the pressure-void ratio relationships of saturated clay–water systems based on the DDL theory is presented at the end of the chapter.

Chapter 3 presents the literature review in the concerned research domain to construct the background of the study. The chapter also discusses the existing experimental and theoretical methodologies for predicting and understanding the behavior of clays under the chemical, hydraulic and mechanical loadings.

Chapter 4 provides the details of various soils used in this study. The basic characterization of the studied soils is presented, in detail. Experimental methodologies adapted for studying the behavior

of the clay under different chemical, hydraulic and mechanical stress states are also discussed in this chapter. The contributions from the present work are presented in chapters 5-9.

Chapter-5 presents the theoretical formulation of ESV of clays using the Gouy-Chapman DDL model at a weak particle interaction. Further, a new methodology was developed for routine estimation of the specific surface area of plastic clays based on the estimated ESV under the salt environment.

Chapter-6 presents a generalized semi-empirical model to predict the compressibility behavior of clayey soils of different plasticity for containment applications at large consolidation pressure. The applicability of the model over 118 consolidation datasets obtained from over 84 different clays across the world is discussed in the chapter.

Chapter-7 presents a theoretical model to predict the compressibility behavior of clayey soil by incorporating the cation size effect into the DDL theory. The Stern DDL theory for constant surface charge condition was developed, for the first time, in this study to establish the potential-distance relationship of the interacting clay-water system. Further, the compressibility of the Stern layer was brought out and incorporated in the theory for a more realistic prediction of the compressibility behavior at a higher pressure range. The developed model was successfully validated against the compressibility data of six different bentonites from the literature.

Chapter-8 presents a detailed microstructural analysis to understand the SPEC characteristics of compacted bentonites under the influence of compaction density and bentonite plasticity. The influence of different electrolyte solutions with strong ionic strength and sand (non-clay) content on the SPEC characteristics of bentonites is also discussed in the chapter.

Chapter-9 presents the wetting-induced volume change behavior of a potentially collapsible kaolin clay under the influence of inundation pressure and compaction density. The applicability of the existing elastoplastic BBM model for the observed behavior of the studied kaolin was discussed. This chapter also discusses the role of various pore-scale forces in the volume change behavior of kaolin based on the microstructural analysis.

Chapter-10 presents important conclusions and scope for future study based on detailed analyses of the results and gaps in the present work.

2 Theoretical background

2.1 General

This chapter presents the basic characteristics of the common clay minerals, viz., kaolinite, montmorillonite, and illite that are primarily present in the clay soils considered in the study. A detailed description of the crystal structures of these clay minerals is presented and the important surface characteristics for understanding the clay-water interaction are discussed. The discussion then proceeds to the clay-water interaction involving various intermolecular forces. The Gouy-Chapman diffuse double layer theory to describe the physicochemical response of the fully saturated clay-water system is discussed, in detail. The relevance of various surface forces in clays at different mechanical, hydraulic, and physicochemical conditions is presented. Further, the theoretical formulation of pressure-void ratio relationships of saturated clays based on the DDL theory is presented at the end.

2.2 Clay minerals

Clay minerals belong to the class of hydrated phyllosilicates, which are formed by a specific combination of two basic structural units– silica tetrahedral sheet (Fig. 2.1a), and the octahedral sheet (Fig. 2.1b). The silica tetrahedron has a silicon atom as the coordinating cation, equidistant from four surrounding oxygens (or hydroxyls whenever needed to balance the structure). A hexagonal network of six tetrahedral is formed through the sharing of the oxygens at the base of the tetrahedra. The network is repeated infinitely in a-and b-direction to form the tetrahedral silica sheet. The octahedral sheet is consists of several octahedron units. The octahedron has a coordinating cation in the form of aluminum, iron, or magnesium atom, equidistant from six hydroxyls or oxygens. In the case of divalent cations, the structure is trioctahedral with all the available positions in the octahedral sheet are being filled. When a trivalent cation is present in the tetrahedral sheet, only two-thirds of the positions are filled to balance the structure and the structure is called di-octahedral. The octahedral sheet is called brucite when magnesium is the coordinating cation in the octahedron and is called gibbsite when aluminum is present (Grim, 1968).

One or more tetrahedral sheets combine with the octahedral sheet to form a layer. Generally, two types of layers are identified in clay minerals, depending on the ratio of the two sheets in the composition: the formation of one tetrahedral sheet and one octahedral sheet (TO) is called 1:1

layer, whereas an octahedral sheet between two opposing tetrahedral sheets (TOT) is termed as 2:1 layer. Clay mineral groups are classified based on the stacking of these layers.

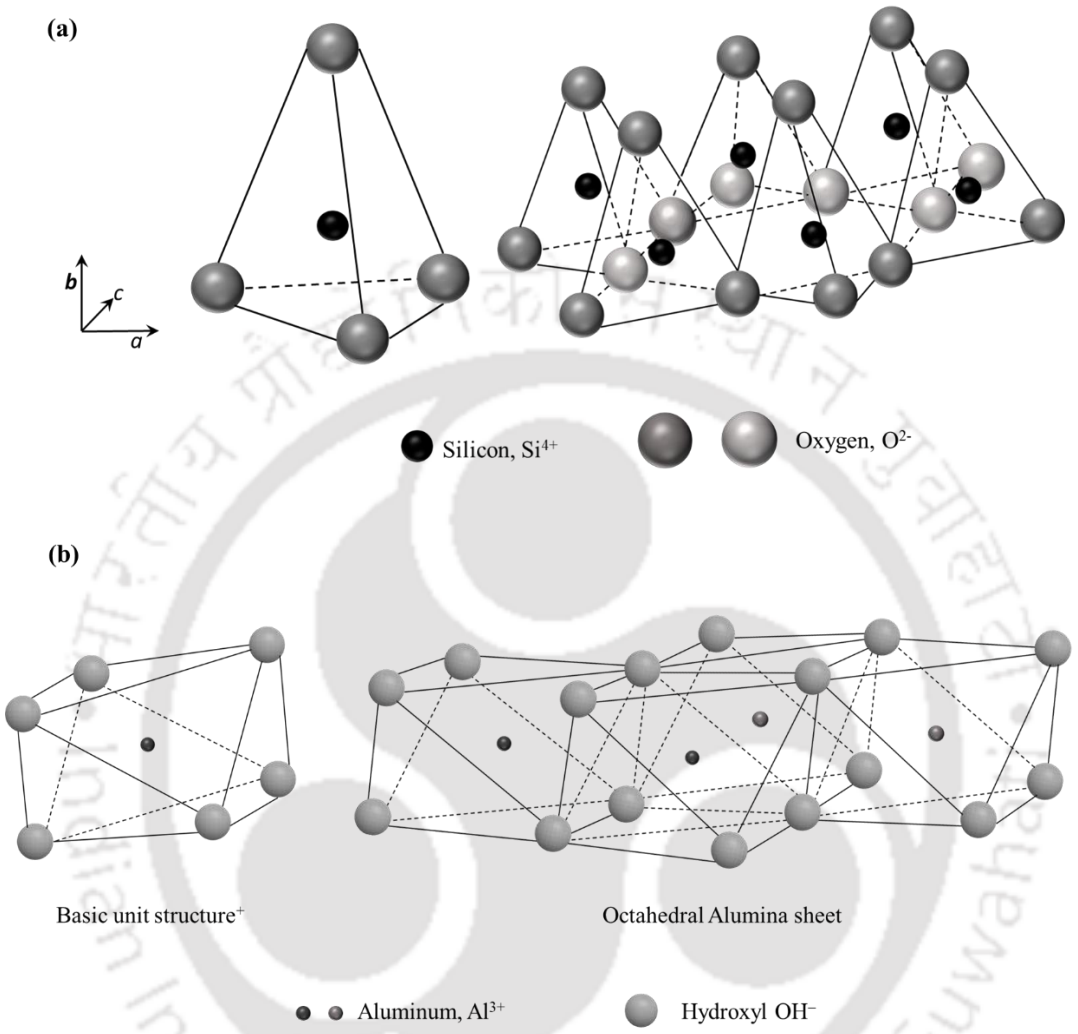

Fig. 2.1. Diagrammatic representation of tetrahedral and octahedral units (modified after Grim, 1968): (a) single silica tetrahedron (left), the sheet of tetrahedra arranged in a hexagonal network (right), (b) single octahedron (left), octahedral sheets (right).

Sometimes, interlayer components viz., cations, hydrated cations, organic molecules, and hydroxyl octahedral groups, may present to separate the stacked layers from one another. A unit or unit structure of a clay mineral represents the complete assembly of the layers and the interlayer components. For example, the unit structure of kaolinite consists of a 1:1 layer, while illite is consists of a 2:1 layer with interlayer potassium cations sandwiched between two such unit layers. Montmorillonite, on the other hand, consists of 2:1 layers and various cations (e.g., Na^{+}, Ca^{2+}, Mg^{2+}, Li^{+}) and water molecules as interlayer components (Grim 1968). Several stacked layers are

combined to form a particle (Tessier & Pedro 1976, Bergaya & Lagaly 2013). The number of layers in a single particle varies for different mineral types. The number of layers per particle also depends on the available amount of water in case of expanding montmorillonite. In a highly diluted suspension, it can be a single layer per particle, while several hundreds of layers per particle can exist at dry conditions (Tessier 1990a).

Isomorphous substitution is commonly observed in the clay structure due to which one type of ions is replaced by another of having different valence (but having a comparable size) in the lattice while retaining the same crystal structure (Grim, 1968). The extent and the type of the isomorphous substitution vary among the clay mineral groups and within the groups as well. Replacement of silicon by aluminum, aluminum by magnesium and iron ($Fe^{2+)}$ and, magnesium by iron ($Fe^{2+)}$ are commonly observed in clay minerals. This substitution results in a net permanent negative charge on the surface of clay particles. Thus, counter-cations (e.g., Na^+, Ca^{2+}, Mg^{2+}, Li^+, etc.) are available on the surfaces of such clay minerals to compensate for the negative surface charges. The surface cations of a particular type can be exchanged by another type thus often referred to as the exchangeable cations. The ease of exchangeability is determined by the type of the surface cations. Exchangeability decreases for the ions given below from left to the right: $Li^+ > Na^+ > K^+ > Mg^{2+} > Ca^{2+} > Sr^{2+} > Ba^{2+} > Al^{3+}$. The common clay minerals are discussed in detail below.

2.2.1 Kaolinite

Kaolinite consists of 1:1 layers stacked with alternating tetrahedral silica and octahedral sheets as shown in the schematic representation (Fig. 2.2). The octahedral sheet contains aluminum atoms at the coordinating position. The tips of the tetrahedral silica layer are towards the octahedral alumina layer. Two-thirds of the common plane atoms are oxygens which are shared by both the tetrahedral sheet and the octahedral sheet. The remaining atoms in this plane are the hydroxyls (OH). Kaolinite has the structural formula of $(OH)_8Si_4Al_4O_{10}$. The kaolinite unit cell exhibits different charge characteristics on its various surface sites. The charge on the basal face of the tetrahedral silica sheet is negative and permanent which is attributed to the isomorphous substitution of Al^{3+} for Si^{4+}(Palomino and Santamarina, 2005; Wang and Siu, 2006b). The negative charge on the silica basal face is small as the reported cations exchange capacity of kaolinite is generally in the range of 1–5 meq/100g (Ma and Eggleton, 1999). The basal face of the octahedral alumina sheet contains hydroxyl groups, thus the charge on this face is slightly pH-dependent and can be either positive or negative. Overall, the charge of the two faces combined is

considered to be negative with a pH-dependent magnitude. The surfaces of the edge of the two sheets contain OH_2, OH^-, and O^{2-} groups due to the termination and, protonation or deprotonation. The edge-sites are strongly dependent on the pH environment leading to either positive or negative charge. The exchangeable surface cations are available only on the external basal surface of the silica sheet as interlayer separation does not take place for the kaolinite structure. Electrostatic attraction, van der Waals forces, and hydrogen bonding between the Al-face site and Si-face site cause strong interlayer bonding for such an alternate arrangement of the silica and alumina sheets.

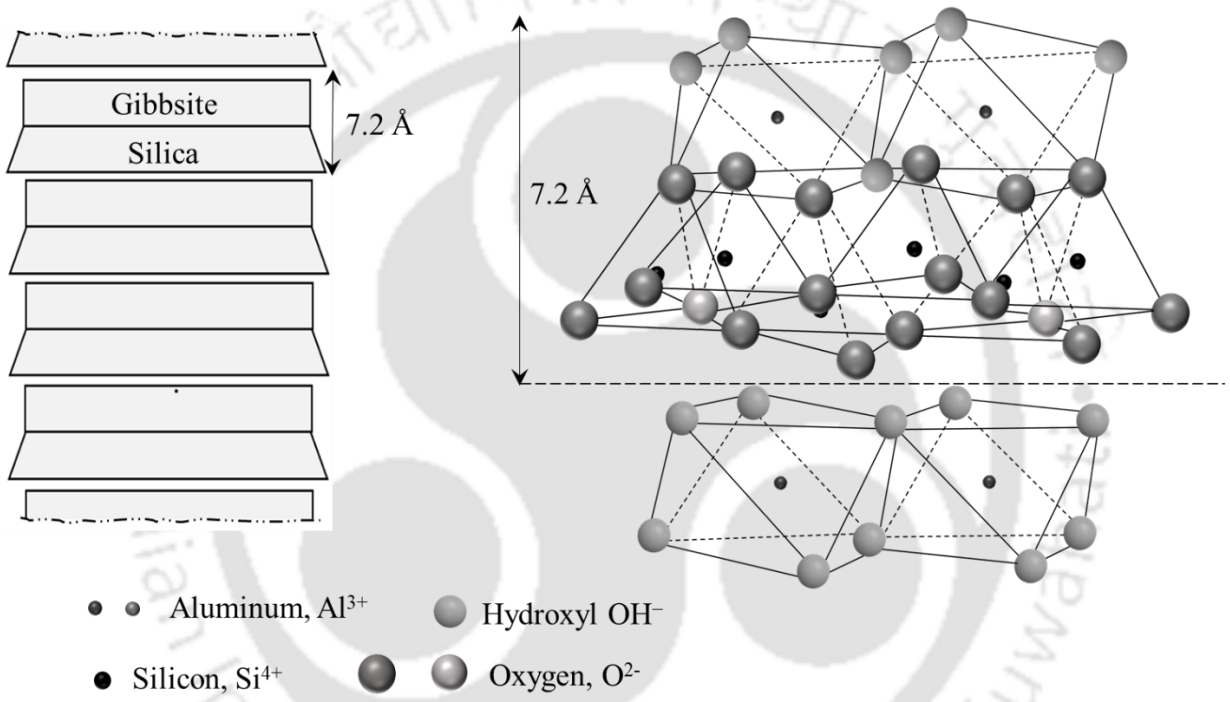

Fig. 2.2. Diagrammatic representation of unit layer of kaolinite: 1:1 layer arrangement (left), the unit structure of kaolinite (right)

2.2.2 Montmorillonite

Montmorillonite is a member of the smectite clay minerals group, which is distinguished from the other member of the smectite group (e.g., beidellite, hectorite, saponite) based on the type, amount, and placement of the substituted cations in the crystal structure. The basic structure for smectite minerals is similar to that of pyrophyllite (Fig. 2.3). It consists of 2:1 layers with an octahedral sheet sandwiched between two tetrahedral silica sheets. The tips of the two silica sheets face towards the octahedral sheet in between them and the oxygen atoms of the tips are shared with the octahedral sheet. The hydroxyl groups of the tetrahedral sheets are in alignment with the hexagonal

holes (often referred to as siloxane cavities) of the bases of the silica sheets. The 2:1 layers are stacked along the c-direction to form a montmorillonite particle. For this arrangement, the faces of the two adjacent layers are similar containing the oxygen plane of the silica sheets, unlike the kaolinite. Thus, the interlayer bonding in the montmorillonite is relatively weak. The bonding between the layers is derived from the van der Waal's forces and the balancing cations on the basal surfaces. The interlayer spaces of the smectite minerals can be accessed by water or other polar molecules leading to expansion of the crystal structure in the c-direction. Thus, the interlayer distance of smectite minerals varies depending on the amount of available water and the type of cations. Completely dry smectite mineral has an interlayer spacing equivalent to the size of interlayer cations which can increase to a value of more than 9.6 Å at full saturation. The structural formula of smectite minerals without considering isomorphous substitution is,

$(OH)_4Si_8Al_4O_{20} \cdot nH_2O$

The actual formula of smectite minerals varies from the above as there is considerable isomorphous substitution in the crystal structure. The silicon atoms in the tetrahedral sheet are replaced by aluminum and possibly phosphorous and/or the aluminum atoms in the octahedral sheet are replaced by magnesium, iron, and, sometimes by zinc, nickel, lithium, and other cations. The type of the smectite mineral is defined based on the type of substituted ions and the number of available positions.

For the montmorillonite mineral, isomorphous substitution takes place for every sixth Al^{3+} by one Mg^{2+} in the octahedral sheet. The tetrahedral silica sheet is free of such substitution. The charge deficiency due to this is about 0.66 C per unit cell. Considering the above substitution of Al^{3+} by Mg^{2+}, the formula for one unit cell of montmorillonite is written as,

$(OH)_4Si_8(Al_{3.34}\ Mg_{0.66})O_{20} \longrightarrow Na_{0.66}$

The group has an overall charge deficiency as indicated by the arrow. External cations (e.g., Na) and water molecules (not shown in the equation) are present on the surface to compensate for the charge deficiency.

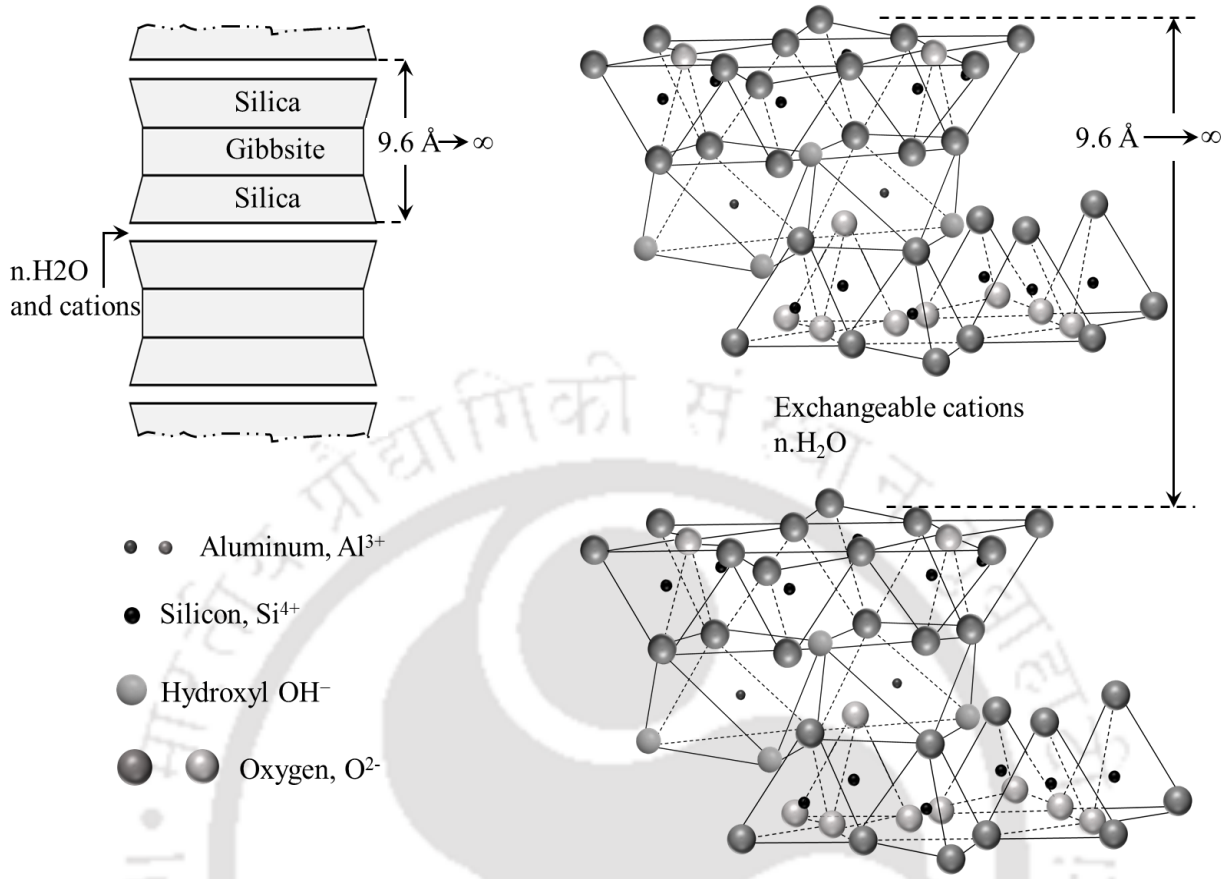

Fig. 2.3. Diagrammatic representation of unit layer of montmorillonite: 2:1 layer arrangement (left), the unit structure of montmorillonite with interlayer water, and exchangeable cations (right)

2.2.3 Illite

Illite has a similar structural unit to that of montmorillonite, which has the 2:1 layer (Fig. 2.4). The difference between the two minerals are, (i) Illite has a charge deficiency of 0.65-0.75 C per half unit cell and montmorillonite has a charge deficiency of 0.33 C per half unit cell, (ii) the charge deficiency of illite are mostly due to the substitution in the tetrahedral silica sheet thus the charge location is in the outer sheets of the unit layer, whereas the substitution in smectite is in the inner octahedral sheets, the position of the charge is relatively inside of the unit layer, (iii) the interlayer cation balancing the charge deficiency is mainly or entirely potassium in the case of illite. The structural unit layer of illite is relatively fixed as the interlayer potassium are not easily exchangeable. The accessibility of polar molecules into the interlayers is very low as compared to the montmorillonite, thus exhibiting minimal interlayer hydration. Slight hydration is observed

sometimes due to the possible replacement of the potassium cations by other cations viz., Ca^{2+}, Mg^{2+}, H^{+}. The general structural formula for illite is, $(OH)_4K_2(Si_6\ Al_2)Al_4O_{20}$.

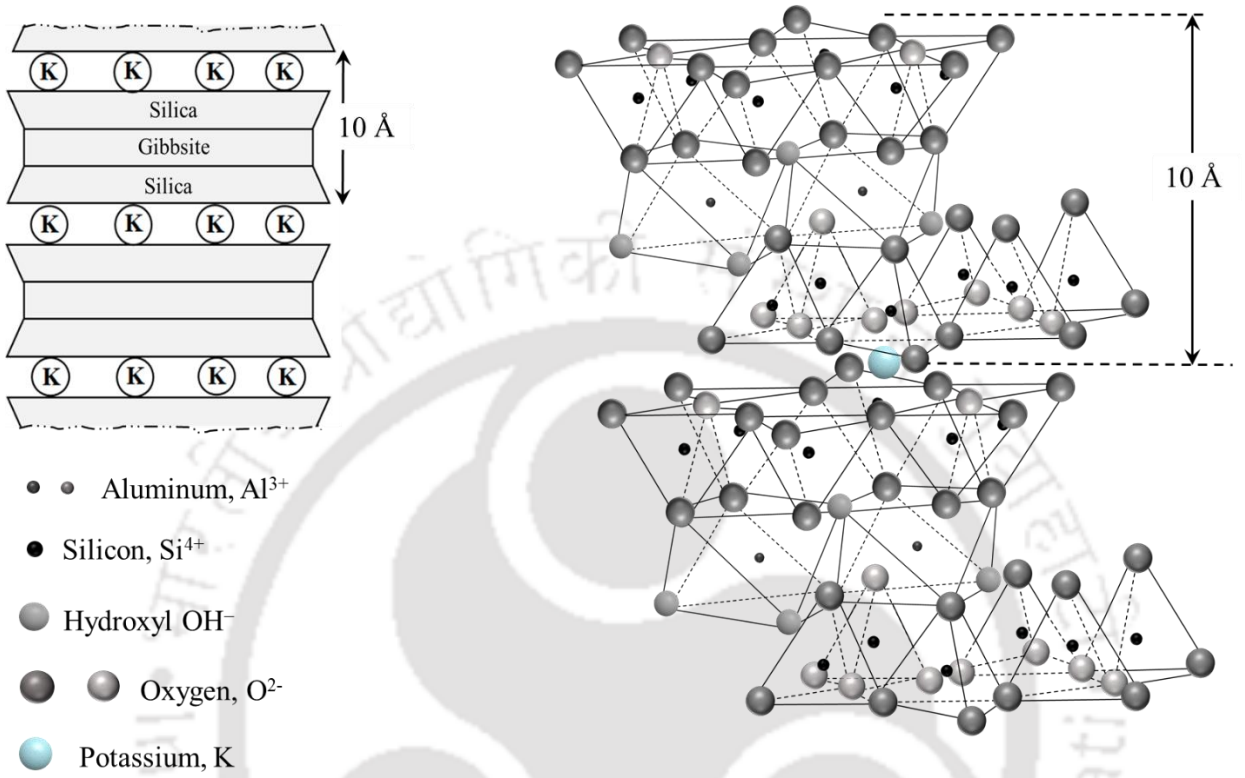

Fig. 2.4. Diagrammatic representation of unit layer of illite: 2:1 layer arrangement (left), the unit structure of illite with interlayer potassium (right)

2.3 Clay-water interaction

The interaction of clays with water or other electrolytes is important in understanding the engineering behaviors of clays *viz*., the volume change behavior, chemical sorption, and flow-related problems. Clay-water interaction at the microscopic particle level involves the physicochemical forces owing to the surface charge characteristics of the clay minerals. In a clay-water system, water can exist in different forms, viz., structural water, adsorbed water, diffuse double layer water, and free (bulk) water depending on the interaction mechanisms/bonding nature. The bonding strength and the properties of the water molecules present in the system depend on the clay mineralogy and the environmental conditions such as temperature, salinity, and amount of available water.

Structural water refers to the H_2O molecules and OH molecules bonded to the cations in the crystallographic sites of the structural units. In clay minerals, the structural water is mostly present in the form of hydroxyl (OH) groups strongly bonded to the cations. Dehydroxylation of the structural water initiates at a temperature of 1000^0C.

Adsorbed water includes the H_2O molecules bonded to the external and internal surfaces of clays and the balancing cations. The thickness of the adsorbed water consists of one or more layers of water molecule thickness. The adsorption of the water molecules on the clay surface is through hydrogen bonding. The positive corner of the H_2O molecule is attracted by the oxygen (O) atom and the negative corner is attracted by the hydroxyl (OH) group present on the surface of the clay minerals. Cation hydration is important at the dry-end (i.e. low water content) state of clay soils. Hydration of the surface cations is a result of the attraction between the negative ends of the water dipoles and the positive charge of the cations. The strong water dipole attraction to the clay surface is attributed to the high energy and hydration number of the aluminum in the octahedral sheet (Ingles, 1968). In general, the adsorbed oriented water molecules are observed close to the clay surface followed by the surface cations at low water contents. The characteristics of the adsorbed water molecules such as structure, density, and viscosity are significantly different from the free water. Further, these characteristics of the adsorbed water can significantly vary from a low-water content to a fully saturated state (Low, 1959; Martin, 1960).

Further, the balancing cations on the clay surface start experiencing an additional diffusive type of force in the presence of water or electrolyte medium, that tries to drive the cations away from the charged clay surface. The diffusive forces are due to the existing concentration gradient of cationic species between the clay surface and the bulk electrolyte solution. A very high cationic concentration exists near the clay surface because of the strong electrostatic attraction by the negatively charged surface. The diffusion of the cations is, however, hindered by the strong electrostatic attraction from the clay surface. As a result, water molecules are diffused towards the clay surface to establish the concentration equilibrium (Fig. 2.5). Thus, a water film is formed around the clay particles, which is termed a diffuse double layer (DDL). This DDL water is held to the clay particles by the hydrated balancing cations and plays an important role in the clay particle-particle interactions. The behavior of expansive clays is often related to the response of the DDL water under different mechanical and physicochemical stress state.

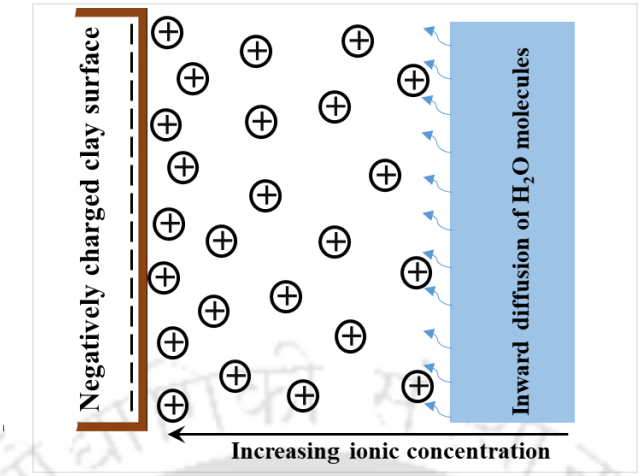

Fig. 2.5. Adsorption of water onto the clay surface driven by osmosis

A schematic representation of the DDL around a single clay platelet immersed in water is presented in Fig. 2.6. The distribution of the cationic and anionic species around the clay platelet at equilibrium is illustrated in Fig. 2.6a. The cations are attracted towards the negative clay surface thus the concentration of the cations near the surface is very high and decreases away from the surface. The anions, on the other hand, are repelled by the negative surface and their concentration increases as the distance from the clay surface is increased. The variation of cationic and anionic concentration with distance is shown in Fig. 2.6b. The concentration of the cations and anions are eventually becomes equal at some distance from the clay surface (theoretically at an infinite distance) which defines the boundary of the diffuse double layer. The electrostatic potential distribution within the DDL is represented by the Poison-Boltzman equation as described in the Gouy-Chapman DDL theory, presented below.

2.3.1 Gouy-Chapman diffuse double layer theory

The potential distribution in diffuse double layer around a clay plate, as suggested by Gouy-Chapman (1910), is illustrated in Fig. (2.7). The following assumptions are involved in the theory: (i) the surface of the clay particles is represented by a flat surface without any edge effects (that is, an infinite surface). (ii) the charges are uniformly distributed over the surface (iii) the electrolyte is considered as a continuous medium (it is immersed in an electrolyte solution), influencing the double layer only through its dielectric properties. The dielectric properties are assumed spatially invariant within the double layer. (iv) the charge on the surface is neutralized by an excess of ions of opposite sign, and all the ions are considered as point charges. (v) the interaction between the

clay surface and the ions are assumed to be only electrostatic and the mutual ionic interactions such as those treated by the Debye-Huckel theory are neglected.

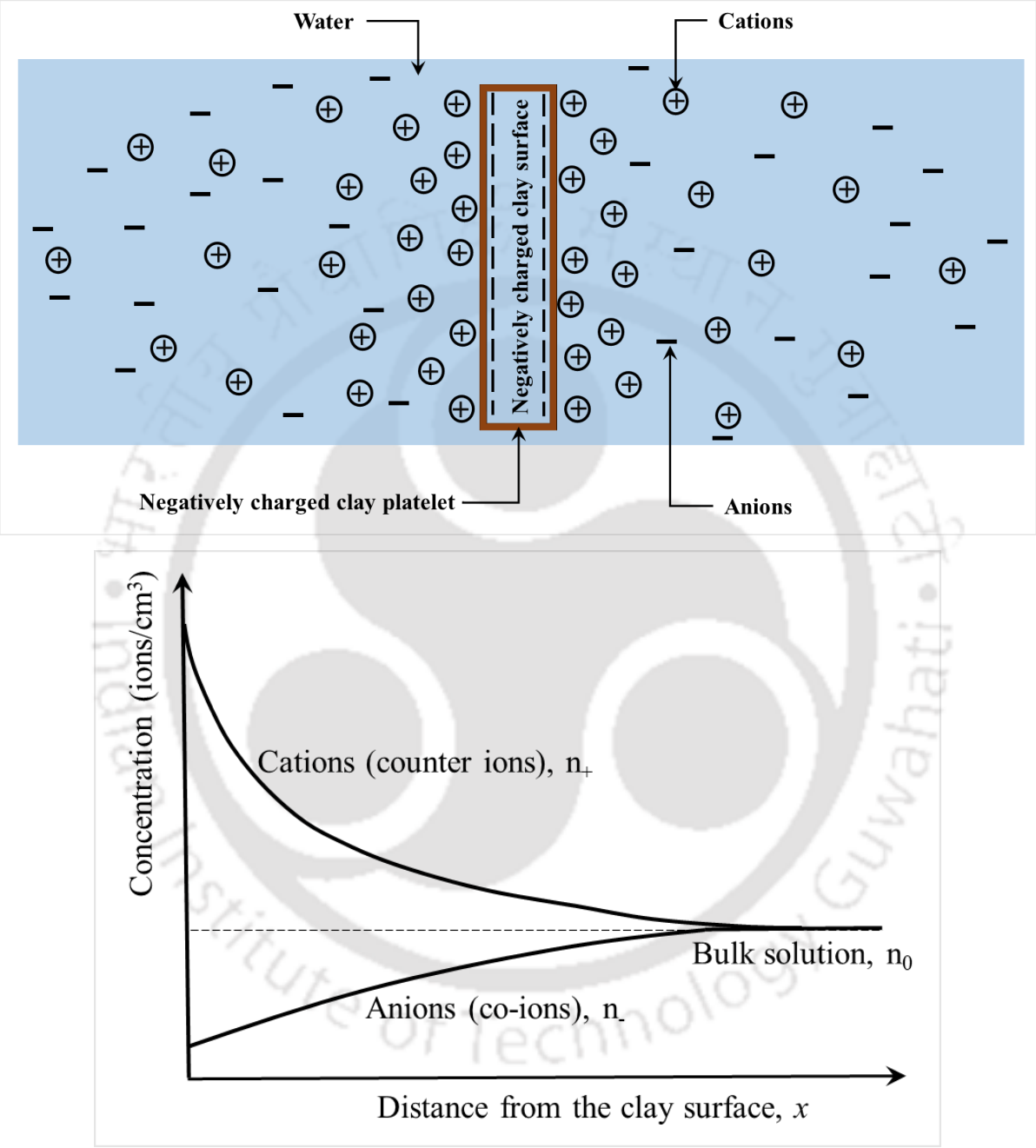

Fig. 2.6. Diffuse Double Layer around a single clay particle in presence of electrolyte/water (a) schematic representation of diffuse double layer, and (b) charge distribution within the diffuse double layer (After van Olphen, 1973)

The electrostatic potential distribution in DDL of a single plate is given by the Poison-Boltzman equation as shown below:

$$y = 2\ln\left(\frac{\exp(\kappa x)+\exp\left(\frac{y_0}{4}\right)}{\exp(\kappa x)-\exp\left(\frac{y_0}{4}\right)}\right) \tag{1}$$

where, y is the normalized electrostatic potential ($= vq\phi / RT$), at a distance x from the surface of the clay platelet, y_0 is the normalized electrostatic potential at the clay surface ($y_0 = vq\phi_0/kT = vF\phi_0/RT$), $\frac{1}{\kappa}$ is the characteristics length or debye length $\left(\kappa = \sqrt{\frac{8\pi q^2 v^2 n}{\varepsilon D_0 kT}}\right)$, q is the electronic charge ($=1.6\times10^{-19}C$), v is the valence, k is the Boltzmann constant, F is the Faraday constant, ϕ is the electric potential at any distance x, ϕ_0 is the electric potential at the clay surface, R is the gas constant, T is the absolute temperature, ε is the dielectric constant, D_0 is the dielectric permittivity of vacuum ($=8.854\times10^{-12}C^2/N-m^2$), and n is the molar concentration of the ions in bulk solution (ions/m^3).

The electric potential near the surface is calculated as,

$$\phi_0 = 0.1725\frac{T}{v}\sinh^{-1}\left(\frac{1256.81\times\frac{C_e}{S_a}}{\sqrt{n\varepsilon T}}\right) \tag{2}$$

where C_e is the cation exchange capacity in meq/100g, and S_a is the specific surface area in m^2/g.

When the distance between two charged plates is such that, the diffuse double layer of both the plates overlap/interact, then the clay-electrolyte system is considered as an interacting system. The resulting potential distribution between the two plates is shown in Fig. (2.8). The mid-plane potential is uniquely related to the separation distance between the clay platelets and represents the degree of interaction in the system. The relationship between the mid-plane potential and the separation distance is given by the Poisson-Boltzmann's equation,

$$t_{DDL} = -\frac{1}{\kappa}\int_{y_0}^{u} (2\cosh(y) - 2\cosh(u))^{-1/2}\, dy \qquad (3)$$

where t_{DDL} is the thickness of the DDL which is equal to half of the separation distance (d) in the Gouy-Chapman DDL model, u is the normalized electrostatic potential at the midplane.

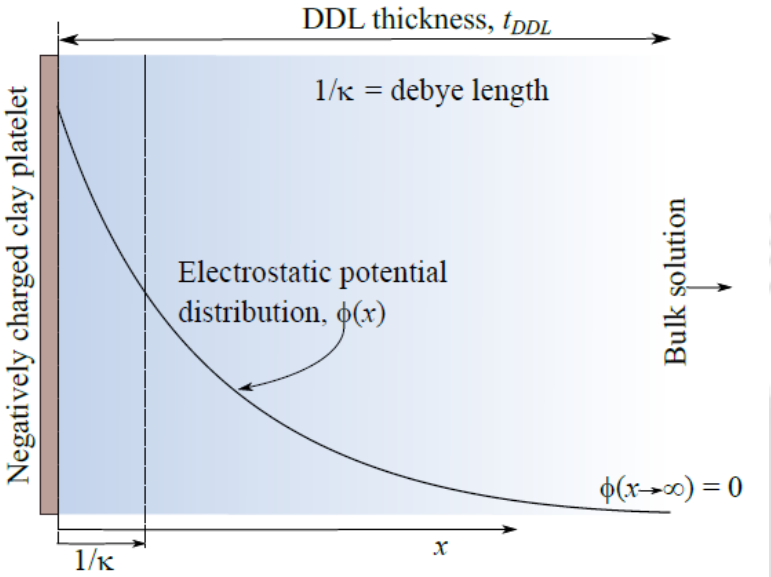

Fig. 2.7. Electrostatic potential distribution in a non-interacting clay-water-electrolyte system (After Bharat and Sridharan, 2015a)

The electrostatic potential at the surface of the interacting clay platelets is estimated for a given soil surface and electrolyte properties based on the following relation,

$$\left(\frac{dy}{d\xi}\right)_{x=0} = \sqrt{2\cosh(y_0) - 2\cosh(u)} = \sigma\sqrt{\frac{1}{2\varepsilon D_0 nkT}} = 0.96352\frac{C_e}{S_a}\sqrt{\frac{1}{2\varepsilon D_0 nkT}} \qquad (4)$$

where $\left(\frac{dy}{d\xi}\right)_{x=0}$ is the slope of the potential distribution curve near the clay surface, ξ is the normalized distance (κx), σ is the total surface charge density on the clay surface.

The interaction between the diffuse double layers of adjacent plates leads to the existence of osmotic (repulsive) forces between the plates. These repulsive forces are predominant in expansive clays and are often termed as long-range DDL repulsive forces. The calculation of the repulsive pressure between two interacting clay platelets due to the long-range DDL repulsive

forces is presented in the next section (subsection 2.4.1). The developed mid-plane potential (ϕ_d) between the interacting diffuse double layers at equilibrium is a measure of the osmotic pressure.

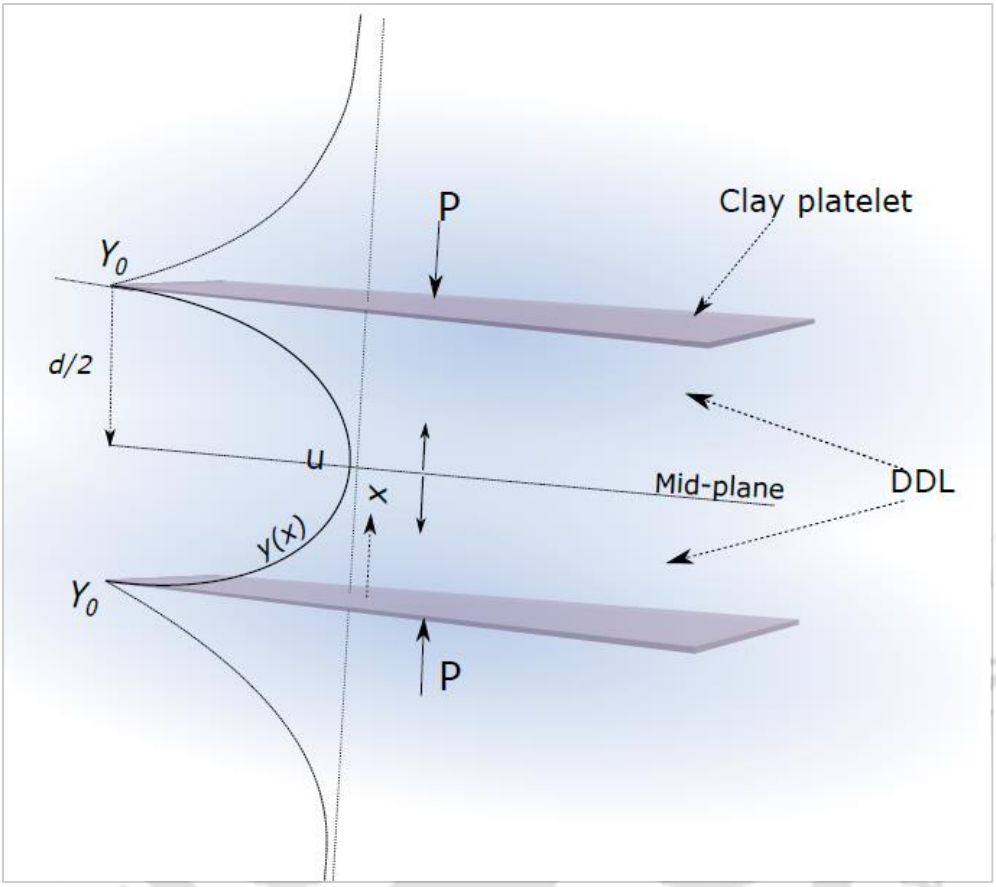

Fig. 2.8. Electrostatic potential distribution in an Interacting clay-water-electrolyte system as per Eq. 3.

The Gouy-Chapman model, however, is applicable only for the homoionic clay-water system and is not applicable for the natural clays that contain mixed-valent cations on the surface. Bresler (1970, 1972) presented a modified equation for the potential-distance relationship by considering the mixed cations in the exchange complex of clays. The general expression for half-space distance in an interacting clay-water system consisting of divalent and monovalent cations is given by (Bresler, 1970; Collis-George & Bozeman, 1970; Bresler, 1972)

$$d = \sqrt{\frac{\varepsilon}{8\pi N_A k_B T}} \sqrt{\frac{r+1}{c_0}} \int_{\phi_d}^{\phi_0} \frac{d\phi}{\sqrt{\left(e^{-y^*} - e^{-u^*}\right) + r\left(e^{-2y^*} - e^{-2u^*}\right) + (1+2r)\left(e^{y^*} - e^{u^*}\right)}} \qquad (5)$$

where c_0 is the Molar concentration of the ions in bulk solution (M), r is the ratio of the molar concentration of divalent ions to monovalent ions i.e., c^{++}/c^{+}), ϕ represents the electrostatic potential at any distance x from the clay surface, y*= y/ν ($=\frac{e'}{kT}\phi$), ϕ_0 is the electrostatic potential at the surface of clay platelet, ϕ_d is the electrostatic potential at the midplane, and $u^* = u/\nu (=\frac{e'}{kT}\phi_d$).

Another serious limitation for which the model has been often criticized is that the specific effect of the size of the cations is neglected as the ions are treated as point charges. Stern model (Stern, 1924) incorporates the effect of the size of cations into the DDL theory through a thin and compact layer of cations next to the clay surface. The electrostatic potential distribution of an interacting clay-water system based on the Stern model at constant charge condition is not established yet. A discussion on the formulation of the potential-distance relationship for the interacting system by the Stern model is presented below.

2.3.2 Stern DDL model considering the finite size of cations

The finite size of the cations at the particle surface limits the closest approachable distance to the charged clay surface (Stern, 1924). This results in a relatively compact and immobile layer of counter-ions close to the surface, which is followed by a diffused layer of the counter-ions. Thus the electric double layer in a clay-water system is characterized by the Stern layer and the outer diffused layer consisting of the Gouy layer. The center of the spherical cations in the stern layer is at a distance of approximately equal to their hydrated radius away from the clay surface (Guven and Pollastro, 1992), which is defined as the outer surface of the Stern layer (Shang et al., 1994). The charge within the Stern layer is zero and the electrostatic potential varies linearly. The adsorbed water molecules in the stern layer are held tightly due to which the dielectric constant of water in the stern layer is significantly reduced to 3-6 by experimental evidence (Verwey & Overbeek, 1955; Sridharan, 1962; van Olphen, 1977; Sposito, 1984; Hunter, 1987; Shang et al., 1994; Sridharan & Satyamurty, 1996). A graphical illustration of the Stern model for the interacting clay-water system was presented in Fig. 2.9. The inter-platelet separation distance, *d*, in the Stern model is the summation of the stern layer thickness δ and the thickness of the Gouy diffuse layer, t_{DDL}.

$$d = 2(\delta + t_{DDL}) \tag{6}$$

The potential varies linearly from a maximum value (y_0) at the clay surface to y_δ at a distance equal to the stern thickness (δ) at the Stern-Gouy interface where the potential is termed as the Stern potential (y_δ). The potential distribution within the Stern layer is dependent on the surface charge density and the dielectric properties of the pore fluid as given in the following equation:

$$\sigma = \frac{\varepsilon' kT}{4\pi\delta vq}\left(y_0 - y_\delta\right) \tag{7}$$

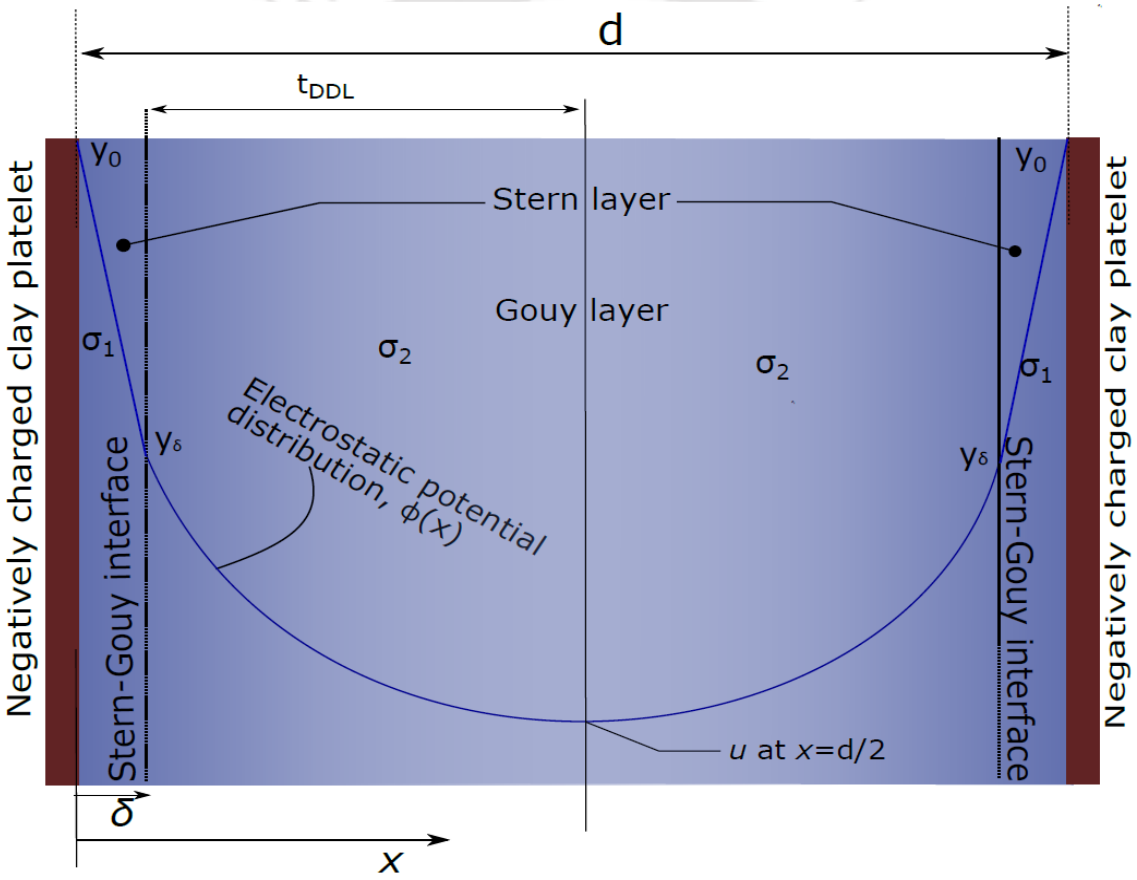

Fig. 2.9. Electric potential distribution in Stern DDL model

Within the Gouy layer, the electrostatic potential distribution varies non-linearly between stern potential (y_δ) at the x = δ and mid-plane potential (y_d) at x = *d/2*, which is represented by the Poisson-Boltzmann equation:

$$\kappa t_{DDL} = -\int_{t_{DDL}-\delta}^{t_{DDL}} d\xi = -\int_{y_\delta}^{u} (2\cosh(y) - 2\cosh(u))^{-1/2}\, dy \qquad (8)$$

The above equation involves one additional unknown in the form of the stern potential and its evaluation is a prerequisite for the estimation of Gouy layer thickness. The relationship between the charge density and potential distribution is utilized to determine the stern potential for a given clay-water-electrolyte system. The stern layer charge (σ_1) and Gouy layer charge (σ_2) together balance the total negative surface charge (σ) on the clay particle:

$$\sigma = -(\sigma_1 + \sigma_2) \qquad (9)$$

The clay particles are treated as constant-charged plates (Grim 1968), for which the total surface charge density can be expressed as,

$$\sigma = 0.96352 \frac{C_e}{S_a} \text{ C/m}^2$$

where C_e is the cation exchange capacity of soil expressed in *meq*/100*g* and S_a is the specific surface area expressed in m^2/g. The charge density in the Stern layer can be obtained as (Verwey and Overbeek, 1948);

$$\sigma_1 = \frac{N_1 v q}{1 + (N_A/Mn)\exp\left(-\left(y_\delta + \psi v q / kT\right)\right)} \qquad (10)$$

where N_1 = no. of adsorption spot per 1 cm^2 area of the clay surface, v is the valence of ions, N_A = Avogadro's number, *M* = molecular weight of the solvent (water), y_δ = Stern potential at the plan separating Stern and Gouy layer, ψ = specific adsorption potential on the counter-ions at the surface. The charge in the Gouy layer can be derived as (Verwey and Overbeek, 1948; van Olphen, 1977);

$$\sigma_2 = \sqrt{2nkT\varepsilon}\sqrt{2\cosh y_\delta - 2\cosh u} \tag{11}$$

Combining Eqs. 7, 9, 10 & 11, the stern potential can be expressed as a function of the mid-plane potential and the pore fluid parameters. However, Eq. 10 is only valid for non-interacting systems and requires refinement for applying to the interacting clay-water system. The number of available spots in the bulk solution, N_1 is dependent on the volume of the diffuse layer which is subjected to change with the change in the degree of interaction under the applied pressure. van Olphen (1963) presented an approximate relationship by applying an approximate treatment to the Stern layer which is reasonably valid for weak interaction. In this treatment, the statistical charge distribution between the Stern and Gouy layer is considered to be proportional to their respective volumes or their respective thickness.

$$\sigma_1/\sigma_2 = \left[\delta \Big/ \left(\frac{d}{2} - \delta\right)\right] \exp\left[y_\delta + (\psi/kT)\right] \tag{12}$$

However, equation (12) leads to erroneous estimations as it does not utilize the correct volume of the Gouy diffused layer considered in the treatment Stern-Gouy interface. The theoretical framework for the potential-distance relationships in an interacting clay-water system is yet to be developed based on the Stern model.

2.4 Surface forces in clays

Because of the charge characteristics on the surfaces of the clay minerals, surface forces govern the clay-water interaction and the clay particle-particle interactions, which control the overall clay behavior. The interplay between the surface forces and the applied mechanical stress determines the clay fabric. The magnitude and nature of the surface forces vary significantly depending on the mineral type, moisture condition, and the type of inter-particle interaction. Knowledge of the relevant surface forces at different moisture states in the clay minerals is important in understanding the hydro-mechanical behavior of clays. This section presents a discussion on the relevant surface forces in clays and presents the existing theoretical formulation for estimating the inter-particle pressure due to each of the surface forces.

2.4.1 Diffuse double layer repulsive force

The diffuse double layer repulsive forces are predominant in a fully saturated clay-water system, especially for the montmorillonite-rich clays. As explained earlier in section 2.3, in the presence of a water/electrolyte medium, the cations on the clay surface experience an additional diffusive type of force that tries to drive the cations away from the charged clay surface. The diffusive forces are developed due to the existing concentration gradient of cationic species between the clay surface and the bulk electrolyte solution. An electric diffuse double layer (cation cloud) is formed around the clay particles as a consequence of the competition between the strong electrostatic attraction between the cations and negatively charged clay surface, and the diffusive forces (Verwey and Overbeek, 1948; van Olphen, 1977). When two clay platelets are brought close to each other, the DDLs around the clay platelets interact. There is a repulsive pressure developed between the two clay platelets due to the interaction of similarly charged DDLs and the diffusive tendency of the cations within the DDL.

The Gouy-Chapman diffuse double layer theory (Gouy, 1910; Chapman, 1913) estimates the repulsive pressure generated between the parallel clay platelets based on the electrostatic potential distribution within the DDL. An illustration of an interacting parallel-plate clay-water-electrolyte system, as per the Gouy-Chapman DDL model is presented in Fig.2.8. The electrostatic potential distribution within the interacting system is represented by the curve *y(x)* with a minimum normalized potential (*u*) at the mid-plane as shown in Fig. 2.8. As the clay platelets are brought close to each other, the midplane potential rises, and a repulsive pressure (P_R) develops between the clay platelets. The mid-plane potential is related to the repulsive pressure between the two platelets as per the equation given by Langmuir (1938) relate the repulsive pressure to the midplane potential as follows,

$$P_R = 2nkT\left(\cosh(u)-1\right) \tag{13}$$

The magnitude of the long-ranged double-layer repulsion is significantly influenced by the amount of available moisture content or the degree of saturation. The repulsive forces are absent in dry clays whereas maximum repulsive pressure develops at full saturation. The formulation based on the Gouy-Chapaman DDL theory provides the estimation of the maximum repulsive pressure between two parallel clay platelets at full saturation and does not apply for the partially saturated

soil. Further, the double-layer repulsion is influenced by various parameters such as the pore fluid properties (e.g., ionic concentration, cationic valence, size of cations, dielectric constant), soil surface properties (e.g., specific surface area and surface charge characteristics), and the mode of particle-particle interaction (i.e. orientation). An increase in ionic concentration and cation valence decreases the repulsive forces at a given separation distance. On the other hand, the repulsion increased with an increase in the dielectric constant. The repulsive forces are generally higher for soils with higher specific surface area and surface charge density such as montmorillonites. The double-layer repulsion is very minimal and can be neglected in the 1:1 layer kaolinite minerals.

2.4.2 Van der Waals attractive forces

The Van der Waals (VdW) attraction between two neutral particles or surfaces arises due to the interactions between their ions, atoms, or molecules because of their inherent polarity or induced polarization by other polar molecules or charges in the proximity. Various interactions viz., ion-dipole, dipole-dipole, dipole-polarized molecule, and between polarized molecules, are considered to contribute to the VdW forces. The VdW attractive force between macroscopic bodies (e.g., particle or surface) is obtained through the integration of the interaction energy of all atoms in the body. Although the VdW atom-atom interaction is short-ranged (~ $1/r^6$), the interaction at the clay particle level are long-ranged (~1/D) (Israelachvili, 2011). The attractive pressure between two parallel clay surfaces due to the VdW interaction can be estimated using the following equation (Israelachvili, 2011),

$$P_{vdw} = \frac{A_h}{6\pi d^3} \tag{14}$$

where A_h is Hamekar's constant and d is the separation distance between the two clay platelets. Further, accounting for the thickness of the clay platelet, δ, the pressure due to VdW attraction can be obtained from the following equation (van Olphen, 1962; Sridharan and Jayadeva, 1982),

$$P_{vdw} = \frac{A_h}{48\pi}\left[\frac{1}{\left(d/2\right)^3} + \frac{1}{\left(d/2+\delta\right)^3} - \frac{2}{\left(d/2+\delta/2\right)^3}\right] \tag{15}$$

VdW attractive force is dependent on the Hamaker's constant and the separation distance between the clay platelets. The Hamaker's constant incorporates the influence of interacting bodies and the intervening medium on the VdW interaction energy. The Lifshitz theory is commonly utilized to estimate the Hamaker constant for macroscopic bodies in various intervening media. Typically, Hamaker's constant is represented in terms of the dielectric constant of the interacting bodies and the intervening medium (Sridharan 1968, Israelachvili 1992, Anandarajah & Chen 1997). The values of the Hamaker's constant for different interacting bodies and intervening media systems relevant for the soil behavior are presented in Table 2.1. For the montmorillonite/kaolinite minerals, the value of Hamaker's constant was presented as a function of the degree of saturation by Sridharan (1968). The reported values (in Table 2.1) for montmorillonite/kaolinite in air and water were estimated for $S_r = 0$ and $S_r = 1$, respectively.

The value of Hamaker's constant is smaller when water is the pore fluid instead of air. Thus, the VdW attractive forces decrease with an increase in the degree of saturation in clays. The attractive forces also decrease with the increase in the separation distance and are significant in clays at a separation distance of a few angstroms to hundreds of angstroms. At a very small separation distance, the VdW forces become repulsive or the Born's repulsion dominates. The estimation of inter-particle pressure due to the VdW forces using Eq. 14 & 15 is valid only for a face-face (parallel) particle arrangement. Estimation of the inter-particle pressure due to the VdW interaction is quite complex due to the presence of edge-face association and variation in the aggregate sizes (Yang et al., 2015). The variation of VdW attraction with the relative orientation of kaolin particles has been studied through DEM simulation in recent studies (Jaradat and Abdelaziz, 2018). The VdW attraction is maximum when the relative inclination is 0^0 (face-face) and 90^0 (vertical edge-face) and the magnitude reduces with changes in the orientation from the configuration to a minimum value at 45^0 inclinations.

2.4.3 Columbic forces

Columbic forces exist in clays due to the varying charge characteristics on the surfaces of different clay minerals. The basal faces often carry a negative charge because of the isomorphous substitution, whereas the edges carry pH-dependent charges which are either positive or negative depending on the pH. Thus, both columbic attraction and repulsion are prevalent in clays and play an important role in the particle-particle association. The basal surface of the alumina sheet in the

kaolinite minerals is also pH-dependent. Thus, these forces are more relevant in kaolin at different particle-particle interactions. Irrespective of whether the interaction is attractive or repulsive, the magnitude of columbic force depends on the charge density and the dielectric constant of the pore-fluid. Estimation of the inter-particle pressure by the columbic interaction is very complex due to the wide variation in the size and shape of the clay particles, different modes of particle-particle association, and the surface charge characteristics. For the simplest case, where two identical clay platelets are in a face-face orientation, the columbic force is inversely proportional to the separation distance and the dielectric permittivity and is given by,

$$F_c = \frac{\pi b^2}{8\varepsilon_0 \varepsilon_r} \rho^2 \left(\frac{d}{\sqrt{b^2 + d^2}} - 1 \right) \tag{16}$$

where b is the average diameter of the clay particle, ε_0 is the dielectric permittivity of air in F/m, ε_r is the relative permittivity of intervening medium, ρ is the surface charge density on the face of the clay particle in C/m^2, and d is the separation distance. The magnitude of columbic forces in clays thus is higher in the dry state and reduces with an increase in the degree of saturation. Additionally, the saturation of the clay particles can alter the pH of the clay-water system which affects the magnitude and the sign of the columbic forces.

Columbic forces are generally very small for the montmorillonite-rich clays as the charges on the edges are negligible compared to the very high surface charge density on the basal surfaces. The double-layer repulsive forces predominate the clay-water interaction in montmorillonite-rich clays. In kaolinite, however, the double-layer repulsion is very minimal and thus the presence of the columbic forces is of significant importance. The basal surfaces of the silica sheet in kaolinite carry a permanent negative charge while the charge on the face of the alumina sheet is pH-dependent. The charges on the edges are meanwhile highly pH-dependent (Celik, 2004; Choudhuri and Bharat, 2018; Delgado et al., 1986, Ramos-Tejada et al., 2001, 2002, Kelessidis et al., 2007) and transform from positive to negative depending on the pH. The charge transformation due to the pH variation is often analyzed based on the isoelectric point (IEP) of the clay particle on its different surfaces. IEP is defined as that pH value where the clay particle exhibits zero electrophoretic mobility i.e., ζ–potential is zero. The ζ–potential refers to the electrostatic potential at the shear plane between the bulk fluid and the tightly bonded thin layer of water next to the clay

surface (van Olphen, 1963). The charge on the kaolinite surface is positive when the pH < IEP and becomes negative when pH > IEP. The IEP of the basal surface (IEP-face) differs from the edges (IEP-edge) causing complex transformation in the charge characteristics and the particle-particle interactions due to the changes in the pore fluid chemistry in kaolinite. In dry kaolinite, the edge-face and edge-edge association are predominant due to the strong columbic attraction between the negatively charged basal face and the positively charged edges (Gupta, 2011; Choudhury and Bharat, 2018).

2.4.4 Capillary forces

Capillary force is another important type of force that acts between two clay particles when a fluid medium is present in between under favorable conditions. In a partially saturated state, the meniscus (i.e., the contractile skin at the fluid-air interface) tends to bring the clay particles towards each other. These pulling forces are attributed to the cohesive and adhesive forces in the fluid medium resulting from the intermolecular interactions viz., the electrostatic and the van der Waal's attractions.

The magnitude of the capillary forces is directly related to the surface tension at the fluid-air interface, the shape of the capillary meniscus, and the wettability of the pore fluid on the clay surface. The wettability is characterized by the contact angle, α, defined as the angle at which the fluid-air interface meets the clay surface. Zero contact angle represents perfect wettability while $\alpha = 180^0$ represents the perfect non-wettability conditions.

A system of the air-water between two parallel clay particles is shown in Fig. 2.10 as viewed on the '*y*-*z*' plane. In the *x*-direction normal to the '*y*-*z*' plane, the water meniscus is extending up to a distance of L_x. Assuming that the meniscus can be approximated by the circular arc of radius *r*, the Young-Laplace equation for the pressure difference across the air-water interface is written as,

$$P_a - P_w = \frac{T}{r} \tag{17}$$

where P_a is the air pressure, P_w is the water pressure within the meniscus, T is the air-water surface tension and r is the radius of curvature for the meniscus. The left-hand side of the equation is called the matric suction, commonly referred to as the soil suction. The meniscus shown in Fig. 2.10 represented a positive radius of curvature indicating $P_a > P_w$.

Table 2.1 Values of Hamaker's constant for various interacting bodies in the presence of air and water as the intervening medium

Medium			Hamaker's constant, A_h	Source
Interacting 1	**Intervening** 3	**Interacting** 2	**(10^{-20})**	
Air	Water	Air	3.7	Israelachvilli (1992)
Mica	Air	Mica	~10	Israelachvilli (1992); Anandarajah & Chen (1997)
Mica	Water	Mica	~2	Israelachvilli (1992); Anandarajah & Chen (1997)
Quartz	Air	Quartz	8.73	Anandarajah & Chen (1997)
Quartz	Water	Quartz	1.61	Anandarajah & Chen (1997)
Fused Quartz	Air	Fused Quartz	6.5	Israelachvilli (1992)
Fused Quartz	Water	Fused Quartz	0.83	Israelachvilli (1992)
Montmorillonite /Kaolinite	Air	Montmorillonite /Kaolinite	19.2	Sridharan (1968)
Montmorillonite /Kaolinite	Water	Montmorillonite /Kaolinite	6.11	Sridharan (1968)
Water	Air	Water	3.7	Israelachvilli (1992)

The water pressure becomes negative when the air pressure is taken as zero. The total force acting between the two clay particles because of the meniscus water is considered to be contributed by

two stress components – firstly, the air-water surface tension and secondly, the water pressure within the meniscus. The surface tension force component acting on the particles in the *z*-direction is,

$$F_{Tz} = -TL_x \sin\alpha \tag{18}$$

Assuming a uniform pressure distribution within the meniscus water, the force exerted on the clay particle surface in contact with the meniscus water is,

$$F_{Pz} = P_w L_x L_y \tag{19}$$

where L_y is the length of the clay particle in contact with the meniscus water. The total capillary force acting between the two particles is the summation of the two force components in the z-direction.

$$F_c = F_{Tz} + F_{Pz} = -TL_x \sin\alpha + P_w L_x L_y \tag{20}$$

Assuming a zero-air pressure condition, the above equation is re-written as

$$F_c = -TL_x \left(\sin\alpha + \frac{L_y}{r} \right) \tag{21}$$

The sign of the second term is opposite when the radius of the meniscus curvature is negative. The radius of meniscus curvature is related to the particle separation distance as, $r = d/2\cos\alpha$ and hence,

$$F_c = -TL_x \left(\sin\alpha + \frac{2L_y}{d}\cos\alpha \right) \tag{22}$$

The capillary force between clay particles at any given separation distance can be estimated by knowing the contact angle and the extent of the meniscus water which is related to the degree of saturation (S_r) or the volumetric water content (θ). The capillary forces in clays are very dominant in the unsaturated regime. For a given particle separation distance or pore size, the magnitude of the capillary forces increases with an increase in the degree of saturation. The capillary forces,

however, decrease as the pore size of clays is increased. At the dry state and fully saturated state, the capillary forces cease to exist.

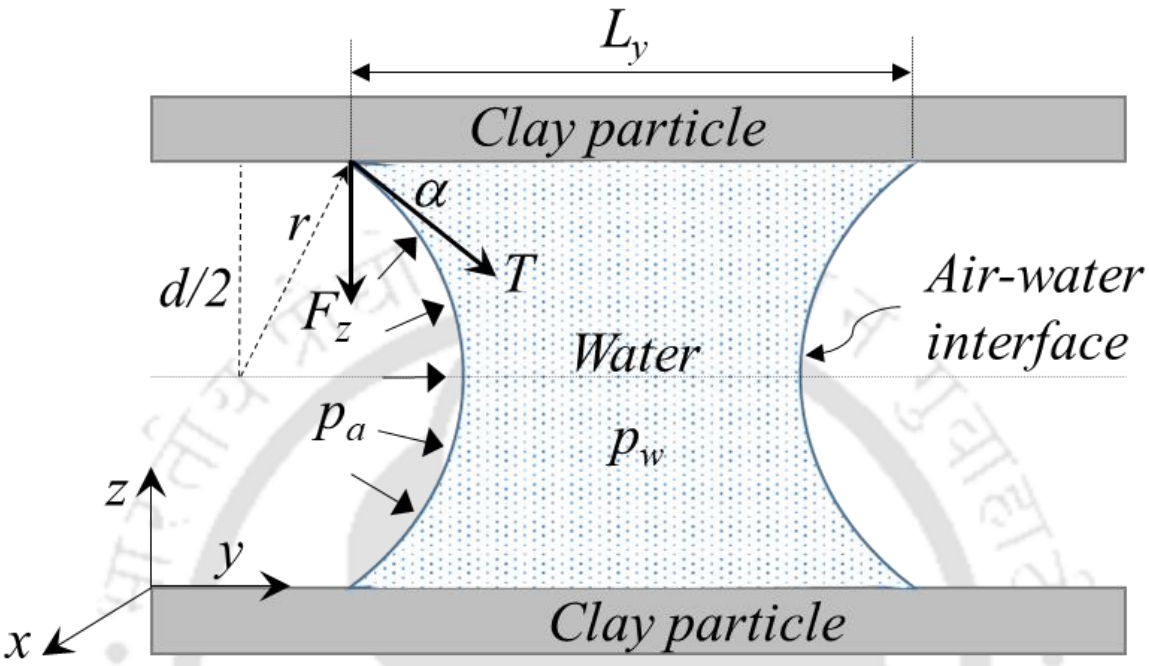

Fig. 2.10. Schematic representation of water meniscus between two parallel clay particles (after Amarasinghe et al., 2014).

2.4.5 Born and Steric repulsion

The Born and Steric repulsion counter-balances other surface forces at the particle contact points (Lu and Likos, 2006) and limits the approaching distance of two neighboring particles. Born repulsion is mobilized when two approaching particles penetrate each other under the action of applied mechanics and the other attractive surface forces (Bennet and Hulbert, 1986; Sjoblom, 2015), otherwise remain inactive. These forces are very short-ranged as their magnitude is inversely proportional to approximately twelfth power of the separation distance between the interacting particles (Bennet and Hulbert, 1986). These forces are significant only at separation distance in the range of 5-30 angstrom (Barnaji et al., 2016, Lu and Likos, 2006), and become insignificant at larger separation distance. Thus, born repulsion is relevant only when the fine intra-aggregate pores are compressed under very high stress, such as air-dry compaction to very high density and heavily consolidated clays.

2.5 Pressure-void ratio relationships of saturated clays using DDL theory

It is well established based on many classical studies that the volume change behavior of saturated clays is primarily controlled by the long-range repulsive forces (Bolt, 1956; Sridharan, 1973; Mitchell, 2005). The Gouy-Chapman DDL theory is often utilized to predict the compressibility behavior of saturated expansive clays (Bolt, 1956; Sridharan and Jayadeva, 1982; Bharat et al., 2013). An illustration of the parallel arrangement of the clay particles in saturated clays as considered in the theory is presented in Fig. 2.11. At an equilibrium separation distance, the repulsive pressure due to the DDL interaction is equal to the externally applied pressure. Thus, the applied pressure is related to the midplane potential by the Langmuir'e equation (Eq. 13),

$$P = 2nkT\left(\cosh(u) - 1\right) \tag{23}$$

Further, the void ratio can be related to the distance between the platelets as follows:
Consider two parallel clay platelets of area A and thickness t_p, separated by an average distance of d under the influence of self-weight (combination of clay platelets and the DDLs) as shown in Fig. 2.12. The volume of the water V_w is

$$V_w = A \times d \tag{24}$$

and the volume of soil solids (i.e., clay platelets) is

$$V_s = A \times t_p \tag{25}$$

The void ratio e can be expressed as

$$e = \frac{V_w}{V_s} = \frac{d}{t_p} \tag{26}$$

The specific surface area (surface area per unit mass), S_a, can be written, after neglecting the contribution of the edges, as

$$S_a = \frac{2A}{M_s} = \frac{2}{t_p \times G \times \rho_w} \tag{27}$$

where G_s is the specific gravity of the solids and ρ_w is the density of the fluid. Substituting for t_p in Eq. 27 using the Eq. 26 gives

$$e = \rho_w G_s S_a \frac{d}{2} \tag{28}$$

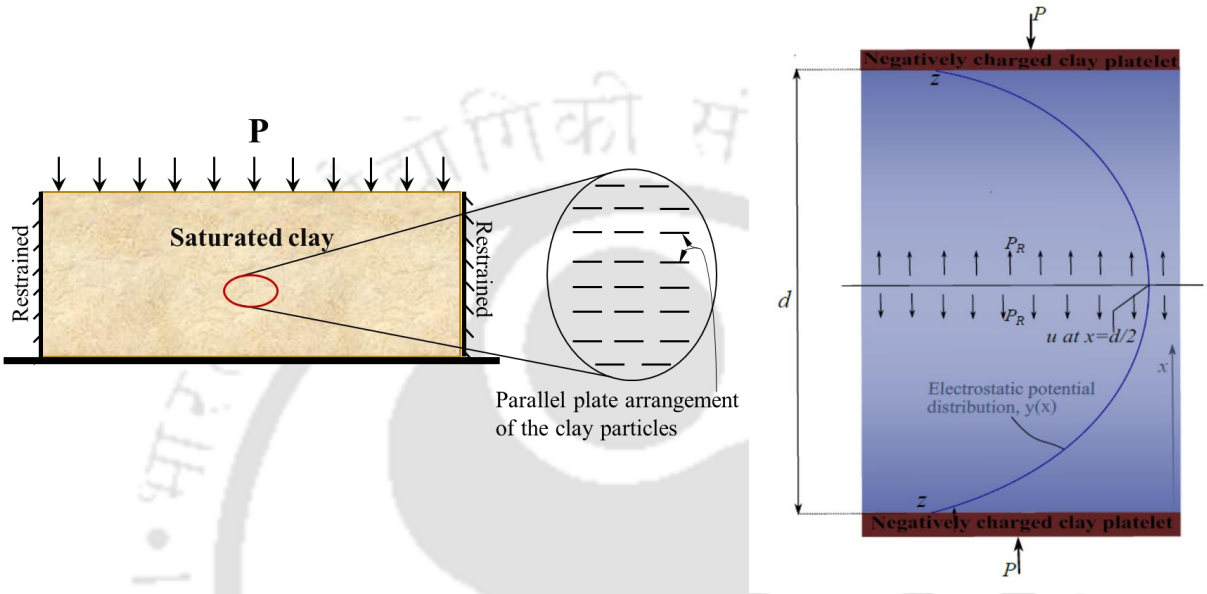

Fig. 2.11. Illustration showing parallel plate arrangement of saturated clay platelets with DDL during compression (After Bharat and Sridharan, 2015b)

Thus, the pressure-void ratio relationship can be established from Eqs. (23) & (28) through relating the midplane potential and the separation based on the DDL theory. As per the Gouy-Chapman model, the 'midplane–separation distance' relationship of a given clay-water system is established using Eq. (3). The integral involved in Eq. 3 is elliptic, which is to be solved numerically to establish the relationship between mid-plane potential and separation distance (Bharat et al., 2013). A flowchart showing various steps in estimating the void ratio for known soil properties and pore fluid parameters at given applied pressure is presented in Fig. 2.13. Discrepancies are often observed between the predicted and the observed clay behavior due to the limitations associated with the Gouy-Chapman model as discussed earlier.

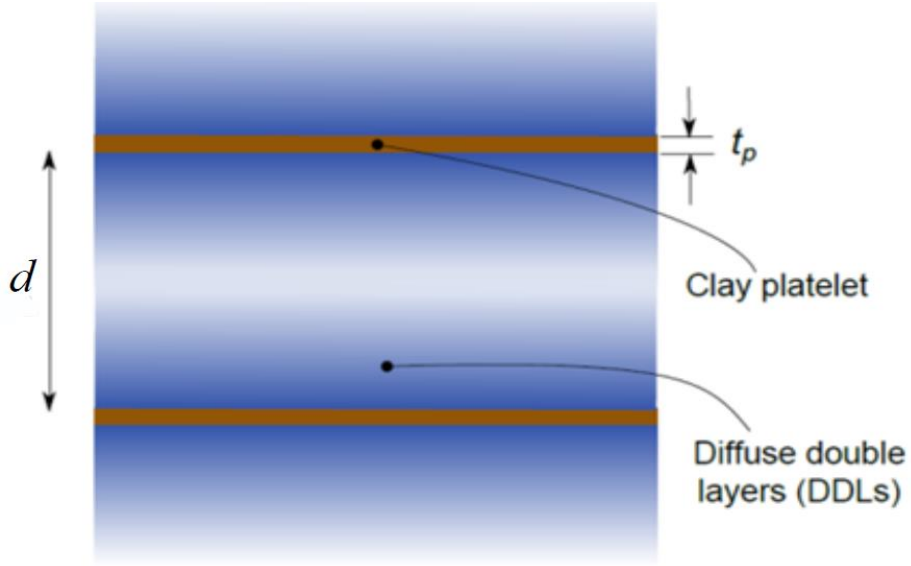

Fig. 2.12. Illustration of void space between the parallel plate clay system

The influence of mixed-valence cations on the 'pressure-void ratio' relationships is incorporated through the use of Eq. 5 (Bresler, 1970, 1972) to establish the 'u-κd' relationships. Further, the mixed valency is also incorporated in the Gouy-Chapman model in the form of weighted average valency as calculated based on the known exchange capacity of individual cations (Tripathy et al., 2014). The 'pressure-void ratio' relationship based on the interacting Stern model at constant charge condition is not available as the formulation for determining the Stern potential is not yet developed. Tripathy et al. (2014) predicted the compressibility behavior of clays using the Stern model by considering a constant surface potential condition which is discussed in Chapter 7.

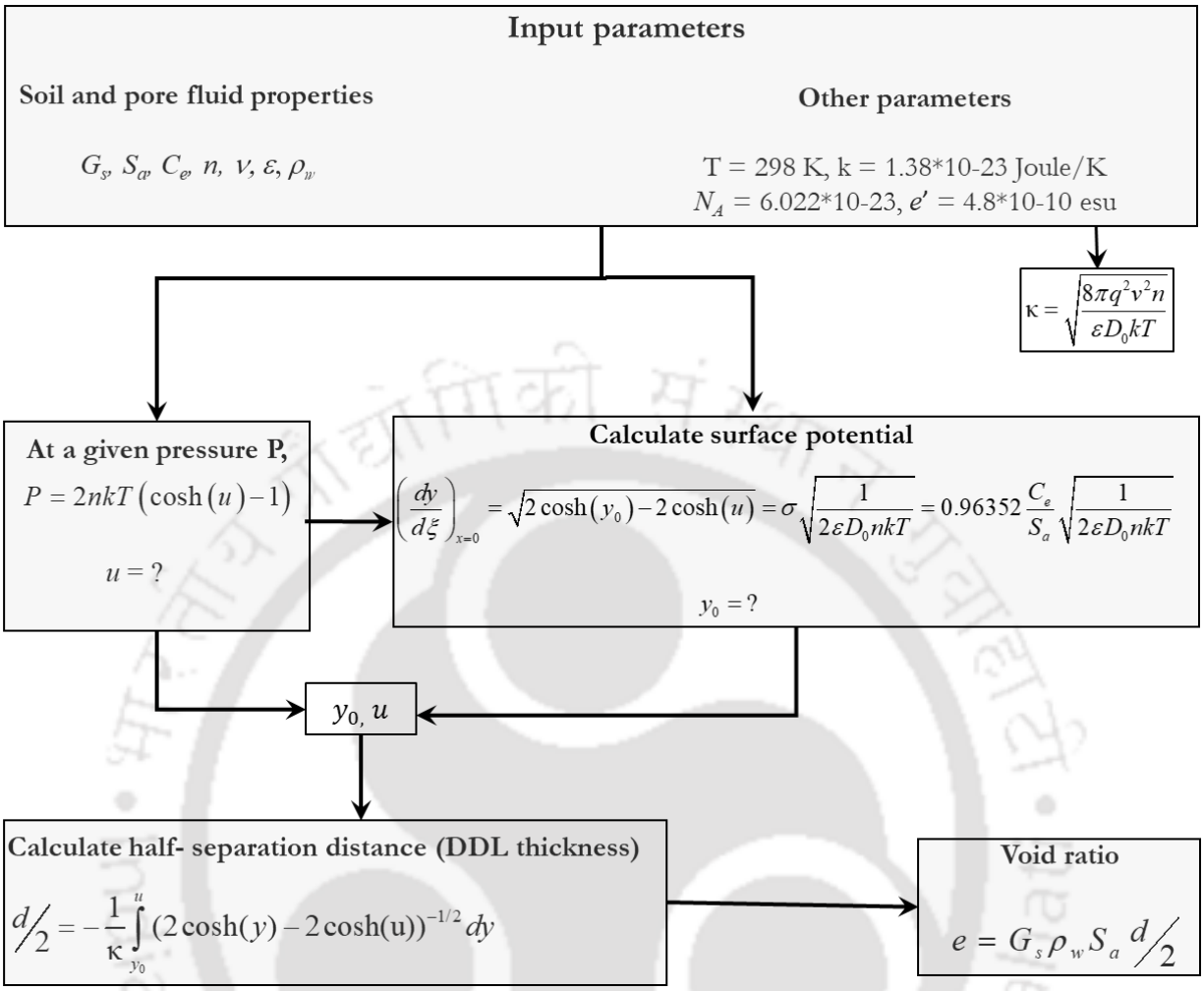

Fig. 2.13. Flowchart showing the estimation of void ratio at a given pressure based on the Gouy-Chapman DDL theory.

3 Literature Review

3.1 Equilibrium sediment volume of clays

Index tests are important for preliminary assessment of the engineering behavior of the clays and the identification of mineral constituents of the natural clay soils. Equilibrium sediment volume (ESV) is an important surrogate compatibility test used for assessing the expansiveness of clays for several decades (American Colloid Co., 1945; Rollings, 1969; Prakash and Sridharan, 2002; Lee et al., 2005). Further, the ESV data are used for the identification of different clay minerals (Wiklander and Andersson; 1955; Kariuki and Meer, 2004), classifying expansive soils (Sridharan and Prakash, 2000; 2016), qualitative understanding of the swelling behavior of clays (Deng et al., 2011), and correlating with different geotechnical properties of clays (Prakash and Sridharan, 2002; Lee et al., 2005). ESV is also used to understand the applicability of natural clay soils and different bentonites as barrier material in the engineered waste-disposal facilities for the isolation of toxic wastes and nuclear wastes. A predetermined amount of clay sample is mixed with water in a graduated glass cylinder to measure the free swell/sediment volume at equilibrium. The measured data is represented in terms of floc volume (Wiklander and Andersson, 1955), percent free swell, differential free swell index (IS 2720-40, 1977), modified free swell index (Sivapullaiah et al., 1987; Prakash and Sridharan, 2004), or specific volume (Sridharan et al., 1986; Sridharan and Prakash, 1999; ASTM D5890, 2003) in different studies. The influence of physicochemical factors on the sediment volume behavior of plastic clays is, therefore, important for understanding the applicability of given clay soil in waste containment facilities (Lee et al., 2005). Sridharan and Prakash (1999) showed qualitatively with limited experiments that the pore-fluid concentration influences the equilibrium sediment volume of expansive clays. A detailed understanding of the influencing parameters on ESV provides useful insights into the fundamental behavior of expansive clays, but such theoretical analysis is not available. A theoretical relationship between ESV and the influencing parameters is useful for many engineering studies, therefore. Mathematical models (Tripathy et al., 2004; Bharat et al., 2013; Bharat and Sridharan, 2015a) are useful for the estimation of soil behavior such as estimation of evapotranspiration, compressibility, swelling, etc. using fundamental material properties.

Physicochemical factors such as cation exchange capacity (CEC), specific surface area (SSA), and pore-fluid chemistry control the engineering behavior of plastic clays (Bolt, 1956; Mesri and

Olsen, 1971; Sridharan and Rao, 1973; Mitchell, 2005; Bharat et al., 2013; Bharat and Sridharan, 2015a). The swelling behavior of clays is qualitatively studied by analyzing the changes in Debye length due to pore-fluid effects (Sridharan and Prakash, 1999). The swelling of clays due to electrolytes is attributed to the development of repulsive pressures between the double layers of the clay platelets (Yong et al., 2012). The repulsive pressure increases with saturation and attains a maximum value at full saturation. The distance between the particles increases to increase the free energy of the system which manifests as swelling in the macro-scale. Clays, therefore, attain a large void ratio at full saturation due to readjustment of the distance between the particles under the influence of repulsive pressures. DDL theory is successfully applied to qualitatively study the swelling characteristics of bentonites (Komine and Ogata, 2004; Tripathy et al., 2004; Schanz and Tripathy, 2009; Bharat et al., 2013; Schanz et al., 2013; Schanz and Al-Badaran, 2014); to qualitatively estimate the hydraulic behavior of bentonites (Komine, 2004; 2008); and to understand the compressibility behavior of bentonites at high consolidation pressures (Bharat and Sridharan, 2015a). Theories based on the surface forces, therefore, provide useful insights into the free swell volume of the clays. However, the theoretical study for understanding the free swell volume of the clays is scarce. Fam and Dusseault (1998) used a model which considers the DDL thickness around the clay platelets to be equal to the 'Debye length' for estimating the free swell volume because of the common notion that 'Debye length' is equal to DDL thickness (Mitchell, 1993; McBride, 1997; Palomino and Santamarina, 2005; Kitazumi et al., 2013). However, Bharat and Sridharan (2015b) showed that 'Debye length' is significantly (orders of magnitude) smaller than the DDL thickness and is not an equivalent DDL thickness. The predicted swell volume, therefore, severely underestimates the measured data. The available models and experimental data report only the qualitative changes in ESV with pore-fluid parameters (Sridharan and Prakash, 1999). Theoretical methodology for quantitative analysis of equilibrium volume of the clay sediments and ESV prediction using surface characteristics of the clays remains to be completed.

In this study, a theoretical framework for the ESV of clays was developed using the DDL theory at a very small particle-particle interaction. An analytical equation was developed to determine the distance between the fully swollen clay platelets when allowed to settle under gravity in different physicochemical environments. The analytical solution was validated against the measured ESV data of different bentonites in salt solutions to bring out the influencing physicochemical parameters on the sediment volume behavior of clays.

3.2 Specific surface area measurement

Several laboratory techniques are available for the determination of the surface area of clay soils. The predicted surface area values often differ based on the adopted methods as the underlying mechanisms are different. The forces such as van der Waals attraction, electrostatic double-layer repulsion, capillary condensation, solvation, and hydration are present at different clay-water-air interactions (Lu and Likos 2006; Ghosh 2009; Khorshidi et al. 2016). The forces due to van der Waals attraction, solvation, and hydration are dominant at the "dry-end" state of the soil (Leao and Tuller 2014). The specific surface area determination based on the principles of adsorption of probe molecules on the clay surfaces utilizes the "dry-end" state of the soil. The water adsorption method utilizes water as probe molecules for the S_a estimation of clay soils based on the water content corresponding to the mono-layer and bi-layer coverage at the dry end state of the soil (Quirk, 1955; Akin and Likos, 2014; Leao and Tuller, 2014; Khorshidi et al., 2016). The DDL thickness around a clay platelet is estimated, in this approach, by considering the van der Waals interaction potential, between a water molecule and the clay surface, to be equal to Kelvin's water potential. The measured gravimetric water content during the adsorption experiment is then related to the S_a after assuming the platelets in parallel orientation. Although the water molecule has better inter-layer accessibility (Newman 1983, Akin and Likos, 2014), the lack of a suitable water sorption model for the clay soils limits the applicability of the adsorption method. The existing t-curve approach (Leao and Tuller, 2014) is not applicable for the smectite clay minerals due to the influence of type and size of exchangeable cations, the extent of interlayer swelling, and the extent of capillary condensation occurring on particle surfaces and interfaces (Low 1980; Viani et al. 1983; Chiou and Rutherford 1997; Quirk and Murray 1999; Salles et al. 2009; Akin and Likos 2014).

The S_a estimation based on the other polar adsorbates such as EGME (Carter et al. 1965) is widely recognized to be the standard test method in geotechnical engineering for expansive clays (Cerato and Lutenegger 2002), mainly due to its higher vapor pressure at room temperature. However, the molecular coverage of all interlayer and external surfaces in expansive clay lattice is not guaranteed. The estimated Sa values might vary from the other methods due to the association of EGME molecules with the exchangeable cations, which results in thicker formation than the monomolecular layer thickness (Khorshidi et al. 2016). Further, the variation in the density of

adsorbed EGME, which is different from the bulk liquid EGME, is not accounted for in the Sa estimation (Carter et al. 1986). The application of responsible mechanisms at the "dry-end" state is, therefore, complex in smectite clays for the S_a estimation.

The surface forces such as electrostatic repulsive forces are significant at the saturated state of the clay soils (Bharat and Sridharan 2015a; Bharat and Das 2017). The MB adsorption technique (Kandhal and Parker 1998; Santamarina et al. 2002) utilizes the slurry state of the soil, which favors the Sa estimation for the smectite clays. However, the dependency of MB sorption on the type of exchangeable cations of the clay surface and the uncertainty in the surface area computation due to different possible orientations of the MB molecules in the adsorbed state are significant concerns (Hang and Brindley 1970; Santamarina 2002). The MB method requires a continuous engagement in adding the MB solution at an increment of 1 ml, subsequent mixing and verifying the color of the droplets on filter paper for accuracy in the estimation. Thus, the chances of human error in this procedure are highly likely. Further, the test procedure becomes laborious for high plasticity soils such as smectite clays, where a large amount of MB is required to be added in small increments. An alternative technique for the Sa estimation is a need of the hour.

In this study, a simple, quicker, and alternative method was developed for the estimation of S_a by utilizing the slurry state of the clay soil. The proposed method was based on the measured equilibrium sediment volume (ESV) of the soils under the salt environment and theoretical estimation of the corresponding DDL thicknesses around the clay platelets in a swollen state.

3.3 Compressibility behavior of clays

Compacted bentonites are extensively used in landfills due to the presence of a high percentage of montmorillonite mineral content for controlling the diffusion rates of degraded waste (Benson et al., 1994; Manassero et al., 2000; Bharat et al., 2009; Das & Bharat, 2017), for controlling the seepage rates from surrounding rock mass in high to low-level nuclear waste repositories (Pusch, 2006; Pusch, 2015), and for improving the stability of excavations under water-logged conditions such as harbors (Pusch, 2015). Different bentonites namely, MX80, FEBEX, Montigel, Gaomiaozi (GMZ), Kutch, Barmer, Yellow bentonite, Kunigel-V1, Ponza, etc. are widely used as landfill liners and are also the likely candidate material in nuclear waste repositories in different countries (Carlson, 2004; Karnland, 2010; Pusch, 2015; Das & Bharat, 2017; Gapak et al., 2017). Their

plasticity (i.e., quality) varies depending on the presence of different minerals, clay content, and percentage of different exchangeable cations. The volume change behavior of such bentonites under mechanical pressure is important in the presence of different saline environments in these applications. The maximum consolidation pressures up to which the compressibility data is required, in these applications, depends on the design considerations. The expected maximum vertical pressure on compacted liner systems in the landfills and tailing impoundments may range between 360 – 6,000 kPa (Peirce et al., 1986; Timmons et al., 2012) depending on the mound height and type of waste expected. On the other hand, the mechanical behavior of the bentonites are studied in the range of 3,000 – 42,000 kPa for various applications in high-level nuclear waste repositories as the stress level at the location of the waste disposal repositories are expected to be similar (Baille et al., 2010; Marcial et al., 2002; Tripathy et al., 2004; Tripathy & Schanz, 2007; Pusch et al., 2011; Bharat et al., 2013; Ye et al., 2014). Similarly, the compressibility behavior of various clayey soils at high mechanical loads is also important for building the infrastructure on reclaimed land (Mesri & Funk, 2014). However, the maximum applied normal pressure in conventional oedometers for studying the compressibility data is limited. Conversely, laboratory estimation of compressibility data beyond certain consolidation pressures using advanced set-ups is laborious, time-consuming, and expensive (Ng et al., 2006). Therefore, the prediction of compressibility data using theoretical and empirical analyses gained significant importance.

The compressibility behavior of smectite dominant clays is often estimated using the diffuse double layer theory (Bolt, 1956; Mesri & Olson, 1971; Low, 1980). However, the theoretical compressibility predictions are accurate only for very high quality (i.e., plasticity) clays such as sodium bentonites, but severely differ for low-medium quality clays containing calcium in the exchangeable state and for illite clays (Bolt, 1956). Nagaraj & Murthy (1986) presented an empirical expression for clayey soils based on fitting a linear relationship to the normalized compressibility data. The void ratio at the liquid limit is used as a normalization factor in this work. However, the proposed relationship is valid for low plastic clayey soils as the obtained relationship is derived using limited data of clayey soils having a liquid limit (w_L) in the range of 36 – 160%. Moreover, the equation is valid for soils consolidated from an initial state of liquid limit water content. Burland (1990) showed the existence of a reasonably unique relationship between normalized void ratio and consolidation pressure on a logarithmic scale. The void ratio is normalized using two normalizing factors; namely, e100 and e1000; represented by void index I_v

which is given by, where e100 and e1000 are the void ratios corresponding to consolidation pressures of 100 and 1000 kPa, respectively. However, the method by Burland (1990) is also applicable for a soil having wL less than 160% similar to the method by Nagaraj & Murthy (1986). Further, the measured compressibility data are required up to a consolidation pressure of 1000 kPa which poses a limitation to the application of this method. Tripathy & Schanz (2007) derived theoretical relationships between the electrostatic potential at the midway between the clay platelets and the mid-plane distance using DDL theory. The theoretical relationships are modified by adjusting the equation coefficients to match the specific experimental compressibility data of commonly used bentonites. The adjusted empirical relations are derived from specific experimental data and are valid for limited ranges of averaged ion valences i.e., 1.66-1.73 and 1.97. The applicability of these equations, therefore, may not be guaranteed for a wide range of clays and clayey soils. This method, further, requires the determination of clay surface and pore-fluid parameters for the prediction. Gurtug (2011) showed on limited measured data of highly plastic clays that the void ratio of the compressible layer at a consolidation pressure of P = 100 kPa, i.e. e100, is an effective normalizing factor for predicting the void ratios at higher consolidation pressures. The relationship between e/e100 versus $1/\sqrt{P}$ for various highly plastic clays is found to be linear and useful for compressibility prediction. Bharat & Sridharan (2015a) showed the existence of a unique relationship between the normalized void ratio and the consolidation pressure for plastic clays using both DDL theory and the measured data. The normalized void ratio is chosen from the compressibility data corresponding to any consolidation pressure beyond the preconsolidation pressure. Since any void ratio on the virgin compression line can be used for the normalization, the proposed equation is very flexible for the compressibility prediction. However, this model might not be applicable for low-medium plasticity clays and natural clayey soils containing non-smectite minerals and significant non-clay constituents.

In this work, a generalized model was presented to predict the compressibility data of clays and clayey soils of different plasticity. The model was validated on 116 compressibility data sets from 88 bentonites and clayey soils from the literature and the current study consisting of different inundation fluids.

3.4 Stern DDL theory

The predicted void ratios are significantly smaller than the measured data at higher pressures due to the assumption of point charges in the theory. The effect of the size of cations is incorporated into the DDL theory through a thin and compact layer of cations next to the clay surface as per the model proposed by Stern (1924). The Stern model is only utilized to determine the potential distribution of a non-interacting clay water system (Verwey and Overbeek, 1948; van Olphen, 1977; Shang et al., 1994; Sridharan and Satyamurhty, 1996). Limited literature is available on the use of the Stern layer for the prediction of compressibility behavior of clays. The existing model using the Stern theory to predict the compressibility behavior of bentonite (Tripathy et al., 2014) is based on the constant surface potential condition which is not suitable for the clays as they exhibit variable potentials or constant charge conditions. A mathematical model for the electrostatic potential variations of an interacting clay-water system utilizing the constant charge condition is yet to be developed.

In this study, the Stern diffuse double layer model for constant charge conditions was developed for studying the compressibility behavior of clays theoretically. Electrostatic potential distribution of an interacting clay-water system was established for the first time using the Stern theory. Further, the compressibility of the Stern layer at large pressure was brought out and incorporated in the prediction of the compressibility behavior of clays.

3.5 Swelling pressure of compacted bentonite

In the underground nuclear waste repositories, the pre-compacted bentonite blocks at air-dry water contents and high compaction densities are placed between the waste canisters and surrounding saturated rock mass for creating an impermeable zone. The stress state of the repository is appropriately maintained from the swelling pressure development of the compacted bentonite blocks during the saturation process, apart from sealing the construction joints (Grindrod et al. 1999, Gens et al. 2002, Ye et al. 2010). The hydration of inter-lamellar layers of the montmorillonite mineral, exchangeable cations, and external surface of the aggregates contribute to the swelling pressure development in the compacted bentonites in the isochoric condition through complex pore interactions. The evolution of swelling pressure with time, which is termed as the swelling pressure evolution curve (SPEC) in this work, and the final swelling pressure is

important for understanding the stress development in the repository during the bentonite saturation process and bentonite hydration process up to saturation (Vaunat and Gens 2005).

The pore water in the buffer material and the surrounding rocks in the underground repositories are likely to possess different chemical compositions (Wang et al., 2014), and continuous long terms interaction with the bentonite exists (Ramírez et al., 2002; Fernández et al., 2014). The degradation of concrete components of the underground structures due to the long-term interaction with the ground-water (Lovera et al., 1997; Faucon et al., 1998; Alonso et al., 2017) acts as a source of alkaline/salt components in the bentonite pore-fluid (Pusch, 1982; Glasser 2001; Nakayama et al., 2004). The release of sodium and potassium hydroxides in the process can result in a pH of as high as ~13.5 and high ionic concentration, and cation domination of Na^+ and K^+ in the pore-fluid (Savage, 1997; Bauer and Velde, 1999). Significant studies have been carried out on the swelling pressure behavior of several bentonites under the influence of pore-fluid chemistry, in the recent past (Castellanos et al., 2008; Herbert et al., 2008; Zhu et al., 2013; Ye et al., 2014; Wang et al., 2014; Ye et al., 2015;). The pore water chemistry significantly influences the swelling pressure of compacted bentonite, e.g., the swelling pressure of bentonite decreases as the salinity of pore water increases (Castellanos et al., 2008; Herbert et al., 2008; Zhu et al., 2013). The specific effect of the cation type and size on the swelling pressure, however, is not studied so far.

Further, a wide variety of swelling pressure evolution curves under the isochoric conditions have been reported for different bentonites at various compaction densities and in the presence of different pore fluids. A unimodal SPEC behavior is generally expected as the swelling pressure starts developing with an increase in the degree of saturation with time under the isochoric wetting. A distinct (bimodal) SPEC is, however, reported for many bentonites at different initial compaction densities (Pusch 1982, Imbert and Villar 2006, Schanz and Tripathy 2009, Zhu et al. 2013, Chen et al. 2018, He et al. 2019). In the bimodal SPEC behavior, the swelling pressure development experiences a sudden drop during the initial water uptake before rising to a final equilibrium swelling pressure value at full saturation. The drop in swelling pressure is found to be significant in French FoCa clay and the qualitative behavior is similar for all the studied initial compaction densities (ρd =1.3-1.6 Mg/m3) (Imbert and Villar 2006). However, the decrease in swelling pressure after reaching the first peak is insignificant to zero with a plateau on the SPEC before swelling pressure increases to a final equilibrium value for GMZ bentonite (Chen et al.

2018, Zhu et al. 2013, He et al. 2019). Further, the decreasing tendency of swelling pressure after the initial phase of water uptake is observed to be dependent on the initial compaction density for German and GMZ bentonites (Schanz and Tripathy 2009, Chen et al. 2018, He et al. 2019), contrary to French FoCa clay. The variable nature of SPEC with compaction density and bentonite plasticity is not understood, albeit, the mechanisms viz. crystalline and osmotic swelling (van Olphen 1977) are well cited and accepted in the literature without relating to the pore size evolution (Bradbury and Baeyens 2003, Savage 2005, Massat et al. 2016) for swelling characteristics. The knowledge of the underlying mechanism responsible for the SPEC behavior of a given bentonite and compaction density is required for the hydro-mechanical analysis of compacted bentonites for the application of nuclear waste repositories (Vaunat and Gens 2005).

The microstructural analysis of compacted bentonite explains many mechanisms for understanding hydro-mechanical behavior. The microstructural changes of bentonite are often determined using the mercury intrusion porosimetry (MIP) tests. The MIP test data are generally represented in terms of differential intrusion volume (dv/dlogD) vs pore size (D), which is termed as the differential intrusion volume curve or the pore-size distribution curve (PSD). Any point on the PSD, corresponding to particular pore size, represents the density or the numbers of pores corresponding to that size. The changes in the pore structure are analyzed by quantifying the intruded volume of various pore size classes. Most of the available studies in the literature accounted for only two major pore-size classes, viz. micro-pore, and macro-pores without any well-defined delimitation of the two size classes and they vary between 2-5μm (Monroy et al. 2010, Villar et al. 2014, Manca et al. 2016). Not many studies have attempted to study the SPEC behavior of compacted bentonites using the PSD-based microstructural analysis. The dual-porosity concept has been used in limited literature for explaining the SPEC behavior of compacted bentonites under the isochoric condition. The decrease in the swelling pressure is attributed to the collapse of the macro-pores due to the loss of shear strength at the aggregate level (Pusch 1982, Schanz and Tripathy 2009). However, the collapse of the macro-pores alone does not explain the observed plateau of SPECs for different bentonite at other densities. Moreover, bimodal SPEC is observed at higher densities for some bentonites (Febex bentonite- Villar and Gómez-Espina 2009, MX80- Herbert et al. 2008) but is not observed even at lower densities for other bentonites (GMZ bentonite- Schanz and Al-Badran 2012). Such anomalies are not supported by the concept of macro-pore collapse. Moreover, accounting for only two pore size classes may lead to oversimplification of the complex pore

geometry in compacted bentonites (Wang et al. 2014, Prikryl and Weishauptová 2010, Sun et al. 2019). The conventional two pore size classes are replaced with more pore size classes in the recent studies on the flow behavior of bentonites. For example, Wang et al. (2014) considered four major pore size classes as inaccessible pores (<0.006 μm), small pores (0.006–0.04 μm), medium pores (0.04 – 2 μm), and large pores (>2 μm) for MX80 bentonite. On the other hand, Pr̆ikryl and Weishauptová (2010) identified four different pore-size classes for Czech bentonite which consist of inter-lamellar pores of size <0.0013 μm. The existing dual-porosity-based approach for studying the SPEC behavior of compacted bentonite under isochoric conditions lacks a comprehensive understanding of the complex microstructural evolution process during the hydration process.

In the present work, swelling pressure tests were conducted on the Indian bentonites in the presence of five different inundating fluids, viz., distilled water, NaCl, LiCl, KCl, and KOH solutions. A strong cationic concentration (1 M) was used for the three salt solutions and the alkaline solution to nullify the influence of the mixed-valent surface cations and better understand the effect of the individual pore-fluid cations. A wide variety of SPECs were observed depending on the bentonite plasticity, compaction density, and wetting pore-fluid. Two distinct SPEC behaviors, namely, a bimodal-SPEC and a monotonous-SPEC were considered for the microstructural investigation to understand the underlying pore-scale mechanisms.

3.6 Wetting-induced volume change behavior of kaolin

Collapsible soils undergo significant volume reduction upon wetting under the pre-existing normal loading. These soils exhibit very high strength in air-dried conditions and can carry up to a considerable magnitude of normal stress without experiencing significant volume change. The soil strength is, however, considerably reduced upon saturation and results in a sudden collapse of the soil structure under the existing normal stress condition. The intrusion of water into the dry deposits of such soil causes ground subsidence leading to damages in the overlying and surrounding infra-structures. Loess soil is a common example of such collapsible soil type which is spread over almost 10% of the land-mass of the world; from Western Europe to China, across North America, and in regions across South America (Phien-wej et al., 1992; Rogers et al., 1994; Rogers, 1995; Al-Rawas, 2000; Nouaouria et al., 2008; Ryashchenko et al., 2008; Gaaver, 2012). Heavy loss of infrastructure and loss of human life in certain scenarios have been incurred due to the collapse caused ground subsidence problems (Derbyshire, 2001; Houston et al., 2001; Peng et

al., 2006; Delage et al., 2008; Sun et al., 2013, Li et al., 2016). Several ground subsidence problems have been encountered in the ongoing infrastructural development projects in the North-Eastern region of India where significant kaolin deposits are present. Kaolin deposits are widely spread over various regions of South Asia; across China and various parts of India (Indian Bureau of Mines, 2018; Nakagawa et al., 2006), especially in the North-eastern part (Saikia et al., 2003; Saikia and Parthasarathy, 2010; Sengupta et. al., 2008). The kaolin deposits exist up to several meters of depth from the ground surface and naturally exists in dry condition. A recent laboratory study showed that the wetting-induced collapse potential of kaolin is much higher than loess (Choudhury and Bharat, 2018). Study on the wetting induced volume change behavior of kaolin, therefore, is of paramount importance in dealing with the ground subsidence problems in the geotechnical engineering practices. The volume change behavior of kaolin soil compacted to MDD and OMC has been extensively studied in the past (Wheeler and Shivakumar, 1995, 2000; Shivakumar et al., 2010). The study on the wetting-induced volume change behavior of kaolin at air-dried state is, however, very limited (Choudhuri and Bharat, 2018; Pedrotti and Tarantino, 2018, Sun et al., 2007). Further, the influence of the natural density of kaolin and the stress state on the collapse behavior is important as the depth of the deposit and mechanical stresses vary in the field. The wetting-induced volume change behavior of kaolin initially at air-dry state, therefore, is necessary to be investigated at different compaction densities and inundation pressure.

The existing critical state-based elastoplastic model for unsaturated soil behavior, commonly known as the Barcelona basic model (BBM) model (Alonso, 1990; Wheeler and Shivakumar, 1995) has been widely used to model the volume change behavior of unsaturated soil. The original model was developed based on the concept that the volumetric path of an unsaturated soil converged to the saturated compression line upon wetting (suction decrease) under any given loading when plotted in 'e-P' space (Alonso, 1990). The compressibility characteristics at the two suction stress states, initial partially saturated case (suction = s) and saturated case (suction = 0), are, thus, utilized to model the volumetric deformation of unsaturated soil. Many studies have been carried out to utilize the BBM model to model the behavior of collapsible soil as well the expansive soil (Josa et al., 1992; Wheeler and Shivakumar, 1995; Sun et al., 2003). The soil response considered in these studies was, however, either under the isotropic stress state or soils with a moderate initial suction value (i.e., compacted at near OMC/MDD). Modeling the wetting-induced volumetric response of air-dry compacted kaolin by using the BBM model is not attempted so far.

The dual porosity concept i.e., micro-pores and macro-pores have been adopted in the available microstructural studies on the kaolin behavior. However, delimitation between the two pore-size classes is not well-defined for kaolin. For example, Shivakumar et al. (2010) considered 2 μm as the delimitation between the micro-pores and macro-pores of kaolin compacted at MDD-OMC. On the other hand, Pedrotti and Tarantino (2018, 2019) classified the micro-pores and macro-pores with an approximate delimitation in the range of 0.2-0.5μm. Further, the complex microstructure of clay is oversimplified due to the consideration of only two broad pore-size classes (Wang et al., 2014; Prikryl & Weishauptová, 2010; Sun et al., 2019). More number of pore-size classes has been, therefore, considered in recent microstructural studies on the flow behavior of clays (Wang et al., 2014; Pr˘ikryl & Weishauptová, 2010). Additionally, a wide range of available pore-size is attributed to the different possible modes of particle-particle association in compacted kaolin. The wetting-induced collapse has been related to the re-orientation of kaolin particle-particle association in recent past studies (Choudhury and Bharat, 2018; Pedrotti and Tarantino, 2018). Thus, classification of pore-size classes based on the particle-particle association is necessary to provide a comprehensive understanding of the microstructural mechanisms behind the kaolin response under the hydro-mechanical stress state.

Surface forces of different origin viz., columbic, van der Waal's, Born's repulsion, capillary, and the electrostatic repulsion significantly influence the kaolin particle-particle interaction and thus play an important role in the evolution of clay microstructure. Many classical studies have demonstrated the significance of van der Waal's forces and the double layer repulsive forces on the saturated clay behavior (Bolt, 1956; Lambe, 1960; Skempton, 1960; Sridharan and Rao, 1973). Studies on the unsaturated soil's behavior further displayed the dominant influence of the capillary forces on the macroscopic responses- shear strength and volume change behavior of soil (e.g., Bishop, 1959; Lamb and Whitman, 1969; Mitchel, 1976). A generalized form of the effective stress framework by explicitly considering each of the relevant surface forces is not available to date. This is due to the lack of a suitable model for upscaling the surface forces to the macroscopic stress component under different hydro-mechanical stress-state. A comprehensive understanding of the role of the surface forces in the microstructural evolution under different hydro-mechanical stress states, therefore, is of utmost importance. Extensive study is required for quantitative analysis on the evolution of PSDs along with the surface forces under different hydro-mechanical

stress state. Study on the volume change behavior of kaolin where the columbic interaction predominantly controls the microstructure, is, however, very limited in this regard.

In this work, the wetting-induced volume change characteristics of air-dry compacted kaolin at various compaction densities were studied under different inundation pressures. An effort was made to understand the role of various pore-scale forces on the observed kaolin behavior through a detailed microstructural analysis.

4 Materials and Methodology

4.1 General

This chapter presents the clays used in this study and their relevant properties. The characterization methodology of the basic geotechnical, physicochemical, and mineralogical properties is discussed in detail. A detailed description of the test setups and the adapted experimental methods were presented next, followed by the testing programs carried out in the study.

4.2 Materials

4.2.1 General

This study primarily used four different commercially available Indian bentonites in powder form, designated by B1, B2, B3, and B4, and a commercial kaolin designated by K. The four bentonites were procured from different locations of the Barmer region of Rajasthan and the Kutch region of Gujarat, India. The characterization of the bentonites and the kaolin is discussed in detail in this section. Additionally, a homoionic sodium clay (Na-B2) was prepared by removing the non-clay content and mixed-surface cations of the B2 bentonite for validating the proposed analytical model for the prediction of equilibrium sediment volume, presented in Chapter 5. The procedure adopted in preparing the homoionic bentonite is described below. Further, three additional soils viz., granular bentonite (GB), kuttanad clay (KTND), and black cotton soil (JBS), were considered in the validation of the proposed method for surface area estimation in Chapter 5. The GB was exhumed from the commercially available geo-synthetic clay liner (Maccaferri, India). The KTND is a natural clay, rich in organic content, which was procured from the Kuttanad region in the state of Kerala, India. The JBS was obtained from the Jabalpur region of Madhya Pradesh, India, and is a typical Indian black cotton soil. The relevant properties of these three clays were presented and discussed along with the other clays. Apart from the studied powder bentonites, a locally available red soil designated as RS was also used in the study for validating the proposed semi-empirical model for predicting compressibility behavior in Chapter 6. Further, 80 different literature bentonites and natural clays were considered for validating the proposed semi-empirical model. Various relevant properties and pore-fluid parameters considered in the analysis for the soils from the literature were presented in Table 6.2 in Chapter 6.

4.2.2 Preparation of homoionic clay

The B2 bentonite specimen was mixed with distilled water in 1:50 (solid to liquid) proportion, mixed thoroughly in a mechanical shaker for 3 h, and centrifuged at 1000 rpm for 1 min to separate the coarse content. The clay suspension was then transferred to a glass jar and mixed with 1 N NaCl solution by maintaining a constant agitation for 7 days in a shaker. The suspension was subjected to centrifugation to separate the excess salt solution. The clay fraction thus obtained was repeatedly washed with distilled water until the conductivity of the suspension approached zero. The homoionic clay was obtained in powdered form in Lyophilizer (FreezeDry System, Labconco FreeZone®) by freeze-drying the final suspension at−60 °c through sublimation. The sample thus obtained was used for the estimation of only the essential properties viz., surface area, specific gravity, and grain size distribution as the adopted procedure yields a very small amount of homoionic clay sample.

4.2.3 Specific gravity and grain size distribution

The specific gravity values of the clay specimens were determined using the density bottle method as per the ASTM D854-92 (1994) and presented in Table 4.1. The specific gravity of the studied powder bentonites and the granular bentonite were higher than the kaolin and other natural clays, in the range of 2.75 to 2.77. The studied kaolin has a specific gravity of 2.62. The organically rich natural clays, KTND and JBS, have the specific gravity of 2.48 and 2.65, respectively. Grain-size distributions of all the four powder bentonites and the kaolin were determined by wet sieving and hydrometer analysis (IS 2720-4, 1985) and results were presented in Fig. 4.1a.

Table 4.1 Measured specific gravity of the studied clays

Soil Name	B1	B2	B3	B4	K	Na-B2	RS	GB	KTND	JBS
Sp. Gravity, G_s	2.76	2.76	2.77	2.77	2.62	2.8	2.67	2.75	2.48	2.65

All four powder bentonites contain a minimal fine sand content of 1 to 4%. The clay-size (< 2 μm) content in these bentonites varied from 62% to 85 % in the order of B1 to B4. A hundred percent of the kaolin clay passed through the 75 μm sieve indicating a zero sand content. The kaolin has a clay content of 72% and 28% as silt size. The particle size distribution of the homoionic clay was based on the dynamic light scattering (DLS) method using Delsa™ Nano C Particle Analyzer

(Beckman Coulter®) with distilled water as a dispersing agent. The homoionic clay exhibited more than 96% particles in the size range of 0.1 μm to 2 μm. The grain distribution data for the GB was obtained from the dry sieving method and presented in Fig. 4.1c.

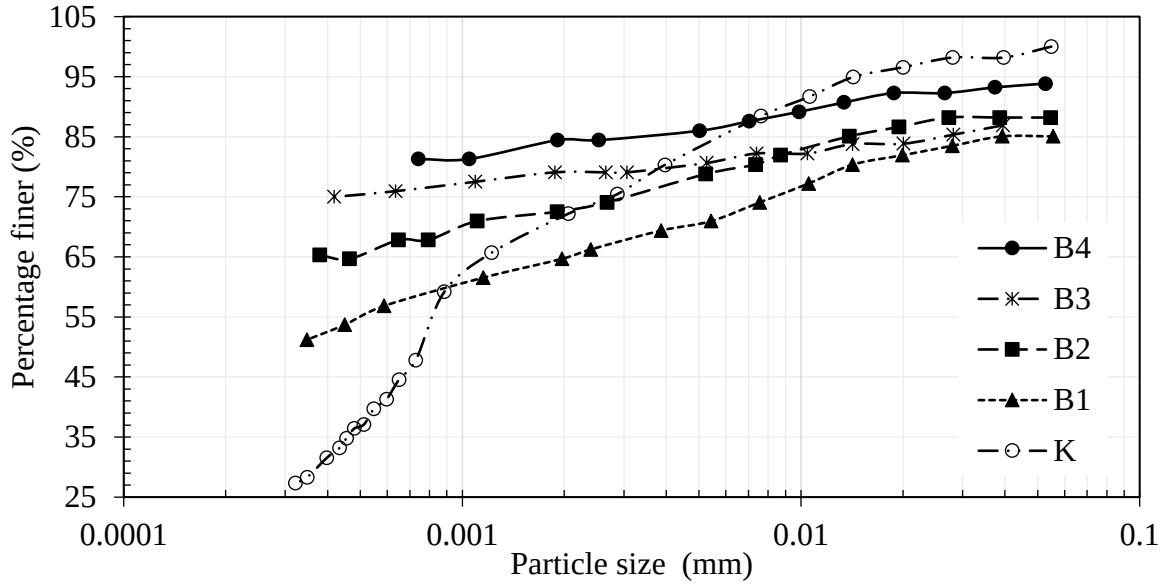

Fig. 4.1a Grain size distribution curves from hydrometer analysis for all soils used in the study

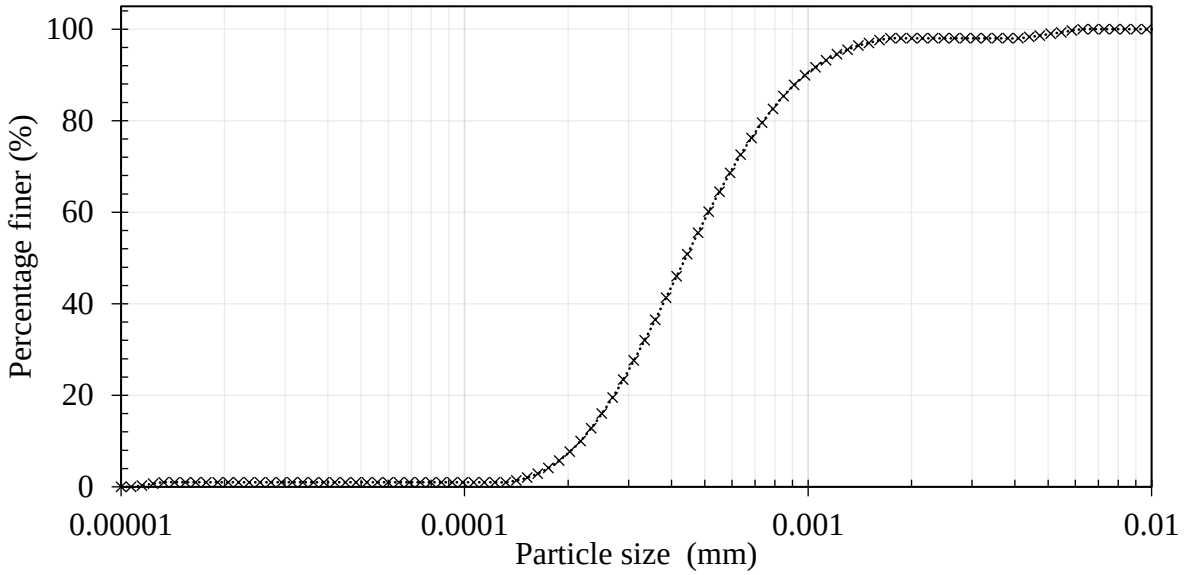

Fig. 4.1b Grain size distribution curves of the homoionic clay (Na-B2) from Delsa™ Nano C Particle Analyzer

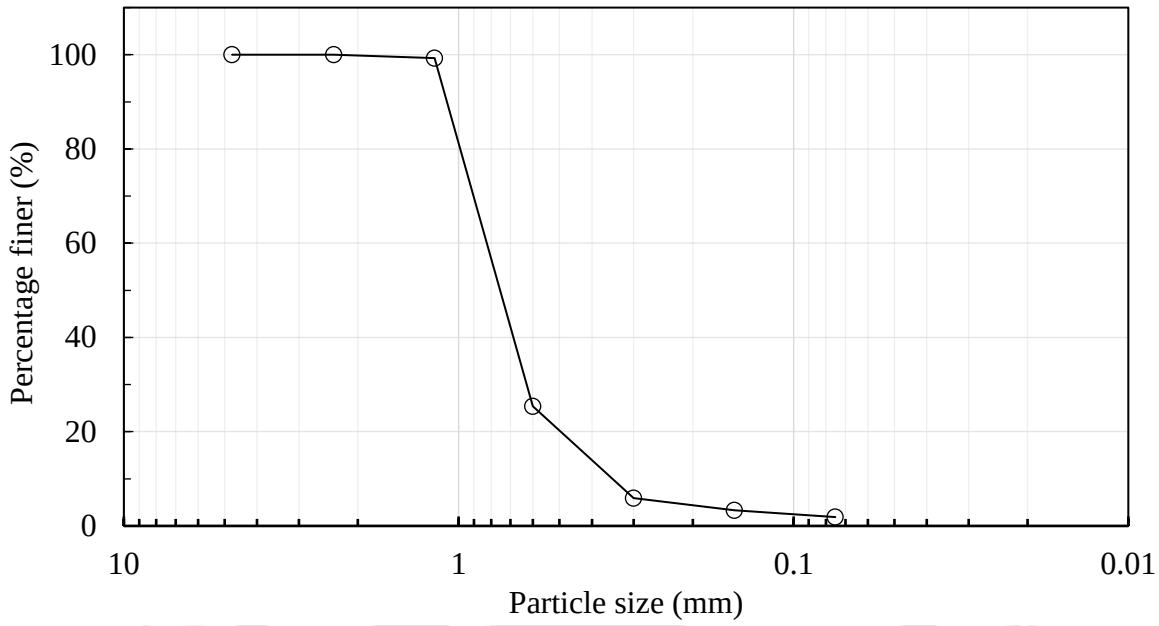

Fig. 4.1c Grain size distribution curves of the granular bentonite (GB) from dry sieving (After Das and Bharat, 2021)

4.2.4 Atterberg limits and activity

The liquid limit, plastic limit, and shrinkage limit of the studied clays were determined as per the ASTM D4318-10e1 (2010) and presented in Table 4.2. The clay-water mixtures were initially allowed for eight days maturation period under saturated vapor pressure in a closed chamber for the liquid limit determination. The moisture equilibrated samples were then used to evaluate the liquid limit water content by the Casagrande method. The four powder bentonites exhibited very high liquid limit water contents in the range of 175% to 597% in the increasing order from B1 to B4. The plastic limit and shrinkage limit of these bentonites also followed the same order. Similarly, the granular bentonite also exhibited a very high liquid limit water content of 458%. The Atterberg limits of the natural clays- KTND and JBS- were taken from existing literature (Suganya and Sivapullaiah 2017; Kumar, Kishor, and Singh, n.d.). The Atterberg limits were higher for the KTND clay, which has a relatively higher organic content than the JBS.

Activity is defined as the ratio of plasticity index to the clay content i.e., percentage finer than 2 μm (Skempton, 1953). A higher activity value indicates a higher influence of the clay fraction on soil properties and the significance of the type of exchangeable cations and pore-fluid composition on soil properties. The activity of the four powder bentonites was in the range of 2.37 to 6.52, in the increasing order of B1 to B4. The reported grain size distribution of GB was obtained from the

dry sieving method, thus representing the apparent grain size only. The measured clay size fraction in GB was therefore very small despite the very high plasticity value. The activity value of GB, therefore, was not evaluated. Kaolin exhibited a very small activity of 0.11. On the other hand, the KTND clay has an activity value of 1.02.

Table 4.2 Atterberg limits of the studied clays

Soil Name	B1	B2	B3	B4	K	RS	GB	KTND	JBS
Liquid limit, w_{LL} (%)	175	296	393	597	40	42	458	137	84
Plastic limit, w_{PL} (%)	27	46	50	51	32	20	56	80	38
Plasticity index, I_P (%)	148	250	343	546	8	22	402	57	46
Shrinkage limit, w_{SL} (%)	12	14	18	23	28	2	15	33	-
Activity	2.37	3.64	4.37	6.52	0.11	0.687	-	1.02	-

4.2.5 Specific surface area

The surface area of all the studied clay soils was estimated by the most commonly used methods, viz. EGME adsorption (Carter et al. 1965) and MB sorption (Kandhal and Parker 1998) methods. A new method was proposed for quick estimation of the surface area of clays as presented in Chapter 5. All the tests were performed consistently on a uniform soil fraction passing through the 425 μm sieve for comparison purposes. The room temperature during the tests varied in the range of 25 – 32°c.

The procedure recommended by Cerato and Lutenegger (2002) was followed in the estimation of the surface area using the EGME adsorption method. A 3 ml EGME liquid was added to 1 gm of oven-dried soil uniformly on a glass plate, and the mixture was placed in the desiccator. The vacuum pressure inside the desiccator was maintained in the range of 500-600 mm Hg during the test. A weighing balance with a precision of 0.1mg was used for measuring the weight of the soil-EGME mixture. The weight of the soil-EGME mixture was regularly monitored at an interval of 8-10 hours until the equilibrium was achieved. The equilibrium time to reach a constant weight

varied from 3 – 7 days, depending on the soil plasticity. Each test was performed on at least four duplicate samples for each soil, and the average values were reported. The standard deviation in the obtained results was found to be varying with the soil plasticity. A maximum standard deviation of 5% was observed for the higher plasticity powdered bentonites.

The surface area of all the clay soils was further estimated based on the spot MB sorption test by the European standard (Kandhal and Parker 1998; Santamarina et al. 2002). However, a much smaller solid to liquid ratio of 1:50 was used to prepare the soil slurries for all the clay soils instead of the suggested 1:3 solid to liquid ratio as mixing of a 10 g of soil in 30 mL distilled water was not feasible for plastic clays exhibiting high swelling capacity. The initial pH of the slurry was measured for all the soil samples using the pH measuring strip. All the soils, except the KTND and JBS, showed a pH value in the range of 5-6. The KTND and JBS soils showed a relatively higher pH in the range of 8-10. However, the addition of the MB solution decreased the pH of the slurry for all the soils. A similar observation is also made earlier for sodium montmorillonite by Hegyesi et al. (2017). While the KTND and JBS showed a pH in the range of 4.5- 5, the pH of all the other soil slurry mixtures with MB was in the range of 3-4 after the MB addition. A consistent pH value for all the soils was maintained for the intended comparative analysis among the various soil samples as MB sorption depends on the pH of the slurry (Hang and Brindley, 1970; Kahr and Madsen, 1995; Amrhar et al., 2015). Moreover, MB molecules tend to assume a different orientation (i.e., tilted) in case of clays with higher cation exchange capacity (C_e) value (Lagaly and Weiss, 1970). The orientation of the MB molecule increases with increase in the MB sorption on the clay surface (Pozsgay et al., 2004), which is favored by high pH. Further, the titled orientation is more likely when the MB molecules are adsorbed on the narrow edges of the clay particles at pH > isoelectric point of the edge (~4). Therefore, to maintain a consistent pH for all the soils for favoring parallel orientation of the adsorbed MB molecules, the pH in the soil slurry was maintained in the range of 2-3.5 by adding HNO3 acid. A 0.015M MB solution was added at an increment of 1 ml to the pH-adjusted soil slurry. After each increment, the soil slurry was mechanically stirred for 2 minutes at 190-200 rpm in an orbital shaker (Borg Lab Shaker). A droplet of soil slurry-MB solution mixture was placed on a filter paper, and the appearance of the droplet on the filter paper was observed. The addition of 1 ml MB solution to the soil slurry was continued until the formation of a light blue halo ring around the droplet on the filter paper. The blue halo ring indicated the endpoint, and the total consumed volume of the MB solution was

recorded. Tests were performed on four duplicate specimens for each of the studied soil. All the duplicate tests showed consistent results in the MB test.

A new method was proposed in this work for quick and accurate estimation of the total surface area of clays by utilizing the equilibrium sediment volume of clays and theoretical estimation of the DDL thickness around the clay platelets. The procedure involved in the proposed method is presented in detail in Chapter 5.

Table 4.3 The specific surface area of the studied clays based on the EGME and MB method

Clay name	**B1**	**B2**	**B3**	**B4**	**K***	**Na-B2**	**GB**	**KTND**	**JBS**
$S_{a\text{-EGME}}$ (m^2/g)	403	376	498	456	–	698	505	117	80
$S_{a\text{-MB}}$ (m^2/g)	380	465	530	560	–	–	620	256	245
$S_{a\text{-BET (N2)}}$ (m^2/g)	–	–	–	–	12	–	–	–	–

4.2.6 Cations exchange capacity

The cation exchange capacity (CEC) was estimated based on the ammonium acetate method (Chapman, 1965; Ross 1995). A 25 gm of oven-dried clay passing through a 425 μm sieve was washed thoroughly with 250 mL of 1M ammonium acetate solution at a pH of 7.0 (Chapman, 1965) in an orbital shaker for four hours and kept for overnight stand (Muurinen, 2011). The mixture was then subjected to centrifugation at 1000 rpm for 3–4 min to extract out the supernatant solution containing the exchanged surface cations. The concentrations of individual major cations (i.e., Na^+, Ca^{2+}, K^+, and Mg^{2+}) in the extracted solution were determined using the flame photometer and atomic absorption spectroscopy. The total CEC was obtained from the summation of all the individual cations. Tests were conducted on three duplicate samples for each clay and the average values were reported in Table 4.4. The CEC of the powder bentonites and the GB varied in the range of 38 –110 meq/100g and followed the order of their liquid limit values. The B4 bentonite with the highest plasticity index among the four studied bentonites showed the maximum cation exchange capacity and the highest percentage of sodium as an exchangeable cation. The percentage of exchangeable sodium in B4 bentonite is ~85%. The B2 and B3 bentonites contain mixed-valent surface cations with sodium and calcium as the dominant cations. The percentages of exchangeable sodium and calcium in B2 bentonite were 60.5% and 21.2%,

respectively, remaining was contributed by the other two cations. The B3 bentonite has a relatively smaller percentage of sodium (~49%) and a significant amount of calcium (~41%). The B1 bentonite with the lowest plasticity value, on the other hand, was dominated by the divalent cations with the lowest percentage of sodium (~36%) among the four bentonites. A significant amount of exchangeable magnesium (~21.4%) was available in this bentonite, unlike others. The individual cations percentages for GB bentonite were not evaluated in this work, however, it is fairly assumed to be sodium-dominant bentonite based on its very high plasticity index (~400). As expected, the cation exchange capacity of kaolin was very small (C_e = 5 meq/100g) as compared to the studied bentonites.

Table 4.4 Total cation exchange capacity and percentage of individual surface cations of the studied clays

Soil name	**B1**	**B2**	**B3**	**B4**	**K**	**GB**
Total C_e (meq/100g)	38.8	55.5	71.7	108.8	5	98
Na^+ (%)	35.8	60.5	48.5	84.7	–	–
Ca^{2+} (%)	39.2	21.2	41	12.6	–	–
Mg^{2+} (%)	21.4	9.6	8.7	2.6	–	–
K^+ (%)	3.6	8.7	1.8	0.1	–	–

4.2.7 Mineralogy and chemical composition

The primary mineral phases in the studied powder bentonites and the kaolin clay were identified based on the X-ray diffraction (XRD) analysis. The XRD data of the studied bentonites and kaolin were presented in Fig. 4.2. The mineral phases were identified based on the d value corresponding to different peak intensities using the standard database (Harris and White, 2008). XRD pattern of all the four bentonites suggested the presence of the montmorillonite minerals along with other minerals, viz., illite, kaolinite, calcite, and quartz. The kaolin exhibited clear and sharp peaks of kaolinite mineral over the entire range of 2θ suggesting it to be a kaolinite-dominated clay.

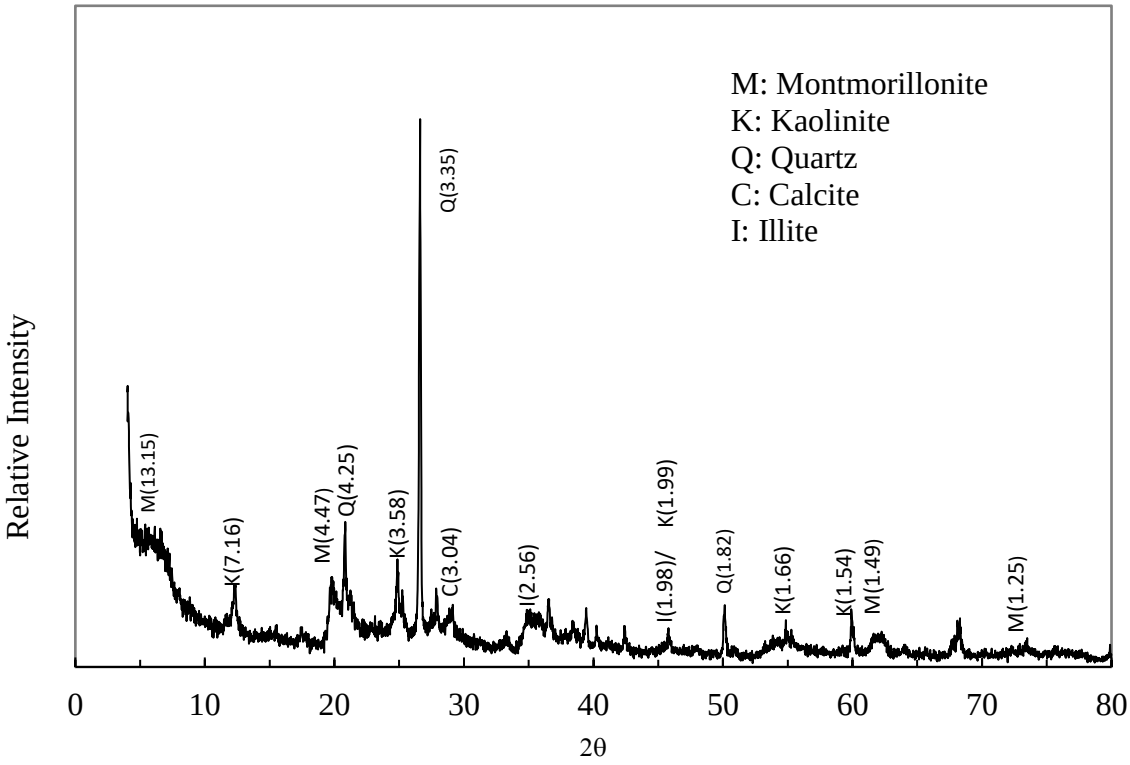

Fig. 4.2a XRD pattern of B1 bentonite

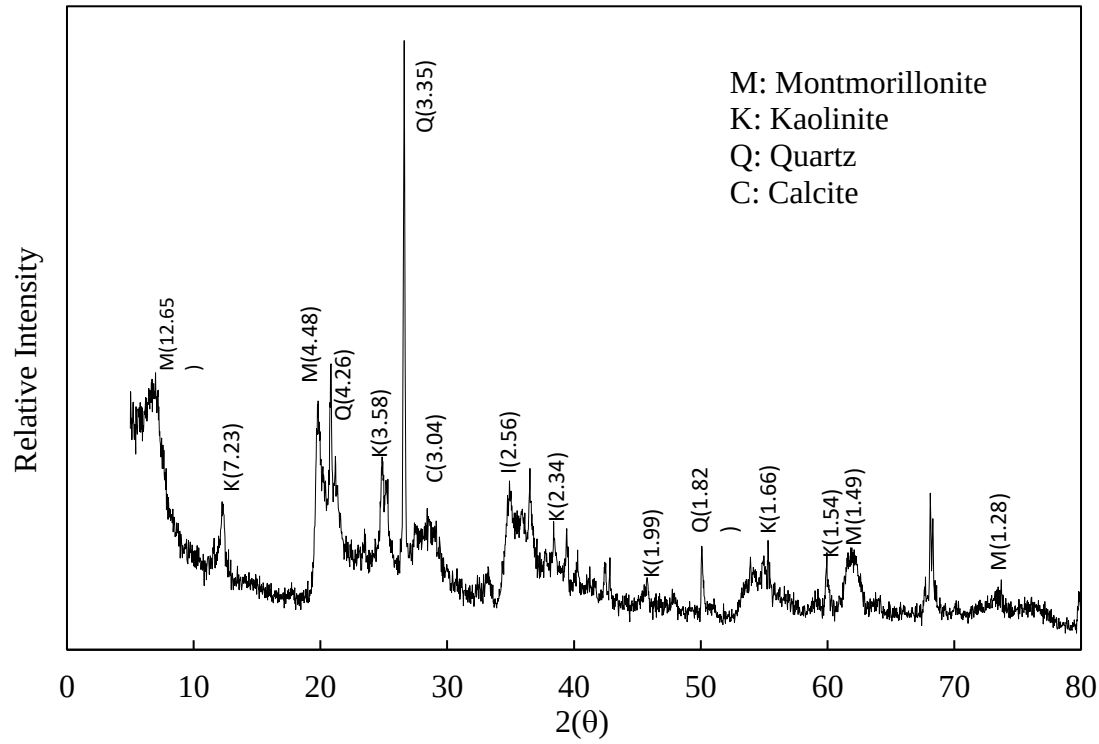

Fig. 4.2b XRD pattern of B2 bentonite

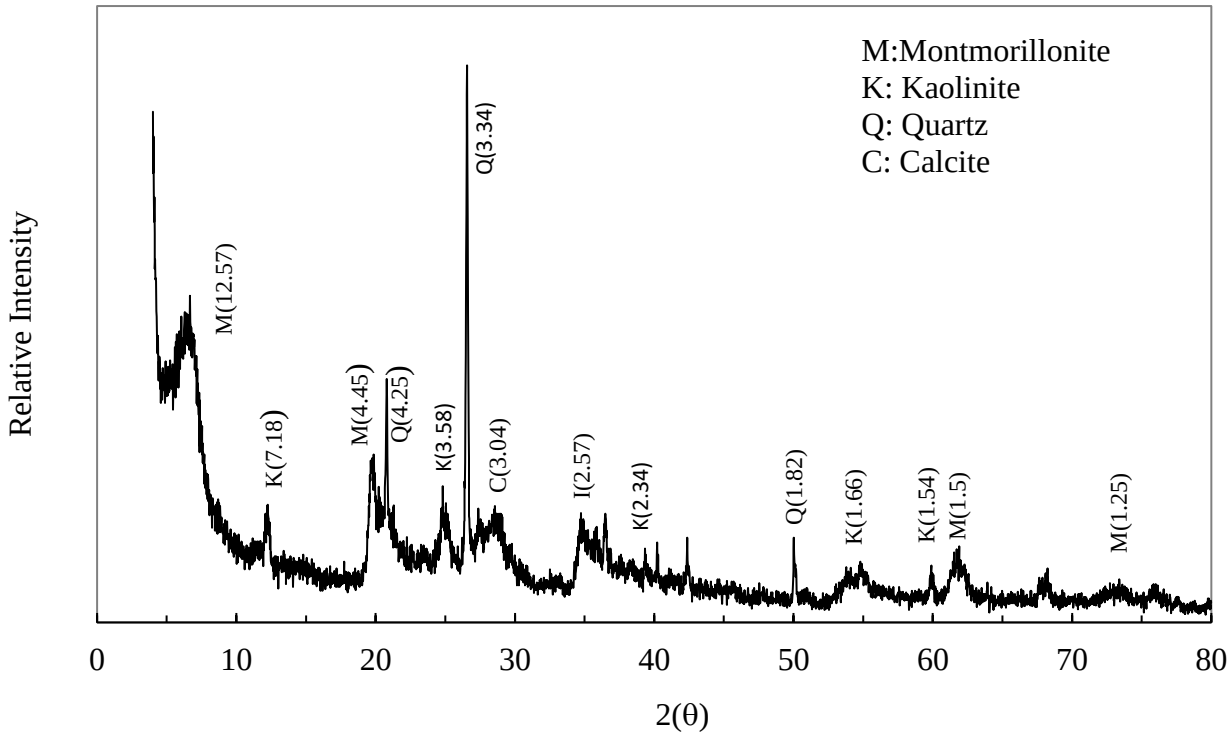

Fig. 4.2b XRD pattern of B3 bentonite

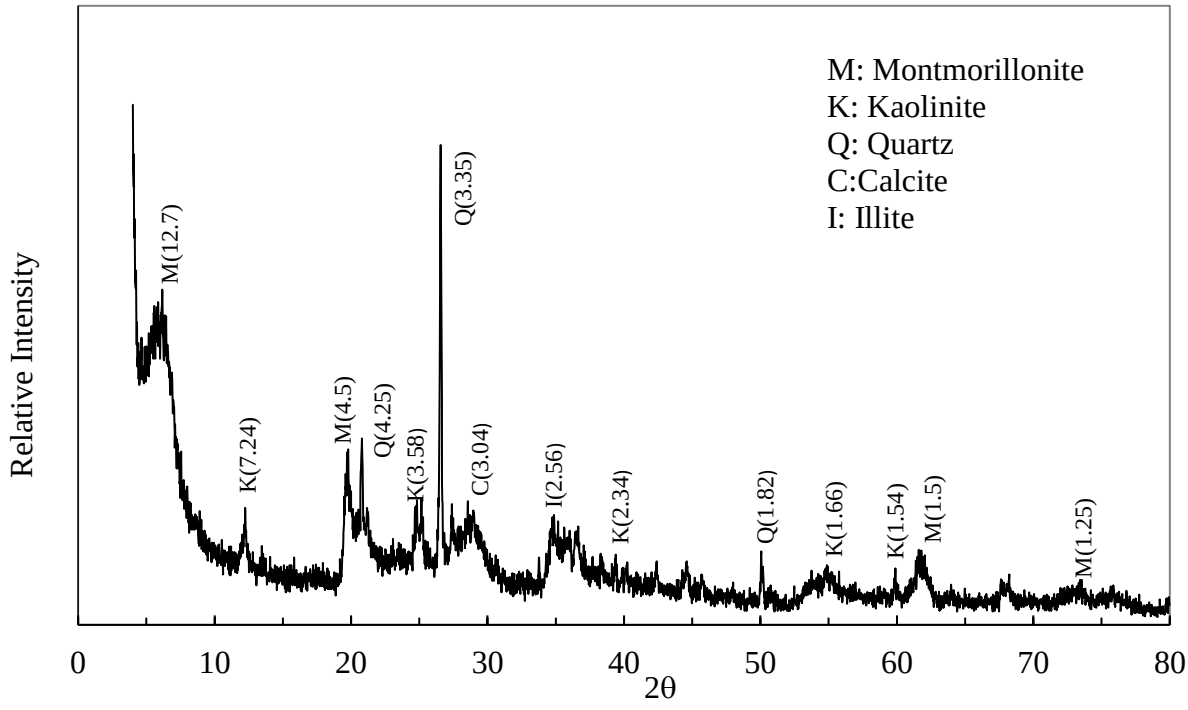

Fig. 4.2d XRD pattern of B4 bentonite

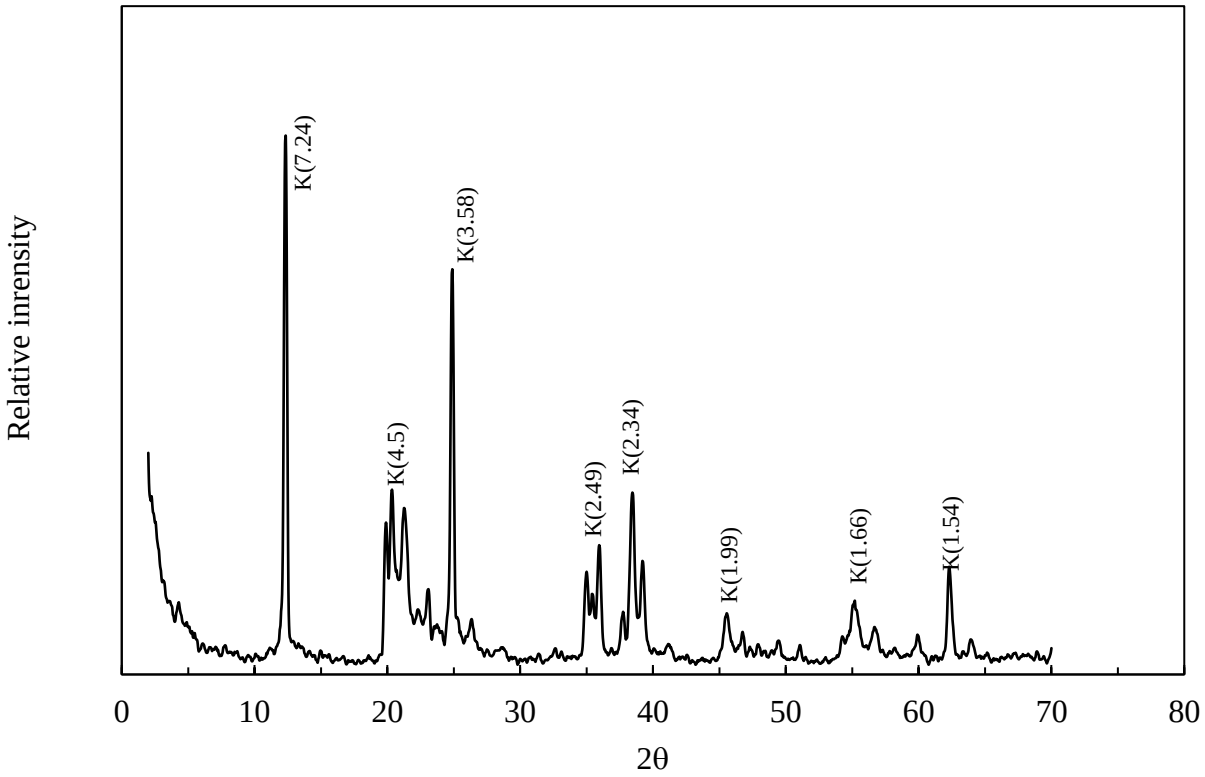

Fig. 4.2e XRD pattern of studied kaolin in powder form

The chemical composition of the bentonites was obtained from the X-ray fluorescence (XRF) analysis and presented in Table 4.5. The results of all the bentonites were similar to the standard MX80 bentonite (Karnland, 2010).

4.2.8 Summary of the properties of the clays used

The considered clays in this study represented a wide range of soil characteristics viz., plasticity, grain size distribution, mineral composition, specific surface area, exchangeable cations, and organic content. The mineral constituents of the four Indian bentonites were identical but differed in the surface characteristics and percentage of silt and sand-size particles. The plasticity of the four powder bentonites varied in a wide range (i.e., 148% to 546%) indicating significant variation in the bentonite quality. The difference in the quality of the four powder bentonites, however, was not captured by the United Soil Classification System (USCS), which classifies all the four powder bentonites into a single category of high plasticity clay (CH). Similarly, the GB bentonite was also classified as highly plastic clay (CH). The studied kaolin was primarily constituted of pure

kaolinite mineral which has a very small surface area of 12 m^2/g and a cation exchange capacity of 5 meq/100g. As per the USCS, the studied kaolin was classified as clayey silt with slight plasticity. The locally available red soil (RS) used in the study is classified as silty clay with low plasticity (CL). The two natural clays, KTND and JBS are rich in organic content and exhibited a plasticity value of 57 and 46, respectively. The former is classified as CH and the latter as organic clay with high plasticity (OH) as per the USCS.

Based on the measured cation exchange capacity and the XRD data, the montmorillonite mineral content of the studied bentonites was approximately estimated using the regression method (Chittoori, 2008; Ashraf, 2008) and presented in Table 4.6. The percentage of montmorillonite minerals in the studied bentonites varied from 39% to 61%. The important properties of the studied clays are summarized in Table 4.6 below.

Table 4.5 Oxide compositions of the studied bentonites from X-ray Fluorescence analysis (After Gapak et al., 2018).

Soil name	**SiO_2**	**Al_2O_3**	**Fe_2O_3 (T)**	**MnO**	**MgO**	**CaO**	**Na_2O**	**K_2O**	**TiO_2**	**P_2O_5**
B1	59.72	23.21	4.72	0.124	1.57	1.09	2.83	1.54	3.54	0.45
B2	57.10	24.88	5.29	0.151	1.57	0.61	3.12	1.04	3.81	0.42
B3	59.55	22.53	4.47	0.154	1.97	1.11	2.97	1.66	3.60	0.48
B4	53.97	20.45	8.71	0.101	1.92	1.15	4.34	1.60	3.25	0.26

Table 4.6 Summary of the important properties of the studied clays

Properties	B1	B2	B3	B4	K	Na-B2	RS	GB	KTND	BCS
Specific gravity	2.76	2.76	2.77	2.77	2.62	2.8	2.67	2.75	2.48	2.65
Liquid limit (%)	175	296	393	597	40	-	42	458	137	84
Plastic limit (%)	27	46	50	51	32	-	20	56	80	38
Shrinkage limit (%)	12	14	18	23	28	-	-	15	33	-
Plasticity index, I_P (%)	148	250	343	546	8	-	22	402	57	46
S_a (m^2/g) (EGME)	403	376	498	456	12	698	-	505	117	80
C_e (meq/100 g)	38.8	55.5	71.7	108.8	5	-	-	98	-	-
Na^+ (%)	35.8	60.5	48.5	84.7	-	100	-	-	-	-
Ca^{2+} (%)	39.2	21.2	41	12.6	-	0	-	-	-	-
K^+ (%)	3.6	8.7	1.8	0.1	-	0	-	-	-	-
Mg^{2+} (%)	21.4	9.6	8.7	2.6	-	0	-	-	-	-
Grain-size (%)										
sand (>75 μm)	2.35	3.79	1.39	1.53	0	0	43	70	4	-
Silt (75–2 μm)	35.33	27.48	20.18	14.71	28	2	25	~30	40	-
Clay (< 2 μm)	62.32	68.73	78.43	83.75	72	98	32	0	56	-
Montmorillonite (%)	39	42	55	61	-	-	-	-	-	-
Activity	2.37	3.64	4.37	6.52	0.11	-	0.687	-	1.02	-

4.3 Experimental methods

4.3.1 Equilibrium sediment volume test

The equilibrium sediment volume test was carried out to study the saturated clay behavior at a very low particle interaction, which is predominantly controlled by the physicochemical forces in the absence of external mechanical pressure. The tests results were intended for validating the developed theoretical model based on the DDL theory, which is based on assumption that the clay platelets are in a parallel arrangement. Dispersion of the individual clay particles during the sedimentation was, therefore, crucial to ensure a parallel arrangement of the clay platelets in the clay-water-electrolyte mixture. A standard procedure was evolved in this study to minimize the flocculation of the clay particles and ensure a complete dispersion in the clay-electrolyte suspension.

As the ESV test was intended for validating the theoretical formulation based on the DDL theory which requires the specific surface area as an input parameter, a soil fraction passing through 425μm was used to maintain consistency with the sample used in the surface area measurement. Further, the parallel plate assumption necessitates a proper dispersion of clay particles in the clay-electrolyte suspension in the measuring cylinder and the elimination of any hindrance on the settlement of individual clay particles and aggregation due to the presence of coarser particles in the soil. A smaller solid to liquid ratio of 1:50 was then chosen to further ensure proper dispersion of clay particles and avoid any particle aggregation. A 2 g of oven-dried clay sample passing through 425 μm was, therefore, used to measure the ESV in a 100 ml cylinder for all the studied soils. The oven-dried soil sample was initially poured into a 250 ml conical flask containing (<100 mL) the desired electrolyte solution and mixed using a mechanical stirrer at 190-200 rpm. Thorough mixing of the soil sample with the electrolyte solution was needed to ensure complete dispersion of the clay particles before the start of the settlement process. Incomplete dispersion or adhesion of fine clay particles onto the coarse silt and sand particles due to insufficient mixing time significantly influenced the settlement behavior of the clay suspension in the electrolyte environment. Hence, the ESV measurement is very sensitive to the stirring duration and type of electrolyte solution. As the standard mixing duration is not available in the literature, tests were performed with different mixing durations to find out the optimal mixing duration to ensure complete dispersion of the clay particles for different quality clay soils. After stirring for a

specified duration, the mixture was then transferred to a 100 ml graduated glass cylinder, and the total volume of the mixture was adjusted to the 100 ml mark by adding the same concentration of the electrolyte. The clay-electrolyte suspension was allowed to reach equilibrium, and the final volume of the soil sediment at the bottom of the cylinder was measured (Fig. 2). The room temperature varied between 25° to 32° C during the testing. For each stirring time, sediment volume tests with at least four duplicate samples were conducted to check the consistency.

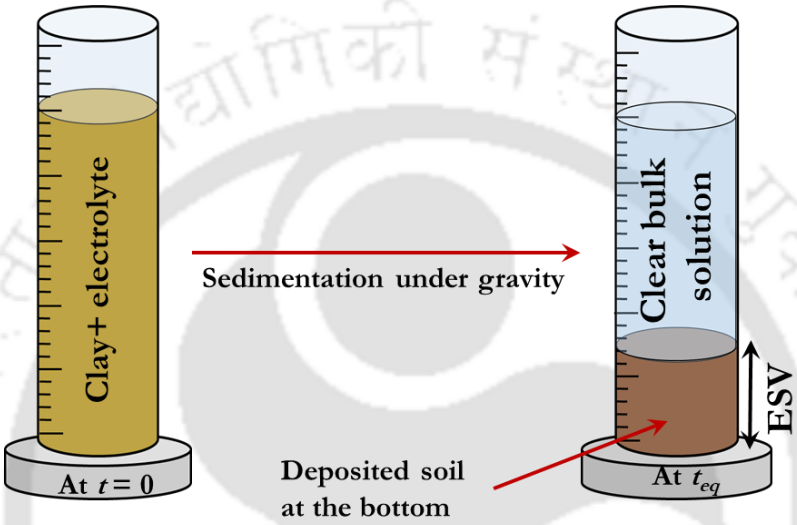

Fig. 4.3 Illustration of equilibrium sediment volume test at the beginning and final equilibrium

The time to achieve the equilibrium sediment volume was 20 minutes to 4 hours, depending on the clay soil. The dispersion of the clay particles was confirmed by the consistency in the ESV with a given mixing/stirring time. The measured ESV of B1 bentonite in the presence of 0.1 N NaCl salt solution for different mixing durations is presented in Fig. 4.4. The ESV of the duplicate samples showed a significant variation for a short mixing duration. As the mixing duration was increased, the ESV of the duplicate samples tend to converge. A consistent ESV for all the duplicate samples was obtained after mixing the clay-electrolyte solution for at least 30 minutes which indicated the dispersion of the clay platelets. The required mixing duration for proper dispersion of clay particles varied depending on the clay type and electrolyte concentration. At least 30 minutes of mixing time were found to be sufficient to obtain a consistent ESV for the powder bentonites and the granular bentonite. However, a longer mixing time of 30 minutes was required for the bentonite-sand mixtures for achieving the equilibrium due to the adhesion of fine clay particles onto the coarse silt and fine sand particles. Overall, the required mixing time to

obtain a consistent ESV was increased with an increase in the non-clay content (> 2μm). A mixing time of 30-45 minutes was found to be sufficient for all the samples to obtain a consistent ESV and thus was recommended.

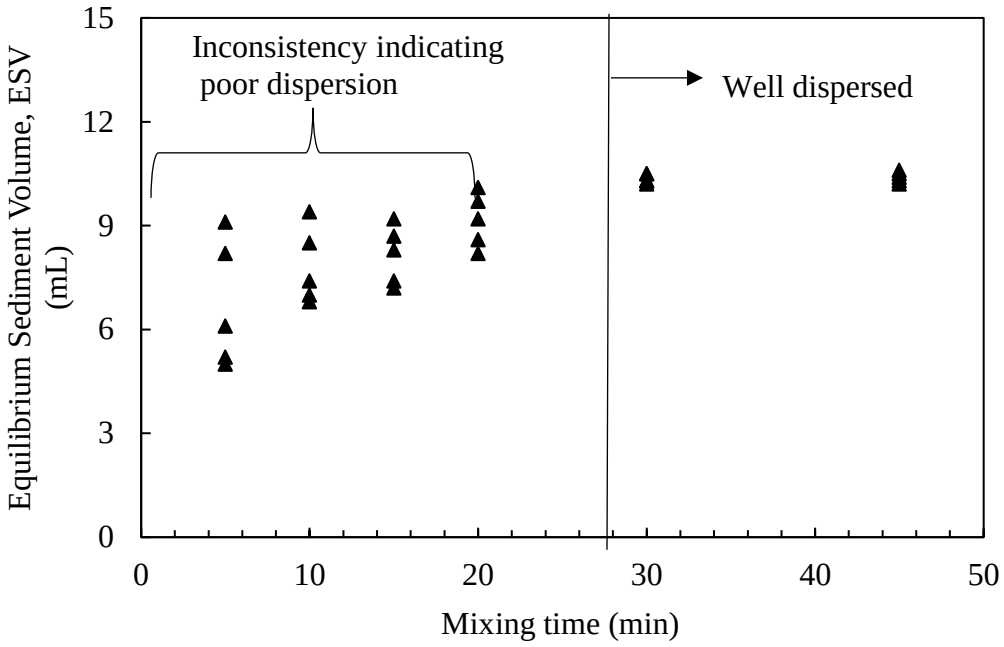

Fig. 4.4 Consistency in sediment volume measurement with different stirring times for B1 bentonite in the presence of 0. 1N NaCl

4.3.2 Consolidation test

The compressibility behavior of the studied clays was determined using the conventional oedometer test setup. The oedometer ring is made of brass and has a dimension of 60 mm diameter and 20 mm height. The inside portion of the rings was lubricated with silicone grease to minimize side friction between the ring and the clay specimen. Clay samples were prepared at an initial water content of approximately 1.1 – 1. 5 times the liquid limit water content. The slurried clay specimens were placed in the oedometer ring to a thickness of 20 mm while tapping on a rubber base to prevent any air entrapment. The oedometer ring along with the clay sample sits on a porous stone. Filter papers were placed between the clay specimen and the porous stones. The porous stones and filter papers were soaked prior to the placement inside the assembly. The ring was then mounted on an oedometer assembly and positioned in the loading frame. The dial gauge was placed on the top plate of the cell for recording the vertical deformation of the sample and inundated with the desired electrolyte solution. The tests were conducted by applying step-wise consolidation

pressures of 5, 10, 25, 50, 100, 200, 400, and 800 kPa. The subsequent load was applied once the sample achieved a 90% consolidation settlement. Taylor's square root method (Taylor, 1948) was used to calculate the time required for 90% consolidation. The void ratio values under applied consolidation pressure were estimated from the final moisture content and dial gauge readings.

4.3.3 Isochoric swelling pressure test

The test assembly for measuring the swelling pressure of air-dry compacted bentonites under isochoric conditions is shown in Fig. 4.5. It consists of an oedometer cell, a digital S-type load cell for recording the upward pressure by the soil, a loading frame for fixing the load cell, a datalogger for reading out the load cell signal, a base for placing the oedometer cell with the compacted bentonite specimen, a reservoir containing the inundating fluid and an LVDT for monitoring any potential movement of the base/pedestal.

Compacted bentonite specimens were prepared by the displacement-controlled uniaxial compaction method. For a targeted compaction density, the required amount of air-dried sample of powdered bentonite was placed in an oedometer ring sitting on a movable base. Plunger was placed vertically on top of the specimen, which was connected to a fixed proving ring/load cell. The base was then raised against the fixed plunger at a constant rate to compact the specimen in the oedometer ring to the desired dry density. The applied uniaxial compression load required to compact the soil specimen to a given density was recorded by the proving ring/load cell. The oedometer ring along with the compacted specimen of 15 mm thickness and 60 mm diameter was then assembled in the oedometer cell. Oven-dried porous stones were placed at the bottom and on top of the compacted specimen, separated by oven-dried filter paper. A perforated loading cap was placed on top of the porous stone to evenly distribute the applied load. A reservoir was connected to the bottom of the oedometer assembly for wetting the bentonite specimen and for the development of swelling pressure as shown in Fig. 4.5. The swelling pressure of the bentonite specimen was continuously recorded by the data logger attached to the load cell. After completion of the test, the bentonite specimens were carefully extracted from the oedometer ring using a mechanical extruder and used for the water content and suction measurement, and microstructural study. The suction was measured using the WP4 dew point potentiometer (Leong et al., 2003; Campbell et al., 2007)

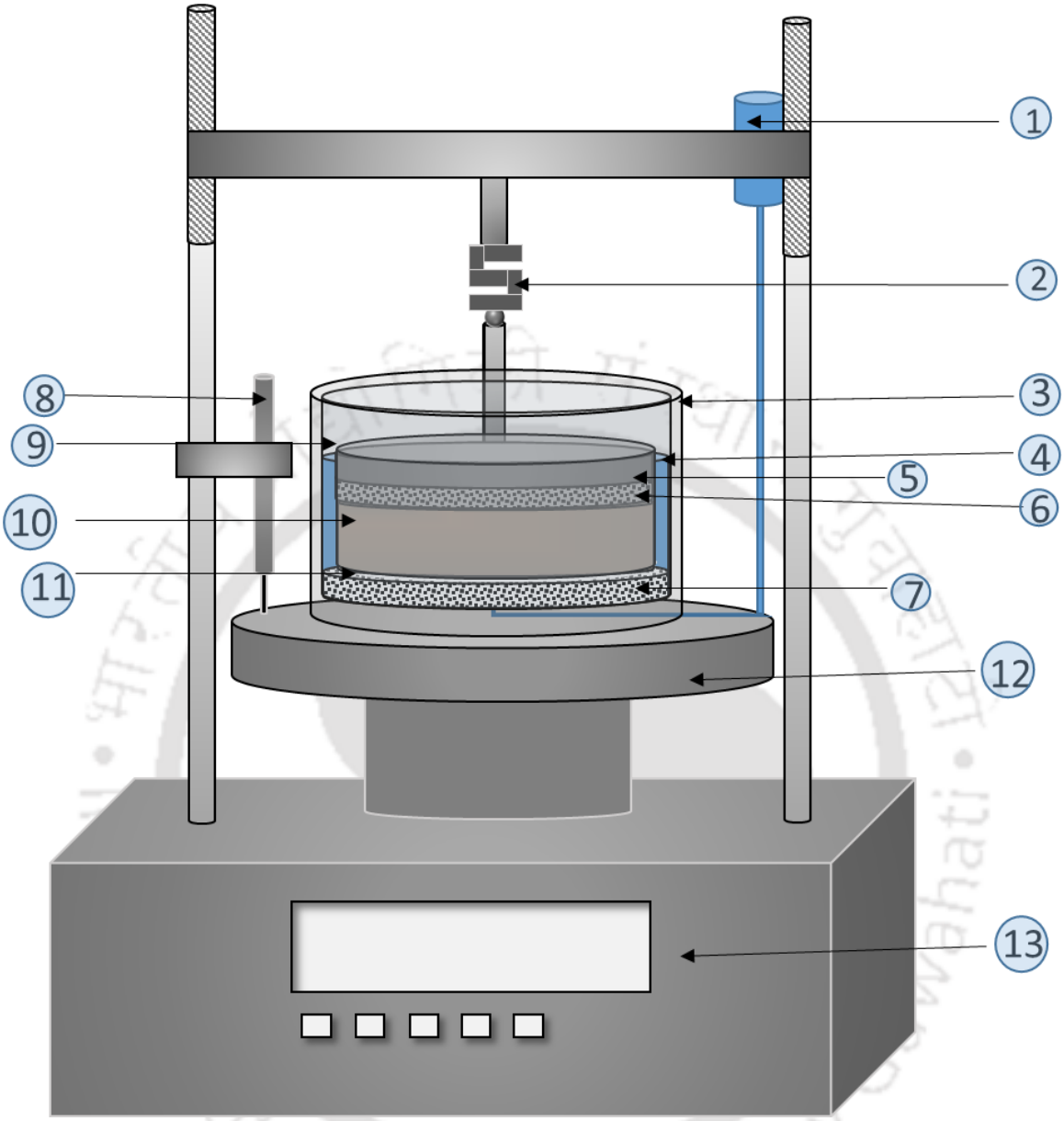

Fig. 4.5 Illustration of the isochoric swelling pressure test set-up.

1. Water reservoir; 2. Digital Load cell (S-type); 3. Outer ring of Oedometer; 4. Water level in the Oedometer reservoir; 5. Top loading plate; 6. Top porous stone; 7. Bottom porous stone; 8. LVDT; 9. Inner mold (oedometer ring) containing bentonite specimen; 10. Compacted bentonite specimen; 11. Filter paper; 12. Pedestal/base; 13. Load display and control unit

4.3.4 Wetting-induced volumetric deformation test

The wetting-induced volumetric deformation behavior of kaolin was studied using the conventional oedometer test assembly. Compacted specimens of kaolin were prepared by the

uniaxial compression as described above. The standard procedure for studying the wetting-induced collapse behavior of soil (Jennings and Knight, 1957; Clemence and Finbarr, 1981; ASTM D 4546-14, 2014; Choudhury and Bharat, 2018) was adopted in this work. The compacted specimen was initially subjected to incremental vertical stress in the air-dry state up to a pre-defined value. The vertical deformation was continuously monitored with the help of a dial gauge placed on the top of the loading assembly. Once the equilibrium was achieved under the applied loading in dry condition, the specimen was subjected to wetting keeping the applied vertical stress constant. The applied vertical stress under which wetting was done is termed as the inundation pressure in this work. The vertical deformation was continuously monitored by the dial gauge reading. The volumetric deformation was represented in terms of volumetric strain, expressed as the ratio of change in height to the height of kaolin specimen at equilibrium under the inundation pressure before the inundation. The volume reduction was reported as positive strain and the swelling was reported as negative strain in this manuscript.

4.3.5 Microstructural study

The microstructure of the clay specimens was analyzed based on the pore size distribution (PSD) from the MIP test and the fabric image from the FESEM analysis. Extreme care was taken to preserve the microstructure of the specimens with minimum disturbance during the sample extraction and the subsequent stages till the completion of the analysis. The samples for the MIP test and FESEM analysis were collected separately from the mid-height of the central part of the extracted specimens. Assuming a uniform microstructure of the specimen in the region of sample collection, the MIP test data and FESEM images together represented the microstructure of the specimen at the mid-height. The location on the specimen for the microstructural study was kept the same for all the cases to maintain consistency for comparison purposes. The collected samples were then freeze-dried using the Lyophilizer (LabconcoFreeZone®) at −60° C (Choudhury and Bharat, 2018) to avoid disturbance to the pore size and fabric of the compacted specimen. A representative freeze–dried specimen of volume 500 mm^3, without visible discontinuities in the sample, was used for the MIP testing and FESEM analysis. The PSDs of the freeze-dried specimens were determined using Pascal 140–440 porosimeter (Thermo Scientific®), which is capable of measuring pore sizes from 100 – 0.005 μm, by controlling the pressure in the range of

0.01–340 MPa. Mercury intruded pore sizes at different pressure steps were determined by the Washburn equation (Washburn 1921) as given by

$$P = \frac{4T_s \cos\theta}{D} \quad (29)$$

where D is the pore diameter, T_s is the surface tension, θ is the contact angle, and P is the applied mercury pressure. The pore volume contribution of different pore sizes was obtained based on the volume change of mercury under each pressure increment. The fabric image of the kaolin specimens was obtained by analyzing the freeze-dried sample in the FESEM sigma 300 instruments.

4.4 Experimental programs

This section describes various experimental programs carried out in the study.

4.4.1 ESV behavior

Two series of tests were carried out on the equilibrium sediment volume behavior of clays in this work. In the first series, the ESV test was performed with two different salt solutions NaCl and $CaCl_2$ by varying the ionic concentration in the range of 0.001N- 2N to understand the influence of pore fluid parameters viz., ionic concentration and valence. The Indian powder bentonites, B2, and B4 were used in this test series. The results were analyzed along with the theoretical ESV data to understand the various influencing factors on the ESV and the applicability of the developed theoretical framework. Further, the ESV behavior of the homoionic clay, Na-B2 was studied in the presence of NaCl solution to validate the proposed model.

In the second test series, ESV tests were performed using 0.1 N NaCl solution and the test results were used to estimate the specific surface area based on the proposed method in this study. Six different clay soils viz., B1, B3, B4, GB, KTND, and JBS were considered in this test series. Further, a fine uniform sand fraction passing through 150 μm and retaining on 75 μm was added to all the three powder bentonites at two different proportions, 10% and 20% by weight, to synthetically produce soil samples of different plasticity. Six such different fine sand-bentonite mixtures were obtained and designated as BM1, BM2, BM3, and so on. The mixing proportions

of all these combinations were presented in Table 4.7. Overall, the studied soil samples represented a wide range of plasticity and specific surface area values.

4.4.2 Compressibility behavior

The compressibility behavior of three powder Indian bentonites viz., B1, B2, and B3, and the locally available red soil were determined in the consolidation pressure range of 0–800 kPa. Further, the red soil was mixed with the B1 bentonite at equal weight proportions to synthetically produce a clay of different plasticity and represent a wide range of plasticity. The compressibility data were also estimated for B3 bentonite using different inundation fluids, viz., water, 0.1 M NaCl, and 1M NaCl, to understand the applicability of the proposed model and the influence of pore–fluid concentration on the intrinsic parameter. Saturated bentonite samples with NaCl solutions were prepared for measuring the compressibility data by mixing the powder bentonite specimen to the liquid limit moisture content using two different NaCl concentrations. The liquid limit moisture content of B3 with 0.1 M and 1 M NaCl concentrations was measured to be 278% and 87%, respectively.

4.4.3 Isochoric swelling pressure of compacted bentonites

In this study, three series of isochoric swelling pressure tests were performed on the two Indian bentonites, B2 and B3. The former has a plasticity index of 250% while the latter has a plasticity of 343%.

The first series of tests were conducted to carry out the microstructural study on the observed two distinct SPEC behaviors. Based on the literature study on several bentonites, viz., Febex bentonite (Villar and Gómez-Espina, 2009), MX80 (Herbert et al., 2008), GMZ bentonite (Schanz and Al-Badran, 2012; Chen et al., 2018; Zhu et al., 2013; He et al., 2019), French FoCa clay (Imbert and Villar 2006), and German bentonite (Schanz and Tripathy, 2009) and the two Indian bentonites (Choudhury, 2019), two distinct SPEC behavior as presented in Fig. 8.6 were considered in this study to investigate the underlying microstructural mechanisms. The b-SPEC (OPQR in Fig. 8.6a) is characterized by a temporary peak after point P, followed by a drop in swelling pressure with a minimum at Q, beyond which swelling pressure increases monotonously before reaching equilibrium at R. The m-SPEC (O'P'Q'R' in Fig. 8.6b), on the other hand, is characterized by a temporary plateau behavior from P' to Q', before the swelling pressure increase and reaches equilibrium at R'. In this study, duplicate tests were conducted and tests were terminated at

specified points on the SPEC (i.e., at P, Q, and R on the b-SPEC and P', Q', and R' on the m-SPEC) and the samples were extracted for microstructural study. Swelling pressure tests were carried out at the dry densities of 1.45 Mg/m^3 and 1.8 Mg/m^3 where both the b-SPEC and m-SPEC behavior were exhibited by the two Indian bentonites (Choudhury, 2019).

In the second test series, the swelling pressure of B3 bentonite was evaluated using four different wetting fluids, viz., water, NaCl, KCl, and LiCl solutions. A strong cationic concentration of 1M was used for the electrolyte solutions to minimize the influence of the mixed-valence surface cations and understand the effect of the cation type present in the wetting electrolyte solution. Tests were performed using the compacted specimens of B3 bentonite at a dry density of 1.45 Mg/m^3.

In the third series, the swelling pressure of bentonite-sand mixtures was evaluated under isochoric conditions using water as the inundating fluid. Four different bentonite-sand mixtures designated as BS-10, BS-20, BS-30, and BS-40, were prepared by mixing the B2 bentonite with fine sand passing through 425 μm and retaining on 75 μm at four different proportions. The mixing proportions of the bentonite-sand mixtures were presented in Table 4.7. The tests were performed using the compacted specimens of the bentonite-sand mixtures at a dry density of 1.45 Mg/m^3.

Table 4.7 Mixing details of the bentonite-sand mixtures used for swelling pressure tests

Bentonite-sand mixture	**BS10**	**BS20**	**BS30**	**BS40**
Sand content (%)	10	20	30	40

4.4.4 Wetting-induced volumetric behavior of kaolin

The influence of compaction density and the inundation pressure on the wetting-induced volumetric deformation of kaolin was investigated in this study. The wetting of the air-dry compacted kaolin was performed at six different compaction densities, viz., 0.71 Mg/m^3, 0.9 Mg/m^3, 1.1 Mg/m^3, 1.25 Mg/m^3, 1.5 Mg/m^3, and 1.7 Mg/m^3 under different inundation pressures in the range of 0.01 MPa to 1.6 MPa. For a few cases, incremental loading was further applied beyond the post-wetting equilibrium point to study the consolidation behavior of the kaolin soil. The microstructure of kaolin specimens at the as-compacted and post-wetting equilibrium state was investigated at two compaction densities and certain inundation pressures identified based on

the observed response of the kaolin. The studied kaolin at 1.25 Mg/m^3 exhibited consistent volumetric collapse under all the inundation pressures. The microstructure of as-compacted and 'post-collapse under 400 kPa' specimens was compared to understand the microstructural mechanisms during the volumetric collapse. On the other hand, at 1.5 Mg/m^3, the studied kaolin exhibited swelling under small inundation pressure and collapse at higher inundation pressure. The microstructure of the kaolin at this density was, therefore, evaluated at different states viz., as-compacted, post-swelling under 10 kPa, and post-collapse under 400 kPa to distinguish the mechanisms behind the volumetric collapse and swelling under different inundation pressures.

5 Saturated clay behavior at weak particle interaction

5.1 General

This chapter deals with the development of a theoretical framework for the behavior of weakly interacting saturated clay particles under zero mechanical stress. The chapter is divided into two parts. The first part presents the theoretical formulation of the ESV of clays using the Gouy-Chapman DDL theory and validation against the measured ESV data of different bentonites in salt solutions. The second part presents a new technique for estimating the total surface area of clays which is a fundamental characteristic of clays important for understanding the physicochemical mechanisms in clays. Further, the surface area is also an essential input parameter for the theoretical prediction of clay behavior. A simple and quick method was developed to accurately estimate the surface area of clays from the measured ESV in a salt solution.

5.2 Theoretical formulation of equilibrium sediment volume of clays

This section presents a theoretical approach based on DDL theory for estimating the equilibrium sediment volume of bentonites in the presence of salt solutions. A simple analytical expression relating equilibrium sediment volume with different influencing physicochemical parameters such as clay surface and pore-fluid parameters was developed. The hypothesis behind the developed framework is discussed first, followed by the developed analytical equation. A detailed sensitivity analysis was carried out to understand the dependency of the DDL thickness on various pore fluid parameters and soil surface properties and is presented next. Experimental validation and discussions were then presented followed by a summary.

5.2.1 Hypothesis

After the clay specimen was thoroughly mixed with a given electrolyte solution and brought to equilibrium as illustrated in Fig. 5.1, the clay platelets settle at the bottom of a glass jar with their fully developed DDLs (Fig. 5.1). Theoretical analysis of the sediment volume at equilibrium was analyzed using the following hypothesis.

The clay platelets were assumed to settle independently without any aggregation after the clay-electrolyte mixture was left in a glass jar for equilibrium. The adapted procedure for the preparation of clay-electrolyte mixture would ensure the formation of clay suspension without the formation

of any aggregates. The individual clay platelets come to equilibrium under the influence of both body and surface forces during the sedimentation. When the clay platelets come close to each other under the influence of body forces due to gravity, electrostatic forces get mobilized due to the interaction of DDLs. The body forces bring the platelets together, but the electrostatic repulsive pressures due to the surface forces separate the platelets away from each other to increase the free energy of the system. At equilibrium, the body forces due to gravity must be equal to the electrostatic surface forces. Body forces due to gravity were considered in this study to avoid the singularity of the integral solution (i.e., Eq. 3) even though they are not dominant in ESV. Electrostatic repulsive forces are dominant at low electrolyte concentrations due to large DDL thicknesses. The platelets assume parallel-plate arrangement at the bottom of the jar at equilibrium under the influence of such forces (see inset in Fig. 5.1b for the illustration). The clay platelets are, however, flocculated at high electrolyte concentrations (n>1 M) (van Olphen, 1977) due to the dominant nature of the van der Walls forces. The van der Waals forces were, however, ignored in this work. The sediment volume was analyzed at different electrolyte concentrations to analyze the influence of concentrations on the clay fabric.

The bentonite samples consisted of small percentages of silt and fine-sand content. The influence of silt and fine-sand content was explicitly not considered on the sediment volume. The decrease in the measured specific surface area values, however, decreased the predicted sediment volumes for different bentonites and electrolytes due to the contribution from the non-clay content. The significance of this assumption was discussed when the experimental results were analyzed with the proposed model.

The size of the clay platelets in the natural soils varies in several orders of magnitude. The measured S_a, therefore, only represents the equivalent value for the bentonite. The bentonite specimen was, however, assumed to be consisting of equal DDL thickness for all the platelets independent of the size of the clay platelet. The DDL thickness was observed to be independent of S_a as shown in the present results. The assumption made here was, therefore, justified. The DDL theory was used to relate the distance between the platelets with the osmotic pressure by solving Eqs. 3, 4, 23 and using the aforementioned hypothesis. The osmotic pressure is equal to the body forces due to gravity at equilibrium which can be computed if the clay platelet thickness is known.

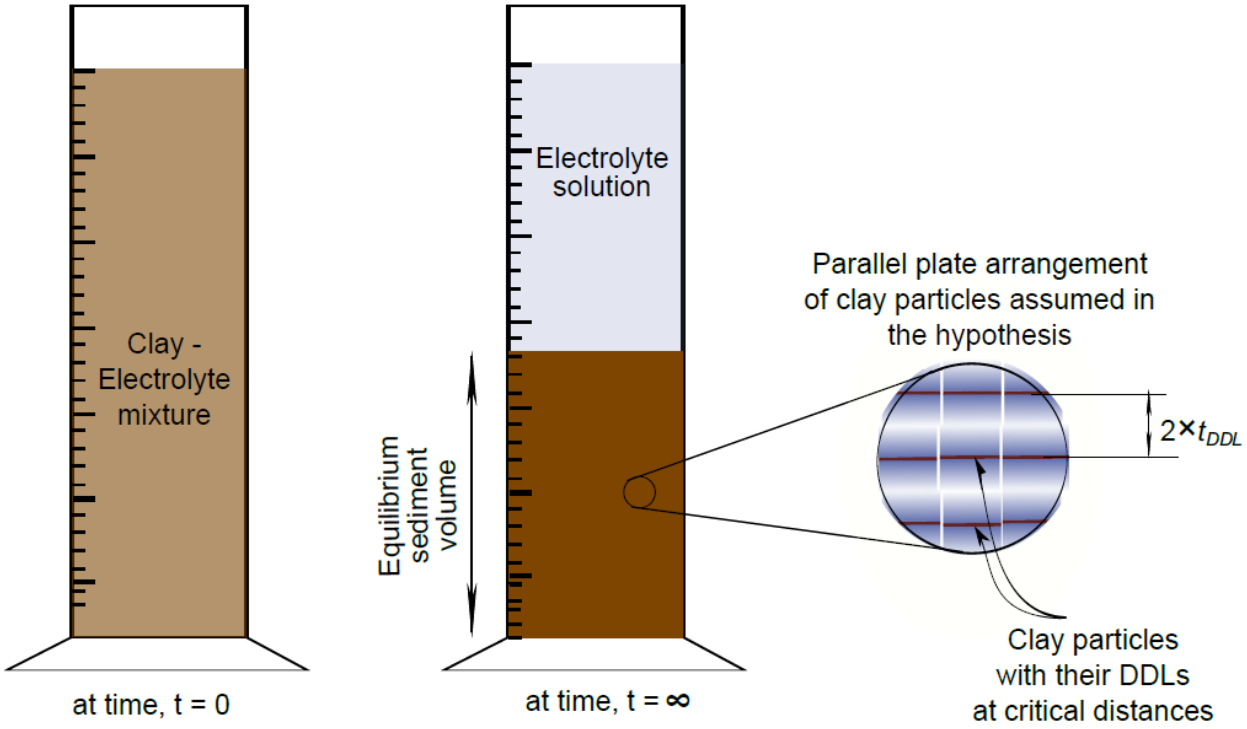

Fig. 5.1 Illustration of the equilibrium sediment volume test (a) at the beginning and (b) at equilibrium (inset: assumed assumption of parallel clay plate arrangement in the sediment)

The equilibrium sediment volume, which is the total measured sediment volume in the tests, can be related to the void ratio as

$$E_{SV} = (1+e)\times V_s = \frac{(1+e)M_s}{G_s\rho_w} = \frac{(1+S_a t_{DDL}\rho_w G_s)M_s}{G_s\rho_w} \tag{30}$$

where M_s is the dry mass of the bentonite. The DDL thickness, t_{DDL}, is unknown for the theoretical estimation of ESV. If the pressure on the clay platelet due to the body force is estimated, the normalized mid-plane potential can be estimated from Eq. 23. The electrostatic potential at the clay surface, z is obtained by solving Eq. 4 for known midplane potential, soil surface, and pore fluid properties. The half-space distance (i.e., $d/2$) between the platelets, which is equal to the DDL thickness (t_{DDL}), was estimated using Eq. 3. Equilibrium void ratio and equilibrium sediment volume thus can be estimated using Eqs. 28 and 30 respectively. The analytical solution of Eq. 3 is, however, not available in its most general form due to the elliptic nature of the integral (Bharat, 2004; Bharat et al., 2013). An analytical solution was developed for estimating the ESV from the pore-fluid and clay surface characteristics.

5.2.2 Analytical Solution

The analytical solution was derived when the osmotic pressure at the mid-plane distance was very small (i.e., equal to the body forces). The DDLs of the platelets undergo very small interaction under such forces (Fig. 5.2). Because the clay platelets are interacting only under the influence of body forces that are negligible compared to the surface forces (i.e., *u* is negligible), Eq. 3 was approximated as

$$\kappa t_{DDL} = -\int_{z}^{u} (2\cosh(y) - 2)^{-1/2}\, dy \tag{32}$$

where u in the upper limit of integration is written as $\cosh^{-1}(1+P/2nRT)$ (from Eq. 23). The normalized mid-plane potential was, however, used and not neglected in the upper limit of the integral to avoid the singularity of the solution. It was shown later that the aforementioned assumption was not significant for the prediction of ESV. The pressure due to body forces can be estimated if the thickness of the clay platelet is known. The mean thickness of the smectite platelets is found to be equal to 10 Å (Nadeau, 1985). The particle thickness of up to 40 Å is observed for randomly interstratified minerals. The mean thickness was used in the calculations as a thickness of 40 Å did not provide significant changes in the theoretically estimated ESV values. The weight of an individual platelet due to body force along with the DDLs can be estimated as

$$P = \frac{\left(t_p \gamma_s + 2t_{DDL}\gamma_w\right)A}{A} = \gamma_w\left(t_p G_s + 2t_{DDL}\right) \tag{33}$$

where A is the cross-sectional area and γ_s is the unit weight of clay platelets, and γ_w is the unit weight of pore-fluid. Substitution of Eq. 33 in Eq. 32 gives

$$\kappa t_{DDL} = -\int_{z}^{\cosh^{-1}\left(1+\gamma_w\left(\frac{t_p G_s + 2t_{DDL}}{2nRT}\right)\right)} (2\cosh(y) - 2)^{-1/2}\, dy$$

which can alternatively be written as

$$\kappa t_{DDL} = -\frac{1}{2}\int_{z}^{\cosh^{-1}\left(1+\gamma_w\left(\frac{t_p G_s + 2t_{DDL}}{2nRT}\right)\right)} \operatorname{csch}\left(y/2\right)\, dy \tag{34}$$

The analytical solution to Eq. 34 was given by:

$$t_{DDL} = -\frac{1}{\kappa}\left[\ln\left(\tanh\left(y/4\right)\right)\right]_{z}^{\cosh^{-1}\left(1+\gamma_w\left(\frac{t_p G_s + 2t_{DDL}}{2nRT}\right)\right)} \tag{35}$$

and after simplification

$$t_{DDL} = \frac{1}{\kappa}\left[\ln\left(\tanh\left(\frac{z}{4}\right)\right) - \ln\left(\tanh\left(\frac{1}{4}\cosh^{-1}\left(1+\gamma_w\left(\frac{t_p G_s + 2t_{DDL}}{2nRT}\right)\right)\right)\right)\right] \tag{36}$$

where $\left(1/\kappa\right)$ is expressed in Å and the dimensionless surface potential can be expressed as (Bharat et al., 2013; Bharat and Sridharan, 2015a):

$$z = \cosh^{-1}\left(1+0.5\left[\frac{C_e}{S_a}\times\frac{2513.6}{\sqrt{\varepsilon nT}}\right]^2\right) \tag{37}$$

where Eq. 4 was solved after substituting for $u = 0$. As the variation of the normalized surface potential with normalized mid-plane potential is negligible at small interactions (i.e., $\kappa t_{DDL} >> 1$), Eq. 37 provides an accurate estimation of normalized surface potential. According to Eq. 36, the DDL thickness of an individual clay platelet in equilibrium sediment volume depends on the normalized surface potential, pore-fluid parameters, and the DDL thickness (which is unknown).

The implicit equation was solved for DDL thickness iteratively as explained in Appendix 1. The equation was quickly converged in just two iterations. Equilibrium sediment volume was then computed by substituting t_{DDL} in Eq. 30. The accuracy of the proposed analytical solution was verified by comparing it with the numerical solution obtained by solving Eqs. 3, 4, 23, 30 as shown in the flowchart presented in Fig. 5.3 to justify the assumption made to Eq. 3 in deriving the analytical solution (Eq. 36). In each iteration, the DDL thickness was computed by calculating the osmotic pressure for the assumed value of DDL thickness. The elliptic integral (Eq. 3) was numerically solved by adding an infinitesimal number to the upper limit of the integral (i.e., u) to avoid the singularity of the elliptic equation (Bharat et al., 2013; Bharat and Sridharan, 2015a). The infinitesimal number varied in the range of 10^{-4} to 10^{-7} for different pore-fluid and surface properties to obtain a finite solution for Eq. 3. The DDL thickness was iteratively obtained by

verifying the computed and assumed values of DDL thickness as explained in the flowchart. The comparison between the analytical and numerical solutions for different pore-fluid and clay surface parameters was presented in Fig. 5.4. The computed DDL thicknesses by proposed analytical solution (Eq. 36) using the approximated equation, Eq. 32, and numerical solution of Eq. 3 followed a 1:1 line over a wide range for different clay surfaces and pore-fluid parameters. The analytical solution was in good agreement with the numerical solution showing a correlation coefficient of $R^2 = 0.999$. The approximation of Eq. 3 to Eq. 32 was, therefore, insignificant. The analytical solution was accurate and simple to predict theoretical ESV for known pore-fluid and clay surface parameters. The numerical solution, on the other hand, required the solution of an elliptic integral in each iteration and was tedious to obtain. The proposed analytical solution was, therefore, recommended for the theoretical estimation of ESV and used for validation experiments on the laboratory test results.

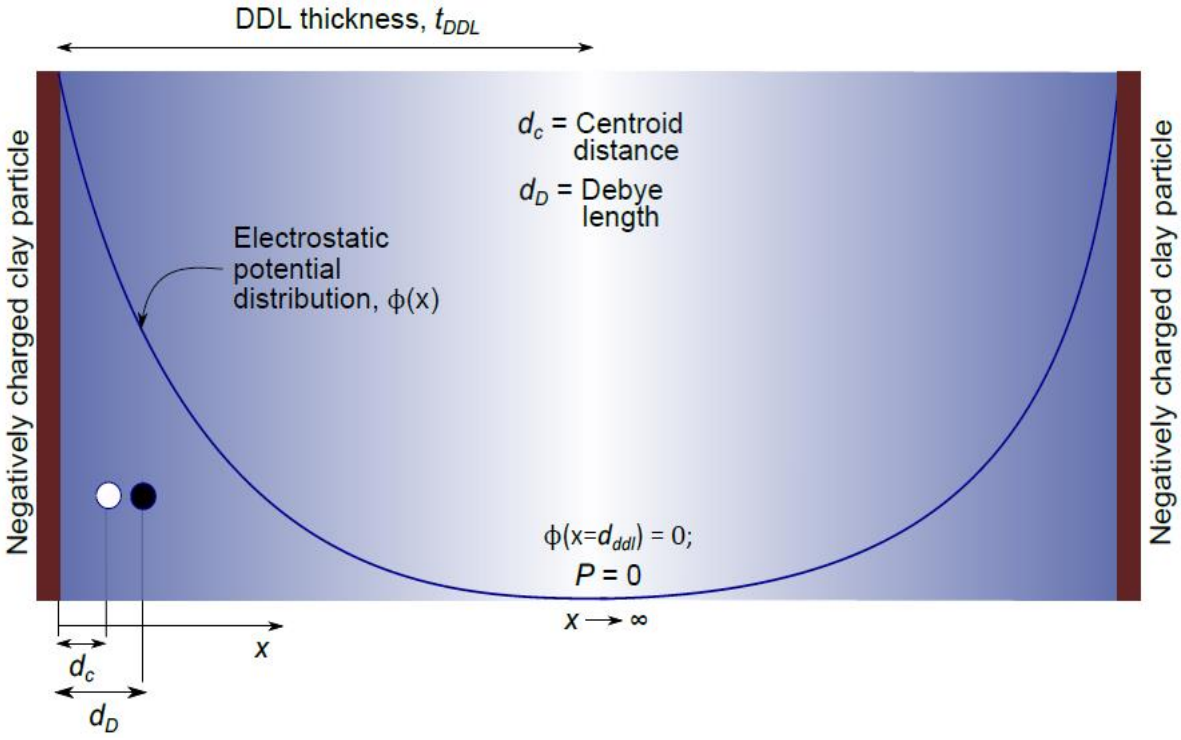

Fig. 5.2 Illustration of the electrostatic distribution around interacting clay platelets at equilibrium under the influence of body forces due to gravity

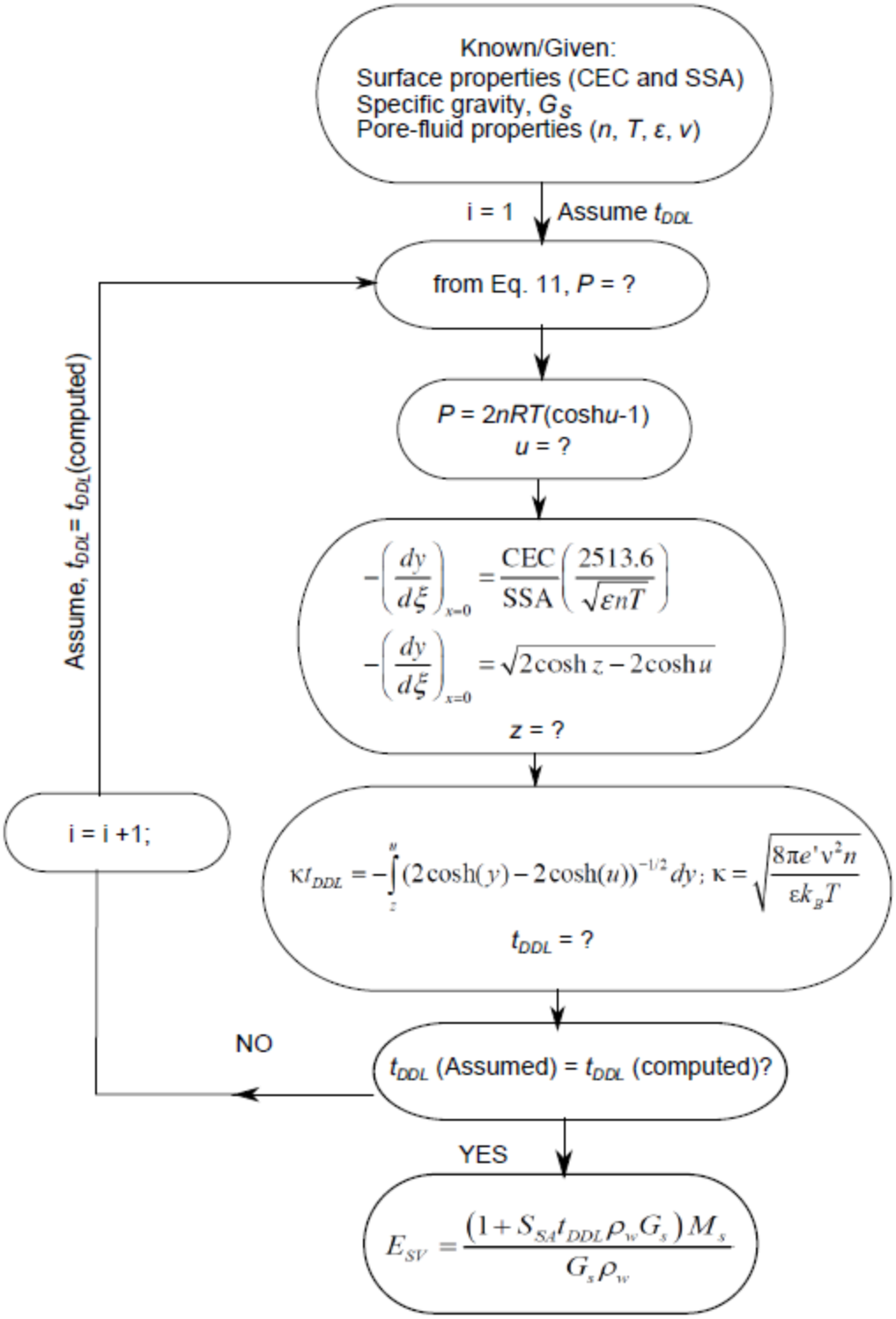

Fig. 5.3 Flowchart showing the iterative numerical procedure for the determination of theoretical sediment volume

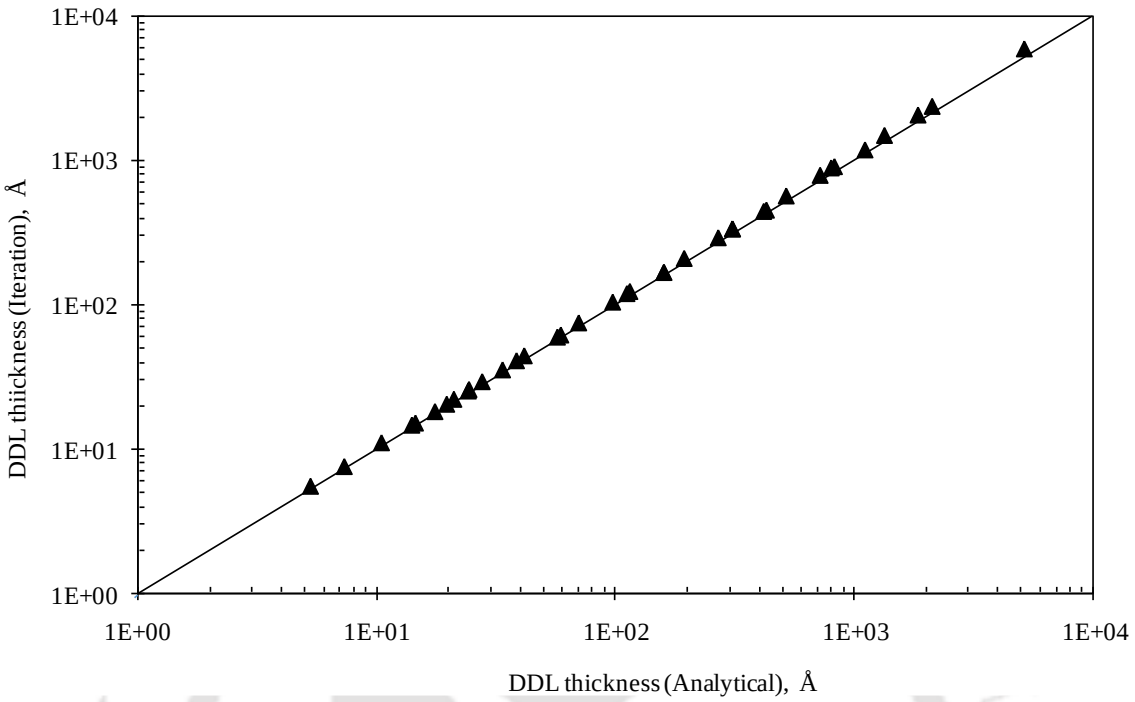

Fig. 5.4 Validation of the analytical model with the numerical solution for DDL thickness computation.

5.2.3 Sensitivity analysis

The influence of clay surface parameters on DDL thickness was analyzed using Eqs. 36 – 37. The details of the pore-fluid and clay surface properties used in the theoretical analysis were listed in the figure titles. The dependency of t_{DDL} and ESV on different pore-fluid and clay surface parameters was analyzed using Fig. 5.5.1–5.5.3. The variation of t_{DDL} with a pore-fluid concentration on the logarithmic scale for two clays having different SSA values showed (Fig. 5.5.1a) that the DDL thickness decreased linearly with an increase in the concentration. The DDL thickness decreases with an increase in the concentration (Bharat and Sridharan, 2015b) to bring the platelets close to each other to maintain the osmotic pressure equal to the body forces due to gravity. The influence of specific surface area on the DDL thickness was not found which suggested that the DDL thicknesses would remain the same for the clay plates having two different specific surface areas. The electrostatic potential distribution around the platelets would, however, be adjusted. The specific surface area, on the other hand, influenced the relationship between ESV vs. c_0 (Fig. 5.5.1b) as the limiting void ratio or ESV is a direct function of the specific surface area (Eq. 30). The relationship between ESV and n was qualitatively similar to the influence of pore-fluid concentration on the theoretical compressibility of plastic clays (Bharat and Sridharan,

2015a). The sediment volume computed using Eq. 36 for clays having different specific surface areas was, therefore, different even though the computed DDL thicknesses were the same.

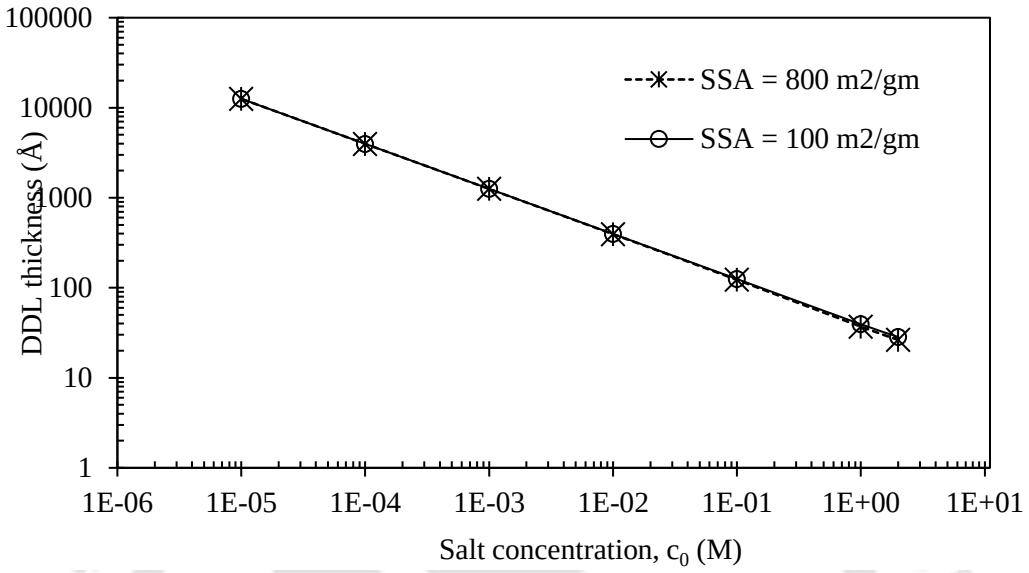

Fig. 5.5.1a Theoretical relationship of DDL thickness vs pore fluid concentration for clays having two different S_{SA} values (CEC = 100 meq/100g, v = 1, G = 2.76, ε = 80.4, and T = 298 K)

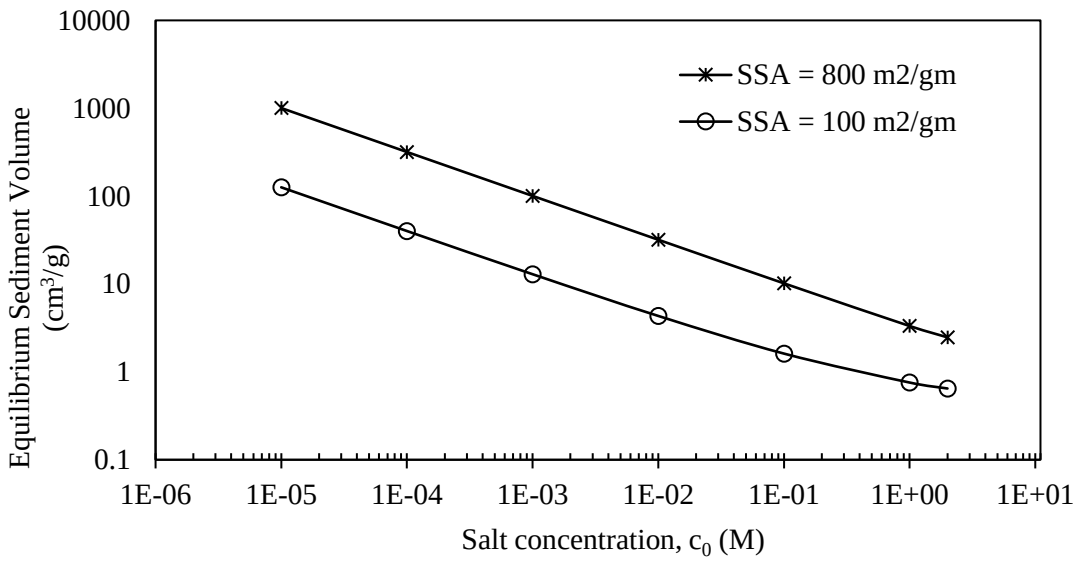

Fig. 5.5.1b Theoretical relationship of DDL thickness vs pore fluid concentration for clays having two different S_{SA} values (CEC = 100 meq/100g, v = 1, G = 2.76, ε = 80.4, and T = 298 K)

The cation exchange capacity showed (Fig. 5.5.2a – 5.5.2b) no influence on both t_{DDL} vs. c_0 and ESV vs. c_0 relationships. The observations were qualitatively similar to the influence of SSA and

CEC on the compressibility behavior of plastic clays (Bharat and Sridharan, 2015a). The increase in cation valence decreased the ESV for a given pore-fluid concentration as shown in Fig. 5.5.3. The effect of pore-fluid parameters on the ESV was, therefore, qualitatively similar to the influence of characteristic length on DDL thickness.

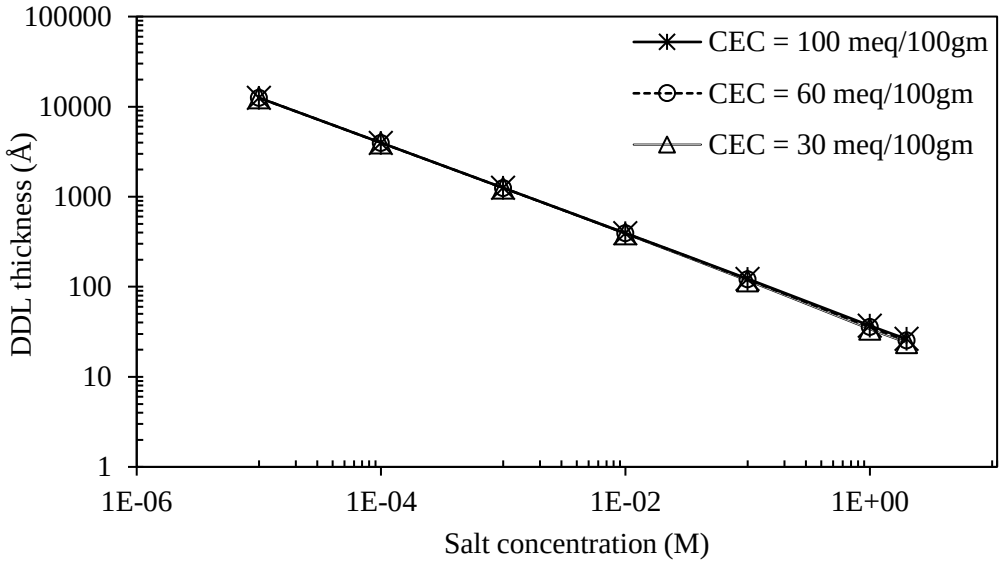

Fig. 5.5.2a DDL thickness vs pore fluid concentration for two different C_e values (S_a = 800 m^2/g, ν = 1, G = 2.76, ε = 80.4, and T = 298 K)

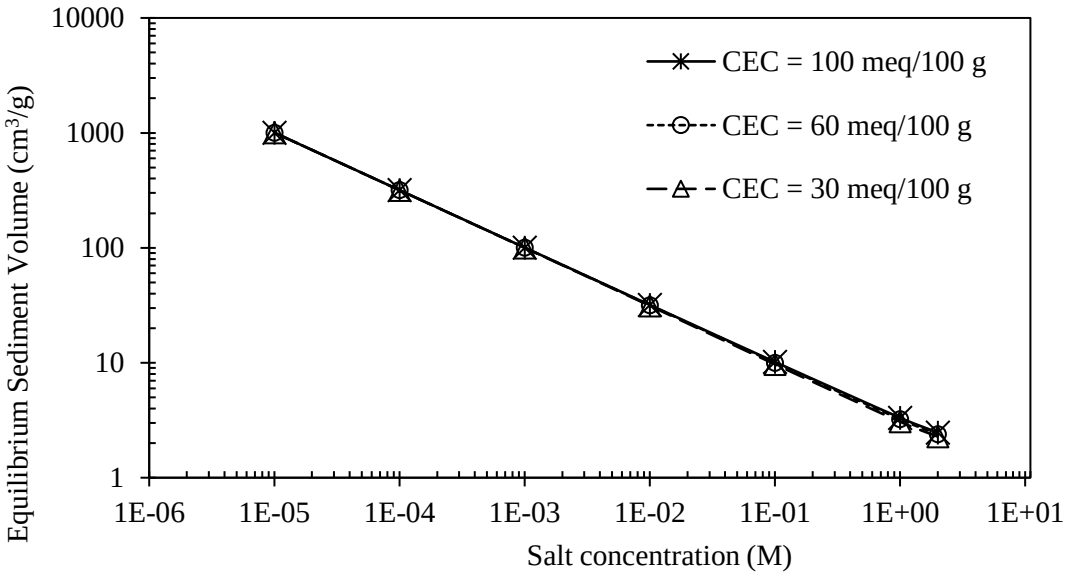

Fig. 5.5.2b ESV vs pore fluid concentration for two different C_e values (S_a = 800 m^2/g, ν = 1, G = 2.76, ε = 80.4, and T = 298 K)

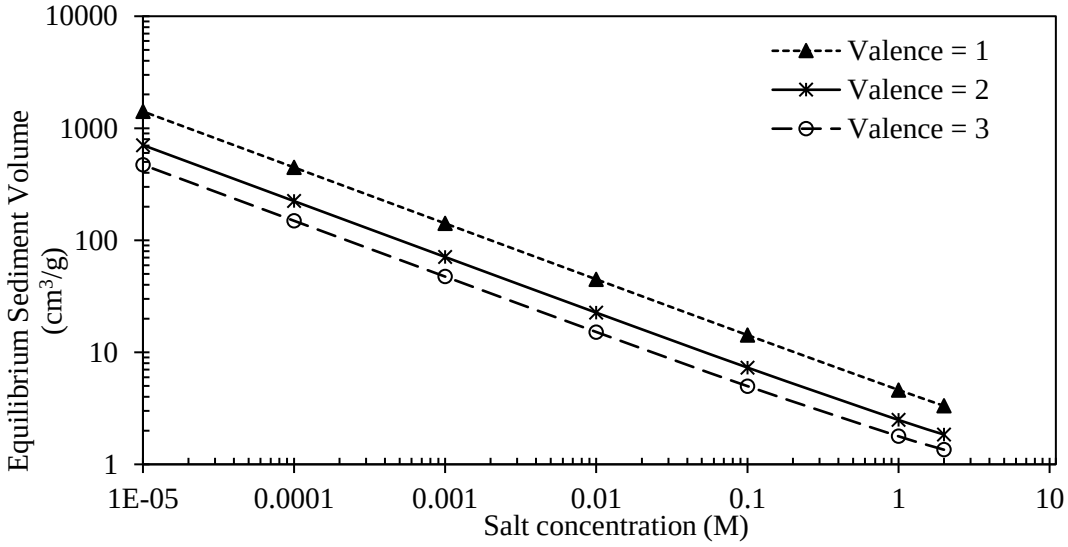

Fig. 5.5.3 Theoretical relationship of E_{SV} vs pore-fluid concentration for different cation valence (C_e = 100 meq/100g, S_a = 800 m^2/g, G = 2.76, ε = 80.4, and T = 298 K).

5.2.4 Experimental validation

The theoretical data of ESV for different electrolyte concentrations were estimated for known pore-fluid and clay surface parameters using both Eqs. 36–37 as described in Appendix1 to compare against the experimental data in Figs. 5.6a–5.6c. The measured ESV data of commercial bentonite (Sridharan and Prakash, 1999) in the presence of different NaCl concentrations, varying from 0.05 to 1 M, were presented against the theoretically predicted data in Fig. 5.6a. The sediment volume data obtained by the proposed method were in very good agreement with the experimental data in the studied concentration range. The predicted and measured ESV data of B2 and B4 bentonites in NaCl and $CaCl_2$ solutions in a wider concentration range varying from 0.001 – 2 M were shown in Figs. 5.6b–5.6c. The theoretical solution over-predicted the ESV in the presence of low NaCl concentrations (c_0 <0.01 M) for B2 bentonite. The theoretical line in the presence of NaCl solution was obtained using cation valance of ν = 1, which represented a homo-ionic system of Na^+ cations. The B2 bentonite, however, contained several cations viz. Na^+, Ca^{2+}, K^+, and Mg^{2+}, in the exchangeable state, on the negatively charged surfaces. Even though B2 had a high percentage of exchangeable sodium cations (61-85%), the presence of small percentages of Ca^{2+} ions can decrease the thickness of the diffuse double layer significantly (Bharat, 2004). The DDL thickness computed from the measured sediment volume data using Eqs. 30 showed in Fig. 5.7 that the thickness was less than the theoretical counterpart (Eq. 36) after considering the

exchangeable monovalent cations. The assumption of $\nu = 1$ in theory overestimated and, on the other hand, $\nu = 2$ underestimated both the DDL thickness and corresponding equilibrium sediment volume. The presence of potassium and magnesium ions, further, reduces the DDL thickness considerably (Sridharan et al., 1986). The theoretical prediction, therefore, deviated from the measured data at low pore-fluid concentrations (c_0 <0.01 M) for B2 bentonite. The clay behavior in the presence of exchangeable mixed cations is complex and was not attempted to model here. The theoretical data approached the experimental counterpart and was in good agreement in the concentration range of 0.01 – 1 M due to the dominance of Na^+ ions in the bulk solution that might have replaced the other exchangeable surface cations on the clay surface. The clay behavior follows homoionic clay behavior at this concentration as such high concentrations are used to prepare homoionic clays (van Olphen, 1977). Therefore, the proposed model derived for homovalent cations accurately predicts the measured behavior of B2 bentonite in the concentration range of 0.01 – 1 M. A small deviation of theoretical data from the measurements was, however, observed at pore-fluid concentration $c_0 \geq 1$ M. The deviation at this electrolyte concentration might be due to the combined effect of clay aggregate formation and the presence of non-clay content. The particle orientation at high electrolyte concentration is observed to be edge-to-face and the interactions are dominated by van der Waals forces in sodium bentonites (van Olphen, 1977; Heller and Keren, 2001). The formation of clay aggregates increased the measured sediment volume. On the other hand, the predicted volume was smaller due to the parallel plate assumption in the theory. A silt content of 10 – 13% and a fine-sand content of 7 – 12% were present in B2 bentonite. The presence of non-clay content influences the sediment volume at higher concentrations as the volume contributed by the clay was insignificant due to the suppression of DDLs. The predicted volume, therefore, was less than the measurements at concentrations higher than 1M. The influence of non-clay content was not observed at $c_0 < 1$ M because the measured specific surface area, which was determined on the constituents passing through 425-μm sieve size (that contain fine sand, silt, and clay fraction), is directly proportional to the clay content in the soil (Petersen et al., 1996). The underestimated S_a values, due to the presence of small silt and sand content, when used in the theoretical analysis (Eq. 32) predicted smaller values of ESV. As discussed earlier, the reported S_a data in Table 4.3 were the mean values from four independent measurements. Therefore, the influence of S_a measurement on the estimated ESV was also investigated. The variation between the measurements varied from 2–10% for the studied bentonites. The influence

of S_a variation on the predicted ESV data was shown in Figs. 5.6b, 5.6c, and 5.8, for the studied bentonites. The predicted data using extreme values of the measured S_a were reported in the figures by showing the percentage of deviation from the mean value. The S_a variation in the measurements did not influence the prediction significantly for B2 bentonite as shown in Fig. 5.6b. Comparison of theoretical and experimental ESV data of B2 in the presence of $CaCl_2$ solution in Fig. 5.6b showed that the ESV data were overestimated for electrolyte concentrations $c_0 \geq 0.01$ M and slightly underestimated for $c_0 < 0.01$ M. Overestimated results for $c_0 \geq 0.01$ M were due to the formation of clay aggregates in the experiments as opposed to the parallel-plate assumption made in the theory, but underestimating the ESV data $c_0 < 0.01$ M might be due to the presence of mixed cations.

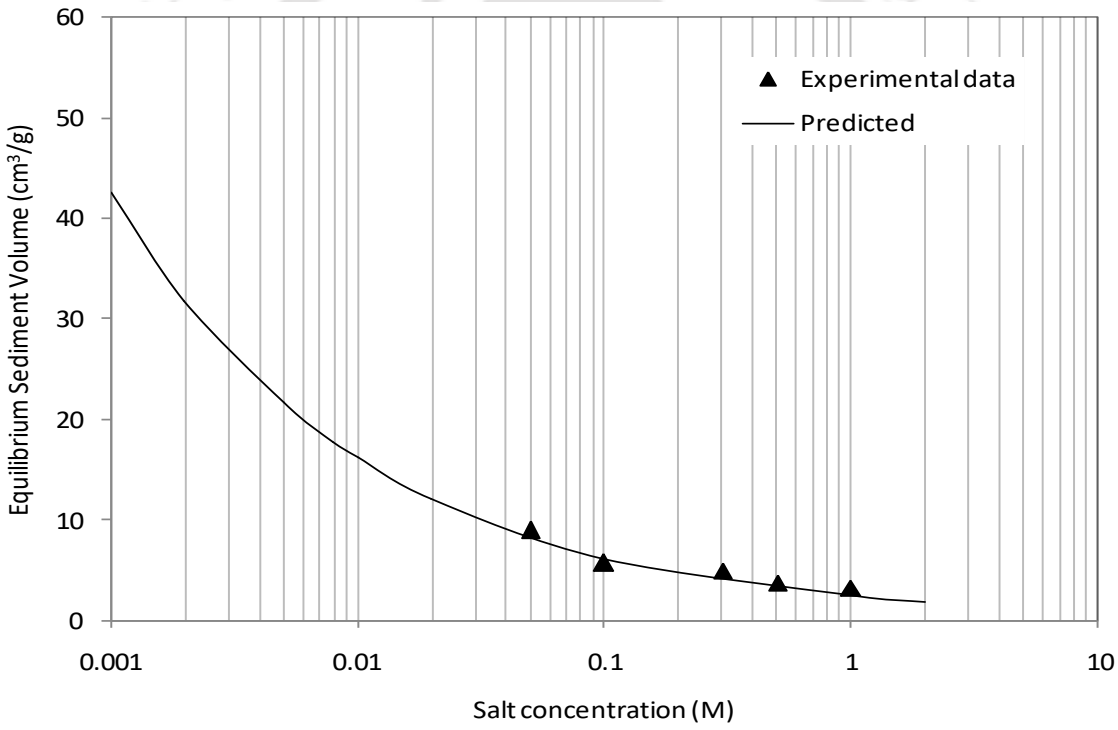

Fig. 5.6a Theoretical and measured data of ESV in the presence of different pore-fluid concentrations for commercial bentonite (experimental data from Sridharan and Prakash, 1999).

The formation of clay aggregates was evident from the high rate of sedimentation observed during the initial equilibrium of the experiments. The aggregate formation changes the clay fabric to edge-

to-face which increases the observed ESV. The predicted data based on parallel-plate assumption was, therefore, smaller than the measured data.

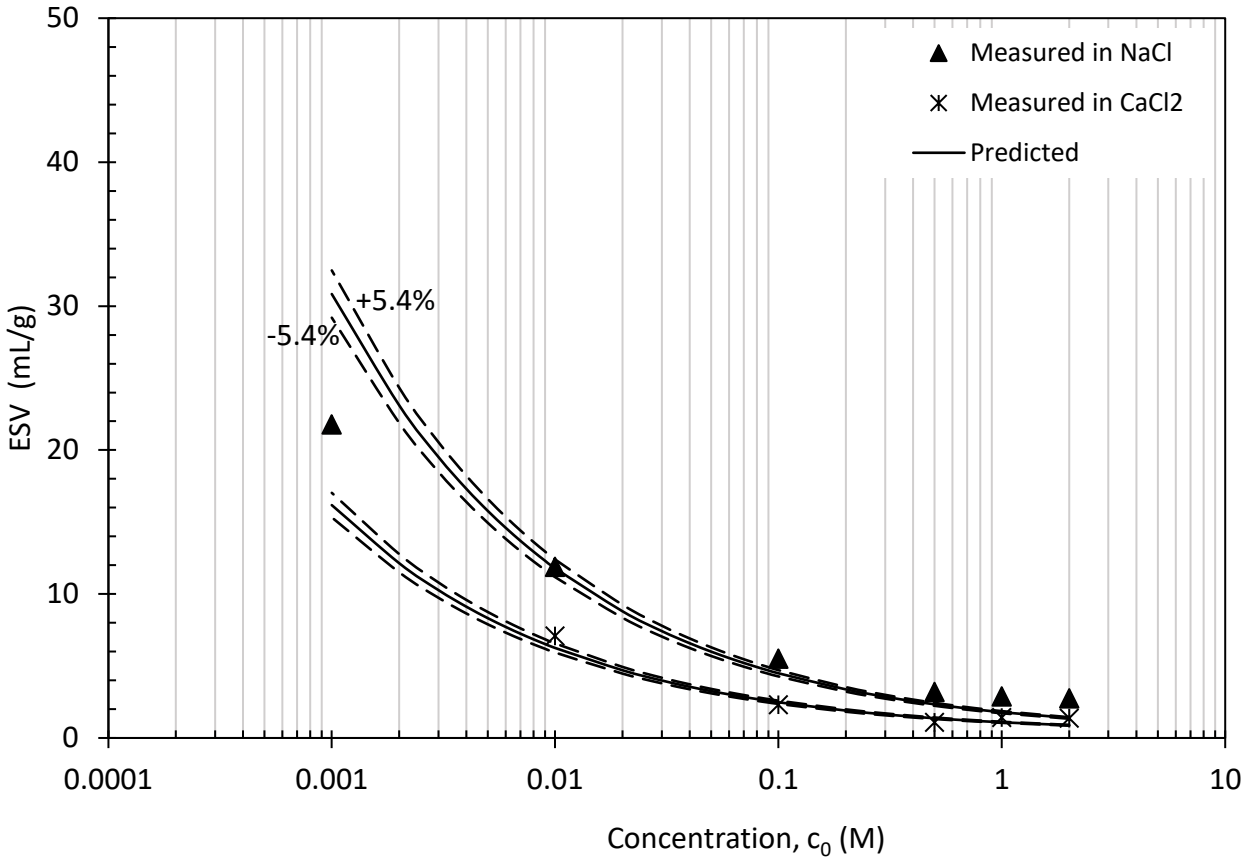

Fig. 5.6b Theoretical and measured data of ESV in the presence of different pore-fluid concentrations for B2 bentonite.

The validation results for the B4 bentonite were similar to the B2 bentonite, but the prediction was very close to the measured ESV even at a very low NaCl concentration (c_0 = 0.001 M). The agreement with the measurements was due to the presence of exchangeable sodium in a very high percentage, i.e., 85%. The deviation between the theory and measurements in the lower NaCl concentration range ($c_0 \leq 0.01$ M), therefore, indicates the significant presence of various exchangeable cations, such as Ca^{2+}, Mg^{2+}, and K^{+}, other than Na^{+}. This finding is significant for the classification of sodium bentonites by carrying out ESV tests in NaCl solutions at low concentrations. However, the predicted data slightly underestimated the measured volumes by showing a small deviation at all the NaCl concentrations $c_0 \geq 0.01$ M. The deviation was

understood to be due to the measurement errors in the S_a. The S_a variation in the measurements was about 10% for B4 bentonite. The influence of this variation on the predicted ESV was also shown in Fig. 10c. The variation in the ESV prediction due to measurement errors in S_a to about 10% was significant up to a concentration of n<0.1 M in NaCl. The S_a of the B4 bentonite could be much higher (> 500 m^2/g) as evident from the predicted ESV data, but the measured value was much smaller as shown in Table 4.3. Several factors are reported to be influencing the S_a measurement by EGME technique such as the age of the desiccant; the amount of soil specimen and EGME used in the tests; size fraction of the soil; exchangeable cations; available mineral groups; and environmental conditions such as temperature, humidity, different variations in the vapor pressures of EGME, and barometric pressure (Tiller and Smith, 1990; Theng, 1999; Cerato and Lutenegger, 2002). The measured S_a may, therefore, be either overestimated or underestimated depending on the above-said factors (Tiller and Smith, 1990). According to Eq. 30, the measured S_a directly influences the predicted ESV. The prediction for the ESV data of B4 in $CaCl_2$ was overestimated for low electrolyte concentrations (c_0 < 0.1 M) due to the presence of mixed cations similar to the B2 bentonite. As the concentration increased, the predicted line crisscrossed the experimental data showing the influence of clay aggregation and the presence of non-clay content. The influence of non-clay content and the presence of mixed cations on the predicted ESV data were explained by validating the proposed model on homoionic sodium clay which contained 98% of clay content. The equivalent size of the coarse content (2%) varied between 2 μm to 9 μm.

The predicted and measured data in the concentration range of 0.01 – 1 M for homoionized bentonite was shown in Fig. 5.8. The prediction was in very good agreement with the measurements even at both low and high electrolyte concentrations. The mixed ion system was absent at the low electrolyte concentration and the volume of non-clay content was insignificant at high electrolyte concentration. Therefore, it showed that these two factors played a major role in the deviation between measurements and prediction at extreme electrolyte concentrations for the studied natural bentonites. Overall, the difference between theoretical and experimental data was not significant in the concentration range between 0.01 M < c_0 < 1 M and the prediction was satisfactory over a wide range of electrolyte concentrations.

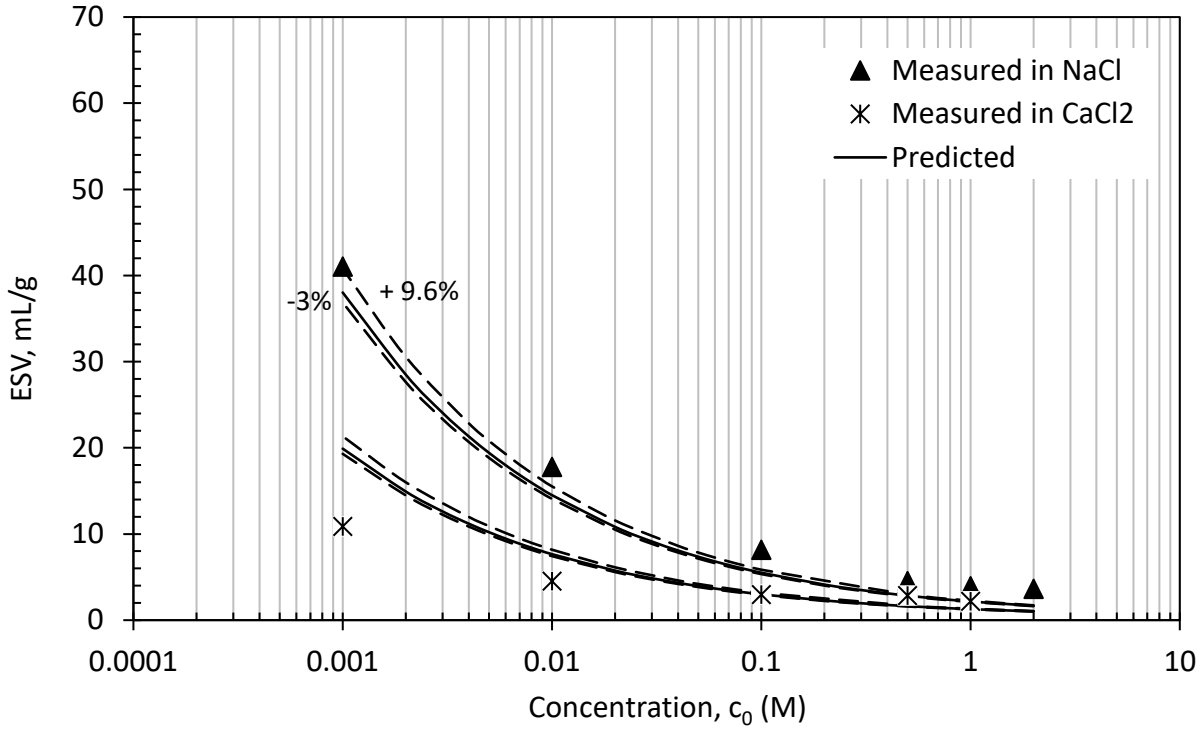

Fig. 5.6c Theoretical and measured data of ESV in the presence of different pore-fluid concentrations for B4 bentonite

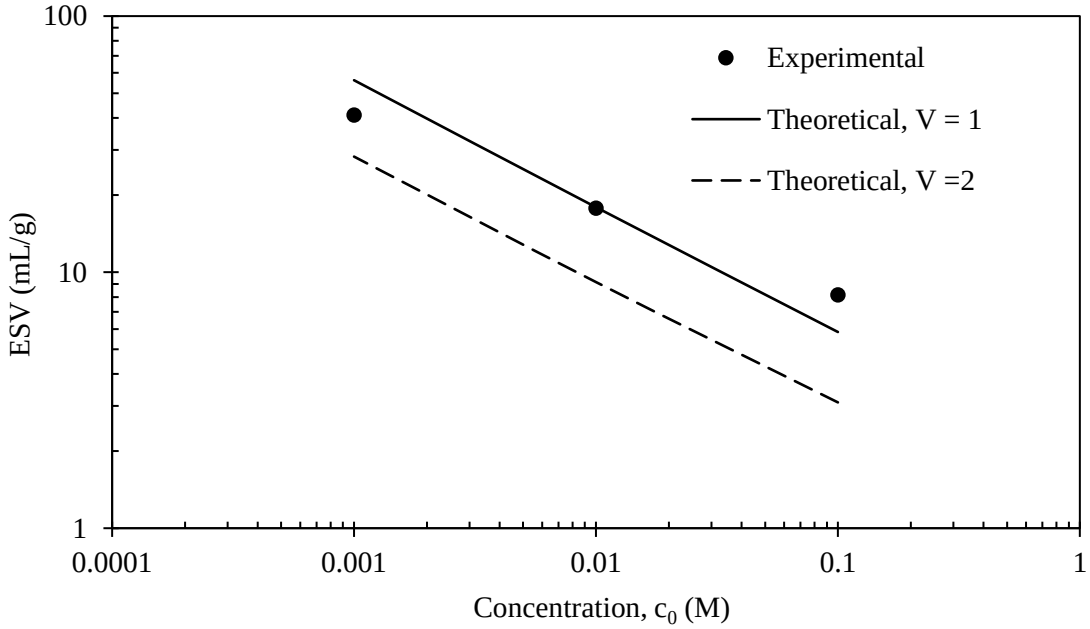

Fig. 5.7 Influence of exchangeable cations on the limiting DDL thickness at dilute electrolyte concentrations

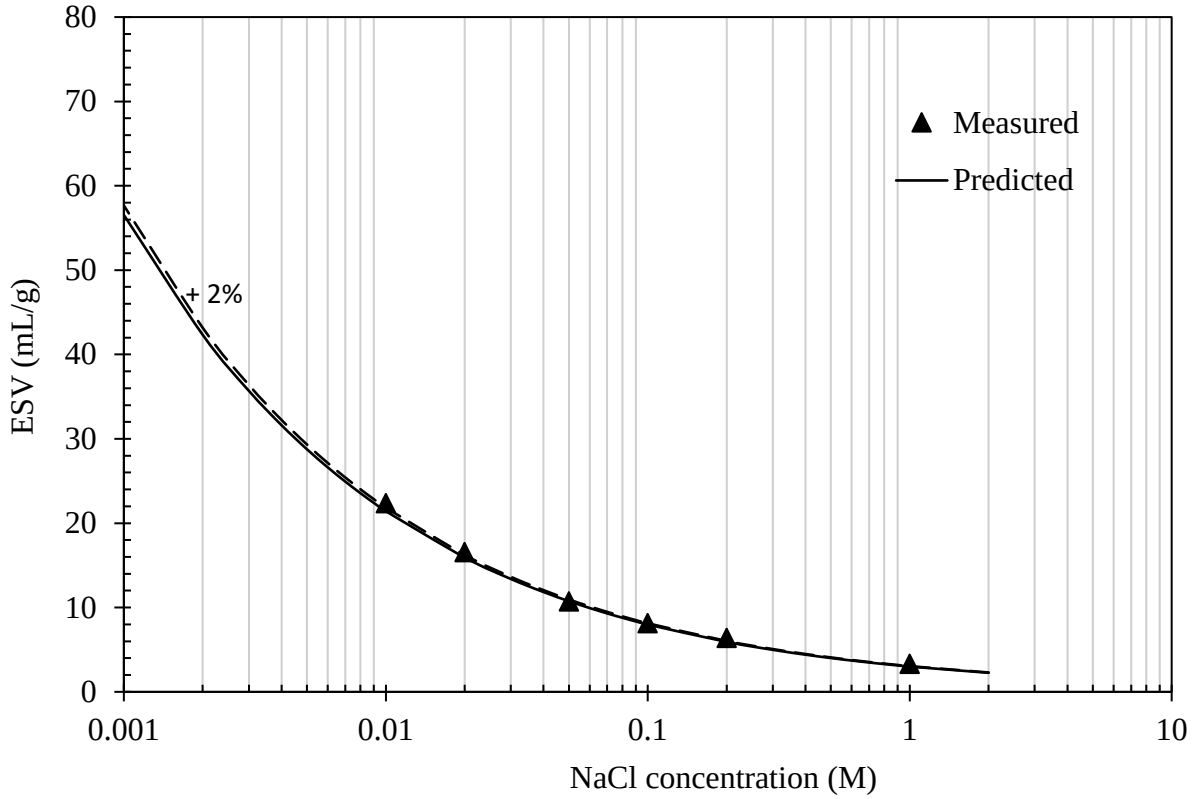

Fig. 5.8 Theoretically predicted and measured data of ESV in the presence of different electrolyte concentrations for homoionized clay.

5.2.5 Summary

A theoretical framework was developed for clay-water electrolyte system at weak particle interaction using the Gouy-Chapamn DDL theory. An analytical expression was derived for estimating the DDL thickness around the fully swollen clay platelets under zero mechanical stress considering the self weight. The ESV of clays was related to the DDL thickness and a model was proposed to study the ESV behaviour of clays under varying physicochemical environment. The body forces due to the self weigth of the clay platelet and the DDL water around it were considered in the model to estimate the equilibrium DDL thickness of the clay particles in the deposited clay sediment volume. A detailed parametric analysis was carried out using the proposed model to understand the influence of various pore-fluid parameters and clay surface properties on the ESV. The specific surface area of clays had a direct relation with ESV. ESV was higher for clays with higher surface area. The toal cation exchange capacity, on the other hand, did not have any

influence on the ESV behaviour. ESV was, however, significantly influenced by the type of cations (valence). ESV was found to be higher when the unit cationic valence used and considerably reduced for the divalent case. Additioonaly, ESV decreased linearly with an increase in the cationic concentration in the pore fluid when plotted on semi-log scale. The ESV data by the proposed model were validated against the measured data of two Indian bentonites, B2 and B4, a homo-ionized bentonite, Na-B2, and a commercial bentonite from literature. Proposed model was in very good agreement with the measured data of the Na-homoionized bentonite in the concentration range of 0.01 – 1 M. Overall, the prediction of ESV was satisfactory in the concentration range of $0.01 < c_0 < 1$ M for all the bentonites. At lower concentration, the proposed model overpredicted the ESV as the influence of the mixed-valence surface cations were not considered in the theory. At higher concentration, predicted ESV data were smaller due to the influence of clay aggregation and the presence of non-clay content. Additionaly, the limitation associated with the existing techniques for surface area estimation adds uncertainity in the correct estimation of the ESV of clays.

5.3 Estimation of the specific surface area of clays

This section presents a new method for routine estimation of the specific surface area of clays based on the sediment volume in the salt environment. The method involves measurement of ESV of clays in 0.1 M NaCl solution and theoretical estimation of the corresponding DDL thickness. Water was utilized as the probe molecule for assessing the surface area of clay soils in a dispersed and fully swollen state of the clay particles. A comparative assessment of the proposed method with commonly used techniques on 12 clay soils is presented and the relative merits of different methods are discussed in detail.

5.3.1 Equations for specific surface area

In the previous section, it was shown that ESV is directly related to the specific surface area (Eq. 30). Rewriting Eq. 30 as

$$S_a = \frac{1}{t_{DDL}}\left(\frac{ESV}{M_S} - \frac{1}{\rho_W G_S}\right) \tag{38}$$

The specific surface area was estimated based on the measured ESV and theoretically estimated DDL thickness, t_{DDL}. The DDL thickness was estimated using the analytical expression presented

in the previous section (Eq. 36) which accounted for the surface and body forces. The equation applies to a clay-water system where the clay particles are in a parallel arrangement. The adopted procedure for ESV measurement ensured a complete dispersion of the clay particles and parallel plate arrangement during the ESV test as illustrated in Fig. 5.9.

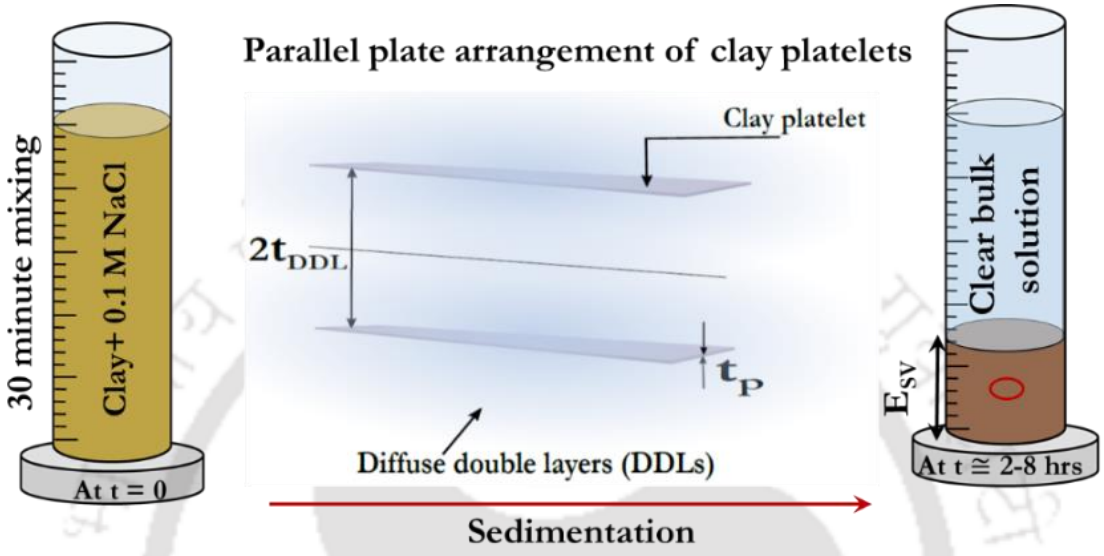

Fig. 5.9 Illustration of parallel plate arrangement of clay particles during ESV test in presence of 0.1 M NaCl solution.

Further, ESV is influenced by other clay surface properties, namely C_e, and G_s; pore-fluid properties such as n, ε, T, and valence, ν; and type of exchangeable cations. In this work, a methodology was proposed for the estimation of S_a based on the developed theoretical framework, and the measured ESV by controlling the influencing parameters. The various influencing parameters that control the surface area prediction were discussed for using the ESV test as the S_a determining methodology.

5.3.2 Parameters controlling the S_a estimation

5.3.2.1 Particle orientation

One of the major assumptions of the theory is that the clay particles are in a parallel or face–face orientation. Such orientation is feasible only when the clay aggregates are dispersed in the presence of a pore-fluid and a sufficiently large water film (DDL) is formed around the individual clay platelet in a swollen state. Water easily penetrates the inter-lamellar spaces of the clay particles

due to smaller molecular size, forms thick water films around the clay platelets, and thus turns into a well-dispersed formation of the clay platelets in a swollen state. In the presence of pore fluids with zero/low ionic concentrations, however, the mixed-valence cations significantly influence the DDL thickness around the clay platelets. Hence the salt solution with sufficient ionic strength was required as pore-fluid to nullify the effect of the mixed-valence surface cations on the measured ESV. The cationic concentration in a clay-distilled water system due to the exchangeable surface ions can be estimated based on the cation exchange capacity of the soil. The maximum C_e for the smectite clays is reported to be in the range of 100-115 meq/100g (Bolt, 1956; Low, 1980, Sridharan et al., 1986). The C_e of one of the studied bentonites (C_e = 109 for B3, see Table 4.6) was also in this range. Considering a maximum of C_e as 110 meq/100g, the maximum possible cationic concentration was estimated to be 0.022 N in a 100 mL of (solid to liquid ratio = 1:50) clay-water solution. The overall clay-electrolyte system acts as homoionized clay when the ionic concentration of the homoionic salt solution is appreciably higher than the concentration of the exchangeable surface cations (van Olphen 1977). Therefore, the ionic concentration of the homoionic salt solution should be ~0.1 N or higher. Further, the DDL thickness around the clay platelets reduces significantly in the presence of the divalent electrolytes such as $CaCl_2$ solution, and the van der Waal's attractive forces become dominant to flocculate the clay particles (van Olphen 1977). The estimation of DDL thickness using Eq. (36), however, is based on the parallel plate assumption and not applicable for a flocculated system. Thus, the ESV measured in the presence of divalent salts was not useful for the estimation of specific surface area. The ESV data in the presence of NaCl solution was, therefore, considered in the sediment volume tests for the estimation of specific surface areas in this study. Thus, the parallel plate assumption is valid under the considered conditions.

5.3.2.2 The sensitivity of S_a estimation

The influence of electrolyte concentration on the theoretical sensitivity of the S_a prediction based on the Eqs. 30 & 36 was studied in Fig. 5.10 by plotting the ratio of $\Delta S_a/\Delta$ESV against the concentration. The ratio, $\Delta S_a/\Delta$ESV, represents the degree of inaccuracy in the surface area estimation due to the least count associated with the sediment volume measurement in the measuring cylinder. The dielectric constant (ε) and ionic valence (ν) were considered to be 80.4 and 1, respectively, in the sensitivity analysis. The non-dimensional surface potential, which

depends on the ionic concentration, varied in the range of 1.34 to 12.49 for the studied concentration range. The ratio increased non-linearly indicating the increase in sensitivity of S_a estimation with the concentration and nearly twofold increase at higher concentrations. A small error in the sediment volume measurement, therefore, results in a significant error in the S_a estimation. As the sediment volume significantly decreases with the electrolyte concentration and increases the measurement error, a minimum possible concentration value of 0.1 N was found to be the optimal concentration to use in the sediment volume tests for the surface area estimation. Also, the parallel plate assumption may not be valid at high concentrations due to the reduction in the DDL thickness and the dominant van der Waals forces.

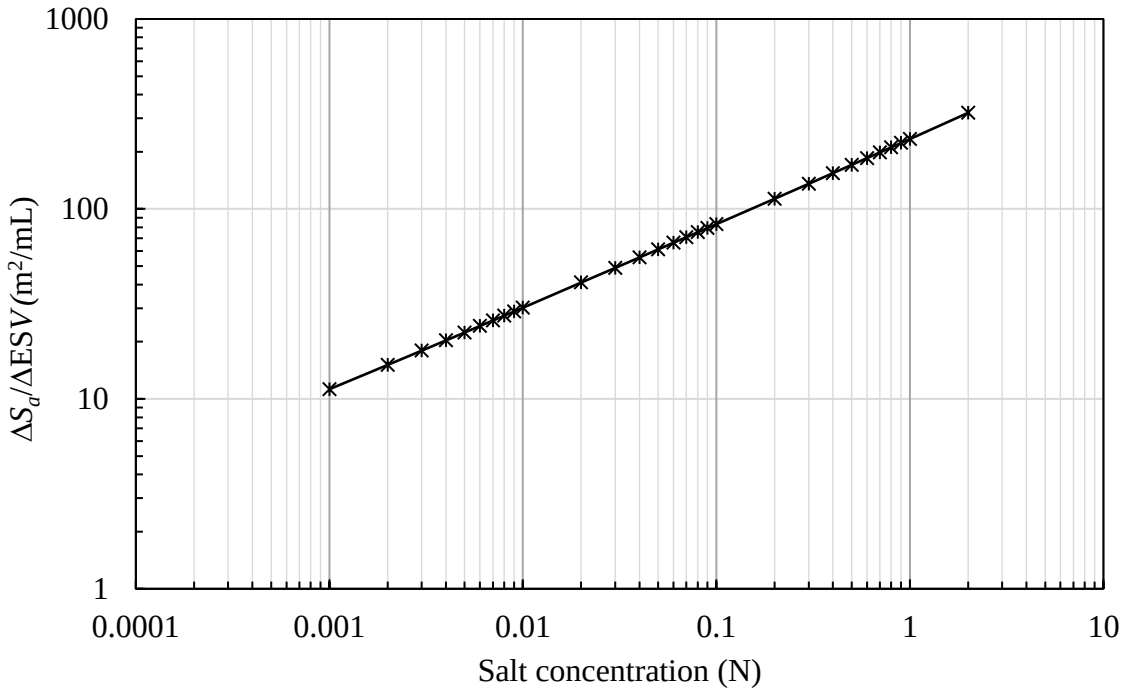

Fig. 5.10 Sensitivity of the S_a prediction using equilibrium sediment volume tests

5.3.2.3 Influence of surface potential

The ESV is directly related to the specific surface area and the DDL thickness of the clay platelets, as presented in Eq 1. The estimation of DDL thickness requires the surface potential (Eq. 3). The surface potential of constant charge platelets, such as clay mineral surfaces, depends on both C_e and S_a, as shown in Eq 4. The influence of clay surface properties on the theoretical DDL thickness in the mechanical stress-free state was, however, found to be insignificant as described in the earlier section. The dependency of DDL thickness on the non-dimensional surface potential was

investigated here, which was shown in Fig. 5.11. As the potential depends on the electrolyte properties, the DDL thickness was analyzed for different electrolyte concentrations in the same figure. The influence of surface potential for a given electrolyte concentration on the thickness was insignificant. The change in the swell volume for such extreme cases was also insignificant, and such extreme electrolyte concentration was not considered for the S_a determination in this study. Therefore, the first term of the theoretical expression for DDL thickness (Eq. 2) was neglected and was simplified to

$$t_f = \frac{1}{\kappa}\ln\left[1\Big/\tanh\left(\frac{1}{4}\cosh^{-1}\left(1+\gamma_w\left(\frac{t_p G_s + 2t_f}{2nRT}\right)\right)\right)\right] \qquad (39)$$

where t_f was estimated by iteratively solving the above implicit equation and then the S_a was estimated using the following expression (after rearranging Eq. 38):

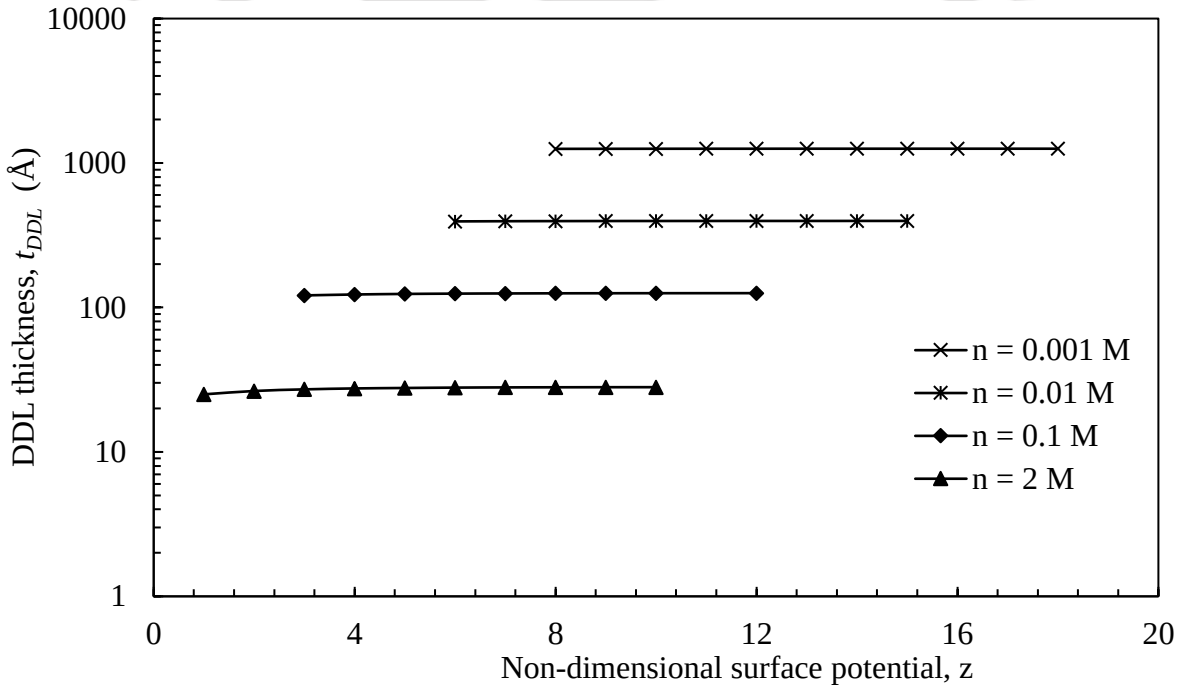

Fig. 5.11 Influence of normalized surface potential on DDL thickness

As both equations (Eq 36 & 39) yielded similar ESV data, the later equation, which is simpler, was used to predict the DDL thickness. As the accuracy of the predicted surface area directly depends on the accuracy of equilibrium volume measurement, the following procedure was evolved.

5.3.3 Comparative assessment of different methods

The predicted surface area of all the studied clay soils by the two standard techniques and the proposed method were presented in Table 5.1. The reported surface area values by all the methods were based on the average value obtained from four duplicate samples for all the soils. A significant deviation was observed between the estimated S_a values by different methods for all the studied samples. The estimated S_a values of the powder bentonites by the MB sorption followed the order of clay content and plasticity of the bentonites (i.e. B1 < B3 < B4). Thus, the estimated S_a values were higher for the bentonite with higher plasticity and higher clay content. The estimated S_a values for the three bentonites showed a significant difference as suggested by their plasticity. The estimated S_a values were ranged between 380 m^2/g and 560 m^2/g for these bentonites whose plasticity index varied between 148 to 546. The EGME estimated S_a values were, however, did not follow the order of the bentonite plasticity and the clay content. The EGME estimated S_a values for B3 was higher than B4, in contrast to the order of plasticity and clay content. The lower plasticity for B3 bentonites as compared to B4 was due to the presence of dominant divalent cations (Table 4.6).

Table 5.1 The estimated specific surface area of the studied clay soils using the two standard methods and the proposed method

SL No.	Soil name	Soil Details	S_a (m^2/g)		
			EGME	MB	Proposed method
1	B1	Kutch-1	403	380	452
2	BM1	B1 + 10% fine sand	244	336	434
3	BM2	B1 + 20% fine sand	208	280	335
4	B3	Barmer-1	498	530	776
5	BM3	B3 + 10% fine sand	429	507	670
6	BM4	B3 + 20% fine sand	324	422	551
7	B4	Barmer-2	456	560	731
8	BM5	B4 + 10% fine sand	307	490	650
9	BM6	B4 + 20% fine sand	270	410	497
10	GB	Granular bentonite	505	620	703
11	KTND	Kuttanad soil	117	80	94
12	JBS	Jabalpur soil	256	245	250

Thus, the plasticity might not represent a correct measure of the S_a values, and the EGME estimated S_a values were qualitatively correct. However, the estimated S_a values by the EGME method were on the lower side for most of the bentonites when compared to the MB and the proposed methods. The S_a values by the MB method exceeded the EGME method by approximately 100 m^2/g for the Na-dominant bentonites, i.e., B4. A smaller S_a value by the EGME method was due to the inability of EGME molecules to access the internal surface area of the clay minerals (Carter et al. 1986; Khorshidi et al. 2016). On the other hand, the MB method predicted smaller S_a values for the B1 and B3 bentonites that have a significant percentage of exchangeable calcium content (Table 4.6) as the adsorption of MB molecules onto the clay particle surface is significantly influenced by the type of exchangeable cations. The MB adsorption is higher in the presence of Na^+ ions and smaller in the presence of divalent cations (Hang and Brindley 1970). Thus the estimated S_a values for the monovalent bentonites, B4, were higher than the divalent bentonite, B3, due to higher MB sorption in the presence Na^+ ions.

The difference between the estimated S_a values by the EGME and MB methods was, therefore, relatively smaller (30 m^2/g) for the divalent-dominant B3 bentonite. For the B1 bentonite, which has the lowest plasticity and lowest percentage of Na^+ ions (~37%) among the three, the EMGE method estimated a slightly higher value than the MB method. Relatively, a poor MB sorption in the presence of the divalent Mg^{2+} and Ca^{2+} ions resulted in smaller S_a values, even compared to the EGME method. A comparison of S_a values of the powder bentonites by the proposed method with both EGME and MB sorption methods were presented in Fig. 5.12a and 5.12b, respectively. The standard deviation and mean in the estimated S_a values by both the methods were shown with the error bars based on the number of trials. Theoretical 10% deviation lines were also shown with dotted lines along with the 1:1 line (i.e., 45^0 line). Comparison of the S_a values by EGME method with the proposed method showed that the data were consistently below the 1:1 line and the deviation increased with the bentonite plasticity, indicating that the EGME technique estimated smaller S_a values due to the limitations mentioned earlier. The proposed method, on the other hand, has greater inter-layer accessibility due to the smaller size of the water molecules and the dispersed state of the swollen clay particles. A maximum deviation of 38% was observed for the highly plastic B4 bentonite. A comparison of the data by the proposed and MB sorption method showed that the proposed method was qualitatively in good agreement with the MB sorption method, but estimated slightly higher S_a values for all the powder bentonites. The difference in the data by the

two methods was higher for higher plasticity clays due to the difference in the ability of the water and MB molecules to access the inter-lamellar surface of the clay minerals.

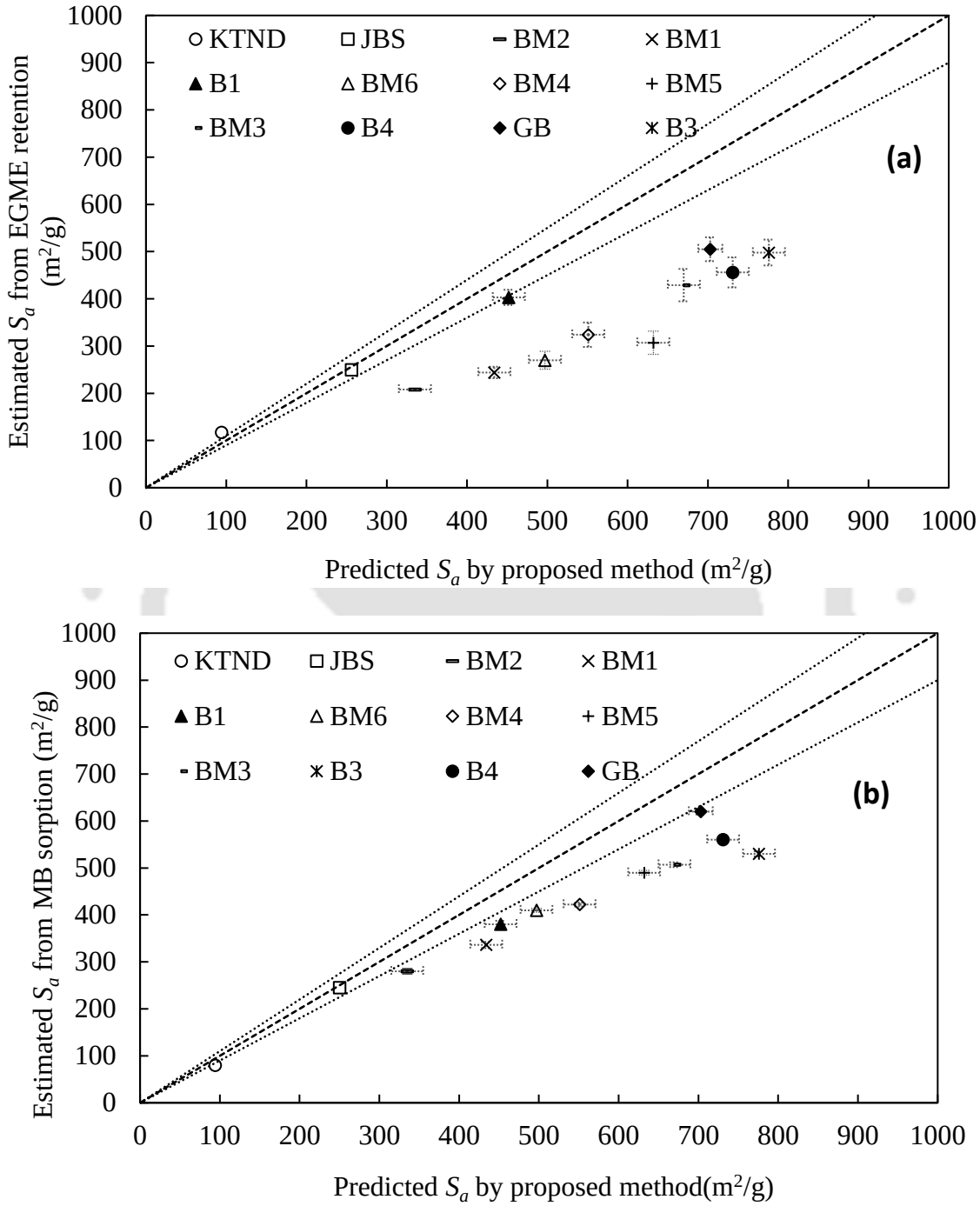

Fig. 5.12 Comparison of the proposed method with (a) EGME retention and (b) MB sorption method

Similar to the sodium-dominant Indian powder bentonites, the MB method also estimated a significantly higher S_a value for the GB when compared to the EGME method. Even though the exchangeable cations information was not available for this bentonite, it is fairly assumed to be Na-dominant bentonite based on its very high plasticity index (~400). Both EGME and MB methods estimated a higher S_a value for this bentonite compared to the three Indian powder bentonites. The estimated S_a value by the proposed method was the highest for the granular bentonite among the studied methods, indicating the efficiency of the method in bringing the clay platelets to parallel orientation in the presence of 0.1 M NaCl solution. The estimated S_a value was, however, smaller than the data for B3 and B4 bentonites, and followed the bentonite plasticity.

The EGME method estimated higher S_a values for the two organic-rich Indian natural clay soils - KTND and JBS - when compared with the MB and the proposed methods. The estimation of higher values by the EGME method might be due to the enhanced EGME sorption in the presence of high organic content as the complex interaction of EGME molecules takes place with the organic matter, such as cation solvation, partitioning, and surface solvation (Pennell et al. 1995). The difference between the two existing methods was higher for the KTND soil, which has a significant organic content of 14% while both the methods estimated a very close value for the JBS, which has a relatively smaller organic content. Despite a slightly higher plasticity value for the KTND soil compared to the JBS soil, the estimated S_a value for the KTND soil is much smaller than the JBS soil by any of the two methods. The higher plasticity was attributed to the very high organic content in the KTND soil. The estimated S_a values by the proposed method were in very close agreement with the MB method for the organic clays.

Based on the added percentage of the fine sand fraction and the measured S_a values of the parent bentonite, the theoretically computed S_a values for the studied bentonite-fine sand mixtures for all three methods were presented along with the measured values in Table 5.2. The S_a value of the bentonite-fine sand mixtures by the three methods showed a similar trend to that of the respective parent bentonites. However, the addition of fine sand fraction significantly reduced the EGME estimated S_a values compared to the MB method for any given bentonite-fine sand mixture when compared to the respective theoretical values (Table 5.2). The EGME method estimated much smaller S_a values when compared to the theoretically expected value for all the bentonite-fine sand mixtures. Overall, the MB method showed a close match with the theoretical S_a values for all the

bentonite-fine sand mixtures. This suggested that the EGME method becomes inconsistent with an increase in the non-homogeneity of the soil particle sizes. The estimated S_a values by the proposed method were also found to be smaller than the theoretically expected values for all the bentonite-fine sand mixtures (Table 5.2). The smaller estimated values can be attributed to the adhesion of the clay particles to the sand particles and the reduced parallel plate orientation among the clay particles in the soil-electrolyte suspension. This adhesion might have hindered the water film formation around the clay particles to its full potential under the salt environment during the sediment volume tests. The observed discrepancy was, therefore, more for the mixtures with higher fine sand fraction and bentonites with higher plasticity (Table 5.2). Overall, the proposed method was in good agreement with MB method for the bentonite-sand mixtures and the predicted S_a values were slightly on the higher side of the MB method which was consistent with the parent bentonites. The proposed method, however, seems to underestimate the S_a value for soils with a significant amount of sand content as the measured sediment volume is reduced due to the aggregation of the clay particles.

Table 5.2 Comparison between the estimated and theoretically expected S_a values of the bentonite-fine sand mixtures

Soil	**S_a value (m^2/g)**					
	EGME adsorption		MB sorption		Proposed method	
	Theoretical	Estimated	Theoretical	Estimated	Theoretical	Estimated
BM1	363	244	342	336	407	434
BM2	322	208	304	280	361	335
BM3	448	429	477	507	698	670
BM4	398	324	424	422	621	551
BM5	410	307	504	490	658	650
BM6	365	270	448	410	585	497

Overall, the three methods showed a qualitatively similar trend in the estimated S_a values for the studied soils, that represented a wide range of plasticity. However, the suitability of each method is subjected to different factors - such as the type of exchangeable cations, clay mineralogy, and

the presence of sand-content and organic content - due to the intrinsic limitations of each method. The EGME method was found to estimate lower S_a values for the highly plastic bentonites as compared to the MB and the proposed method, due to the greater accessibility for probe molecules in the latter methods in a slurry state. The MB method was significantly influenced by the presence of divalent exchangeable cations on the clay surface. Whereas, the EGME and the proposed methods were not influenced by the exchangeable cations, significantly. A very good agreement was observed among the three methods for the soils in the low-medium plasticity range. The EGME method, however, estimated higher S_a values for the organic soils, with a relatively lower plasticity value due to the complex interaction with organic matter. The proposed and EGME methods were sensitive to the added sand fraction and underestimate the S_a value with increasing fine-sand fraction in the bentonite-sand mixtures.

5.3.4 Summary

A new and simple methodology was then proposed for surface area estimation of clays based on the measured ESV and the development theoretical framework. The method utilized water as the probe molecule to assess the total surface of clays in a fully swollen state. Equation for surface area was presented relating the DDL thickness and the ESV. Further, various influencing factors on the surface area estimation were discussed and a suitable methodology was proposed for correct estimation of the surface area from the measured ESV and the theoretical DDL thickness. NaCl solution having a cationic strength of 0.1 N used to minimize the influence of the mixed-valence cations present in the exchange complex of the clay surface. The proposed methology was compared with the two standard methods, EGME and MB sorption, for 12 different clay soils.

The estimated S_a values by the MB sorption method are subjected to uncertainties based on the orientation of the adsorbed MB molecules on the clay surface. Further, MB sorption and orientation of the MB molecules depend on the pH (Hang and Brindley, 1970; Lagaly and Weiss, 1970; Kahr and Madsen, 1995; Pozsgay et al., 2004: Amrhar et al., 2015). On the other hand, the EGME method is very sensitive to the controlled ambient conditions such as vacuum pressure inside the desiccator and the age/strength of desiccant used in the test (Cerato and Lutenegger, 2002), and tests may go on up to 6-7 days depending upon the soil plasticity. The estimated S_a values by the proposed method are more accurate for plastic clays due to parallel plate assumption (Eq. 4). The proposed method may lead to erroneous results for soils dominated by kaolinite and

fine-sand content as the flocculation and aggregation of clay particles become dominant in such soils. The proposed method, however, showed a reasonable agreement with the two existing methods for all the studied soils. The proposed method is simple and provides a quick estimation of surface area with good repeatability. The following procedure was recommended for measuring the ESV of different clay soils for the S_a estimation.

5.3.5 Recommended procedure

1. Take approximately 90 ml of the desired electrolyte solution in a 250 ml capacity conical flask and gently pour 2 g of oven-dried soil into it. Try to avoid sticking soil particles to the flask surface (near the neck of the flask).

2. Place the conical flask containing the soil-electrolyte solution mixture on a mechanical orbital shaker for 30 minutes operating at 190-200 rpm.

3. Carefully transfer the soil-electrolyte solution into a 100 ml measuring cylinder and avoid loss of soil particles during the process. In case of any soil particles left out in the conical flask, 10 ml of the same electrolyte solution can be utilized to rinse off the conical flask and can be added to the cylinder to adjust the total volume to 100 ml. In any case, the final volume in the measuring cylinder should be adjusted to 100 ml by adding the same electrolyte solution.

4. After adjusting the volume to 100ml, manually stir the mixture with the help of a glass rod for 1-2 minutes to maintain homogeneity of the suspension.

5. Allow the mixture to stand and settle under gravity, and monitor the height of the soil suspension in the column until the equilibrium soil deposit is formed at the bottom of the cylinder (Fig. 4.3). The time to reach the equilibrium varies with the soil plasticity and the pore fluid properties. A maximum of 4 hours was sufficient to achieve the equilibrium in the presence of 0.1 M NaCl solution for the studied soils.

6. Note down the final equilibrium height of the soil deposit and report the sediment volume per unit mass of the soil as the ESV.

The iterative procedure for predicting the specific surface area based on the measured ESV and the proposed theoretical equations was presented in Appendix 2.

5.3.6 Limitations of the proposed method and prospective alterations

1. The theoretical estimation of water film thickness is based on the assumption of parallel plate arrangement of clay platelets. Thus, the proposed method may not be suitable for low plastic clays having very high non-clay content and clays dominated by kaolinite minerals as parallel plate assumptions may not hold true for these clays.
2. The least count in the S_a estimation by the proposed method is relatively poor, which is in the range of ~30-40 m^2/g. However, it can be improved by using a measuring cylinder having a smaller diameter to achieve greater accuracy in the ESV measurement. However, one should carefully choose the size of the cylinder such that the cylinder wall causes minimum hindrance to the settling clay platelets in the soil suspension.

6 A semi-empirical model for compressibility behavior of clays

6.1 General

This chapter presents a generalized model to predict the compressibility data of clays and clayey soils of different plasticity. The compressibility data of several bentonites and clayey soils from the literature and the current study were presented and discussed first. The existing models for predicting the compressibility behavior were then presented and their limitations were brought out. Normalized '*e*–*P*' relationships based on the theoretical and measured compressibility data were obtained using the procedure given by Bharat and Sridharan (2015a) and discussed next. The theoretical compressibility data were obtained based on the Gouy-Chapman DDL theory considering the mixed-valence cations. The issues with the existing linearization technique to establish a unique relationship were discussed based on the normalized theoretical and measured compressibility data. The proposed model was then presented next, followed by validation and discussion.

6.2 Compressibility data of clays from literature and present study

Several measured compressibility datasets for over 80 clays and clayey soils were considered from the literature to validate the existing and proposed predictive models. The commonly used bentonites such as Wyoming, German Bentonite, Kunigel, Fourges, sodium montmorillonites, Kaolin clays, homoionized bentonites with different cations, natural clayey soils such as Mattagami, Osaka Bay, Bothkennar, Pappadai, Vienna, Boston blue, Lagumillas, Whangamarino, Bedford, London clay, Baimahu, etc. were considered. The compressibility behavior of some of the clays is studied in the presence of different electrolytes (Mesri & Olson, 1971; Di Maio et al., 2004; Horpibulsuk et al., 2011; Ye et al., 2014) and with different initial water contents (Hong et al., 2010). The specific gravity of soil solids, G_s, moisture content at the liquid limit, w_L, plastic limit, w_P, specific surface area, S_a, and cation exchange capacity, C_e, of the studied soils, as reported in the literature, were presented in Table 6.1. Compressibility data of few highly plastic clays (10 data sets) namely, Na-Wyoming, Wyoming (with salt solutions), Na-Ca MX80, Upton#1, and Yugoslav used in the present study are used earlier to successfully validate the previous model by Bharat & Sridharan (2015a). The compressibility tests for most of these clays are carried out in an oedometer with initial moisture content either equal to or greater than the liquid limit moisture

content of the respective clayey soil. The inundation fluid used in the tests and maximum consolidation pressure, P_{max}, were also presented in the table.

The measured compressibility data of over 80 clays with different inundation fluids from the literature were presented in Fig. 6.1a on a semi-logarithmic scale. The enlarged plot of Fig. 6.1a was shown in Fig. 6.1b for void ratios below 5. The data included highly plastic clays such as sodium bentonites (Marcial et al., 2002), medium to low plastic clays such as poor quality bentonites (i.e., dominated by divalent cations in the exchangeable complex) (Low, 1980; Di Maio et al., 2004), clayey soils consisting of different percentages of clay-size fraction, and non-expansive clays such as kaolinite (Horpibilsuk et al., 2011). The data of clayey soils with different inundation fluids and varying electrolyte concentrations were also included. The initial void ratios for different clayey soils varied between 0.83 (Gens, 1982) to 43 (Low, 1980) and the maximum consolidation pressures considered in the study were in the range of 400 (Sridharan et al., 1986) – 42,000 kPa (Ye et al., 2014). The void ratio data are highly scattered nearly up to 1000 kPa pressure. The available data beyond this pressure is also limited to few soils.

The compressibility data of the studied clayey soils were obtained in oedometers by incremental load application after inundation with distilled water. The data were presented in Figure 6.2a. The water contents of these clayey soils under a seating pressure of 5 kPa varied between 48 – 440% that were proportional to the liquid limit water contents of the respective soils. The void ratios of these clays at any given pressure were directly dependent on the plasticity. The void ratio was higher for the bentonites with higher plasticity at any given pressure. The difference between void ratios of different clays at a given pressure decreased with the consolidation pressure. The measured compressibility data of B3 with three different inundation fluids viz., distilled water, 0.1 M NaCl, and 1 M NaCl solution were presented in Fig. 6.2b. Different e – log P trends exhibited by the bentonite with increasing concentration was due to a decrease in the diffuse double layer thickness around the clay platelets with increased electrolyte concentration and, therefore, the void ratio for a given pressure decreased.

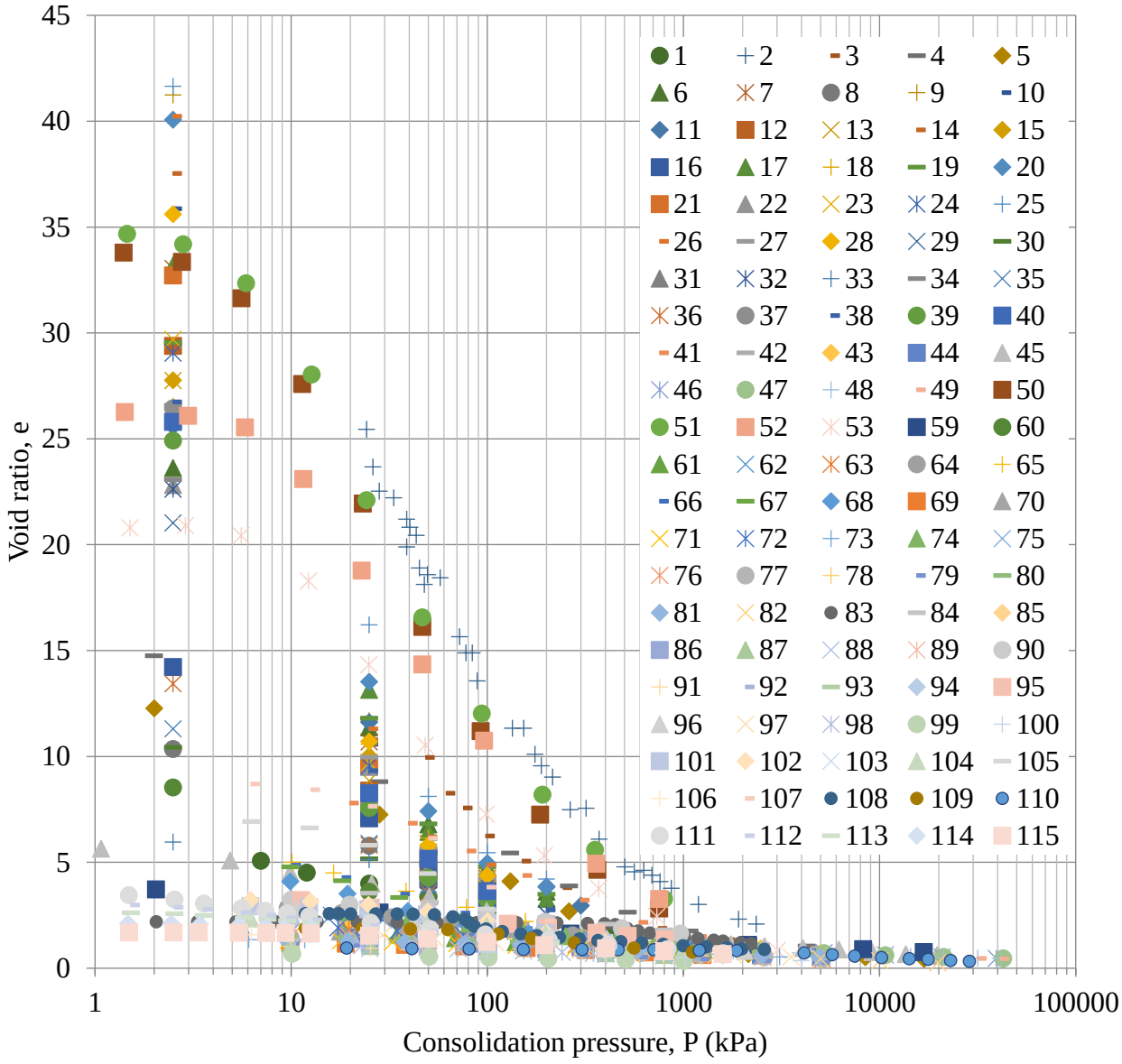

Fig. 6.1a Compressibility data of clay soils reported in Table 6.1

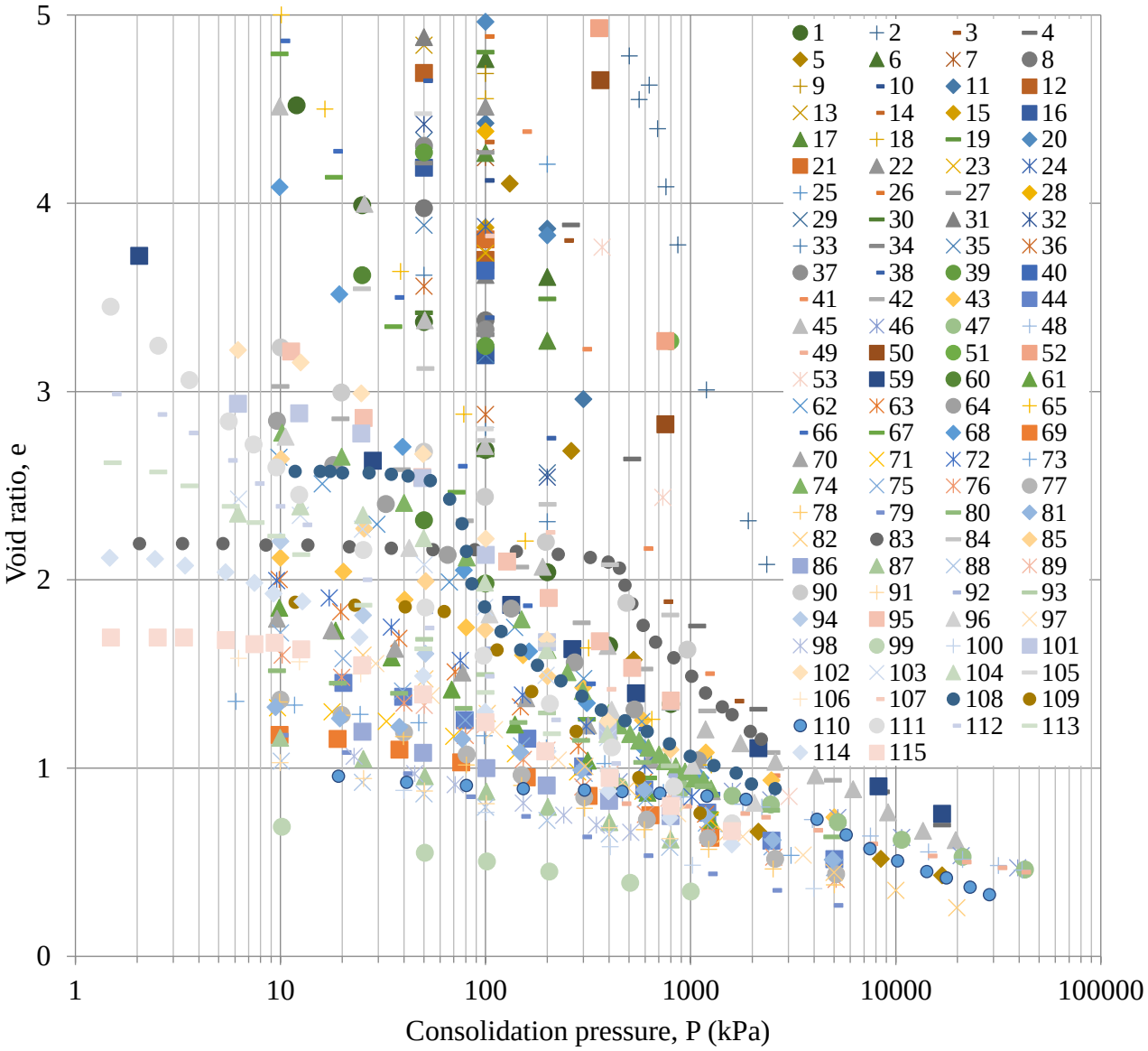

Fig. 6.1b Enlarged representation of the compressibility data of clay soils (Fig. 6.1a) for void ratios below 5.

Table 6.1. Properties of the studied clays from the literature and present study

S.No.	Soil	Inundation fluid	S_a (m^2/g)	C_e (meq/100 g)	Gs	w_{LL} (%)	w_{PL} (%)	P_{max} (kPa)	Intrinsic Parameter, a	Reference
1	German Bentonite	Distilled water	650	74	2.8	178	56	800	0.325	Tripathy & Schanz (2007)
2	Na-Wyoming Bentonite	0.001 M NaCl	800	100	2.65	-	-	2400	0.48	Bolt (1956)
3	Na-Ca-MX80 Bentonite	Distilled water	700	68	2.65	520	62	30000	0.4897	Marcial *et al.* (2002)
4	Na-Kunigel Bentonite	Distilled water	687	73.2	2.79	474	27	30000	0.6051	Marcial *et al.* (2002)
5	Aberdeen Montmorillonite	Distilled water	761	85.5	2.72#	868.2*	-	700	0.3862	Low (1980)
6	Argentine Montmorillonite	Distilled water	729	81.5	2.72#	1215.1*	-	700	0.5376	Low (1980)
7	Arizona Montmorillonite	Distilled water	701	115	2.72#	380.8*	-	700	0.3166	Low (1980)
8	Belle Fourche Montmorillonite	Distilled water	771	85	2.72#	1516.3*	-	700	0.5008	Low (1980)
9	Blue Western Montmorillonite	Distilled water	753	80	2.72#	1318.4*	-	700	0.5957	Low (1980)

10	California Montmorillonite	Distilled water	603	65	2.72#	941.2*	-	700	0.4992	Low (1980)
11	California Red top Montmorillonite	Distilled water	605	62	2.72#	1080.5*	-	700	0.4999	Low (1980)
12	Czechoslovakia #1 Montmorillonite	Distilled water	701	73	2.72#	1020.1*	-	700	0.5274	Low (1980)
13	High Grade Western Montmorillonite	Distilled water	779	85	2.72#	1379.8*	-	700	0.5497	Low (1980)
14	Italian Montmorillonite	Distilled water	696	100.5	2.72#	1020.9*	-	700	0.5221	Low (1980)
15	Louisiana Montmorillonite	Distilled water	654	58	2.72#	522.9*	-	700	0.4595	Low (1980)
16	Mexican Montmorillonite	Distilled water	617	96.5	2.72#	1220.4*	-	700	0.5331	Low (1980)
17	New Mexico Montmorillonite	Distilled water	734	114	2.72#	975.6*	-	700	0.4672	Low (1980)
18	Otay Montmorillonite	Distilled water	634	112	2.72#	1086.6*	-	700	0.4185	Low (1980)
19	Polkville Montmorillonite	Distilled water	729	90	2.72#	1473*	-	700	0.4425	Low (1980)

20	Rio Escondido Montmorillonite	Distilled water	664	91.5	2.72#	1202.8*	-	700	0.5288	Low (1980)
21	Romanian Montmorillonite	Distilled water	753	82	2.72#	838.7*	-	700	0.4354	Low (1980)
22	Sardinian Montmorillonite	Distilled water	713	105	2.72#	1091.7*	-	700	0.502	Low (1980)
23	Smithville Montmorillonite	Distilled water	733	79	2.72#	1067.8*	-	700	0.5135	Low (1980)
24	Upton#1 Montmorillonite	Distilled water	800	90	2.72#	1531*	-	700	0.4896	Low (1980)
25	Upton#2 Montmorillonite	Distilled water	782	84	2.72#	1479.3*	-	700	0.5026	Low (1980)
26	Western Ca Montmorillonite	Distilled water	735	91	2.72#	977.4*	-	700	0.4889	Low (1980)
27	Yellow Western Montmorillonite	Distilled water	777	74.5	2.72#	1309.2*	-	700	0.5372	Low (1980)
28	Alaska Montmorillonite	Distilled water	522	62.5	2.72#	773.1*	-	700	0.3913	Low (1980)
29	Cameron Montmorillonite	Distilled water	351	68	2.72#	383.4*	-	700	0.3764	Low (1980)
30	Chiguagua Montmorillonite	Distilled water	541	76.5	2.72#	952.3*	-	700	0.4298	Low (1980)

31	Czechoslovakia #650 Montmorillonite	Distilled water	438	54.5	2.72#	831.9*	-	700	0.4104	Low (1980)
32	Guam Montmorillonite	Distilled water	483	47	2.72#	219.8*	-	700	0.2891	Low (1980)
33	Indian Montmorillonite	Distilled water	495	70	2.72#	848.2*	-	700	0.4814	Low (1980)
34	Missouri Montmorillonite	Distilled water	431	51	2.72#	415.4*	-	700	0.3282	Low (1980)
35	Monte America Montmorillonite	Distilled water	484	56.5	2.72#	494*	-	700	0.4016	Low (1980)
36	Nevada Montmorillonite	Distilled water	487	73.5	2.72#	972.4*	-	700	0.528	Low (1980)
37	New Zealand Montmorillonite	Distilled water	450	74	2.72#	983.4*	-	700	0.4597	Low (1980)
38	Texas Montmorillonite	Distilled water	568	76.5	2.72#	916.2*	-	700	0.5019	Low (1980)
39	Yugoslav Montmorillonite	Distilled water	559	89.5	2.72#	948.7*	-	700	0.4826	Low (1980)
40	Ponza bentonite	Distilled water	500	-	2.77	390	-	2500	0.4542	Di Maio *et al.* (2004)
41	Ponza bentonite	0.6 N NaCl	500	-	2.77	142	-	5000	0.213	Di Maio *et al.* (2004)

42	Ponza bentonite	1.0 N NaCl	500	-	2.77	104	-	5000	0.1827	Di Maio *et al.* (2004)
43	Ponza bentonite	Saturated NaCl sol.	500	-	2.77	80	-	5000	0.2223	Di Maio *et al.* (2004)
44	Bavaria bentonite	Distilled water	525	74	2.8	178	56	20000	0.2977	Baille et al., 2010
45	GMZ01 Bentonite	Distilled water	570	62.6-82.06	2.66	276	37	42000	0.1989	Ye et al., 2014
46	GMZ01 Bentonite	0.1 N NaCl solution	570	62.6-82.06	2.66	-	-	42000	0.1902	Ye et al., 2014
47	GMZ01 Bentonite	0.5 N NaCl solution	570	62.6-82.06	2.66	-	-	42000	0.1864	Ye et al., 2014
48	GMZ01 Bentonite	1 N NaCl solution	570	62.6-82.06	2.66	-	-	42000	0.1659	Ye et al., 2014
49	Wyoming bentonite	0.001 N NaCl	500	-	2.65	1140	-	800	0.4856	Mesri & Olson (1971)
50	Wyoming bentonite	0.005 N NaCl	500	-	2.65	1160	-	800	0.5305	Mesri & Olson (1971)
51	Wyoming bentonite	0.01 N NaCl	500	-	2.65	960	-	800	0.4466	Mesri & Olson (1971)
52	Wyoming bentonite	0.1 N NaCl	500	-	2.65	880	-	800	0.4779	Mesri & Olson (1971)
53	Indian bentonite - B1	Distilled water	402	38.8	2.76	175	27	800	0.3433	Present Study

54	Indian bentonite - B2	Distilled water	376	55.2	2.76	296	46	800	0.3791	Present Study
55	Indian bentonite - B3	Distilled water	495	71.7	2.77	470	50	800	0.5497	Present Study
56	Indian bentonite - B3	0.1 N NaCl	495	71.7	2.77	278	-	800	0.4204	Present Study
57	Indian bentonite - B3	1 N NaCl	495	71.7	2.77	87	-	800	0.2713	Present Study
58	Ca-Fourges Bentonite	Distilled water	300	54	2.67	112	50	30000	0.23	Marcial *et al.* (2002)
59	Danish Montmorillonite	Distilled water	288	38	2.72#	313.9*	-	700	0.3303	Low (1980)
60	Bangkok clay	0.01 M NaCl	83	24	2.72	71	28	1200	0.2207	Horpibulsuk *et al.* (2011)
61	Bangkok clay	0.1 M NaCl	83	24	2.72	100	28	1200	0.2168	Horpibulsuk *et al.* (2011)
62	Bangkok clay	0.01 M $CaCl_2$	69	20	2.72	77	29	1200	0.2305	Horpibulsuk *et al.* (2011)
63	Bangkok clay	0.1 M $CaCl_2$	78	26	2.72	105	29	1200	0.2591	Horpibulsuk *et al.* (2011)
64	Bentonite	0.0001 M NaCl	156	85	2.72	131	26	1200	0.3005	Horpibulsuk *et al.* (2011)
65	Bentonite	0.001 M NaCl	156	85	2.72	127	26	1200	0.37	Horpibulsuk *et al.* (2011)

66	Bentonite	0.0001 M $CaCl_2$	101	42	2.72	129	26	1200	0.3972	Horpibulsuk *et al.* (2011)
67	Bentonite	0.001 M $CaCl_2$	87	32	2.72	102	24	1200	0.3371	Horpibulsuk *et al.* (2011)
68	Kaolin	0.001 M NaCl	23	8	2.72	54	26	1200	0.1848	Horpibulsuk *et al.* (2011)
69	Kaolin	0.01 M NaCl	23	8	2.72	78	27	1200	0.2003	Horpibulsuk *et al.* (2011)
70	Kaolin	0.001 M $CaCl_2$	21	7	2.72	59	26	1200	0.1654	Horpibulsuk *et al.* (2011)
71	Kaolin	0.01 M $CaCl_2$	28	10	2.72	81	28	1200	0.2997	Horpibulsuk *et al.* (2011)
72	Speswhite Kaolin	Distilled water	48	-	2.62	51.9	28	3200	0.3466	Tripathy *et al.* (2011)
73	Bisaccia clay	Distilled water	190	-	2.78	110	-	1250	0.3133	Di Maio *et al.* (2004)
74	Bisaccia clay	0.6 N NaCl	190	-	2.78	-	-	5000	0.2018	Di Maio *et al.* (2004)
75	Bisaccia clay	1.0 N NaCl	190	-	2.78	-	-	5000	0.2188	Di Maio *et al.* (2004)
76	Bisaccia clay	Saturated NaCl sol.	190	-	2.78	-	-	5000	0.203	Di Maio *et al.* (2004)
77	Marino clay	Distilled water	130	-	2.75	50	-	5000	0.2122	Di Maio *et al.* (2004)

78	Marino clay	1 N NaCl solution	130	-	2.75	-	-	5000	0.249	Di Maio *et al.* (2004)
79	Kaoline	Distilled water	17	-	2.63	50	-	5000	0.2131	Di Maio *et al.* (2004)
80	Kaoline	Saturated NaCl sol.	17	-	2.63	-	-	50000	0.2523	Di Maio *et al.* (2004)
81	La Bouzule clay	Distilled water	219	25	2.7	68	-	20000	0.2684	Djeran-Maigre *et al.* (1998)
82	Osaka Bay clay	Distilled Water	110	16.5	2.67#	108.7	40.2	2200	0.3423	Tanaka & Locat, 1999
83	SAIL soil	Distilled Water	-	-	2.83	158.3	-	800	0.1901	Nagaraj & Murthy (1983)
84	Black Cotton soil	Distilled Water	-	-	2.73	97.3	-	800	0.2078	Nagaraj & Murthy (1983)
85	Silty clay	Distilled Water	-	-	2.75	56.4	-	800	0.1336	Jennings & Burland (1962)
86	Vienna clay	Distilled Water	-	-	2.76	47	-	800	0.1419	Hvorslev (1960)
87	Red soil	Distilled Water	-	-	2.67	45.3	-	800	0.1249	Nagaraj & Murthy (1983)
88	Silty clay	Distilled Water	-	-	2.78	69	-	800	0.1791	Wahls & Godoy (1964)
89	Whangamarino clay	Distilled Water	-	-	2.75	136	-	800	0.1587	Newland & Alley (1957)

90	Boston blue clay	Distilled Water	-	-	2.76	38.8	-	800	0.1086	Taylor (1942)
91	Lagumillas clay	Distilled Water	-	-	2.75	79	-	800	0.2684	Lambe (1964)
92	Soft clay	Distilled Water	-	-	2.75	78	-	800	0.1844	Sowers (1964)
93	Bedford clay	Distilled Water	-	-	2.74	87	-	50	0.1997	Altschaeff (1960)
94	Kleinbelt Ton clay	Distilled Water	-	-	2.77	127.1	36	800	0.2147	Hvorslev (1937)
95	Argile plastique clay	Distilled Water	-	-	2.58	128	31	2000	0.2359	Skempton (1944)
96	London Clay	Distilled Water	-	-	2.71	67.5	26.5	3600	0.2093	Som (1968)
97	Wiener Tegel clay	Distilled Water	-	-	2.76	46.7	22	500	0.1568	Hvorslev (1937)
98	Lower Cromer Till	Distilled Water	-	-	2.65	25	13	1000	0.1441	Gens (1982)
99	Magnus Clay	Distilled Water	-	-	2.73	35	17.2	4000	0.1854	Jardine (1985)
100	Ammonium bentonite	Distilled Water	-	113	2.59	223	55.8	400	0.4004	Sridharan *et al.* (1986)
101	Potassium bentonite	Distilled Water	-	113	2.72	233	57.8	400	0.414	Sridharan *et al.* (1986)

102	Sodium bentonite	Distilled Water	-	113	2.81	495	49.2	400	0.7086	Sridharan *et al.* (1986)
103	Aluminium bentonite	Distilled Water	-	113	2.43	108	60.5	400	0.2445	Sridharan *et al.* (1986)
104	Lithium bentonite	Distilled Water	-	113	2.61	675	49.1	400	0.7141	Sridharan *et al.* (1986)
105	Magnesium bentonite	Distilled Water	-	113	2.65	129	49.9	400	0.3297	Sridharan *et al.* (1986)
106	Calcium bentonite	Distilled Water	-	113	2.65	125	40.6	400	0.3514	Sridharan *et al.* (1986)
107	Mattagami clay	Distilled Water	-	-	2.67#	74-48	25-28	3000	0.2419	Tavenas et al.,1983
108	Bothkennar clay	Distilled water	-	-	2.67#	80	31	1100	0.3396	Smith et al., 1992
109	Pappadai clay	Distilled water	-	-	2.67#	65	30	3000	0.3967	Cotecchia&Chandler, 2000
110	Baimahu Clay	Distilled water (w_0 = 143%)	-	-	2.65	91	38	1600	0.2201	Hong *et al.* (2010)
111	Baimahu Clay	Distilled water (w_0 = 119%)	-	-	2.65	91	38	1600	0.2175	Hong *et al.* (2010)
112	Baimahu Clay	Distilled water (w_0 = 101%)	-	-	2.65	91	38	1600	0.2163	Hong *et al.* (2010)
113	Baimahu Clay	Distilled water (w_0 = 83%)	-	-	2.65	91	38	1600	0.2297	Hong *et al.* (2010)

114	Baimahu Clay	Distilled water (w_0 = 64%)	-	-	2.65	91	38	1600	0.1919	Hong *et al.* (2010)
115	Red soil (RS)	Distilled water (w_0 = 63%)	-	-	2.67	42	20	800	0.1	Present Study
116	Red soil + B1 mixture	Distilled water (w_0 = 176%)	-	-	2.72	117	-	400	0.199	Present Study

*Water content corresponds to 25 kPa pressure; #Assumed

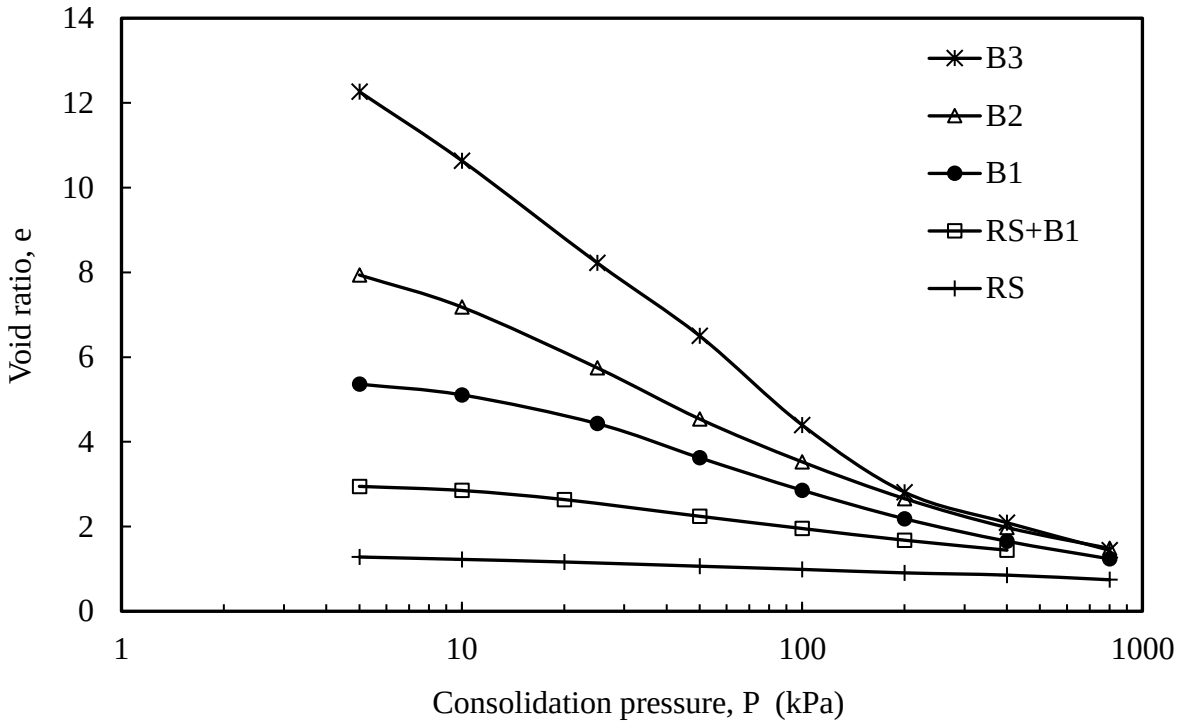

Fig. 6.2a Measured compressibility data of bentonites obtained from the laboratory oedometer tests

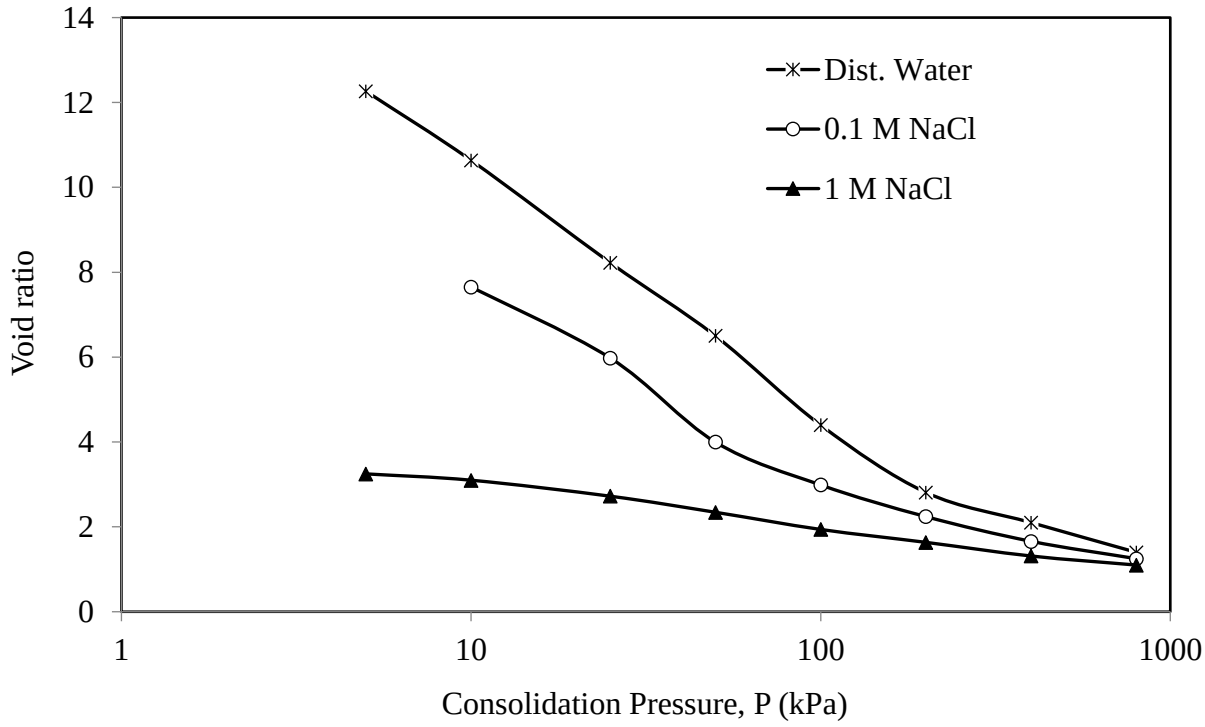

Fig. 6.2b Measured compressibility data of B3 with different inundated fluids

6.3 Existing compressibility models and limitations

The widely used empirical and theoretical models for predicting the compressibility behavior of clayey soils are discussed here. Nagaraj and Murthy (1986) provided a linear relationship for compression index based on the effective stress and the normalized void ratio as shown below

$$C_c = 0.2343 e_L \tag{40}$$

On the other hand, Burland (1990) obtained a unique relationship between a normalizing parameter and vertical effective stress (on a logarithmic scale) which is given by

$$I_v = 2.45 - 1.285x + 0.015x^3 \tag{41}$$

where x is the log P in kPa and I_v is the normalizing parameter termed as the void index, which is defined by $\left(e - e_{100}\right)/\left(e_{100} - e_{1000}\right)$. The void ratio is then obtained by

$$e = I_v C_c + e_{100} \tag{42}$$

where C_c is obtained from the difference between e_{100} and e_{1000}. Two empirical relationships are suggested for obtaining C_c and e_{100} based on the void ratio at the liquid limit value.

The compressibility curves of plastic clays at large consolidation pressures are estimated recently (Bharat & Sridharan, 2015a) by normalizing the theoretical compressibility curves. The compressibility curves are obtained based on the Gouy-Chapman DDL theory as described in the flowchart presented in Fig. 2.13. The void ratio at a predefined consolidation pressure is used to normalize the estimated void ratios at different consolidation pressures. The normalized compressibility curves followed a unique power relationship with an exponent of 0.5 for the pressure which can be mathematically expressed as

$$\frac{e_i}{e_{P_N}} = \left(\frac{P_N}{P_i}\right)^{0.5} \tag{43}$$

The curves are linearized by plotting the normalized void ratio against $1/\sqrt{P}$. All the compressibility curves obtained for different pore-fluid and clay surface parameters are converged to a smooth and unique curve beyond the normalization pressure. However, it was shown in the

present study that the predictive model by Bharat & Sridharan (2015a) underestimated the measured data for many clays and natural clayey soils. The deviation of the DDL theory from the measured compressibility data of clayey soils was analyzed using theoretical analyses and using the measured compressibility data of over 80 clayey soils

The aforementioned empirical and theoretical models for the compressibility behavior of different clayey soils were analyzed on experimental data through Figs. 6.3a – 6.3c. Predicted compressibility curves by different methods for the measured data of Na-Ca-MX80 bentonite were shown in Fig. 6.3a. The model by Nagaraj and Murthy (1986) based on a linear correlation between compression index and liquid limit void ratio (Eq. 40) showed a linear compressibility relationship on a semi-log scale and significantly underpredicted the compressibility data. Similarly, the compressibility curve based on the method proposed by Burland[2] (1990), based on Eqs. 41 –42 and estimation of C_c and e_{100} using the empirical relations with the liquid limit void ratio, significantly deviated from the measured data. Estimation of C_c from the measured e_{100} and e_{1000} (Burland[1], 1990) showed an improvement over the theoretical estimation, but the compressibility curve deviated from the measurements beyond 1000 kPa consolidation pressure. The predicted compressibility curve based on Bharat and Sridharan (2015a) using Eq. 43 and based on the normalizing void ratio of e_{100} showed an excellent match with the measured data. The empirical predictive models by Nagaraj and Murthy (1986) and Burland (1990) are valid for low plastic soils such as w_L < 160%. On the other hand, a good match is found by Bharat and Sridharan (2015a) model as this theoretical model is valid for very high-quality clays such as Na-Ca MX80 bentonites (w_L = 520%). Prediction of compressibility curves by different models for Ca-Fourges bentonite was shown in Fig. 6.3b along with the measured data. The prediction by empirical models was slightly improved on this bentonite, but the theoretical model (Bharat and Sridharan, 2015a) significantly deviated from the measured data due to the low-quality nature of the bentonite (w_L = 112%) carrying a significant presence of Calcium ions in the exchangeable state. Figure 6.3c validates the applicability of different models for predicting the compressibility behavior on B1 bentonite. All the available models studied in this work provide a poor match with the measured data. The estimation of C_c from the measured e_{100} and e_{1000} was not possible for this clayey soil as the measured data were obtained up to a consolidation pressure of 800 kPa only. As the C_c varies with the consolidation pressure for most of the clayey soils, the empirical models predicted a poor match with the experimental observations. While Bharat and Sridharan (2015a) consider the non-

linear nature of the '*e* – log *P'* relationship in their model, theoretical prediction deviated due to the low-quality nature of the clayey soil (w_L = 166%). Thus the empirical models are useful for predicting the compressibility behavior of very low-quality clayey soils and the theoretical model based on the normalization approach is valid for very high-quality bentonite clays.

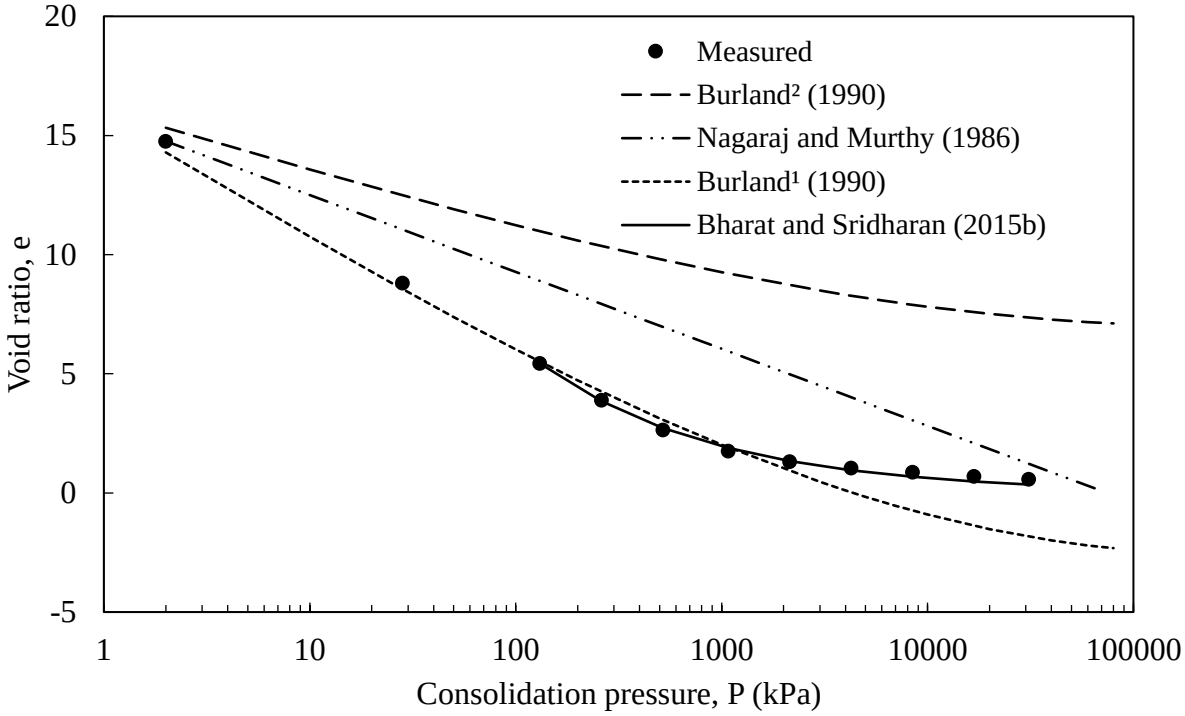

Fig. 6.3a Measured compressibility data of Na-Ca-MX80 bentonite along the predicted data using the theoretical model by Nagaraj and Murthy (1986); Burland (1990) and Bharat and Sridharan (2015a)

Prediction based on the normalization approach using different normalization void ratios for the clayey soils of varying plasticity was analyzed through Figs. 6.4a – 6.4e. The measured data and predictions for B1 were shown in Fig. 6.4a. The predicted curve was obtained based on different normalization void ratios beyond the preconsolidation pressure, P_p (which was less than 25 kPa for all the bentonites), and using Eq. 43. The predictions based on void ratios at consolidation pressures viz. 25, 50, 100, or 200 kPa did not match the measured data and a significant deviation was noticed between the measurements and predictions. The measured compressibility data and predictions for B2 was shown in Fig. 6.4b. The prediction was underestimated for B2 similar to B1, but the deviation between predicted and measured void ratios was smaller. On the other hand, the deviation between the measured compressibility data and predictions was insignificant and the prediction was in good agreement with the measurements for B3 as shown in Fig. 6.4c. The present

validation experiment on the measured data using the existing predictive model (Eq. 43) qualitatively showed that the prediction improved with the plasticity of the clay. This observation was qualitatively in agreement with the earlier claim by Bharat & Sridharan (2015a) that the model is applicable only for very high plasticity clays, studied in their work. However, the definition of high plasticity clays is not clear which was addressed here. The prediction for B3 with different inundation fluids was shown in Figs. 6.4d – 6.4e. The prediction was in very good agreement with the measured data for B3 with an inundation fluid of 0.01 M NaCl. However, the prediction deviated from the measurements with 1 M NaCl solution as shown in Fig. 6.4e. The plasticity of the bentonites decreased with the increase in the electrolyte concentration and the model deviated from the measurements. As shown elsewhere (Bharat and Sridharan, 2015a), the normalized theoretical relationship between e/e_{100} and $1/\sqrt{P}$ deviated from the unique linear relationship for higher electrolyte concentrations and the theoretical prediction is not valid. Thus the theoretical compressibility model is not valid for the low –medium quality clayey soils and high-quality clays in the presence of higher electrolyte concentrations.

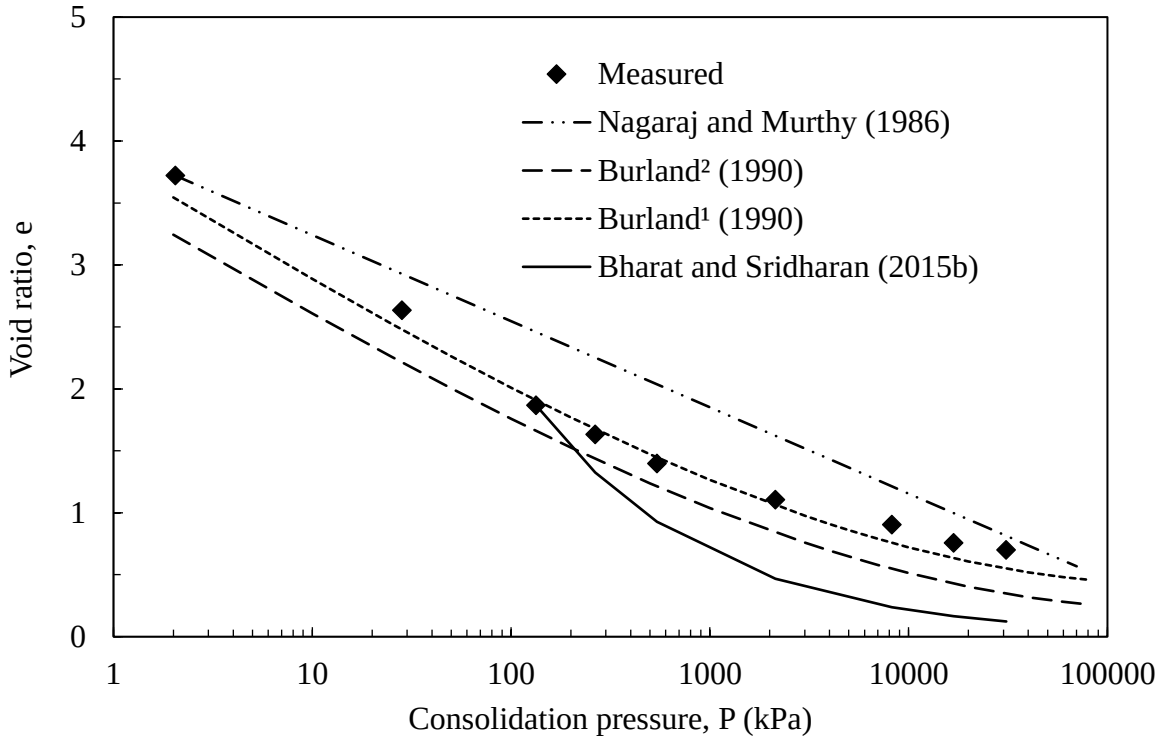

Fig. 6.3b Measured compressibility data of Ca-Fourges bentonite along the predicted data using the theoretical model by existing models

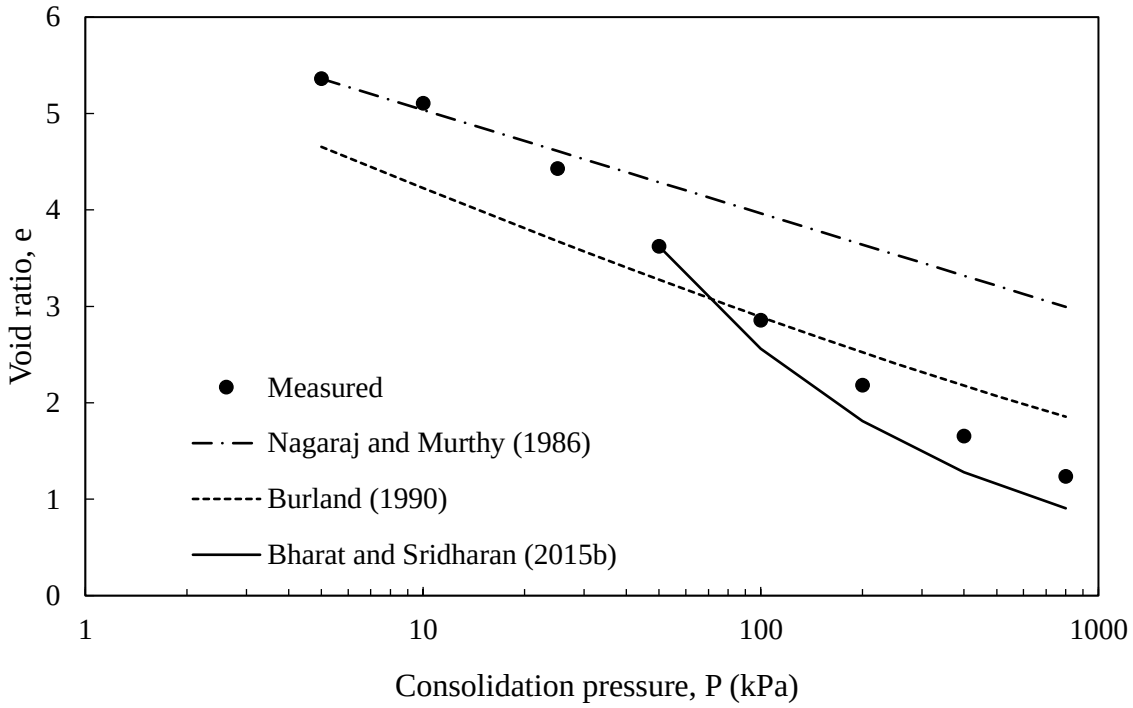

Fig. 6.3c Measured compressibility data of B1 bentonite along the predicted data using the theoretical model by existing models

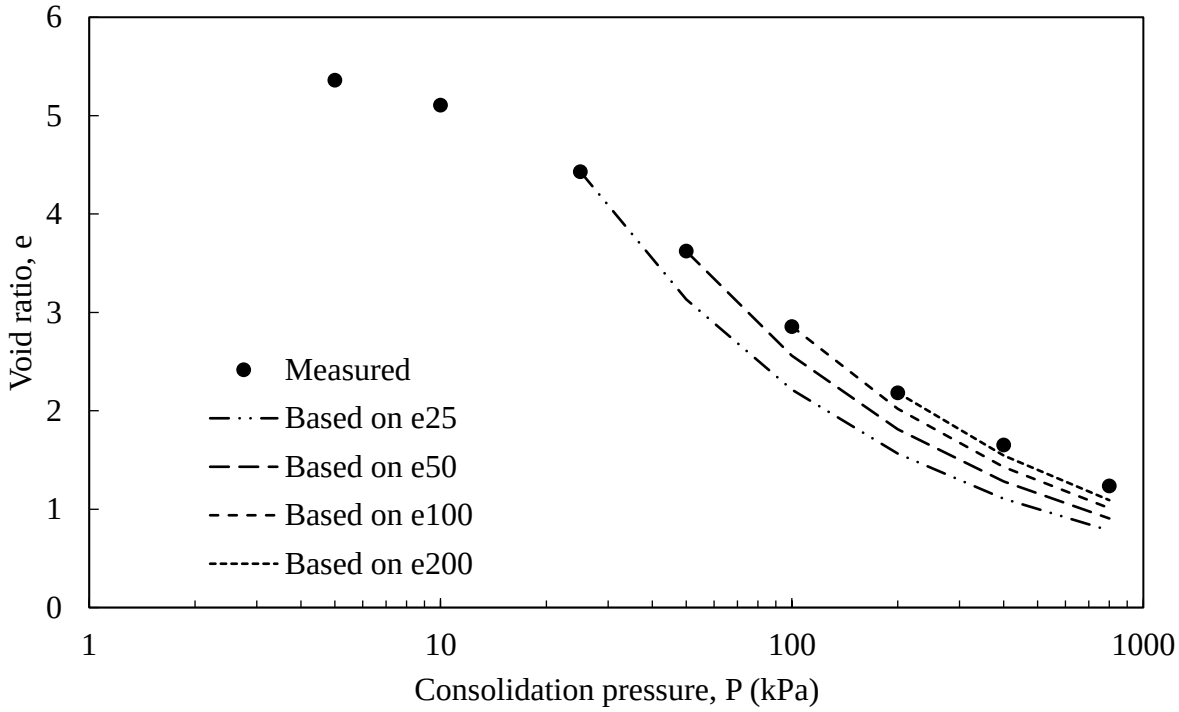

Fig. 6.4a Measured compressibility data of B1 with the predicted data using the theoretical model by Bharat and Sridharan (2015a)

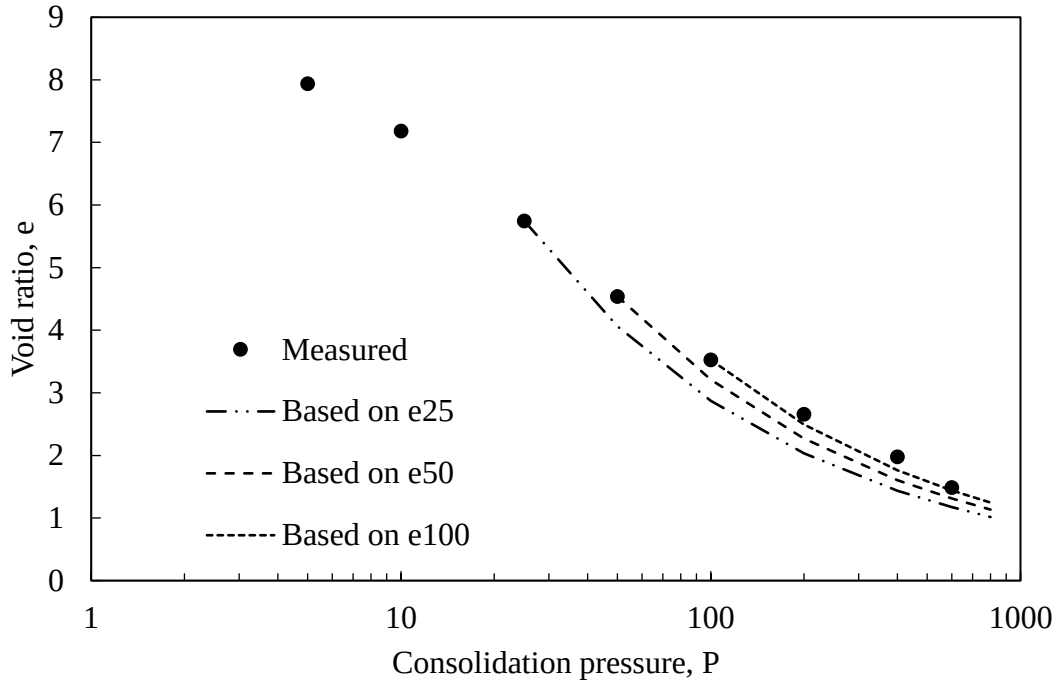

Fig. 6.4b Measured compressibility data of B2 with the predicted data using the theoretical model by Bharat and Sridharan (2015a)

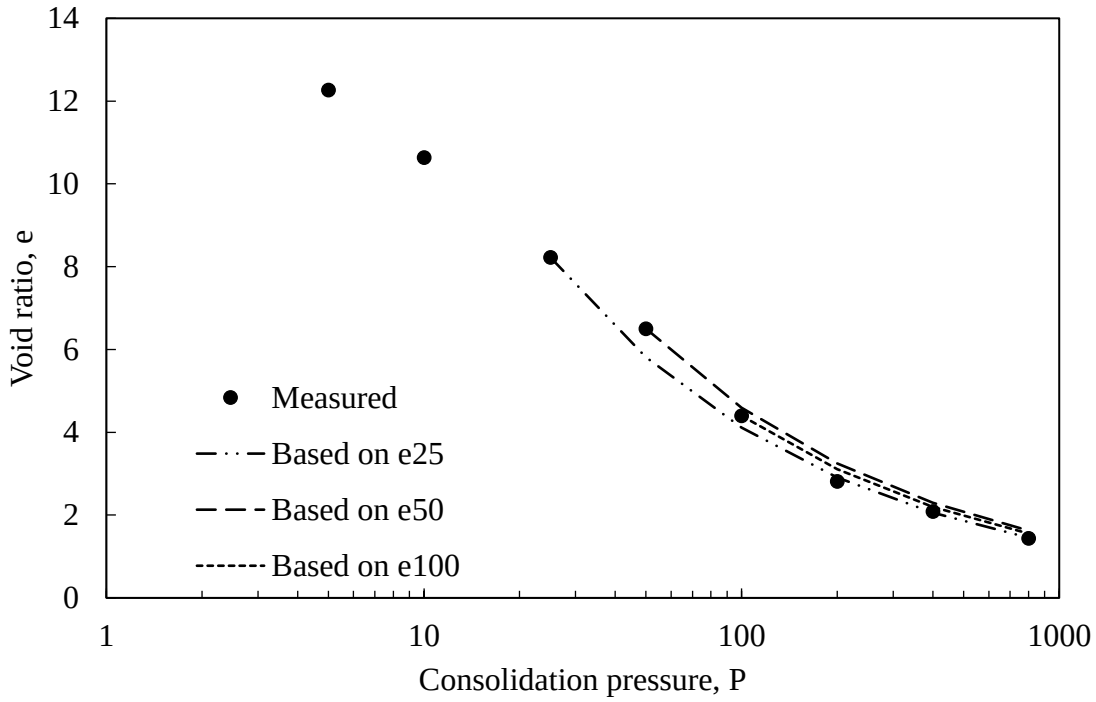

Fig. 6.4c Measured compressibility data of B3 with the predicted data using the theoretical model by Bharat and Sridharan (2015a)

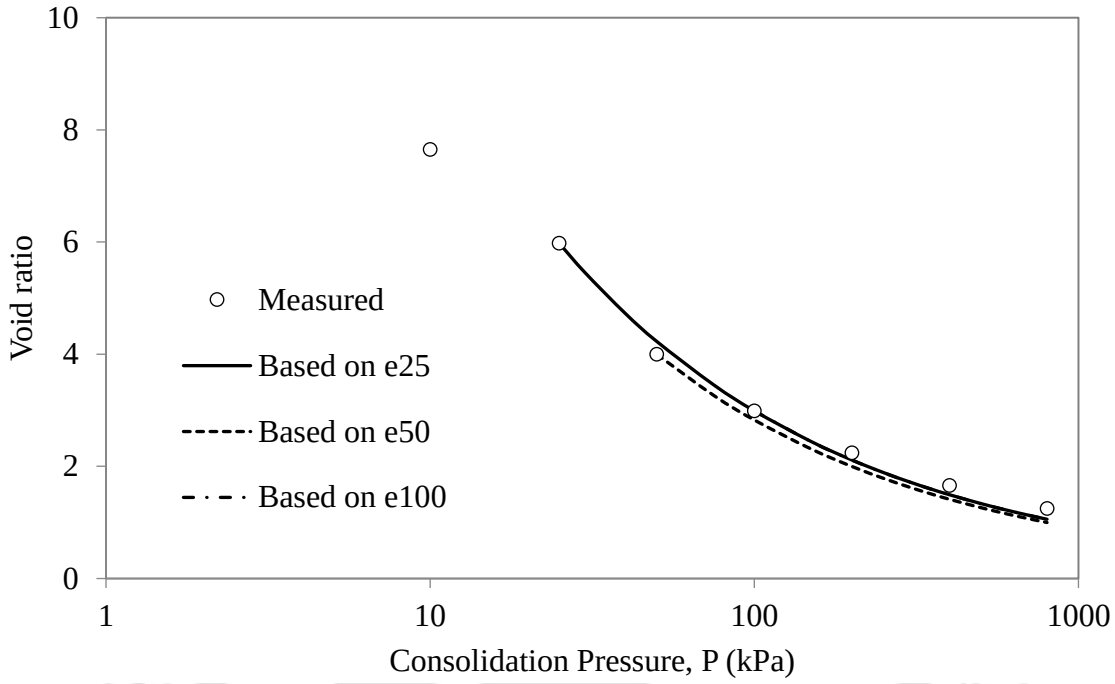

Fig. 6.4d Measured compressibility data of B3 when 0.1 M NaCl was used as a pore-fluid with the predicted data using the theoretical model by Bharat and Sridharan (2015a)

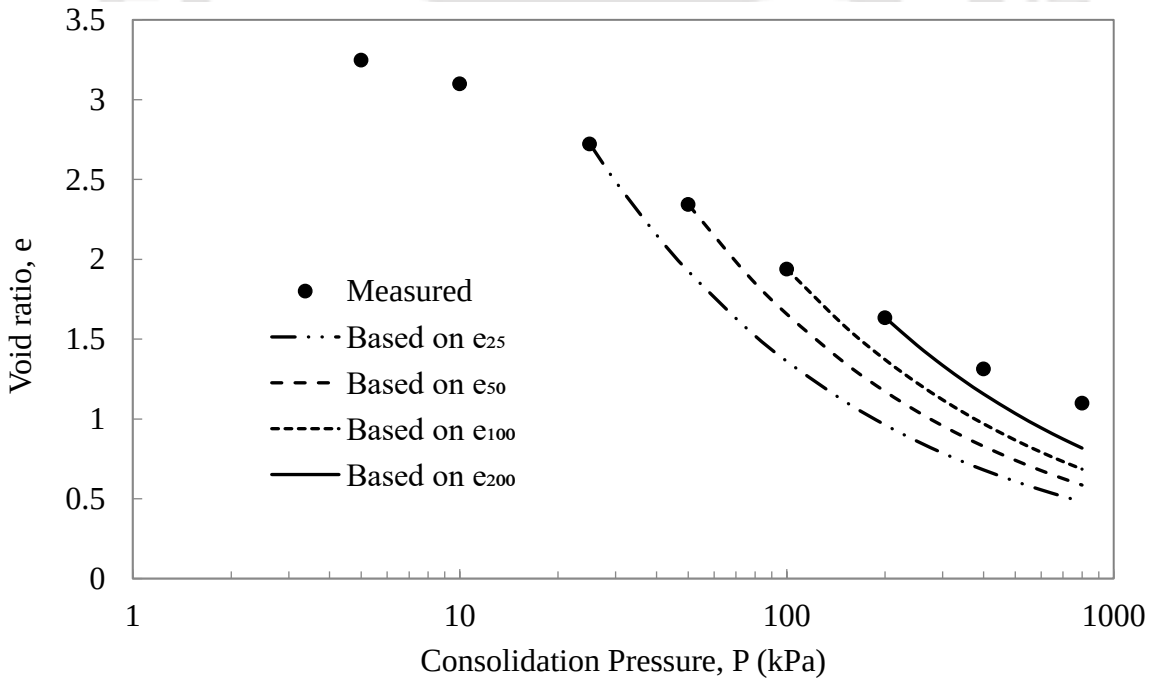

Fig. 6.4e Measured compressibility data of B3 when 1 M NaCl was used as a pore-fluid with the predicted data using the theoretical model by Bharat and Sridharan (2015a)

6.4 Normalization of compressibility curves

The limitations of the earlier approach were analyzed for the presence of mixed cations in the exchange complex here. The influence of different proportions of sodium-calcium cations on the theoretical e – log P relationship was shown in Fig 5a. The theoretical relationship was established by obtaining u using Eq. (23) for a given consolidation pressure; solving Eq. (4) for y_0 and y_0^*; obtaining mid-plane distance, t_{DDL} or $d/2$, using Eq. (3); and estimating the void ratio using Eq. (28). Theoretical data for the mixed ion system showed that the presence of divalent cations, even in small percentages, decreased the void ratios significantly for a given pressure. The compressibility curves with different r values shifted towards theoretical curves for divalent cation alone. This observation was in accordance with the earlier report by Bharat (2004). The compressibility predictions for different r values were qualitatively similar to the mid-plane potential – half-space distance relationship (not shown here). The normalized representation of the theoretical curves in Fig 6.5b for clays with monovalent and divalent cations followed a linear relationship, but the predictions for clays with mixed-valence cations deviated significantly from the ideal linear relationship. The predictions for clays with only monovalent cations and mixed-valence cations intersected at 100 kPa (i.e., $1/\sqrt{P} = 0.1$) as the normalized void ratio with respect to e_{100} for all the predictions was unity. Similarly, the influence of anions on the compressibility predictions showed (not shown here) that the curves diverged over the entire pressure range except at 100 kPa ($1/\sqrt{P} = 0.1$) as the normalized void ratio with respect to e_{100} for all the predictions were a unity. The compressibility predictions in the presence of mixed-valence cations and anions thus were not linearized and did not follow the unique behavior observed using DDL theory for the homovalent cations. The measured data in Fig. 6.1a were normalized using both e_{50} and e_{100} and normalization data with e_{100} alone was presented in Fig. 6.6. The data scattered in the entire range of pressures showed a poor regression coefficient. The R^2 was 0.652 (not shown) and 0.816 when normalized using e_{50} and e_{100}, respectively. The exponent of pressure in the linearized form of the compressibility data was about 0.35 (see the fitted line in Fig. 6.6) which was different from the earlier observed value, 0.5, (Eq. 43) for highly plastic clays. The compressibility data in linearized form (i.e., e/e_{P_N} versus $1/\sqrt{P}$) in Fig. 6.7 does not follow linear relationships as opposed to the earlier observation on highly plastic clays (Bharat & Sridharan, 2015a). The normalized void ratios for different clays are plotted above the trend line. The deviation of the normalized data from the

typical behavior observed by DDL theory and the compressibility data of natural clays was due to the presence of mixed-valence cations in the exchange complex, the effect of anions, or due to the presence of high electrolyte concentrations in the pore fluid as demonstrated theoretically using DDL theory as shown from the theoretical observation (Fig. 6.5a – 6.5b). Therefore, Eq. (43) deviated from the observed compressibility behavior for such cases. Further, the presence of different percentages of non-clay content (Present study), non-Smectite mineral content (Carlson, 2004; Karnland, 2010; Gapak et al., 2017; Bharat & Das, 2017), and the presence of cations with different sizes such as Li^+, K^+, NH_4^+, Mg^{2+}, etc. (Sridharan et al., 1986; Komine, 2004; Tripathy et al., 2014; Gapak et al., 2017) may significantly alter the ideal compressibility behavior observed by the DDL theory for homovalent cations (van Olphen, 1977). Further, the theoretical estimation was based on the initial concentration of the salt solution which may differ from the bulk solution concentration after mixing with the clay soil and may and differ due to the application of the loading. Therefore, the normalized and linearized representation of the measured data from the literature showed that the exponent was different from 0.5 in Eq. 43.

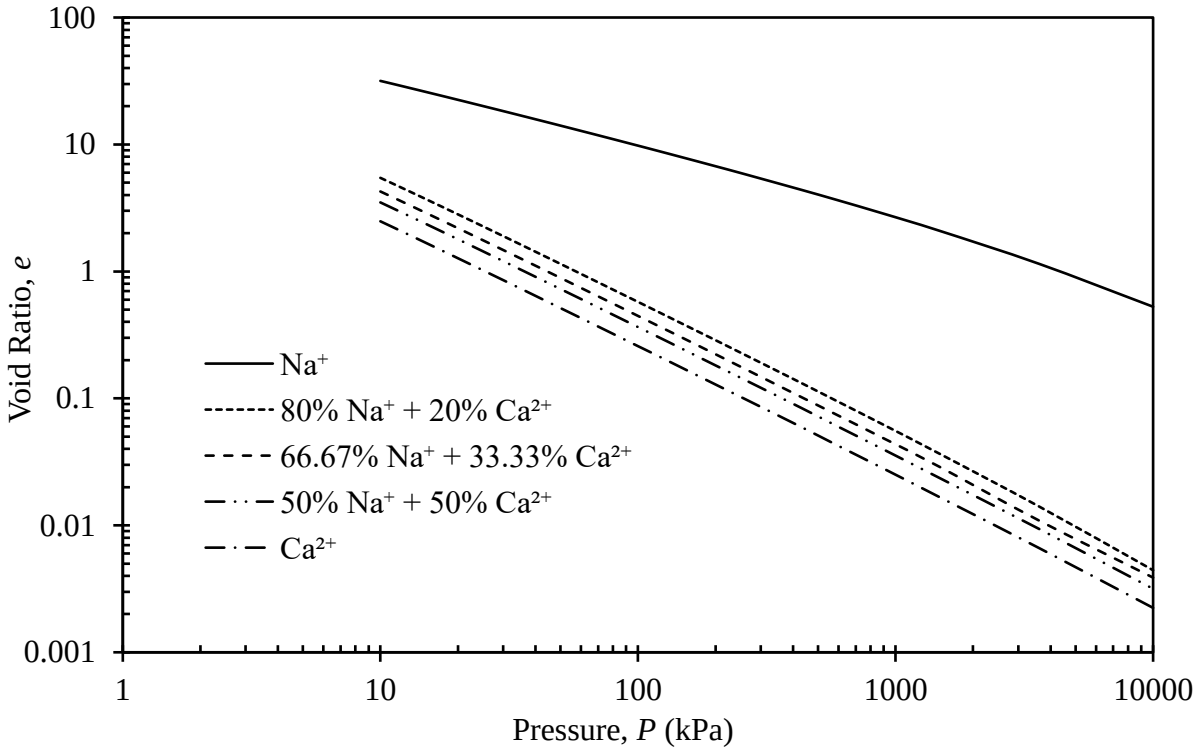

Fig. 6.5a Theoretical compressibility curves (Eqs. 3,4,23, and 28) in the presence of mixed ions for $c_0 = 10^{-4}$ M, $S_a = 800$ m^2/g, $C_e = 100$ meq/100g, $\varepsilon = 80.4$.

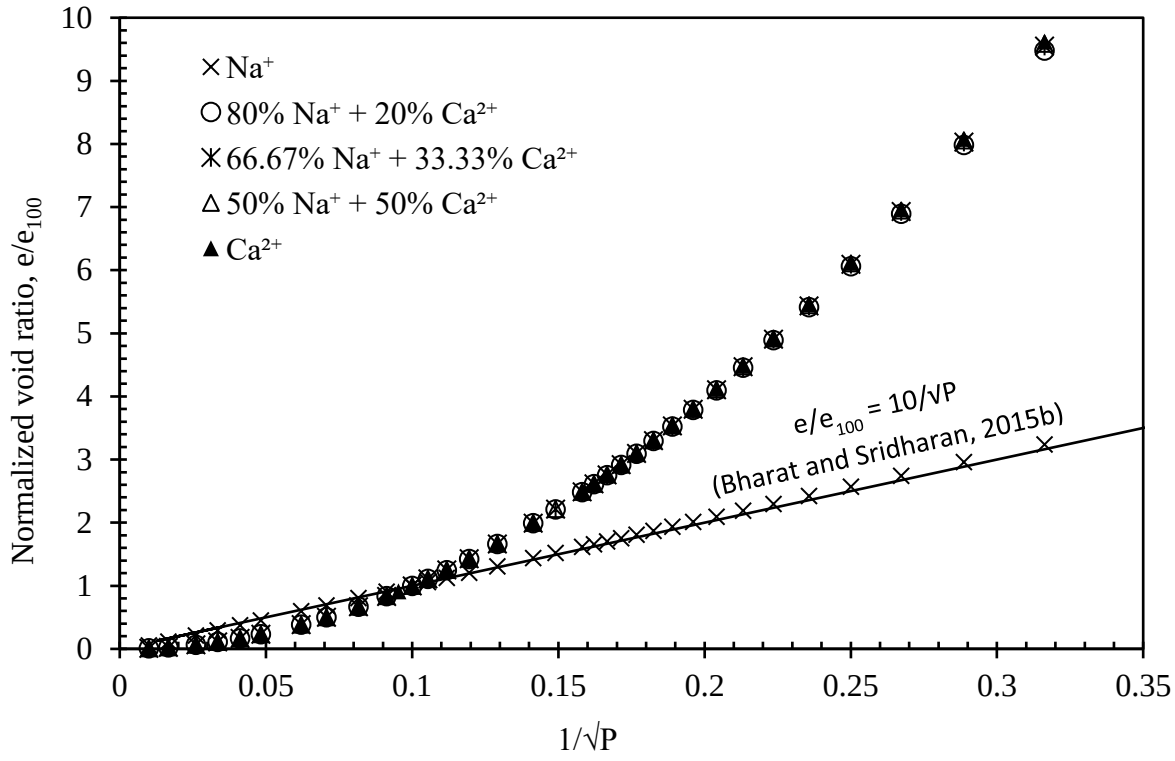

Fig. 6.5b Theoretical compressibility curves as a normalized void ratio against consolidation pressure for mixed ion system for the data presented in Fig. 6.5a.

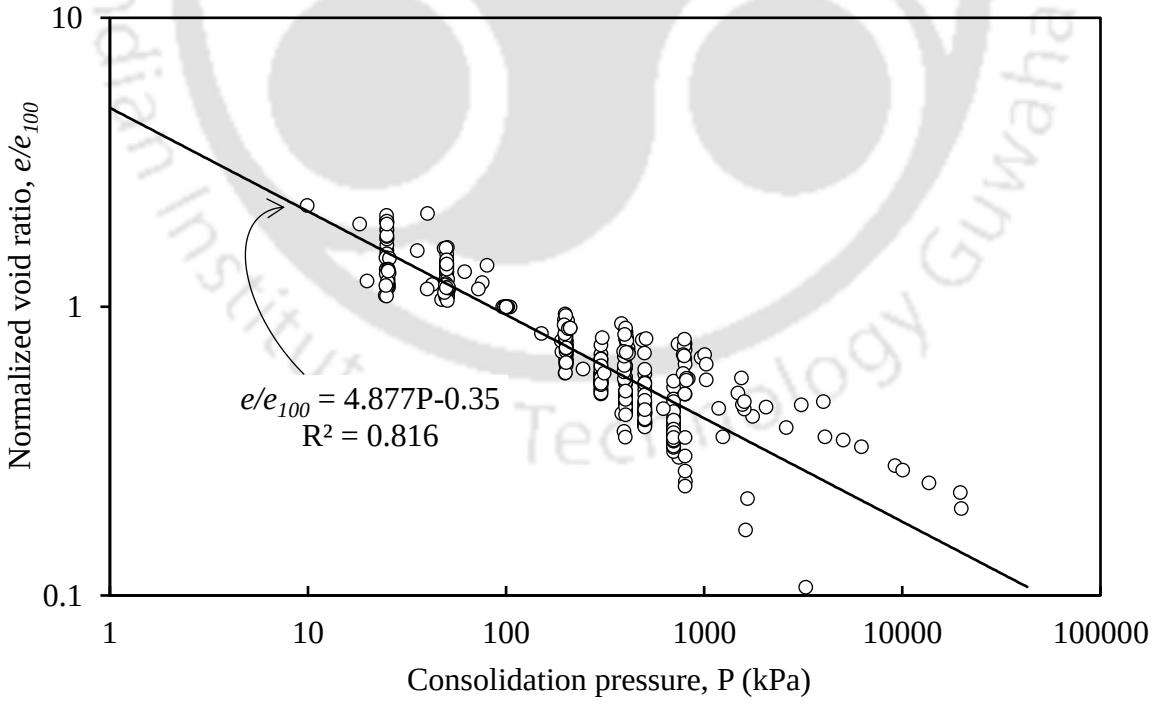

Fig. 6.6 Normalized measured compressibility data (Fig. 6.1a) using e_{100}

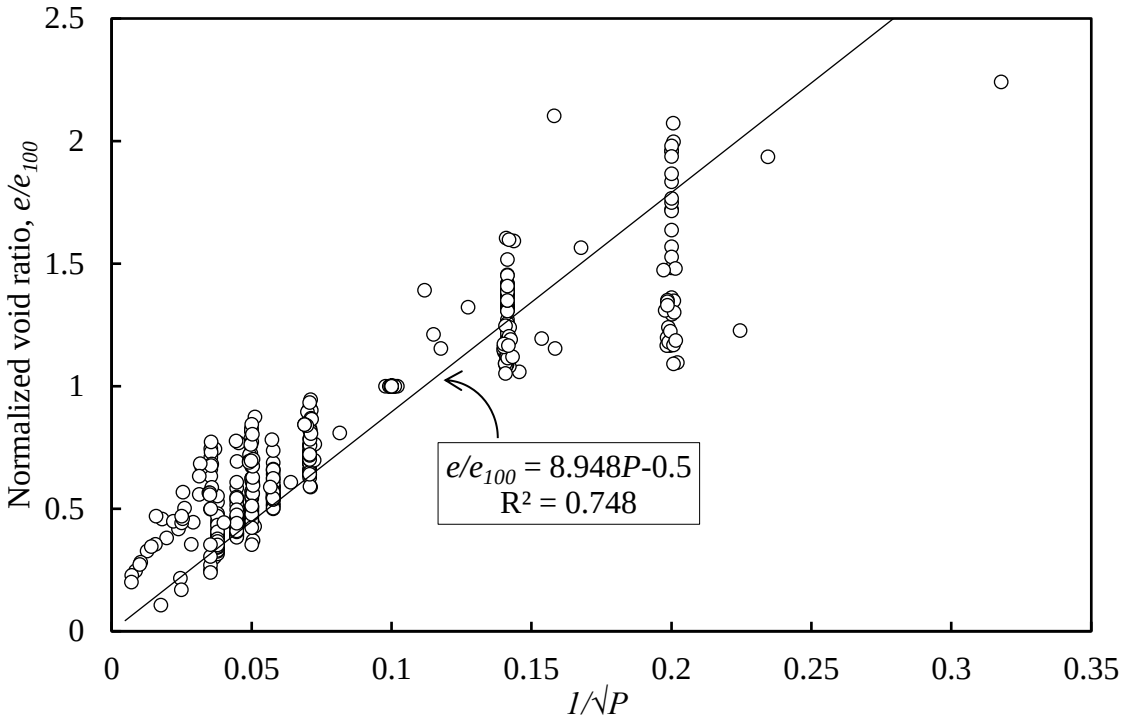

Fig. 6.7 The linearized curve of measured compressibility data (Fig. 6.1a) using e/e_{100}

6.5 Proposed model

A generalized predictive model was developed here to accommodate the deviation by different clayey soils from the ideal compressibility behavior observed based on the DDL theory. The predictive equation was modified by incorporating the variable exponent in Eq. 43 and was given by

$$\frac{e_i}{e_{P_N}} = \left(\frac{P_N}{P_i}\right)^a \tag{44}$$

where *a* is the empirical parameter that is constant for a given clay. As it would be shown in the following work that the empirical parameter was directly dependent on the plasticity of the clayey soil, the parameter was termed as the *intrinsic* parameter. Therefore, the proposed model is applicable for clayey soils of different plasticity. The intrinsic parameter was 0.5 for the predictive model obtained from the ideal DDL theory which was applicable only for highly plastic clays. The intrinsic parameter accounted for the deviations from the ideal behavior observed in highly plastic clays. The parameter was determined for over 110 compressibility curves by fitting Eq. 44 on the compressibility data at low consolidation pressures but beyond the preconsolidation pressure. The

parameter *a* was obtained in this work by minimizing the error between theoretical and measured void ratios in the low consolidation pressure range using *fmincon* MATLAB® program, featuring a constrained optimization of a multivariable function (Bharat et al., 2009). Root mean square error (RMSE) was used as an error norm for the minimization (Bharat et al., 2013). Three to four compressibility data points after the preconsolidation pressure was found to be sufficient for estimating an accurate intrinsic parameter for many clayey soils. The fitted parameter for different studied clays and clayey soils were presented in Table 6.1. The intrinsic parameter for most of the montmorillonites (Low, 1980) and bentonites dominated by sodium smectite content ranged between 0.4 – 0.6. The increase in the salt concentration decreased the intrinsic parameter for montmorillonite clays (Horpibulsuk et al., 2011), but the opposite trend was observed for kaolinite clays (Di Maio et al. 2004; Horpibulsuk et al., 2011). The opposing behavior of bentonite and kaolinite clays in the presence of salt solution is well documented (Sridharan & Prakash, 2000) and the obtained variation to the intrinsic parameter with the salt concentration for both clays was in good agreement. The empirical parameter in Eq. 44 was, therefore, a true intrinsic parameter of the clayey soils. The intrinsic parameter of most of the natural clayey soils (Nagaraj & Murthy, 1983; Jennings & Burland, 1962; Hvorslev, 1960; Wahls & Godoy, 1964; Newland & Alley, 1957; Taylor, 1942; Sowers, 1964; Altschaeff, 1960; Gens, 1982; Hvorslev, 1937; Jardine, 1985; Hong et al., 2010) was ≤0.2 due to high non-clay content. The compressibility data for homoionized bentonites by Sridharan et al. (1986) are available only up to a maximum consolidation pressure of 400 kPa and the virgin compression data started only beyond 50 kPa. As the limited data are available for these homoionized bentonites on the virgin compression curve (i.e., void ratios corresponding to 100, 200, and 400 kPa pressures), the estimated intrinsic parameter was not used in the validation experiments and further analysis. Alternatively, the parameter *a* may be estimated using two data points beyond the preconsolidation pressure from the following equation derived using the aforementioned Eq. 44:

$$a = \frac{\ln\left(e_1/e_2\right)}{\ln\left(P_2/P_1\right)} \tag{45}$$

where e_1 and e_2 are the void ratios at consolidation pressures P_1 and P_2. However, it was noticed that a slight measurement error in the estimated void ratio resulted in a significant error in the estimated intrinsic parameter. Therefore, only the optimized parameters were used in the work.

6.6 Validation of the proposed model

The validation of the generalized model, proposed in this work, on various clays and clayey soils from the present study and the literature were presented in Figs. 6.8–6.9. The compressibility data point, just after the preconsolidation pressure based on the shift in the nature of the curve, was highlighted with a circle in these figures for the computation of *a* parameter. The prediction using the generalized model was in very good agreement with the measured data for all the bentonites and clayey soils. The theoretical prediction by the proposed model on the measured data of B1, B2, B3, RS, and mixture RS+B1 clays were shown in Figs. 6.8a – 6.8b. The intrinsic parameter

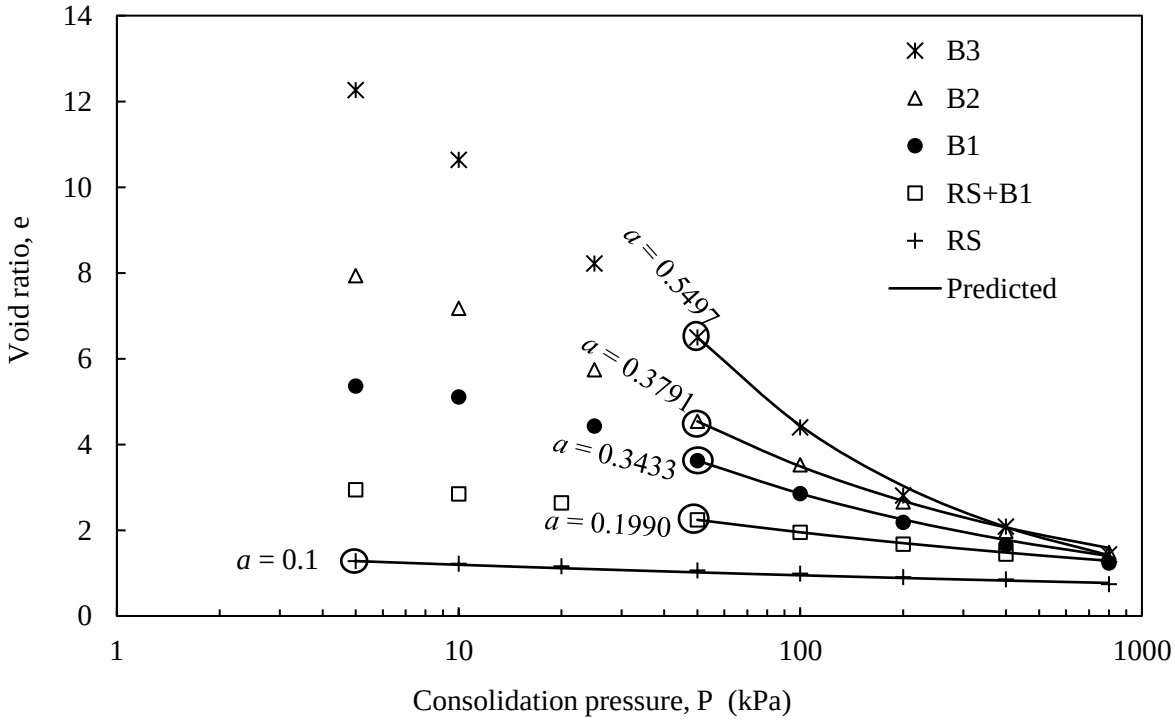

Fig. 6.8a Measured and predicted compressibility data of the Indian bentonites using the proposed method

increased with the plasticity of the bentonite. The '*a*' parameter was found to be 0.55 for B3 which was the very high-quality clay among the studied clays. Therefore, the theoretical compressibility curve using $a = 0.5$ was also in close agreement with the measurements for this case (Fig. 6.4c), but the error between the predicted and measured was minimal when $a = 0.55$ as shown in Fig. 6.8a. The proposed equation is equivalent to the predictive equation by Bharat & Sridharan (2015a) when $a = 0.5$. A lowest value, $a = 0.1$, for the intrinsic parameter was obtained for the studied RS

indicating the lowest plasticity or compressibility soil. Further, the parameter *a* decreased from 0.55 to 0.27 (Fig. 6.8b) when the concentration of the NaCl solution increased from 10^{-5} M NaCl (i.e., equivalent value for distilled water as observed by Bharat & Sridharan, 2015b) to 1 M. This observation was in accordance with the earlier discussed theoretical results. As the observed compressibility behavior of clayey soils under low electrolyte concentration follow DDL theory, the exponent of the proposed model becomes equal to 0.5 for such cases.

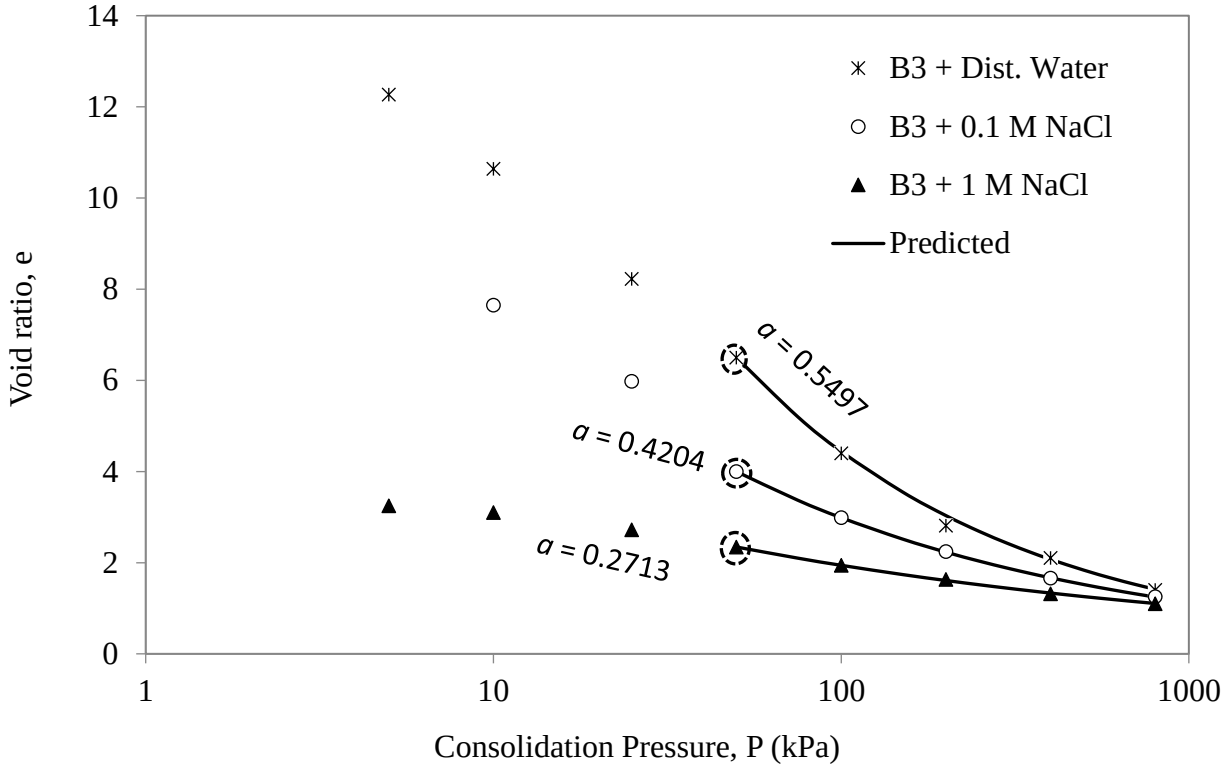

Fig. 6.8b Measured and predicted compressibility data for B3 in the presence of different electrolyte concentrations using the proposed method.

The proposed model was validated on the measured data obtained from the literature. The theoretical predictions and measured compressibility data using the proposed model for Na-Ca MX-80, Na-Kunigel, and Ca-Fourges (Marcial et al., 2002) were presented in Fig. 6.9a. The optimized intrinsic parameter for Na-Ca MX-80 bentonite was found to be 0.49 which predicted the measured data very accurately as observed in Fig. 6.9a. The intrinsic parameter was the same as the exponent of Eq. 43 used by Bharat & Sridharan (2015a) for Na-Ca MX-80 bentonite. The estimated parameter for Na-Kunigel was 0.61 which was higher than the value for MX-80, which may be due to the presence of a higher percentage of Na-smectite content in Na-Kunigel bentonite and other monovalent cations such as Li^+ in the exchangeable complex. The estimated parameter

was lowest, i.e., 0.23, for Ca-Fourges due to the presence of kaolinite content and exchangeable calcium ions (Marcial et al., 2002).

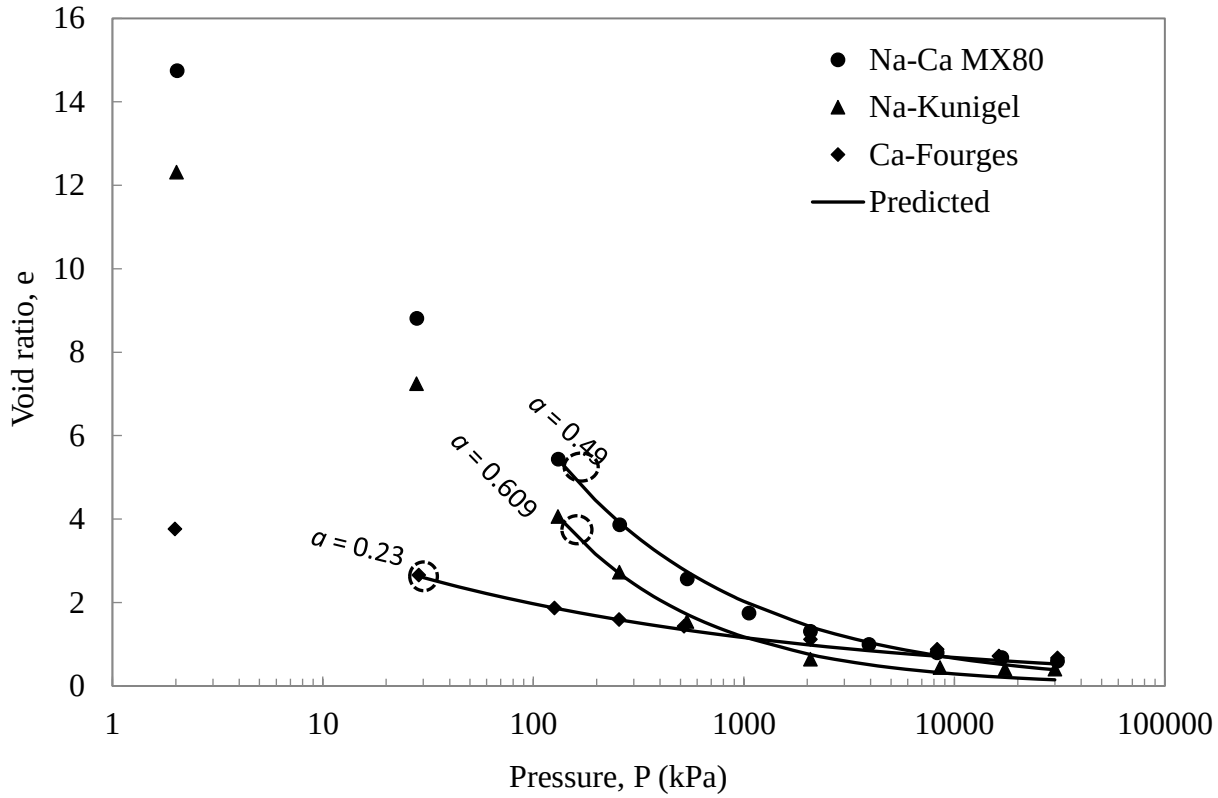

Fig. 6.9a Measured and predicted compressibility data for MX-80, Na-Kunigel, and Ca-Fourges (Marcial et al., 2002) using the proposed method.

The validation experiments on Ponza bentonite and Bisaccia clay with different electrolyte concentrations (Di Maio et al., 2004) were shown in Fig. 6.9b –6.9c. The parameter increased from 0.22 to 0.45 for bentonite when inundation fluid changed from saturated NaCl solution to distilled water. The observed trend for the intrinsic parameter with the inundation fluid concentration was qualitatively similar to the B3 bentonite, but the values varied significantly in the presence of different electrolyte concentrations. The compressibility data of Bisaccia clay with different inundation fluids was qualitatively similar to Ponza bentonite, but the '*a'* parameter was very small in the presence of distilled water. The parameter was smaller due to the low plastic nature of the bentonite similar to B1. The estimated intrinsic parameters for all the datasets were also presented in Table 6.1. The parameter varied between 0.596, for Blue Western montmorillonite, to 0.289, for Guam montmorillonite, for various plastic clays considered by Low (1980).

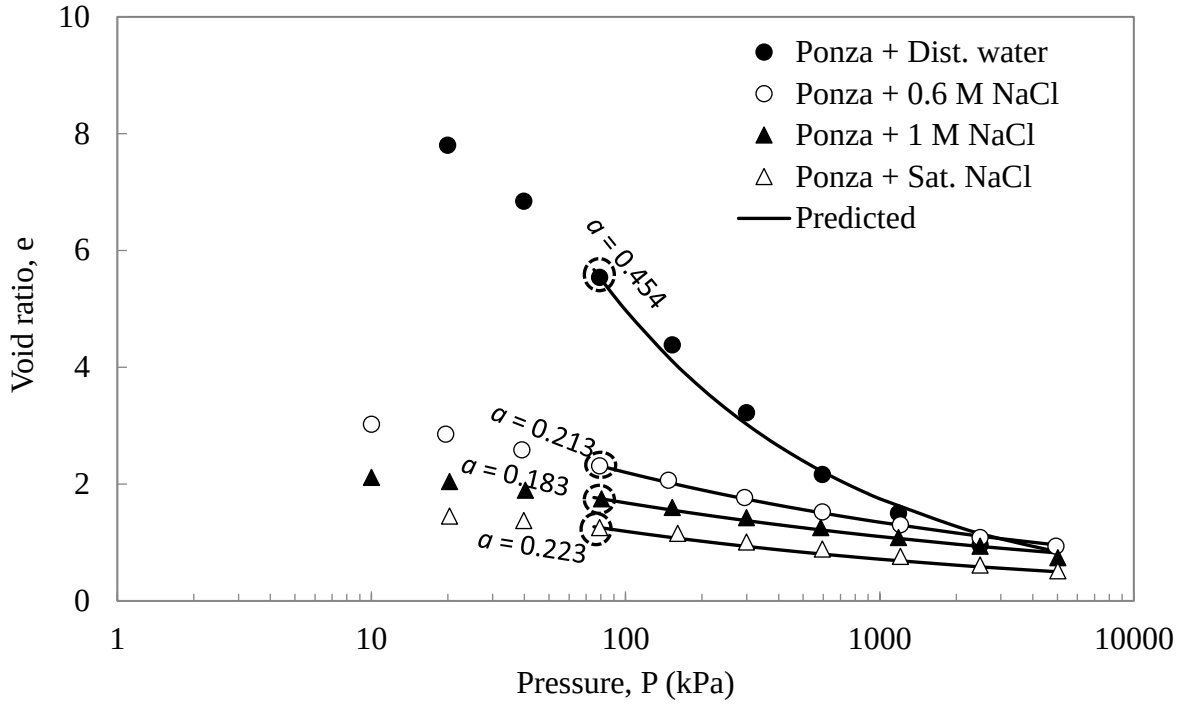

Fig. 6.9b Measured and predicted compressibility data for Ponza bentonite inundated with different electrolyte concentrations (Di Maio et al., 2004) using the proposed method.

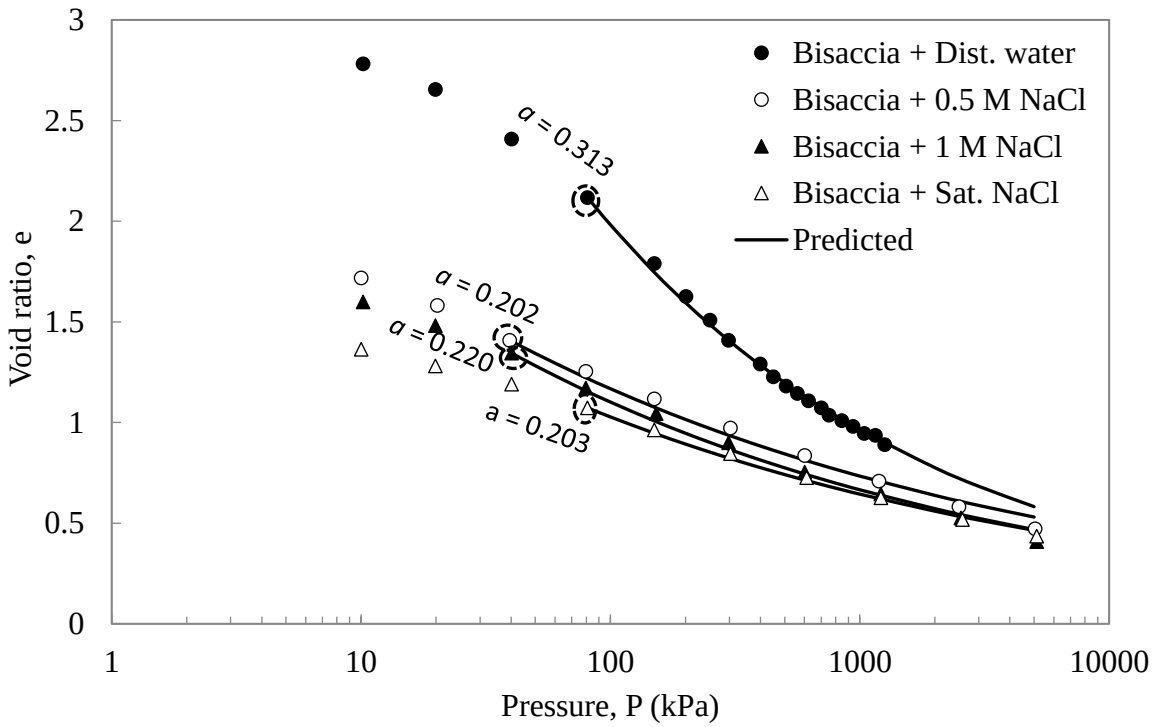

Fig. 6.9c Measured and predicted compressibility data for Bisaccia clay inundated with different electrolyte concentrations (Di Maio et al., 2004) using the proposed method.

Further, it was clear from the variation in the intrinsic parameters of different homoionized bentonites (S. No. 101-105 in Table 6.1) that the intrinsic parameter was proportional to the hydrated size of the cation (Fig. 6.10). The intrinsic parameter increased with the ratio of hydrated cation radius to valence. The variation of intrinsic parameter with liquid limit void ratio was investigated for all the studied clays in Figure 6.11. The trend line followed a logarithmic variation with a regression value of $R^2 = 0.91$ using the re-weighted least square method (Das and Basudhar, 2006). In this method, the regression value was estimated by identifying and eliminating the outliers based on the variance. The line with $a = 0.5$ was also shown in the figure. The clays with void ratios at a liquid limit higher than 14 were found to approach the horizontal line for which the model by Bharat & Sridharan (2015a) was closely valid. Therefore, the clays with void ratios at the liquid limit higher than 14 (or $w_L \approx 500\%$) can be considered highly plastic clays. Overall, the proposed model was very satisfactory in predicting the compressibility data at high consolidation pressures using the data in the low-pressure range for different clayey soils.

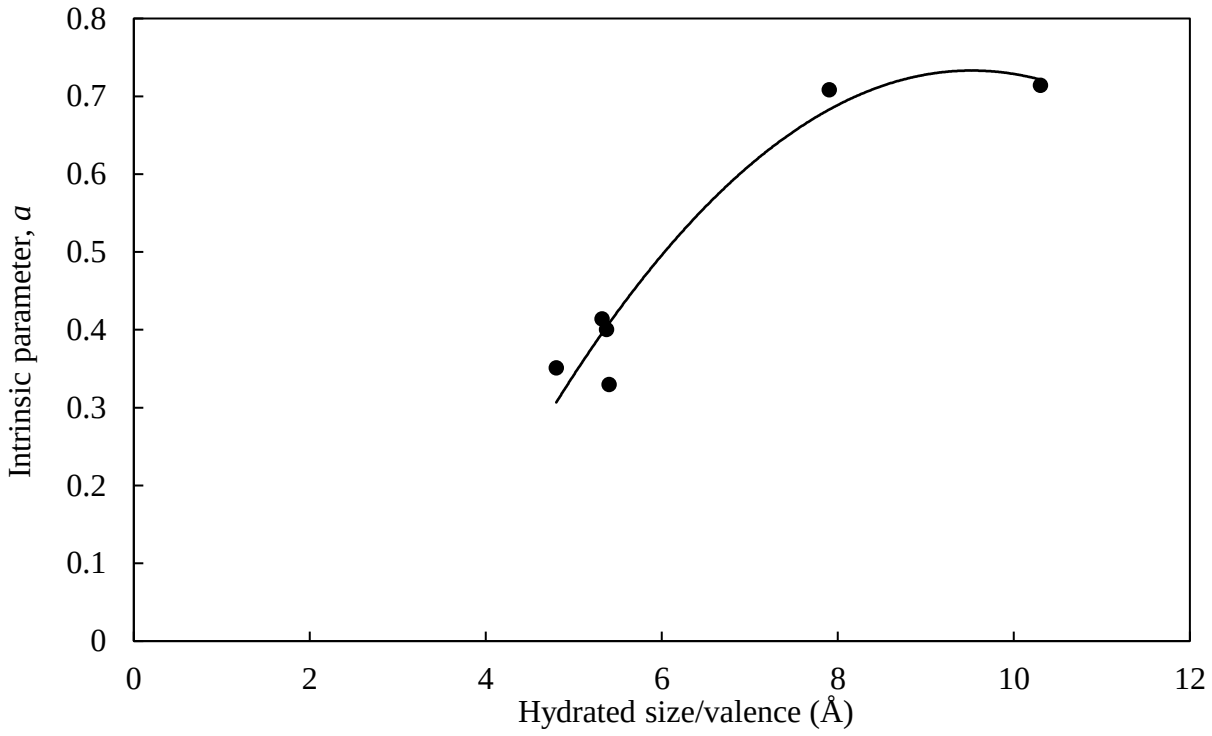

Fig. 6.10 Influence of hydrated cation size on the intrinsic parameter

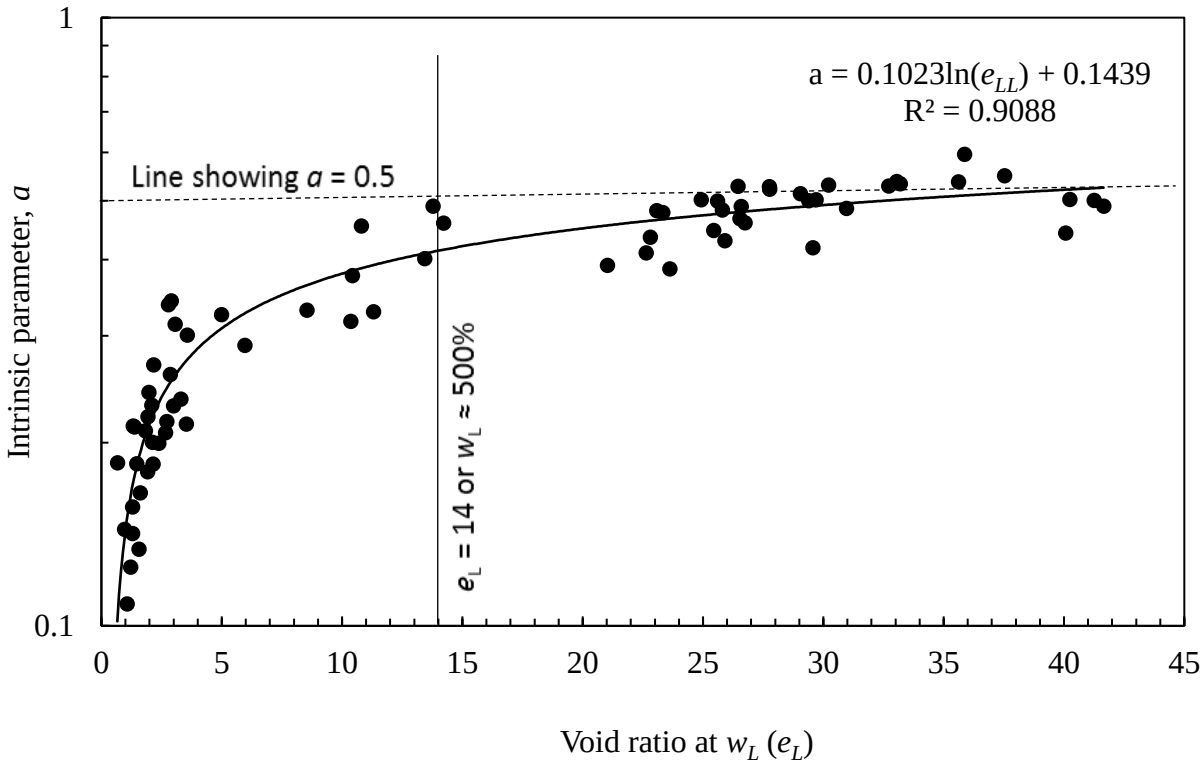

Fig. 6.11 Relation between Intrinsic parameter and liquid limit void ratio

6.7 Summary

A general theoretical model was proposed in this work by relating normalized void ratio with P^{-a} for predicting the compressibility data up to very high consolidation pressures for clayey soils with different plasticity. The model required the compressibility data at low consolidation pressure range, just beyond the preconsolidation pressure, for estimating the intrinsic parameter, a. As the intrinsic parameter was found to be related to the plasticity of the clayey soil, the parameter captured the intrinsic properties and compressibility nature of the given clayey soil for predicting the compressibility data at high consolidation pressures. The intrinsic parameter varied between 0.71 to 0.1 for different clayey soils and with different salt interactions. The estimated intrinsic parameter for highly plastic bentonites ($e_L \geq 14$) was found to be approaching a = 0.5, but decreased with the decreasing plasticity. The proposed model satisfactorily predicted over 110 sets of compressibility data from higher pressures to a maximum consolidation pressure ranging between 800 kPa – 42000 kPa for 88 clays studied in this work.

7 Compressibility behavior of bentonites by Stern theory

7.1 General

This chapter presents a numerical approach to predict the compressibility behavior of clays based on the Stern diffuse double layer theory. The predictive model based on the Stern theory at constant surface potential condition (Tripathy et al., 2014) was presented first and the associated limitations were discussed. The proposed model was then presented to establish the potential distribution in an interacting Stern DDL model at constant surface charge conditions for the first time. The computed potential distribution based on the proposed model was compared with the Gouy-Chapman model and discussed. Validation of the proposed model against measure compressibility data was presented next, followed by a summary at the end.

7.2 The Stern theory at constant surface potential case

Tripathy et al. (2014) established the potential-distance relationship in an interacting Stern layer by considering the potential near the surface of the clay platelet to be constant. The main challenge in this approach is to determine a suitable constant surface potential (y_0) value for different clay-water-electrolyte interactions. An approximate estimation of surface potential can be obtained from equation (4) by assuming that the diffused double layer consists of the Gouy layer alone. However, the issue with this approach is that the parameter, σ in Eq. 4, is calculated from the surface parameters (C_e and S_a), which is valid only for a constant surface charge (variable surface potential) system. An average normalized value of 10.66 (true value = 274 mV) is generally considered for water-saturated slurried clays based on the reports from various literature, however, it can be of any value depending upon the pressure and the type of interacting dielectric medium present in the system. For a constant surface potential value, the total charge density (σ) is estimated by knowing ε' using Eq. 7, by varying the value of y_δ. The chosen value of y_δ must be such that the charge in the Stern layer (σ_1) estimated by Eq. 10 will produce a positive charge in the Gouy-layer (σ_2) and should satisfy the equation Eq. 9. Knowing the value of σ_2 using Eq. 8, u is computed from Eq. 10. Consequently, the inter-platelet distance d is estimated from Eqs. 6 & 8. The potential-distance relationship thus obtained, is expressed in the form of pressure-void ratio relationships of clays using Eqs. 23 & 28.

The major issue with this approach is that the surface potential is always treated as constant over the applied pressure range. In a clay-water-electrolyte system, the surface potential varies significantly as the applied pressure and the bulk fluid properties are changed. The assumption of constant surface potential, therefore, is proven to be inappropriate for the compressibility behavior of clays. Also, for a given value of surface potential, both *u* and *d* are treated as unknown, which is then estimated by randomly varying the stern potential. The established potential-distance relationships are, therefore, only approximate. Secondly, the distribution equilibrium of charges between Stern and Gouy layers is subjected to vary due to the interaction between the double layers. The effect of the DDL interaction on the Stern layer charge is not considered in the existing approaches as it utilizes Eq. 10 for computation of charge in the stern layer which is valid only for the non-interacting systems. The theoretical model based on the Stern layer for an interacting system for constant surface charge condition is yet to be developed to bring the effect of cation sizes on the compressibility behavior of clays.

7.3 Proposed model for constant charge condition

The charge densities in the Stern and Gouy layers are related through a special treatment (van Olphen, 1963). The charges in the Stern and Gouy layers were considered to be proportional to their respective areas under the electrostatic potential distribution curve i.e.,

$$\frac{\sigma_1}{\sigma_2} = \frac{\text{Area of the Stern layer } (A_s)}{\text{Area of Gouy layer } (A_{Gouy})} \tag{46}$$

The estimation of stern layer charge (σ_1) in an interacting system for constant charge conditions is not available due to the difficulties involved in estimating the two parameters– the number of available adsorption sites and specific adsorption potential on the counter-ions at the clay surface (see Eq. 10). The influence of platelet interaction on the number of available adsorption sites is not understood yet. Determination of ψ for a given clay-water-electrolyte system is also challenging. The σ_1 estimation was, therefore, eliminated by considering

$$\frac{\sigma}{\sigma_2} = \frac{A_{Stern}}{A_{Gouy}} + 1 \tag{47}$$

Substituting the expression for the Gouy layer charge (σ_2) from Eq. 11 in the above equation and re-arranging,

$$\sigma A_{Gouy} = \sqrt{2nkT\varepsilon}\sqrt{2\cosh y_\delta - 2\cosh u}\left(A_{Stern} + A_{Gouy}\right) \tag{48}$$

Area of Stern layer was estimated by,

$$A_{Stern} = \frac{(y_0 + y_\delta)}{2}\delta \tag{49}$$

After substituting for y_0, from Eq. 7,

$$A_{Stern} = \left(y_\delta + \left(vq\sigma 2\pi\delta/\varepsilon' kT\right)\right)\delta \tag{50}$$

Combining Eq. 48 and 50, we get

$$\sigma A_{Gouy} = \sqrt{2nkT\varepsilon}\sqrt{2\cosh y_\delta - 2\cosh u}\left(\left(y_\delta + \left(vq\sigma 2\pi\delta/\varepsilon' kT\right)\right)\delta + A_{Gouy}\right) \tag{51}$$

The area under the hyperbolic potential distribution curve for the Gouy layer (A_{Gouy}) can be calculated by following the method of slices. Dividing the entire Gouy layer thickness into N number of thin slices of equal thickness Δx, the area can be computed as,

$$A_{Gouy} = \sum_{i=1}^{N+1}\frac{(y_i + y_{i+1})}{2}\Delta x \tag{52}$$

where $y_{i+1} = y_i - (slope)_i \Delta x$, and i denotes the number of nodal points, $d = N\Delta x$. The boundary conditions are– $y_i = y_\delta$ at $i=1$, and $y_i = u$ at i = N+1. The slope of the potential distribution in the Gouy layer at any point can be obtained as per the following equation,

$$(slope)_i = \kappa\sqrt{2\cosh y_i - 2\cosh u} \tag{53}$$

Thus the Gouy area can be estimated by knowing the Stern and mid-plan potentials in an interacting clay-water-electrolyte system. Therefore, Eq. 51 provides an implicit solution for the Stern potential. For a known value of mid-plan potential, Stern potential is obtained through

optimization. The objective function to determine the Stern potential based on Eq. 51 was as follows,

$$f\left(y_\delta\right)=\sigma A_{Gouy}-\left\{\sqrt{2nkT\varepsilon}\sqrt{2\cosh y_\delta-2\cosh u}\left(\left(y_\delta+\left(vq\sigma 2\pi\delta/\varepsilon' kT\right)\right)\delta+A_{Gouy}\right)\right\} \qquad (54)$$

The nature of the above objective function was evaluated at different applied mechanical pressures and pore-fluid concentrations and presented in Fig. 7.1. The soil surface properties and pore-fluid parameters used in the computation were presented in Table 7.1. The value y_δ considered in the function evaluation was ranged from a minimum value equal to the mid-plan potential ($u+10^{-9}$) to a maximum of 20. A small value was added to the midplane potential at the lower boundary to avoid the singularity (Bharat et al., 2013). The function exhibited two minima– one at the lower boundary followed by the true minimum at a higher value of y_δ. The true minimum tends to approach the local minimum at the lower boundary with the increase in the mechanical pressure (Fig. 7.1a). A similar trend was also observed when the pore-fluid concentration was increased (Fig. 7.1b). Overall, the minimum was observed in the range from 0 to 10 for all the considered cases. The 'fminbnd' function was used to optimize the objective function in Matlab for the Stern potential in the range of u to 20 (Bharat et al., 2009). The algorithm in the 'fminbnd' function is based on the golden section search and parabolic interpolation method. A detailed flow chart showing the stepwise procedure for obtaining the stern potential in a clay-water-electrolyte system subjected to applied mechanical stress was presented in Fig. 7.5.

7.3.1 Electrostatic potential distribution

The complete electrostatic potential distribution in an interacting clay-water system was established using the Stern DDL model for the first time. The electrostatic potential distribution of an interacting clay-water system at two different applied pressure was computed based on the developed formulation for the Stern model was presented in Fig. 4a along with the Gouy-Chapman model as presented. The soil surface properties and pore-fluid parameters considered in the computation were presented in Table 7.1. The potential distribution for the entire DDL in the Gouy-Chapman model and the Gouy-layer in the Stern model followed the poison's distribution. The mid-plan potential *u*, at a given pressure was determined using Eq. 23. The surface potential

was obtained for known soil surface properties and pore-fluid parameters using Eq. 4 in the Gouy-Chapman model. The Stern potential in the proposed model was obtained through optimization (Eq. 54) as presented in the earlier section, which was then used as the upper boundary to establish the potential distribution in the Gouy-layer using Eq. 4. The potential distribution within the Stern layer was varied linearly from a maximum value at the clay surface to Stern potential at the Stern-Gouy interface. The surface potential was estimated by Eq. 7 after knowing the Stern potential value at a given pressure.

Table 7.1 Parameters used to establish electrostatic potential distribution in the Gouy-Chapman model and the proposed Stern model (Fig. 7.1 & 7.2)

Parameters	**Value**
Specific gravity, G_s	2.76
Specific surface area, S_a (m^2/g)	800
Cation Exchange capacity, C_e (meq/100g	100
Valence, ν	1
Dielectric constant of bulk pore fluid, ε	80.4
Stern thickness/hydrated cationic radius, δ (Å)	7.9
Dielectric constant of water within stern layer, ε'	6
Temperature, T (K)	298

The potential distributions from both models were presented from the surface to mid-plane distance under a given applied pressure at equilibrium (Fig. 7.2a). The equilibrium separation distances at 0.01 MPa and 1 MPa pressure were about 280 Å and 30 Å, respectively, by the Gouy-Chapman and proposed Stern modelS. Both the models showed similar potential variation for distance from the clay surface over 20 Å at the applied pressure of 0.01 MPa. The two models, at this pressure, deviated from each other when the distance from the clay surface was reduced below 20 Å. The potential curves of both models were significantly different near the surface of the clay platelet. The electrostatic potential varied linearly from a maximum value at the clay surface to a minimum value at the Stern-Gouy interface due to the incorporation of the finite-sized cations in

the Stern model. On the other hand, the electrostatic potential distribution across the entire distance of the clay-water system varied as per Poisson-Boltzmann's equation in the Gouy-Chapman model.

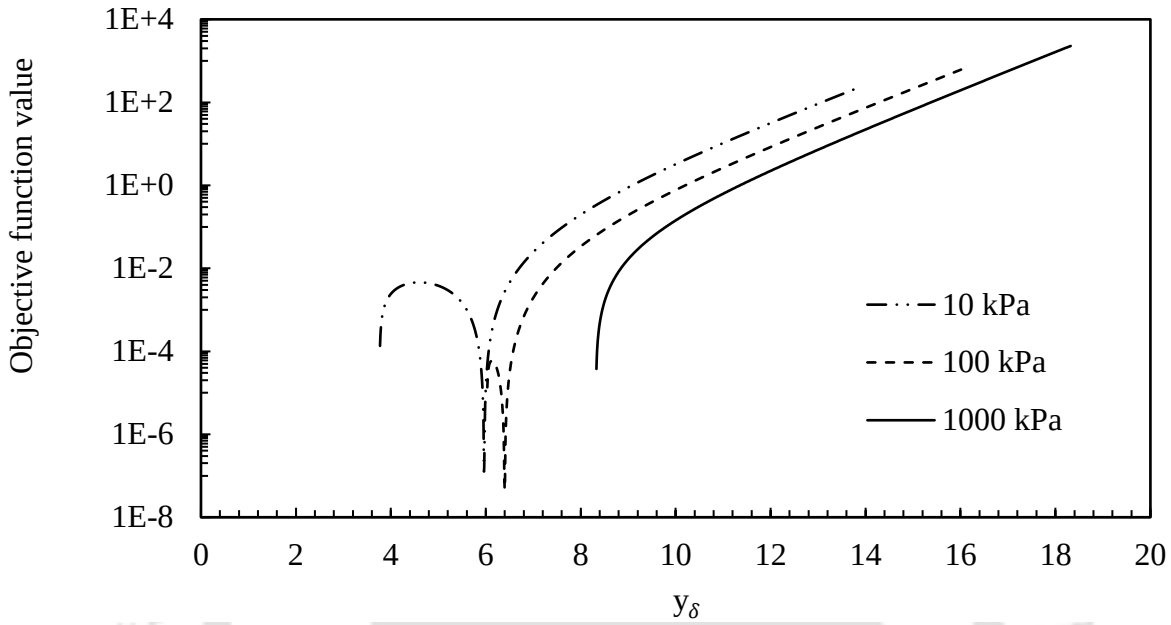

Fig. 7.1a Nature of objective function at 0.0001 M pore fluid concentration for three different pressure values

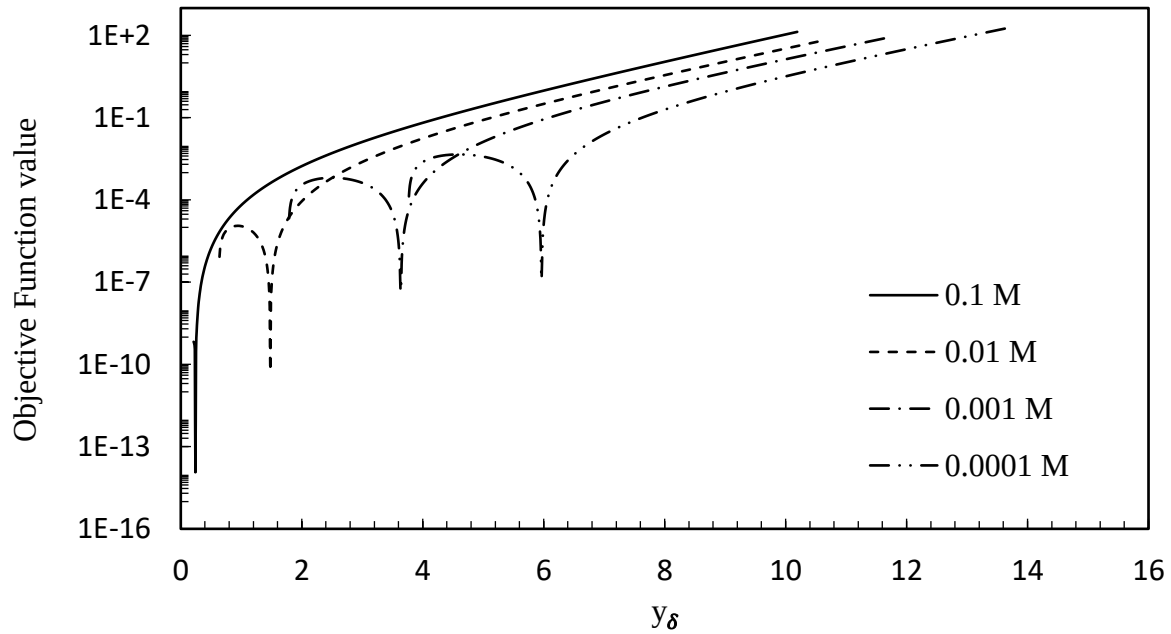

Fig. 7.1b Nature of the objective function at 10 kPa pressure for four different pore fluid concentrations

Treatment of rigid Stern layer near the clay surface in the proposed model resulted in a very high electrostatic potential near the clay surface as compared to the Gouy-Chapman model. The normalized surface potential by the Stern model was 78 (i.e., ψ_0 = 2005 mV) and was 10.63 (i.e., ψ_0 =273 mV) by the Gouy-Chapman model. The normalized mid-plan potential increased from 3.75 to 8.3 due to the increase in the DDL interaction as the separation distance reduced from 280 Å to 30 Å with the increase in the pressure value from 0.01 MPa to 1 MPa. Similarly, the Stern potential increased from ~8 at 0.01 MPa to 8.8 at 1 MPa pressure. The potential curves from the two models, at this pressure, were distinctly different along the entire half-space distance, unlike at smaller pressures. Thus the effect of cation size on the electrostatic potential distribution of the interacting clay-water system is more pronounced at smaller separation distances and under the higher applied pressures.

Fig. 7.2b presents the variation of Stern potential, mid-plane potential, and the DDL thickness (on the third axis) with the applied pressure by the proposed Stern model. A dilute cationic concentration of 0.0001 N was considered to represent the clay-water system. The values of all other parameters considered in the simulation were presented in Table 7.1. The applied pressure was varied in the range of 0.01 MPa to 40 MPa. The DDL thickness was maximum (~145 Å) at 0.01 MPa, but decreased exponentially with the applied pressure. A minimum DDL thickness, 7.9 Å (equivalent to the hydrated radius of Na^+ cation) was observed at ~ 5 MPa pressure. The DDL thickness remained constant with a further increase in the pressure as the Stern layer was treated as a rigid layer in this model. The mid-plane potential showed a linear increase with the increase in the applied pressure on the semi-log scale. The increase in the DDL interaction with a decrease in the separation distance (DDL thickness) leads to a consistent increase in the mid-plan potential value. The Stern potential, on the other hand, showed a relatively slower rise in magnitude as compared to the mid-plan potential. The two potential curves eventually converged beyond ~ 7-8 MPa pressure. The two potential curves, overall, tend to converge due to the increased DDL interaction as the separation distance decreased under the applied mechanical pressure. The ratio between the Stern and mid-plan potential, thus, is a more appropriate parameter to represent the degree of interaction between the double layers than the mid-plane potential alone.

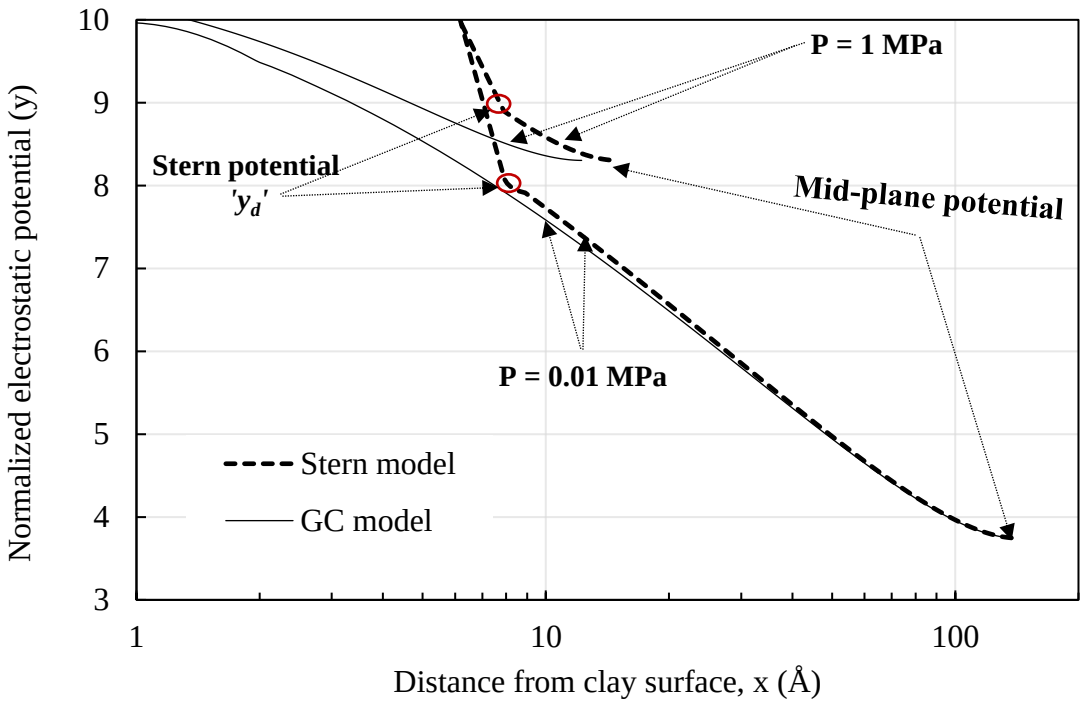

Fig. 7.2a Computed electrostatic potential distribution in the clay-water system (c_0 = 0.0001M) based on GC and stern model under two different applied mechanical pressure

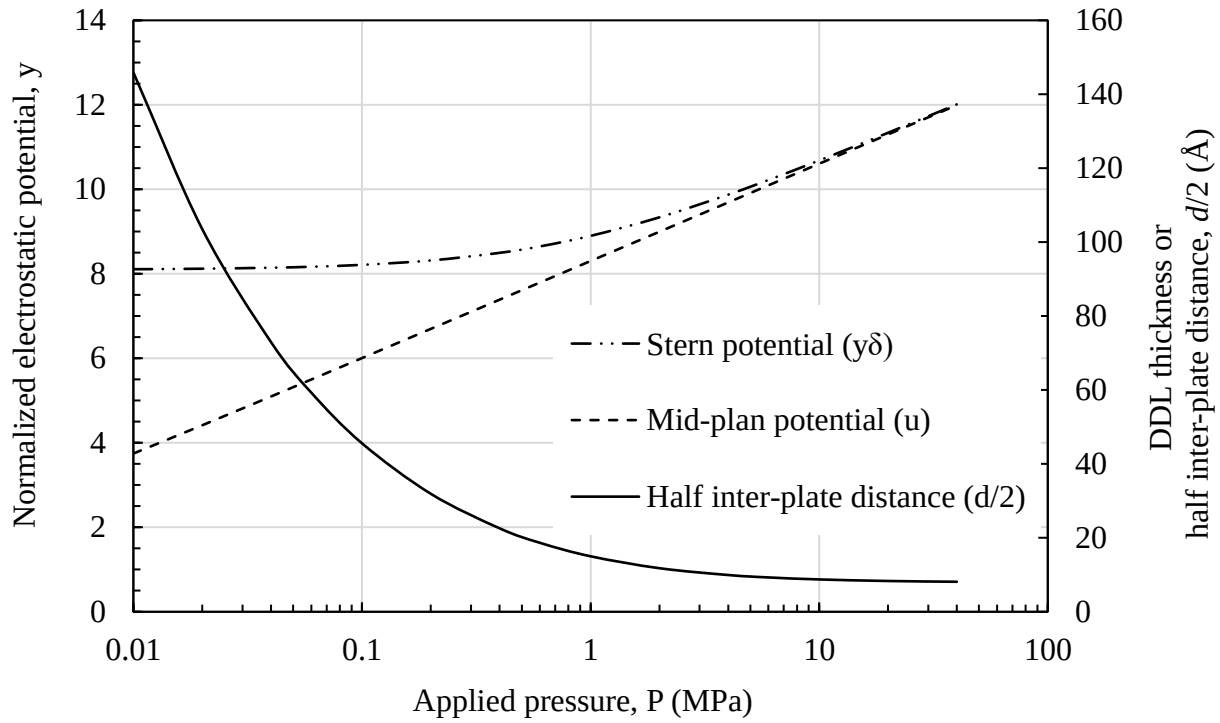

Fig. 7.2b Variation of Stern potential and midplane potential in the clay-water system (c_0 =0.0001M) with change in the degree of interaction (separation distance) under loading

7.3.2 Compressible Stern layer

The Stern layer is treated as an incompressible layer in the conventional Stern model. The minimum theoretically computed void ratio to which a saturated clay is mechanically compressed (i.e., the closest approachable distance between two interacting clay platelets) is, therefore, depends on the thickness of the Stern layer. Choosing an appropriate thickness of the Stern layer is crucial for predicting the pressure-void ratio relationship, especially in the higher-pressure range, where the Gouy diffused layer gets compressed significantly. The thickness of the Stern layer is generally assumed to be equivalent to the hydrated radius of the cations (Shang et al., 1996). However, a well-defined value of the Stern layer thickness is not available for the clays (Verwey and Overbeek, 1948; van Olphen, 1973; Shang et al., 1994; Sridharan and Satyamurhty, 1996). The type of exchangeable cations, charge distribution, and size and shape of siloxane cavity on the surface of the montmorillonite influence the adsorption of cation on the clay surface (Sposito, 2008), which can significantly influence the Stern layer thickness. Further, the cations from the diffused Gouy-layer may enter the Stern layer at a very high-applied pressure (Jiang et al., 2001), which affects the Stern layer thickness. Additionally, the surface cations might penetrate the siloxane cavities of the clay surface at a sufficiently high-applied pressure. The Stern layer, thus, gets compressed at a high applied pressure to facilitate further volumetric compression of clays once the Gouy-layer is compressed significantly.

Measured compressibility data of seven different bentonites from the literature were considered in this study to understand the minimum achievable separation distance between the clay platelets (DDL thickness) under the applied mechanical pressures. The relevant properties of the bentonites are presented in Table 7.2. The DDL thickness was derived from the measure void ratio for these clays using Eq. 28 by considering the parallel plate assumption. The parallel plate assumption is valid at this high-pressure range as the platelets are ought to be in a parallel manner at such a small measured void ratio under the saturated condition, where the long-range repulsive pressure is significantly high. The DDL thickness was plotted against the applied pressure and presented in Fig. 7.3a. Variation of the DDL thickness with the applied pressure for all the bentonites suggested that the thickness of the DDL is compressed to the smallest value of 2.3Å in the pressure range of 10 MPa- 40 MPa for different bentonites. The minimum possible separation distance between the two clay platelets surrounded by a rigid Stern layer is shown in Fig. 7.3b(i). When the DDL

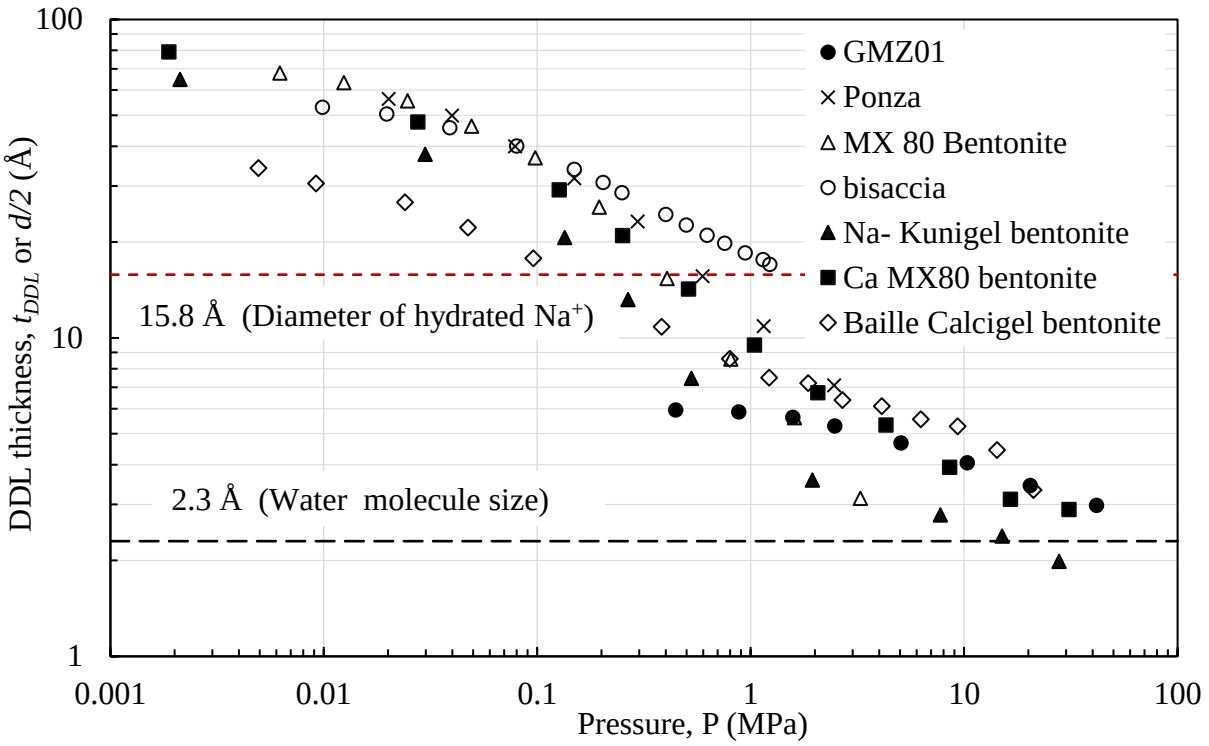

Fig. 7.3a Variation of DDL thickness with applied mechanical pressure derived from the measured compressibility data (using Eq. 28 with the parallel plate assumption) of different quality bentonites

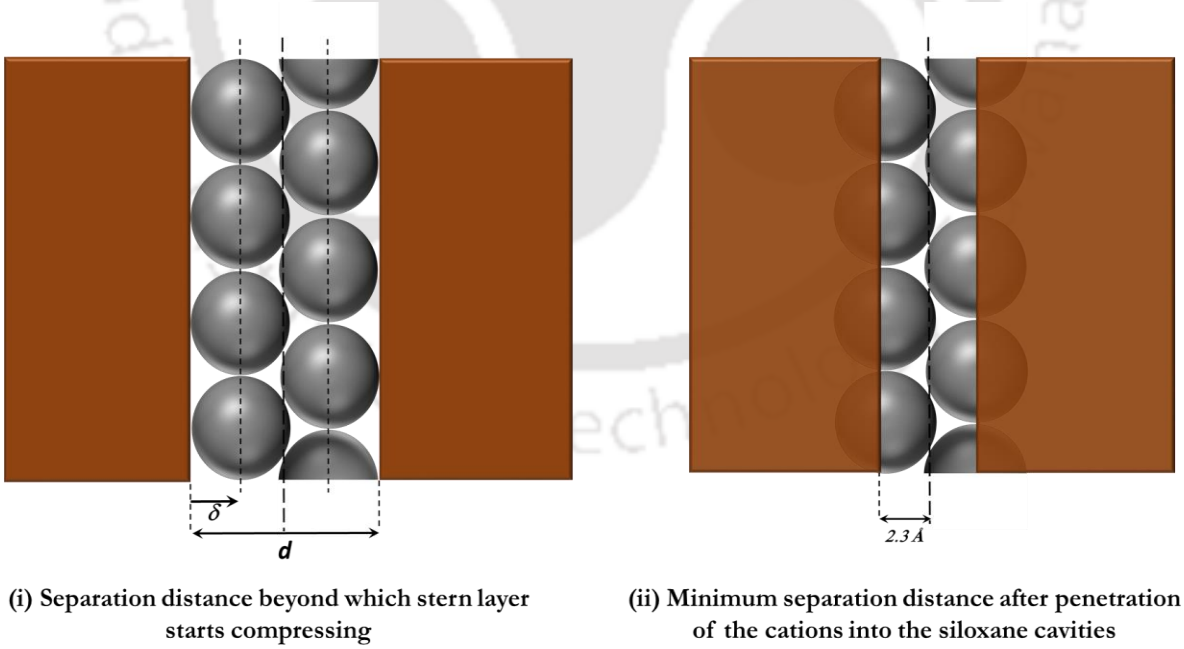

Fig. 7.3b Illustration showing cations penetrating the siloxane cavities on clay surface resulting in compression of Stern layer under very high applied mechanical pressure

thickness or the half of the separation distance is decreased beyond the value equivalent to the diameter of the exchangeable cation, the Stern layer thickness consequently got compressed. The Stern layer compression can be attributed to the penetration of the cations into the siloxane cavities of the clay surface (Fig. 7.3b (ii)). Generally, the diameter of the siloxane cavity is about 2.6 Å, which is approximately 1/3rd of the hydrated size of Na^+ (Sposito, 2008).

Fig. 7.4 presents the variation of the ratio between the mid-plan and stern potentials (u/y_δ) as the DDL thickness was compressed under the applied pressure, for three different bentonites namely Na-Kunigel, Ponza, and Na-Ca-MX80. The three bentonites represented a wide range of surface cation characteristics and surface charge density (σ). The Na-Ca-MX80 is a sodium dominant bentonite (exchangeable sodium percentage –ESP ~88%) with a surface charge density of 0.094 C/m^2. The Na-Kunigel, on the other hand, possesses a mixture of divalent and monovalent cations as exchangeable cations, with an ESP of ~ 55% and a surface charge density of 0.102 C/m^2. The Ponza bentonite is dominated by divalent cations (ESP~16%), which contains a relatively higher surface charge density of 0.164 C/m^2. The ratio between the two potentials indicated the degree of interaction between the two interacting clay platelets. The relevant properties of the respective bentonites and other parameters related to the pore-fluid and stern layer used in the estimation are presented in Table 7.2. A cationic concentration of 0.0001N was used to represent water as pore fluid (Das and Bharat, 2021). The valence was taken as the weighted average valence calculated based on the known percentage of individual exchangeable cations (Tripathy et al., 2014). The dielectric constant within the stern layer was taken as 6. The stern layer thickness was taken as the hydrated radius of Na^+ for Na-dominated bentonite. For the divalent dominated and mixed-valence bentonites, the larger cationic size (i.e., Ca^{2+}) was considered as the Stern layer thickness.

The potential ratio increased with the applied pressure for all the three bentonites as the DDL thickness was compressed resulting in a higher degree of DDL interaction. The Stern layer compression began for the di-valence-dominated Ponza bentonite when the potential ratio was ~ 0.65 (Fig. 7.4a). for Na-Kunigel bentonite, which contains mixed-valence surface cations, the stern layer compression started when the potential ratio was ~ 0.65 (Fig. 7.4b). On the other hand, Stern layer compression was observed at ~ 0.75 for the Na-dominant Na-Ca-MX80 bentonite (Fig. 7.4c). The difference in the potential ratio at the start of the Stern layer compression for different bentonites was related to the variation in the surface cation composition and surface charge density.

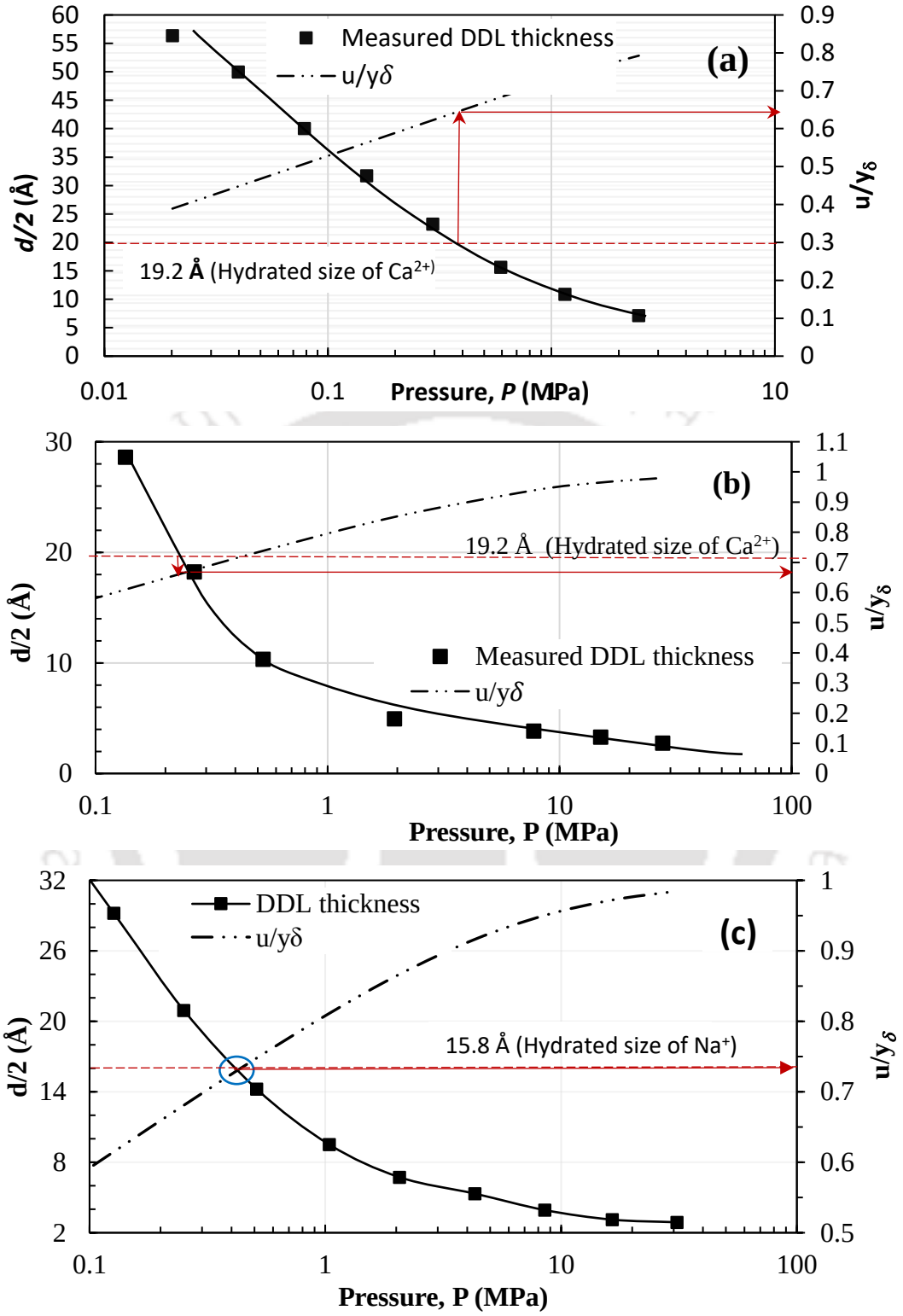

Fig. 7.4 Variation of double-layer thickness with pressure at different degrees of interaction for a) Ponza bentonite, b) Na-Kunigel Bentonite, and c) Na-Ca-MX80 bentonite

Stern layer compression started early for the bentonites containing higher surface charge densities and di-valent cations. Overall, the Stern layer compression begins when the potential ratio was in the range of 0.65-0.75 for different bentonites.

The DDL thickness requires correction at higher pressure through the incorporation of Stern layer compression. An S-curve relation between the Stern layer thickness (δ) and the ratio between the mid-plan and Stern potential was assumed to predict the void ratio, which follows the typical compressibility behavior of clays, as given by

$$\delta = r \exp^{-\left\{a\left(\frac{u}{y_\delta}-R_y\right)\right\}} \quad ; \frac{u}{y_\delta} - R_y > 0 \tag{55}$$

where r is the hydrated radius of cation in Å, R_y is the potential ratio at which Stern layer thickness starts getting compressed, varies in the range of 0.65-0.75, depending on the surface charge characteristics of the clays. The parameter 'a' defines the slope of the curve, which was determined based on the observed minimum achievable thickness of the Stern layer (~2.3 Å) when the potential ratio becomes unity, as given by

$$a = (R_y - 1)\ln\left(\frac{2.3\,\mathring{A}}{r}\right) \tag{56}$$

The above correction for Stern layer thickness was applied in Eq. 6 for total DDL thickness estimation when the potential ratio reaches a specified value at a given pressure. The Stern layer compression was incorporated only to the void ratio computation in Eq. 28. The effect was not considered in the computation of Stern potential and the thickness of the Gouy-layer, as the theoretical formulation for such a complex interaction is not available. A flowchart for the computation of the pressure-void ratio relationship based on the proposed approach was presented in Fig. 7.5.

7.4 Validation of the proposed Stern model

The proposed compressible Stern model was validated on six different bentonites from the literature and the validation results were presented in Fig. 7.6. The predicted compressibility data of these bentonites from the Gouy-Chapman model and the Stern model for constant surface

potential conditions (Tripathy et al., 2014) were also presented along with the proposed model to carry out a comparative analysis. The procedure outlined by Tripathy et al., (2014) was followed in the prediction of compressibility data based on the Stern constant surface potential (SCSP) condition.

Table 7.2 presents the relevant properties of the bentonites used in the prediction of the compressibility data of the bentonites using the three models. The weighted average valence (ν_{avg}) was estimated from the known percentage of individual exchangeable catios of each bentonite and was considered in the prediction by the Gouy-Chapman and the proposed model. The valence was taken as 1 for the Na-dominated bentonites and 2 for the Ca or other divalent cations–dominated bentonites in the SCSP model as considered by Tripathy et al. (2014) in this study.

Table 7.2 Relevant bentonite properties used in the theoretical prediction of compressibility behavior

Soil name	S_a (m^2/g)	**Total C_e** (meq/100g)	**Individual cations**				ν_{avg}	G	δ_0 (Å)
			Na^+	Ca^{2+}	Mg^{2+}	K^+			
MX80 bentonite	676	90.31	51.24	28.24	9.43	1.28	1.42	2.76	9.6
Na-Ca MX80 bentonite[a]	700	68	60	5	3	-	1.12	2.65	7.9
Na-Kunigel[a]	687	73.2	40.5	28.7	3	0.9	1.45	2.79	9.6
Bisaccia bentonite[b]	190	85*	-	-	-	-	1.42	2.78	9.6
Ponza[b]	500	85	14	22	46	-	1.76	2.77	9.6
Mexico Montmorillonite[c]	734	114	92	1	-	1	1	2.7	7.9

[a]Marcial et al. (2002), [b]Di Maio (2002), [c]Low (1980), *assumed

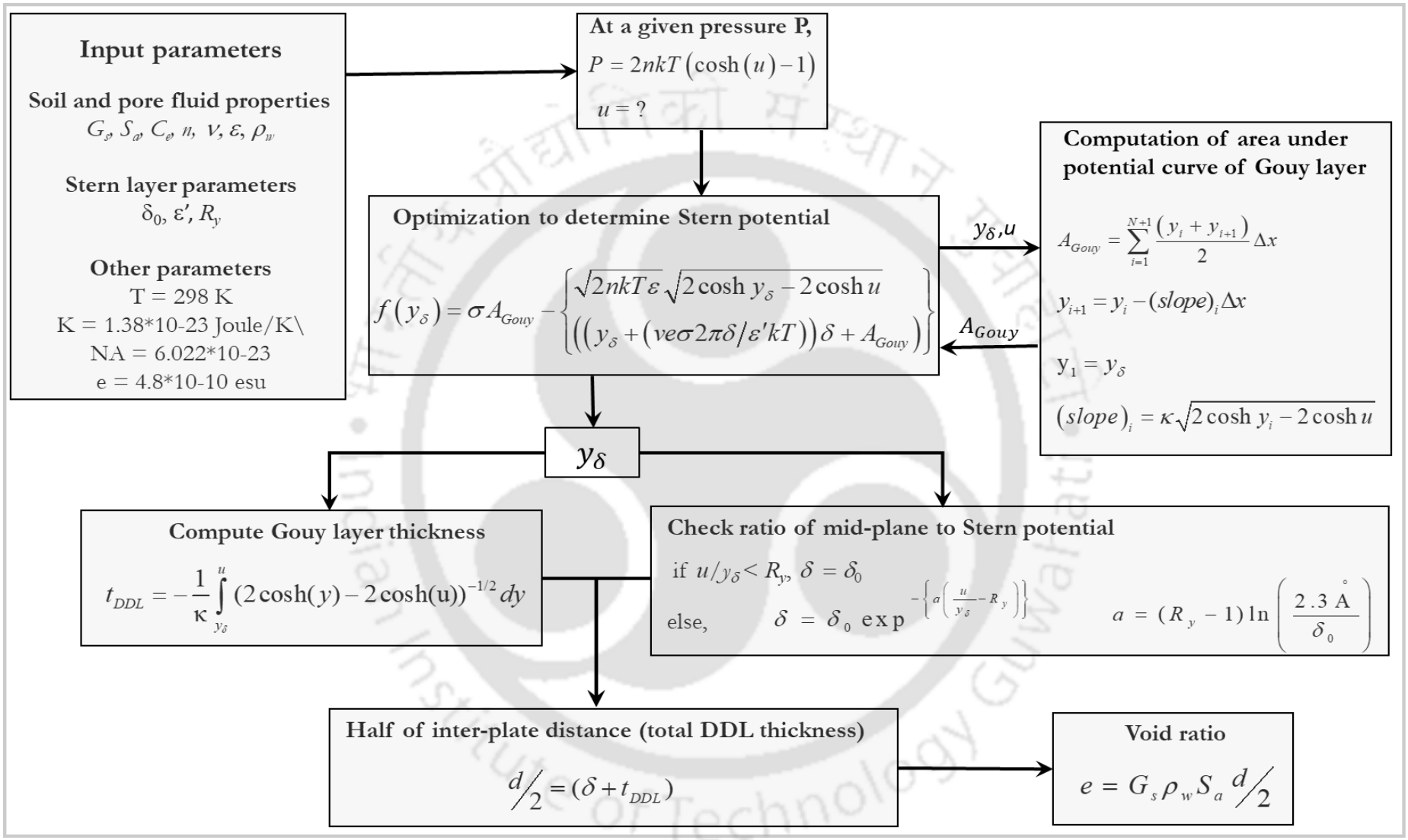

Fig. 7.5 Flow chart showing the computation of void ratio at a given pressure using the proposed Stern model

The initial Stern layer thickness (δ_0) at zero pressure was considered to be equivalent to the hydrated radius Na^+ cation for the Na-dominated Na-Ca-MX80 bentonite and Mexico montmorillonite in the proposed model. For the other bentonites, which have either mixed-valence or divalent-dominated surface cations, the hydrated radius of Ca^{2+} cation was taken as the Stern layer thickness, being the largest among the available exchangeable cations. The stern layer compression was applied when the potential ratio (u/y_δ) reached a specified value (R_y) for the given bentonite. However, a fixed value of 5 Å was used in the SCSP model as the Stern thickness for all the bentonites. The pore fluid parameters and other relevant parameters used in the three models were presented in Table 7.3. The cationic concentration was taken as 0.0001 N to represent water as pore fluid for all three models. The dielectric constant of water (ε') within the Stern layer was taken as 6 for all the bentonites in the proposed and SCSP models.

Fig. 7.6a presents the measured and predicted compressibility data of Na-Ca MX80 bentonite by the three models. A value of 1.12 was used for ν_{avg} in the proposed and Gouy-Chapman models for this Na-dominated bentonite, while a unit valence was considered in the prediction based on the SCSP model. The initial Stern layer thickness was taken as equivalent to the hydrated radius of Na^+ cation in the proposed model. The stern layer compression was imposed through Eq. 23 once the potential ratio reached the value of 0.75, as was observed for this bentonite in Fig. 7.4c. The proposed model showed a noticeable improvement over the two existing models and was in very good agreement with the measured data in the pressure range of 0.1 MPa – 40 MPa. The SCSP model was considerably away from the proposed model and the measured data at lower pressures (0.1MPa -1 MPa). The SCSP model was found to be close to the measured data only in the pressure range of 2MPa – 5 MPa. Further, the prediction by the SCSP model is limited to a maximum pressure of 5 MPa for this bentonite, as reported by Tripathy et al. (2014). The predicted void ratios by the Gouy-Chapman model were slightly higher than the proposed model at lower pressures (0.1 MPa - 4 MPa) but predicted much smaller void ratios at > 4 MPa. Also, the model deviated from the proposed model and the measured data significantly.

The prediction based on the three models and the measured data of Na-Kunigel bentonite was presented in Fig. 7.6b. The prediction by the proposed and Gouy-Chapman model was carried out by considering the ν_{avg} (~1.45) for this mixed-valence bentonite. The δ_0 was taken as 9.6 Å, which is equivalent to the hydrated radius of the largest among the available exchangeable cations (Ca^{2+})

for this bentonite. The stern layer compression was considered for the potential ratio of ≥ 0.65 (as observed in Fig. 7.4b). The SCSP model showed a good agreement with the measured data in the pressure range of 0.1 MPa - 0.5 MPa. At higher pressure, however, the compressibility prediction was very poor as the model deviated completely from the measured data. The Gouy-Chapman model over-predicted the void ratio at lower pressures up to a maximum pressure of 2 MPa. At higher pressures, however, the Gouy-Chapman model predicted smaller void ratios than the measured data. The proposed model showed a relatively better agreement with the measured data at the lower pressure range in comparison to the Gouy-Chapman model although the predicted void ratios were slightly higher than the measured data in this pressure range. At higher pressures, the proposed model showed a very good agreement with the measured void ratio for this bentonite.

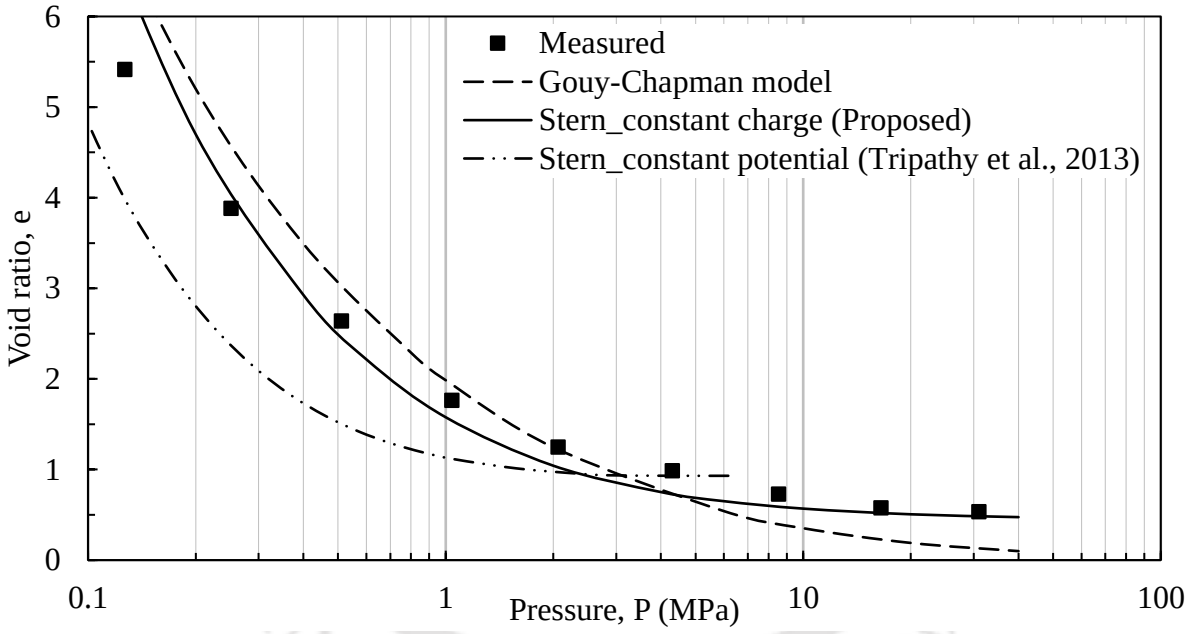

Fig. 7.6a Theoretically predicted and measured pressure-void ratio data of Na-Ca MX80 bentonite (Marcial et al., 2002)

The ν_{avg} was taken as 1.42 in the prediction of compressibility behavior of MX80 bentonite by the Gouy-Chapman and the proposed model and δ_0 was taken as 9.6 Å for the proposed model. The predicted void ratios by the proposed and Gouy-Chapman model were in close agreement for MX-80 bentonite. The proposed model showed a slight improvement at both lower and higher pressure ranges (Fig. 7.6c). The SCSP model showed very pore agreement with the measured data and the other two models. The proposed model, overall was in good agreement with the measured data in the pressure range of 0.2 MPa - 3.2 MPa, for this bentonite.

Table 7.3 Parameters used in the prediction of compressibility behavior of the considered bentonites by the three models

Parameters	Value		
	GC	**Stern constant potential**	**proposed**
Cationic concentration, n (N)	0.0001	0.0001	0.0001
Valence, ν	$^{*}\nu_{avg}$	$^{\#}$1 or 2	$^{*}\nu_{avg}$
Dielectric constant of water	80.4	80.4	80.4
Stern thickness, δ (Å)	N/A	5	$^{\$}\delta_0$
Dielectric constant of Stern pore fluid, ε'	N/A	6	6
Surface potential, ϕ_0 (mV)	N/A	274	N/A
Normalized surface potential, y_0	N/A	10.66	N/A
Specific adsorption potential, ψ	N/A	0	N/A
Number of adsorption spot, N_1 (ions/m^2)	N/A	$^{\&}4.10^{-17}$	N/A
Density of water, ρ_w (Mg/m^3)	1	1	1
Molecular weight of solvent (water), M (Mg/mol)	N/A	18	N/A
T (K)	298	298	298

*weighted average valence (see Table 7.2), $^{\#}$1 for Na-d0minated and 2 for di-valence dominated, $^{\$}$initial Stern layer thickness at zero pressure (see table 2), $^{\&}$for Na^+.

The Ponza bentonite, which is dominated by Mg^{2+} and Ca^{2+} ions, was considered for the validation of the proposed model and comparison of other models. The ν_{avg} for this bentonite was taken as 1.76 in the Gouy-Chapman and the proposed models and δ_0 was taken as 9.6 Å in the proposed model. The prediction by the SCSP was in very poor agreement with the measured data (Fig. 7.6d). The Gouy-Chapman and the proposed model were found in close agreement with the measured

data. Overall, the proposed model provided an improved prediction over the two existing models for this bentonite as well.

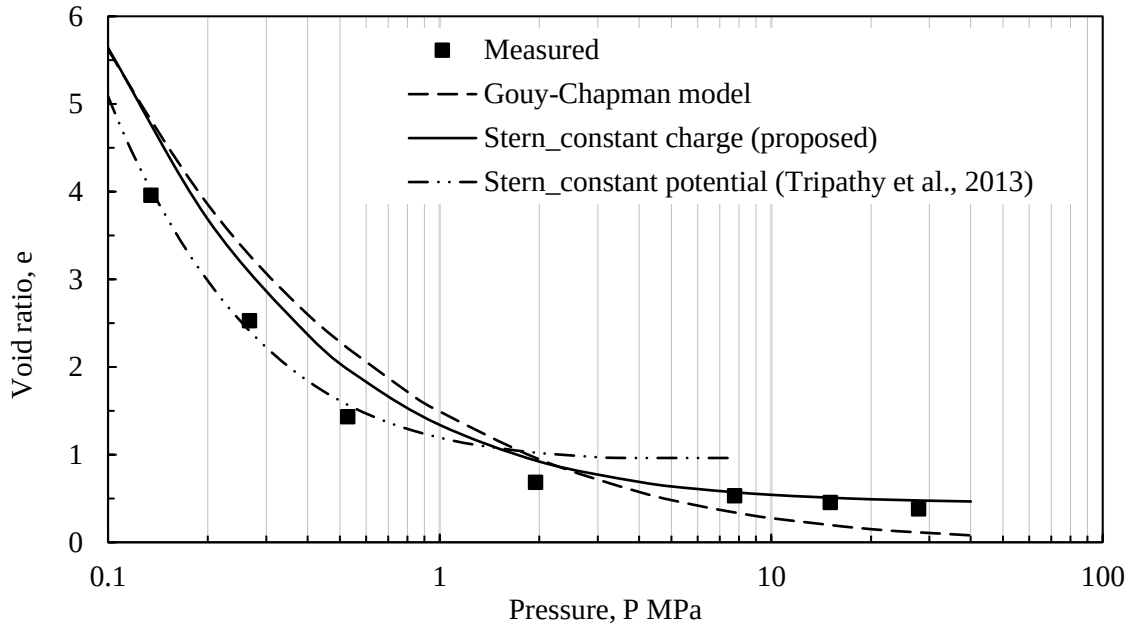

Fig. 7.6b Theoretically predicted and measured pressure-void ratio data of Na-Kunigel bentonite (Marcial et al., 2002)

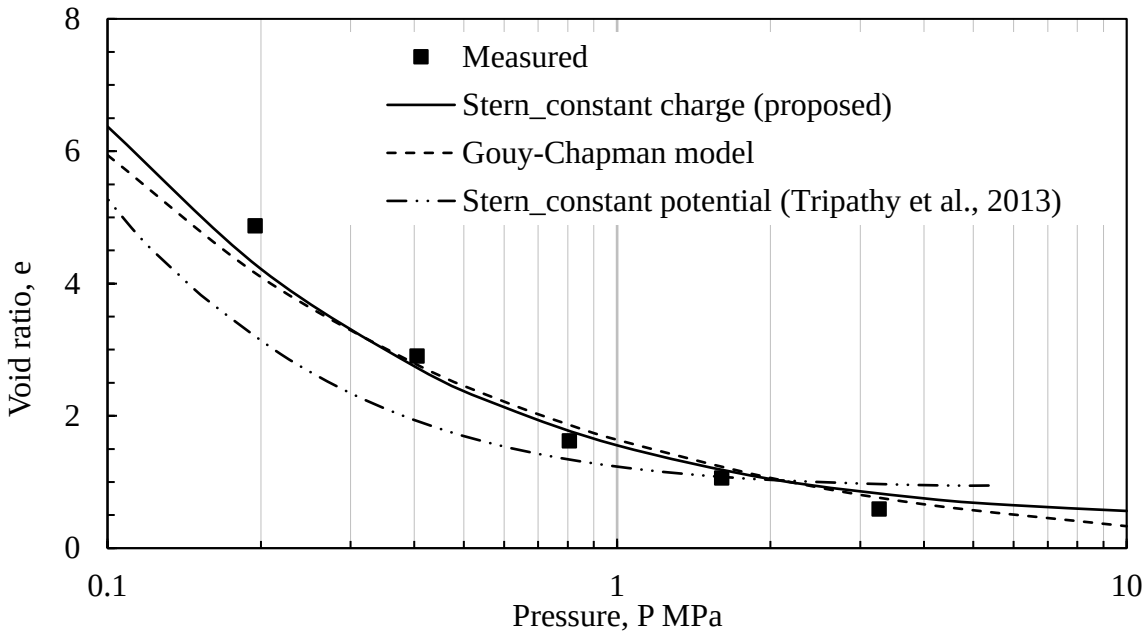

Fig. 7.6c Theoretically predicted and measured pressure-void ratio data of MX-80 bentonite (Tripathy et al., 2014)

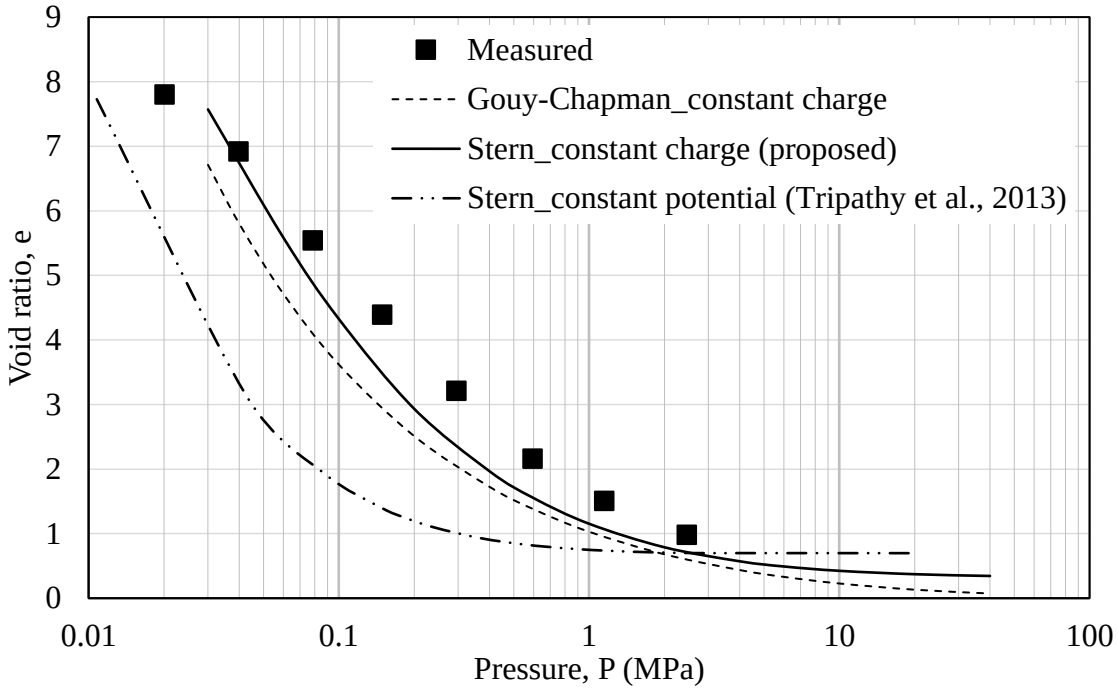

Fig. 7.6d Theoretically predicted and measured pressure-void ratio data of Ponza bentonite (Di Maio, 2011)

For the Bissaccia bentonite, the value of ν_{avg} and δ_0 were taken as 1.42 and 9.6 Å, respectively. In the Stern constant potential condition, valence was taken as 1. The two existing models were in poor agreement with the measured data for this bentonite (Fig. 7.6e). The proposed model overpredicted at the lower pressure range (0.01MPa - 0.1 MPa), however, showed very good agreement at higher pressures. The observed discrepancies observed at the lower pressures were attributed to the dominant presence of edge-face clay particle orientation as the theory is based on the assumption of parallel arrangement of the clay platelets.

In the case of Mexico montmorillonite, which is a Na-homo-ionized soil, unit valence was considered in the prediction by all three models. The value δ_0 was taken as 7.9 Å in the proposed model. The proposed model and the Gouy-Chapman model were relatively closer to each other for this soil, while the Stern model for the constant potential condition was considerably away (Fig. 7.6f). The proposed model showed an overall improved agreement with the measured data for this bentonite as well. The predicted void ratios by the proposed model were, however, slightly smaller than the measured data at all the pressures for this bentonite, which was attributed to the possible underestimation in the surface area determination (Das and Bharat, 2021).

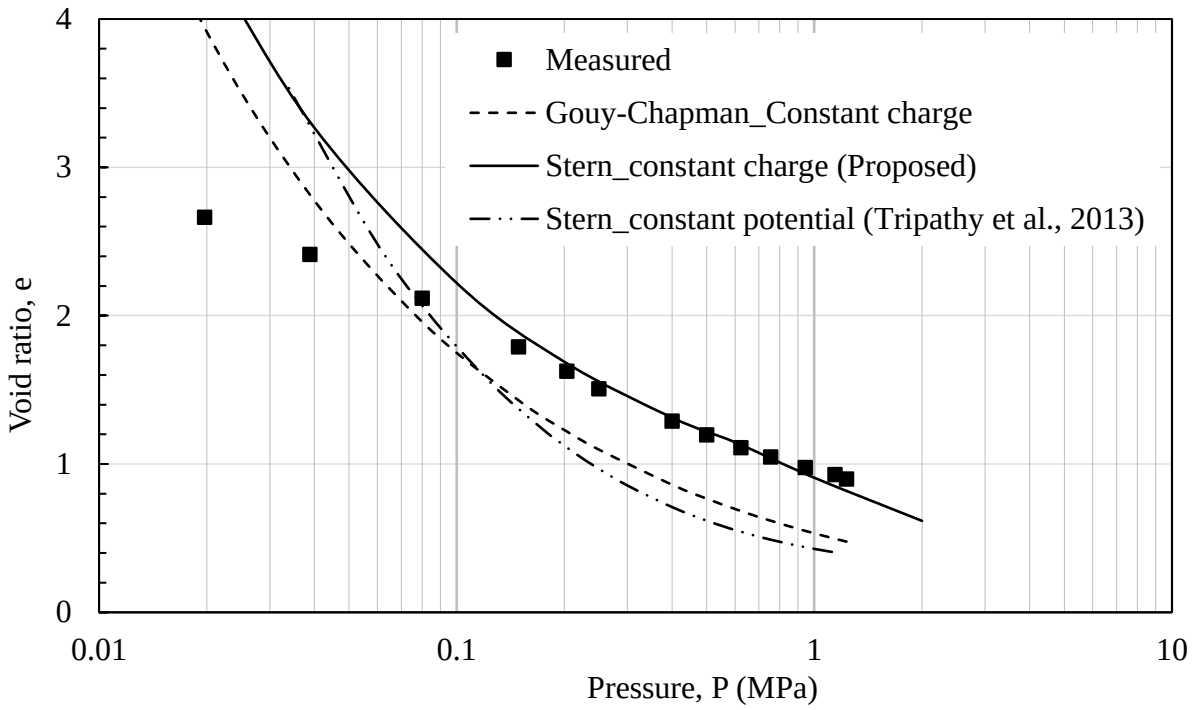

Fig. 7.6e Theoretically predicted and measured pressure-void ratio data of Bissaccia bentonite (Di Maio, 2011)

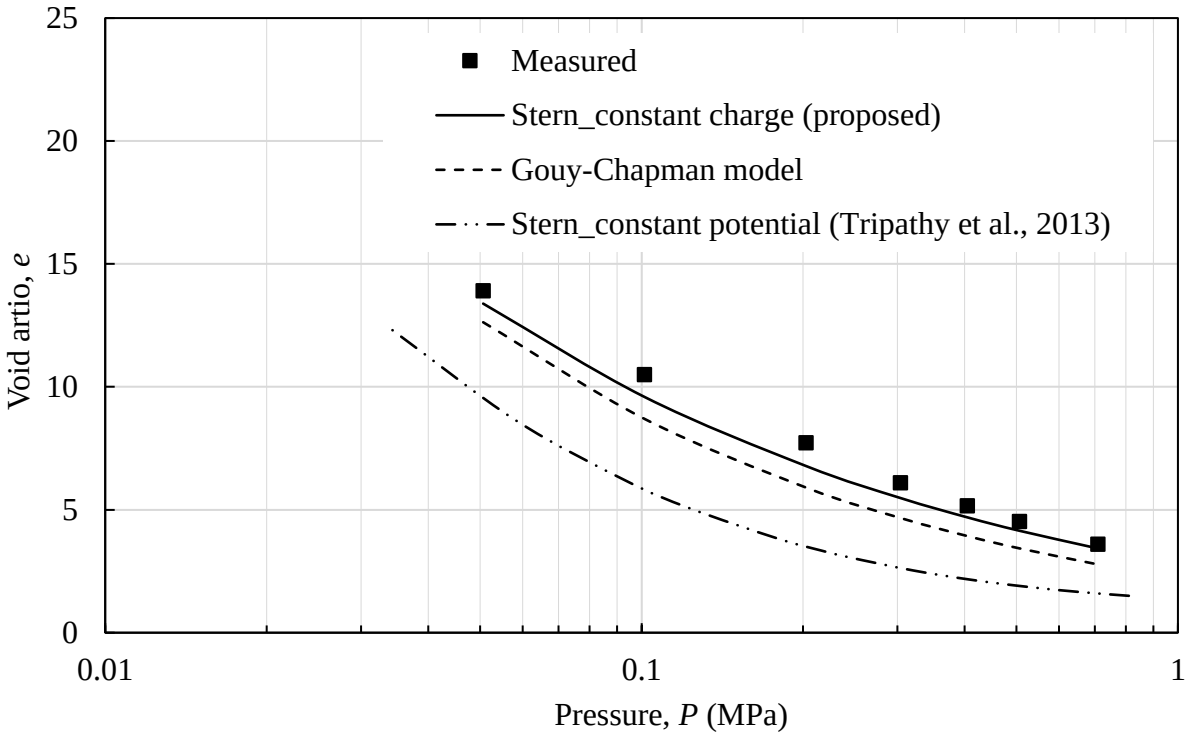

Fig. 7.6f Theoretically predicted and measured pressure-void ratio data of Mexico Montmorillonite (Low 1980)

Overall, the proposed model provided an improved prediction of the compressibility data especially, in the higher pressure range for all the six studied bentonites. The SCSP model either underpredicted or overpredicted the compressibility data in the lower pressure range. The model was found to agree with the measured data of Na-Kunigel bentonite for a very narrow pressure range. The model, overall, was not able to capture the shape of the compressibility curve in the given pressure range for the considered bentonites. This was mainly attributed to the assumed constant surface potential condition, which is not applicable for the clays. On the other hand, the Gouy-Chapman model predicted much smaller void ratios than the measured data at high pressures. As the ions are treated as point charges in the Gouy-Chapman model, the whole of the DDL thickness can be theoretically compressed with the application of mechanical pressure. Thus, the predicted void ratios tend to approach zero at high pressures which is quite unrealistic. The presence of the Stern layer in the Stern model eliminated this issue and provided an improved prediction at higher pressures. While the Gouy layer was completely compressed at high pressure, the presence of a relatively rigid Stern layer resulted in a higher void ratio in the prediction by the proposed model when compared to the Gouy-Chapman model. At low pressures, however, the Gouy layer thickness is much larger than the Stern layer thickness. Thus, the Gouy layer primarily determines the separation distance, consequently, the void ratio and the Stern layer thickness becomes insignificant. The accumulation of cations within the narrow Stern layer, however, affected the charge distribution in the Gouy layer and the potential distribution in the interacting clay-water system. The Gouy layer thickness at a given pressure or degree of interaction was, therefore, different in the proposed and Gouy-Chapman model. Thus, the two models predicted different void ratios at a given pressure in the lower pressure range as well. The predicted void ratios by the proposed model at low pressures showed a better agreement with the measured data of all the bentonites considered in this study.

7.5 Summary

A theoretical model was proposed to predict the compressibility behavior of clays over a wide pressure range by considering the finite size of the cation in the diffuse double layer. The Stern model for the diffuse double layer was utilized to capture the effect of cation size on the electrostatic potential distribution in an interacting clay-water system. Electrostatic potential distribution in an interacting clay-water-electrolyte system was established for the first time using

the Stern model at constant charge conditions. The ratio of mid-plan potential to the Stern potential is a unique parameter representing the degree of interaction between the DDLs of two interacting clay platelets. The potential ratio increased as the void ratio decreased with an increase in the applied pressure and reached the maximum value of 1 on achieving the complete consolidation. Further, the compressibility of the Stern layer at very high pressure was brought out based on the measured data of bentonites from the available literature. The surface cations penetrate the siloxane cavities available on the clay surface at high pressure causing the reduction in the Stern layer thickness. The Stern layer compression was triggered when the potential ratio was in the range of 0.65-0.75, which was observed at a pressure value of about 0.4 MPa, for different bentonites. Beyond the specified potential ratio, the Stern layer compression was incorporated in the prediction of the compressibility behavior. The incorporation of cation size and the compression of Stern layer thickness provided significant improvements over the two existing models. The predicted compressibility data by the proposed model showed a very good agreement with the measured data of six different bentonites considered in this study.

8 Swelling pressure of compacted bentonites

8.1 General

Swelling pressure evolution characteristics of compacted bentonites and bentonite-sand composites under the isochoric condition were studied at various initial compaction densities with different inundating fluids. The swelling pressure evolution curves (SPECs) at three different compaction densities with water as inundating fluid were presented in the first part of this chapter. A microstructural investigation was carried out to understand the two distinct SPEC behaviors that were identified based on the SPECs of the studied bentonites and bentonites from literature at various compaction densities. The microstructures of the compacted bentonite specimens were evaluated at different stages on the SPECs and presented next. The underlying mechanisms responsible for the two distinct SPEC behaviors were brought out based on the intruded volume of various pore-size classes at different stages on the SPECs. Two critical pore-size parameters were then introduced to identify the SPEC behavior with different plasticity and compaction densities. Further, the influence of non-clay content on the development of different macro-size pore classes was brought out and direct influence on the SPEC development was presented based on the present study and literature bentonites.

8.2 Swelling pressure evolution curves (SPECs)

The SPECs of the studied bentonites at various compaction densities with water as the inundating fluid have been established by Choudhury (2019). In this study, a detailed microstructural analysis was carried out to bring out the underlying mechanisms behind the variable SPECs under the influence of compaction densities and bentonite plasticities. The SPECs at three different densities were reproduced in this study and discussed in this section before presenting the SPECs of the bentonites in the presence of different electrolytes solutions. The SPECs of the bentonite-sand mixtures at different densities are discussed next.

8.2.1 SPECs in presence of water

The observed SPEC for B2 and B3 bentonites at different initial compaction densities were presented in Fig. 8.1–8.2. Temporal changes in swelling pressure of B2 bentonite with different compaction densities, varying between 1.45 – 2.0 Mg/m^3, were separately presented in Fig. 8.1a – 8.1b to clearly represent different evolution characteristics with compaction density. The swelling

pressure continuously increased up to 6 *h* to reach the first peak for specimens compacted at 1.45 Mg/m^3 (Fig. 8.1a). The swelling pressure decreased with time for a sufficiently long time after attaining the first peak of swelling pressure, indicating an alteration in the pore geometry under constant volume conditions. The decrease in the swelling pressure was ~14% of the pressure value at the first peak. The swelling pressure increased temporally with further water uptake after the swelling pressure reduction until attaining the equilibrium pressure at full saturation. The difference between the first peak and the asymptote, at equilibrium, on the swelling pressure plot was insignificant. The swelling pressure at higher compaction densities (Fig. 8.1b), similarly, increased continuously with inundation time and reached a meta-equilibrium state with a plateau before the increase in the swelling pressure to a final maximum value. The swelling pressure increased with further water uptake after 0.5 – 6 *d* of meta-equilibrium state to reach a final equilibrium value. The temporal behavior of swelling pressure for these densities thus followed a monotonic behavior. The SPECs were qualitatively similar at higher compaction densities albeit the equilibrium swelling pressure significantly varied with the initial compaction density. The final equilibrium swelling pressure was related to the applied mechanical pressure (yield stress) in compacting the air-dried bentonite specimens at a given density. A minimum final swelling pressure value of 0.56 MPa was recorded at the lowest density (1.45 Mg/m) among the three, where the yield stress was minimum (9.5 MPa). The final swelling pressure value increased to 2.1 MPa at 1.8 Mg/m with a yield stress of 30.5 MPa. At 2 Mg/m, where the yield stress is as high as 51 MPa, a much higher swelling pressure of 7.7 MPa compared to the other two densities was recorded. Overall, the final equilibrium swelling pressure showed an exponential relationship with the compaction density similar to the yield stress. Further increase in the swelling pressure rate of B2 at different compaction densities was nearly the same during the initial water uptake but deviated significantly after 10 minutes of inundation.

The SPECs of B3 bentonite at different compaction densities were shown in Fig. 8.2a – 8.2b. The B3 bentonite exhibited a very marginal swelling pressure reduction (~0.5%) at ρ_d = 1.45 Mg/m^3, unlike the B2 bentonite. At the higher compaction densities (i.e., ρ_d = 1.8, & 2 Mg/m^3), the temporal evolution of the swelling pressure for B3 bentonite was qualitatively similar to the corresponding densities of B2 bentonite. However, the magnitude of swelling pressure was significantly higher for B3 compared to B2, even at the same compaction density, due to the

presence of higher clay and montmorillonite content (Table 4.6). Overall, the SPEC behavior of B3 bentonite at all the compaction densities was monotonic.

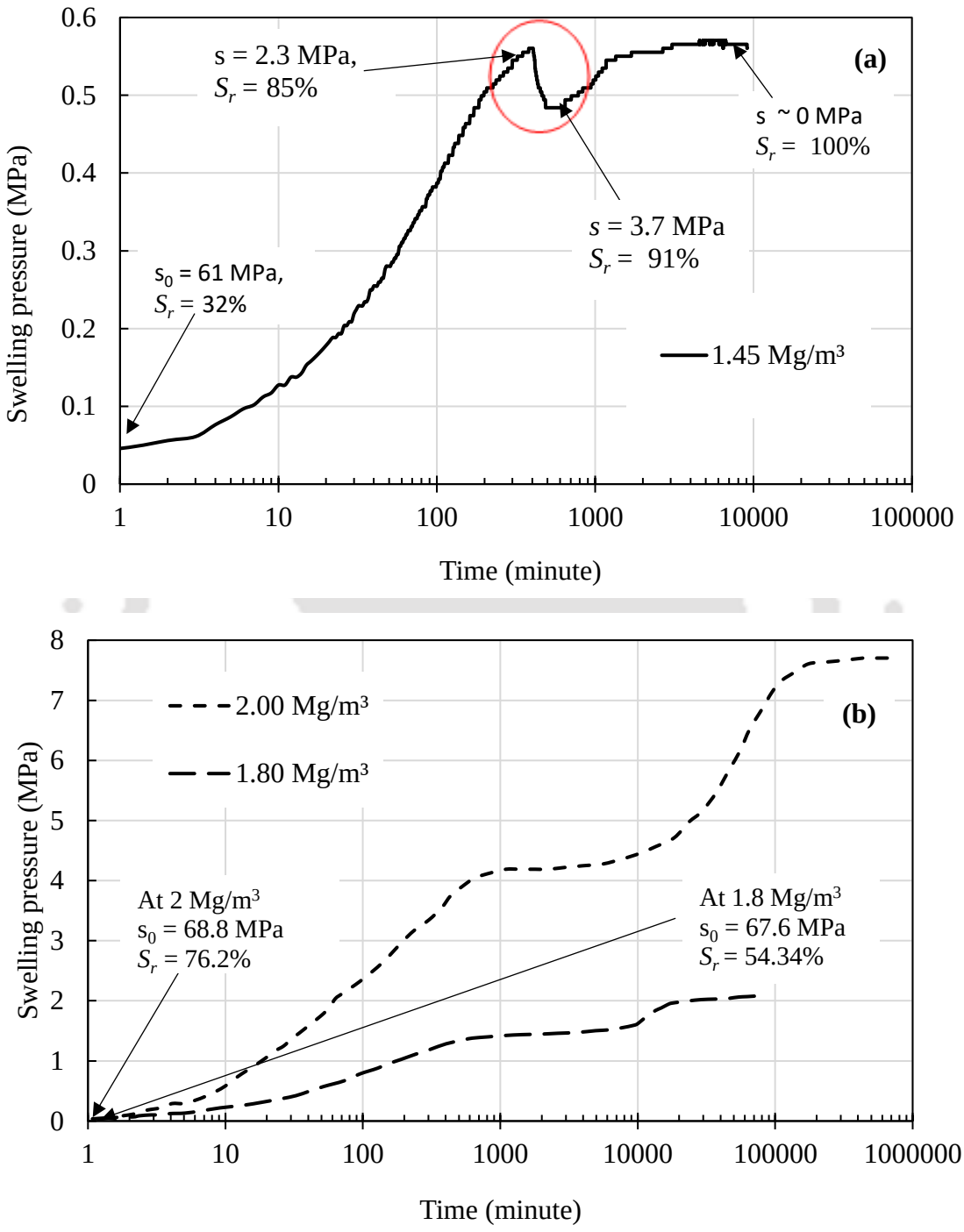

Fig. 8.1 Temporal variation of swelling pressure for B2 at initial dry densities of (a) 1.45 Mg/m^3 (b) 1.8 Mg/m^3, 2 Mg/m^3 (After Choudhury, 2019)

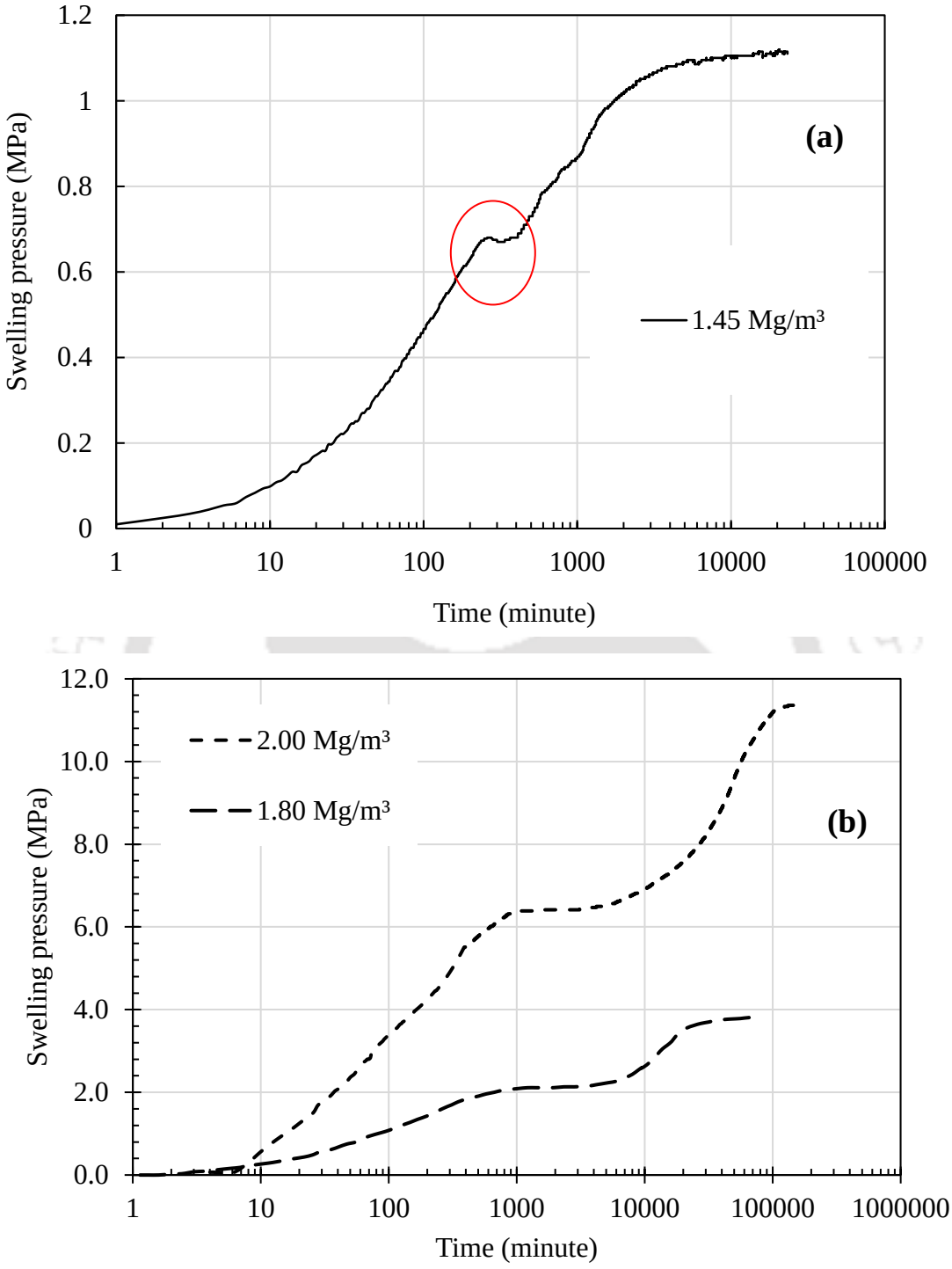

Fig. 8.2 Temporal variation of swelling pressure for B3 at initial dry densities of (a) 1.45 Mg/m^3, and (b) 1.8 Mg/m^3 & 2 Mg/m^3 (After Choudhury, 2019)

In summary, the B2 bentonite at lower compaction density (ρ_d = 1.45 Mg/m^3) exhibited a bimodal behavior similar to the literature studies on FoCa clay at all compaction densities (Imbert & Villar, 2006) and German bentonite at higher compaction density (Schanz & Tripathy, 2009). The monotonously increasing SPEC with an intermediate plateau behavior exhibited by the B2 bentonite at higher compaction densities or B3 bentonite at all the studied densities was similar to the GMZ and German bentonites (Schanz and Tripathy 2009, Chen et al. 2018, He et al. 2019). Thus the temporal evolution of swelling pressure of bentonites exhibited either a bimodal or monotonously increasing behavior depending on the bentonite quality and initial compaction density. The influence of compaction density and bentonite plasticity on the SPEC during the water uptake was studied through the microstructural evolution in the following section.

8.2.2 SPECs in presence of strong electrolyte solutions

Fig. 8.3 presents the SPECs of B3 bentonite in the presence of water and three different strong electrolytes viz., 1M NaCl, 1M KCl, and 1M LiCl at a dry density of 1.45 Mg/m^3. As described earlier, the SPEC in presence of water was monotonously increasing with an intermediate plateau for a duration of ~2 hrs. In the presence of 1M NaCl, swelling pressure developed at a much slower rate compared to water. The swelling pressure increased continuously with time to reach a final swelling pressure of 0.485 MPa without any intermediate plateau or drop. The SPEC in the presence of 1M LiCl showed a similar pattern, however, the swelling pressure development rate was relatively slower than NaCl. The swelling pressure at a given time was initially higher in the presence of 1M NaCl as compared to 1M LiCl up to 300 hrs from the time of inundation. Swelling pressure in the presence of 1M NaCl already reached its maximum value by this time, while it was still increasing in the presence of 1M LiCl and reached a final swelling pressure of 0.57 MPa after ~1000 hrs from the time of inundation. The SPEC in the presence of 1M KCl exhibited a unique trend. Swelling pressure development during the initial stage was at a much faster rate in 1M KCl as compared to the other solutions and water. The swelling pressure rapidly increased to a maximum value of 0.38 MPa at ~6 hrs from the time of inundation and started decreasing gradually thereafter. The final swelling pressure was recorded as 0.23 MPa after ~1000 hrs from inundation.

Overall, the SPECs of B3 bentonite in the presence of different inundating fluids were distinctly different. While the SPEC in presence of water exhibited an intermediate plateau, a monotonous SPEC was observed in the presence of 1M NaCl and LiCl. The SPEC in presence of 1M KCl, on

the other hand, exhibited a unimodal SPEC with an intermediate peak. Strong cationic concentration in the inundating fluid significantly influenced the water uptake process and thus affected the swelling pressure development. Additionally, the type of cations significantly influenced the bentonite-water interaction and the DDL formation around the clay particles which affected the swelling pressure development rate and the final swelling pressure. The final swelling pressure decreased considerably in the presence of the strong electrolytes as compared to water. Among the three electrolytes, the final swelling pressure was maximum in the presence of 1M LiCl, followed by 1M NaCl and then 1M KCl. This was attributed to the different hydrated sizes of the cations. The swelling pressure magnitude is directly related to the diffuse double thickness which is influenced by the hydrated size of the cations. The hydrated size of the cations are in the increasing order from K^+ to Na^+ to Li^+ , and hence the swelling pressure magnitude followed the same order. The decrease in the overall swelling pressure after reaching the peak in the case of 1M KCl could be due to the K^+–fixation onto the interlamellar surfaces of montmorillonite which reduces the swelling ability.

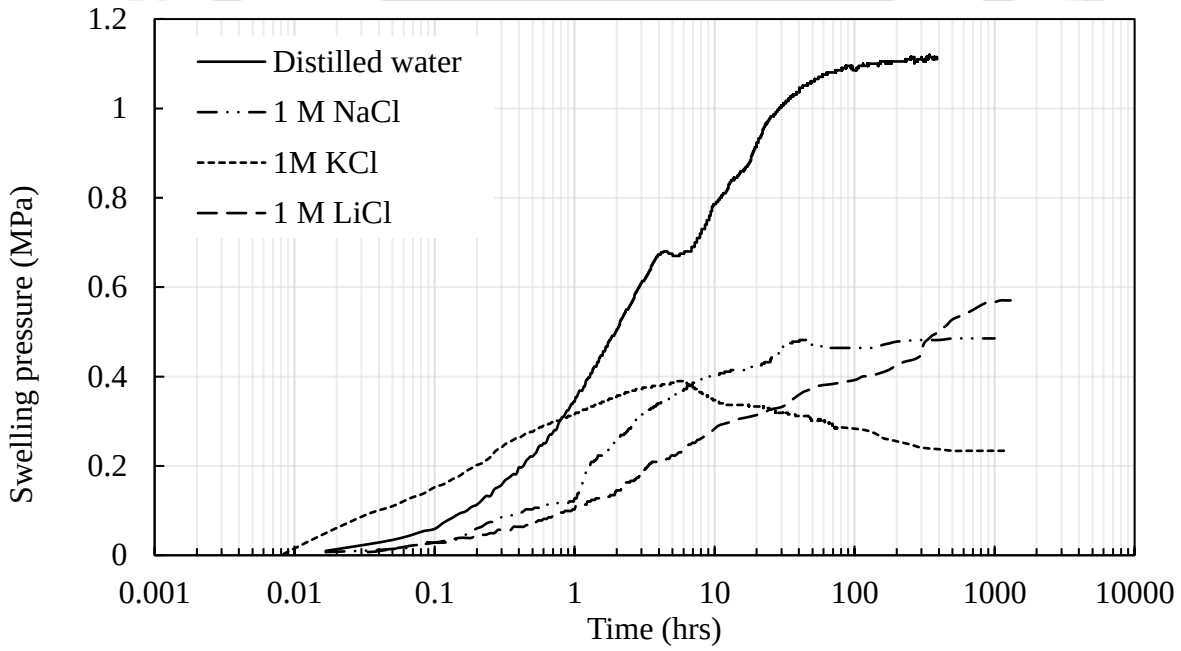

Fig. 8.3 Temporal variation of swelling pressure for B3 at an initial dry density of 1.45 Mg/m^3 saturated with different pore fluids.

Fig. 8.4 presents the SPECs of B3 bentonite in the presence of two alkaline solutions, 1M KOH, and 0.1 M KOH. The swelling pressure increased at a slower rate in the presence of the weaker electrolyte than the stronger electrolyte solution. The SPEC in the presence of 1M KOH was

similar to that with 1M KCl, however, the swelling pressure depleted to a much smaller value (~0.03 MPa). The swelling pressure depletion was more in the presence of the alkaline environment (KOH) than the salt solution (KCl) due to superior K-fixation in the favorable alkaline environment. In the presence of a weaker solution (0.1M KOH), however, a bimodal SPEC was observed with an intermediate swelling pressure drop. The first peak (~0.27 MPa) was achieved after 16 hours from the time of inundation. The reduction in the swelling pressure after the first peak was 8.75% of the first peak value before reaching a final swelling pressure of 0.374 MPa.

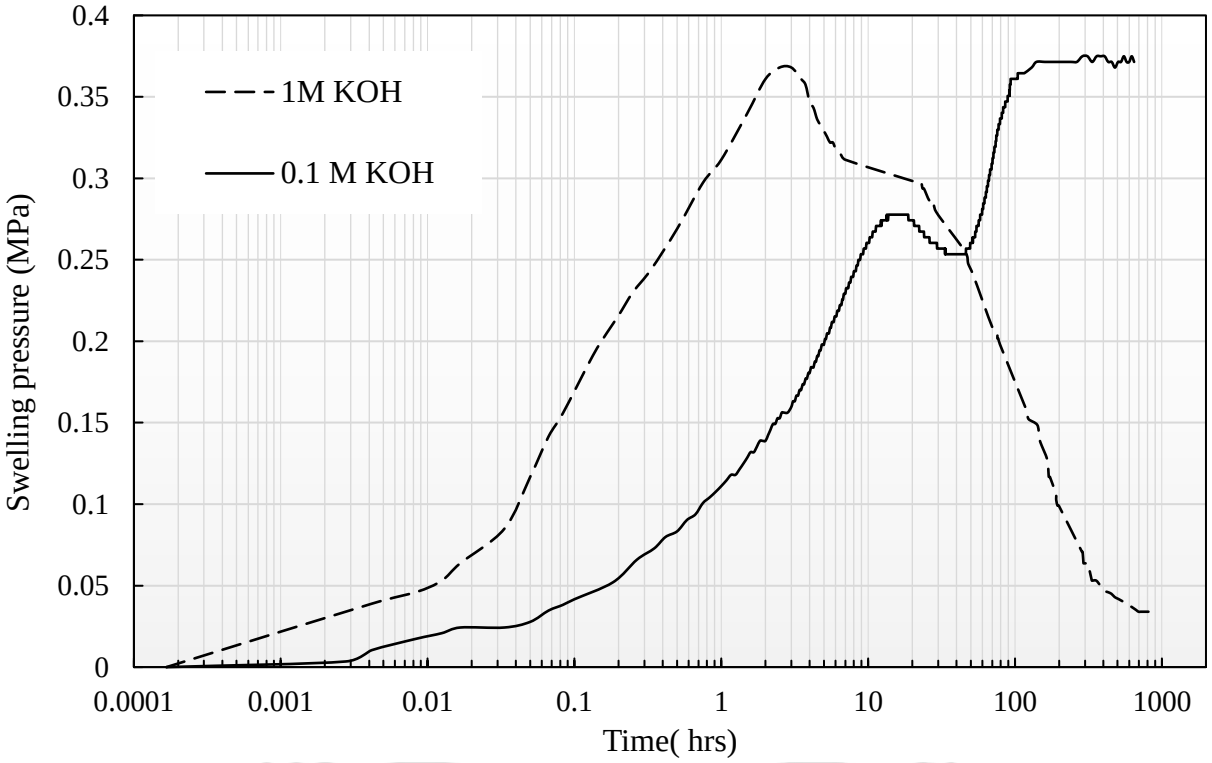

Fig. 8.4 Temporal variation of swelling pressure for B3 at an initial dry density of 1.45 Mg/m^3 saturated with KOH solutions.

8.2.3 SPECs of bentonite-sand mixtures

The SPECs of B3 bentonite-sand mixtures with four different mixing proportions were obtained in the presence of water at a compaction density of 1.45 Mg/m^3 and presented in Fig. 8.5. The SPEC of B3 bentonite at this compaction density was monotonously increasing with an intermediate plateau (Fig. 8.2a). The bentonite-sand mixtures, however, exhibited the bimodal SPEC at all the mixing proportions considered in the study. The BS-10 exhibited the first peak (~25 MPa) after ~ 12.16 hrs from inundation, followed by a sharp decrease to a value of ~0.22

MPa at 25.92 hrs. The swelling pressure then increased monotonously to a final swelling pressure of ~0.35 MPa. The overall trend was similar for the other mixtures, however, the initial rate of swelling pressure development was significantly different. The initial swelling pressure developed at a faster rate for BS-20 and BS-30 as compared to BS-10 and BS-40. The swelling pressure rate significantly increased for BS-10 after 0.2 hrs from the inundation. Further, the magnitude and the rate of intermediate swelling pressure drop were reduced with an increase in the sand percentage of the bentonite-sand mixtures. For BS-40, the swelling pressure drop was marginal and it exhibited an intermediate plateau on the SPEC.

Overall, the addition of sand to B3 bentonite transformed the monotonous SPEC to the bimodal SPEC behavior. An increase in the sand content decreased the final swelling pressure and magnitude in the swelling pressure drop. With further increase in the sand content, however, the SPEC tends to exhibit the intermediate plateau behavior.

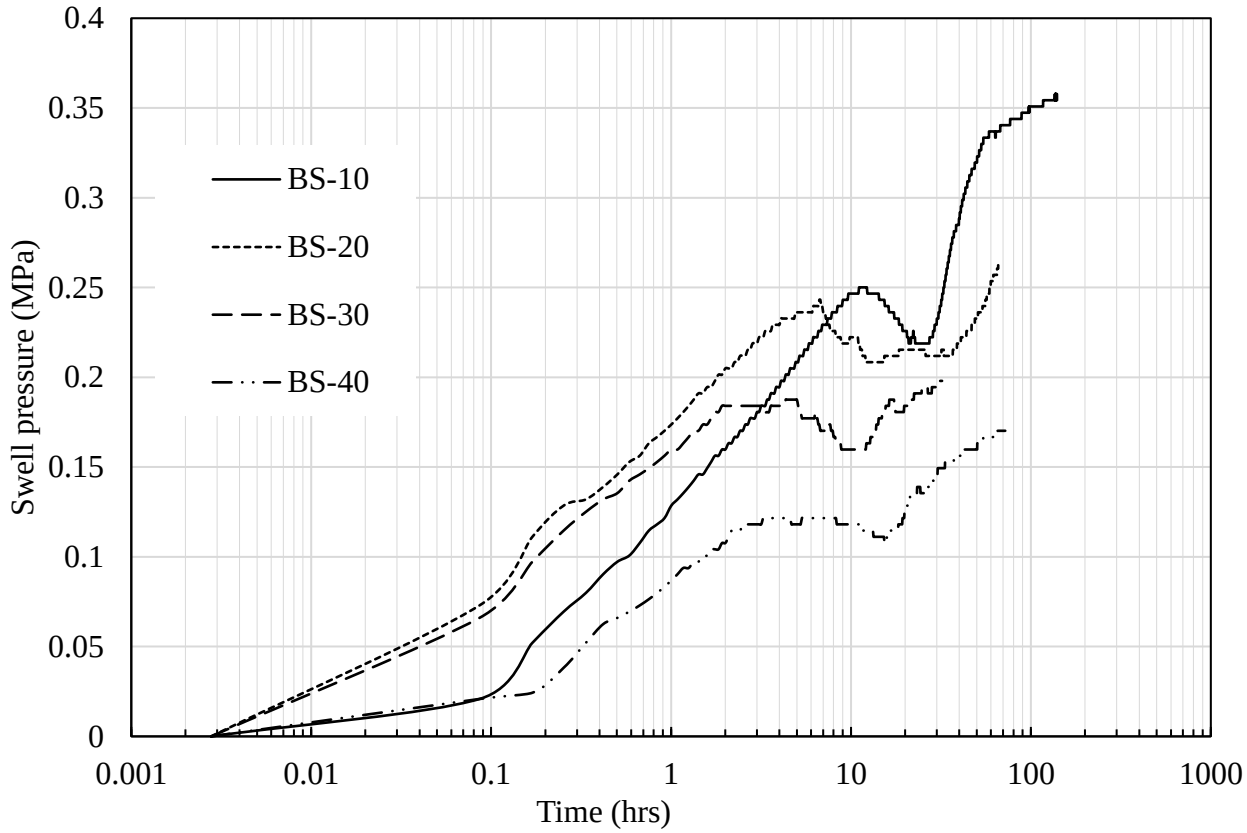

Fig. 8.5 SPEC behavior of different bentonite (B3) -sand mixtures at the compaction density of 1.45 Mg/m^3.

8.3 Microstructural analysis of SPECs

Two distinct SPEC behaviors through different stages of swelling pressure development commonly observed for bentonites at different compaction densities were summarized through illustrations in Fig. 8.6a – 8.6b. The increase in the swelling pressure due to initial water uptake was depicted by *OP* (Fig. 8.6a) or *O'P'* (Fig. 8.6b), followed by either decrease in the swelling pressure or no change (or marginal decrease) in swelling pressure with time using *PQ* or *P'Q'*, and immediately followed by a relatively slower rate of swelling pressure development until the equilibrium value as shown by *QR* or *Q'R'*.

The MIP test data were presented in terms of differential intrusion volume (dv/dlogD) vs pore size (D). Further, the available pore size range from the MIP study was divided into eight distinct pore-size classes and the pore volume contribution of each size class was analyzed for more detailed interpretation on various pore-size interactions during the hydration and the corresponding influence on the swelling pressure development.

8.3.1 As-Compacted State

The variation in differential specific mercury intrusion volume with pore size was presented for the *as-compacted* specimens of B2 and B3 for two compaction densities in Fig. 8.7. The differential mercury intrusion volume data for both the bentonites, at a given density, were qualitatively similar. The PSD curve, however, shifted towards the finer size (leftward) in case of higher plasticity bentonite. The PSD of B2 bentonite at ρ_d = 1.45 Mg/m^3 exhibited more like a bimodal behavior with a primary broad peak in the size range of 1 – 20 μm and minor peaks around 0.02 μm size (Fig. 8.7). The B3 bentonite, at the same density, exhibited a distinct bimodal pattern with a narrow sharp peak at 0.009 μm size and a broad peak in the size range of 1-20μm. As the density increased further to 1.8 Mg/m^3 for both the bentonites, the peaks were reduced and the PSD curve exhibited a uniform distribution without the pore size larger than 10μm.

The estimated porosity derived from the intruded pore volumes for different studied cases was represented by a bar diagram using eight different pore-size classes (Fig. 8.8). The contribution of different pore-size classes to the total porosity was clearly brought out in this bar diagram. The structure of critical pore size classes was, further, characterized by the FESEM images (Fig. 8.9a).

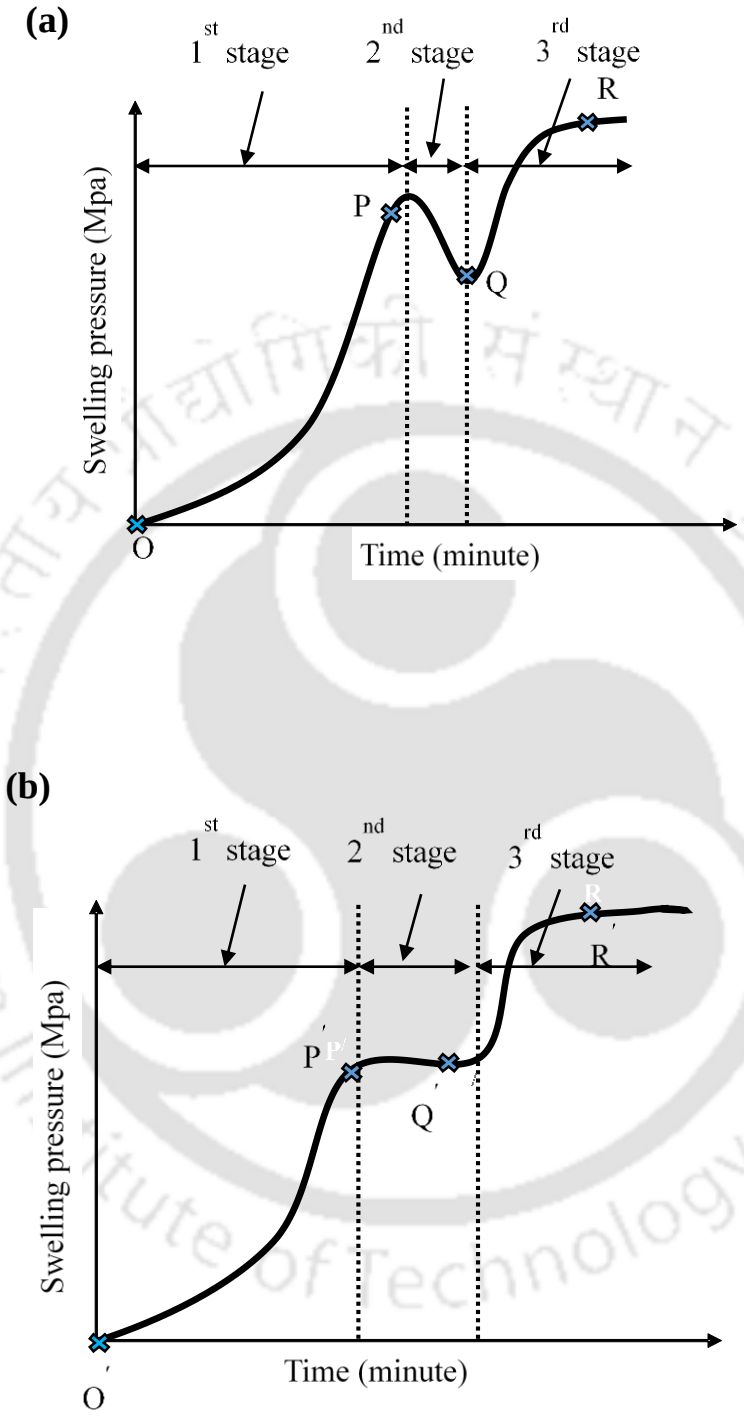

Fig. 8.6 Typical swelling pressure characteristic curve exhibiting (a) b-SPEC and (b) m-SPEC (After Choudhury, 2019).

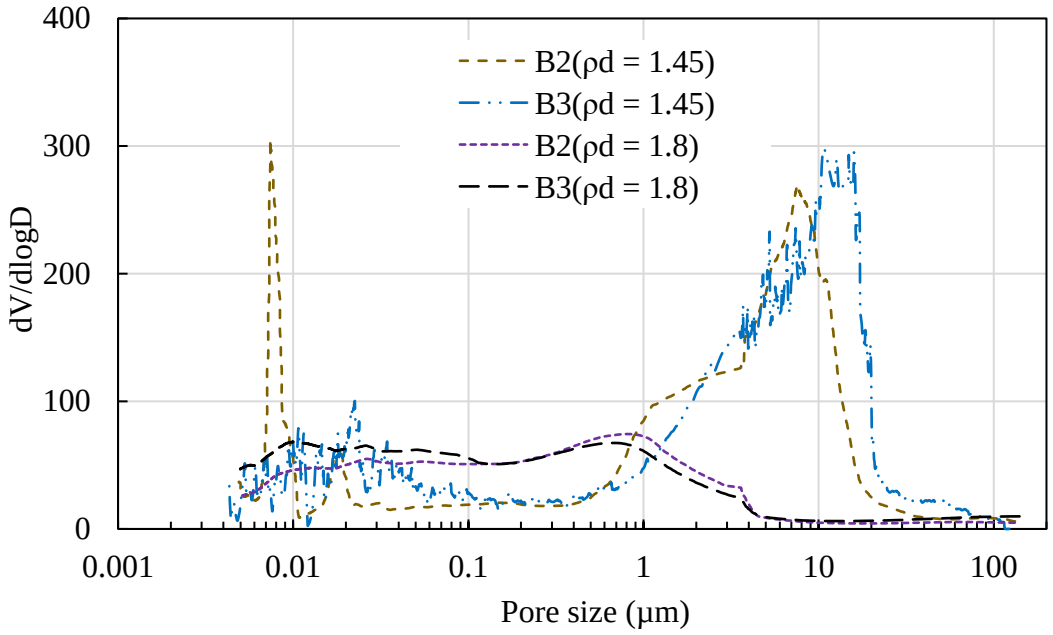

Fig. 8.7 MIP data of B2 and B3 bentonites in as-compacted conditions at different compaction densities.

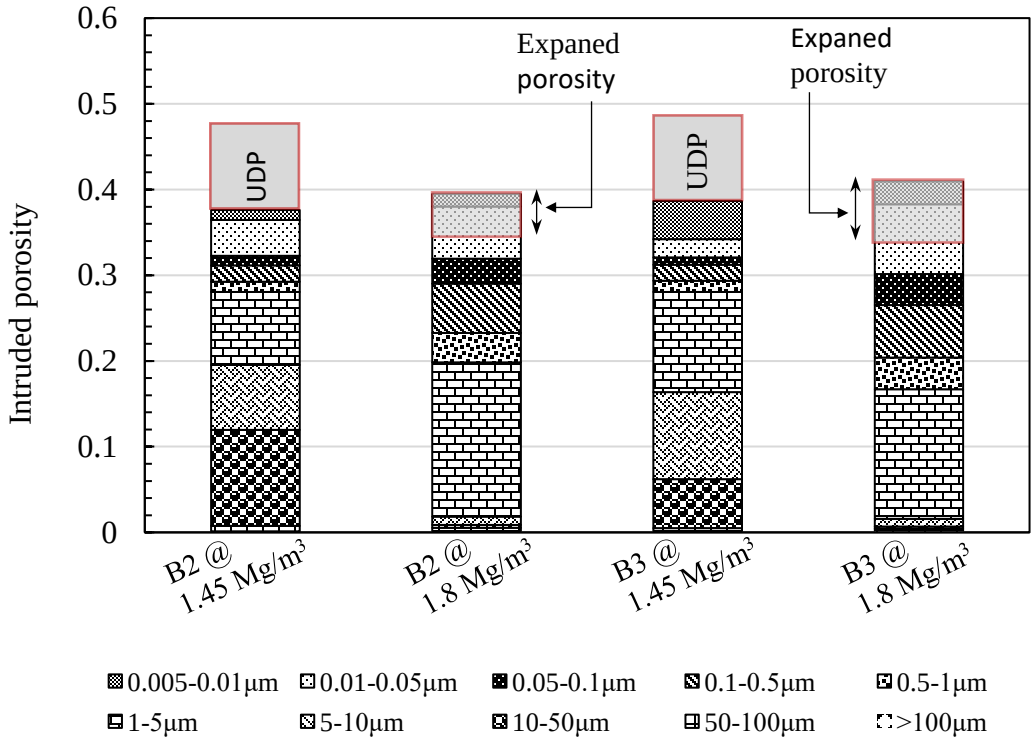

Fig. 8.8 Typical pore size distribution bar diagram of B2 and B3 for as compacted state.

The macro-pore size classes, 1-5μm, 5-10μm, and >10μm, were observed to be present among the inter-aggregate pore spaces. Micro-pores ($0.001 < D < 1$ μm) were present among the aggregate forming clay particles (i.e., intra-aggregates). The smaller micro-pores (<0.005 μm), inter-crystalline pores (<0.001 μm), and larger macro-pores (>100 μm) were undetected in the MIP test due to associated limitations. The limitations are due to the inability of mercury to enter into finer micropores and entrapped pores. Further, the larger macro-pores are filled by the mercury under very low induced pressures even before the start of the test and the small specimens used in the MIP testing might ignore the larger inter-aggregate pores. A similar observation was also made in the literature studies (Koliji et al. 2012, Farulla and Rosone 2012). The combined porosity from these undetected pores was termed as "undetected porosity" (UDP) and marked in the bar diagram.

The mercury intruded porosity of B2 bentonite at ρ_d = 1.45 Mg/m^3 was dominated by the coarser macro-pore size class (10-50μm). On the other hand, the finer macro-pore size class of 1-5μm dominated the pore volume in B3 bentonite (Fig. 8.9c). The number of larger inter-aggregate pores (10-50μm) in B3 bentonite was less than B2 bentonite at any given density due to higher plasticity. The increase in the plasticity decreased the average pore size for the same compaction density, due to the presence of higher clay and montmorillonite content (Table 4.6), which was seen as a shift in the PSD curve towards the left (Fig. 8.7). The coarser macro-pore size class (10-50μm) got completely suppressed at 1.8 Mg/m^3 (Fig. 8.7) for both the bentonites. This was evident from the closure of coarser macro-pores in the FESEM image of B2 bentonite at 1.8 Mg/m^3 (Fig. 8.9b). Similar observations were also made for B3 bentonite (Fig. 8.9d).

The mercury intruded porosity for both the bentonites at ρ_d = 1.45 Mg/m^3 was less than the initially targeted porosity calculated based on the targeted compaction density. This was attributed to the undetected pores (UDP) as discussed earlier. Further, B3 bentonite showed a higher UDP for a given density due to higher plasticity. The increase in plasticity increases a greater number of inaccessible finer pores. At 1.8 Mg/m^3, unlike the lower densities, the intruded porosity was slightly higher than the targeted porosity for both the bentonites. This was attributed to the rebound of the compacted bentonite specimen after the release of the compaction load (Tripathy et al. 2014). The rebound is significant only at very high compaction density ($\rho_d \geq$ 1.8 Mg/m^3), hence

the influence was not visible for lower densities. The difference was more for B2 bentonite since rebound increases with an increase in plasticity.

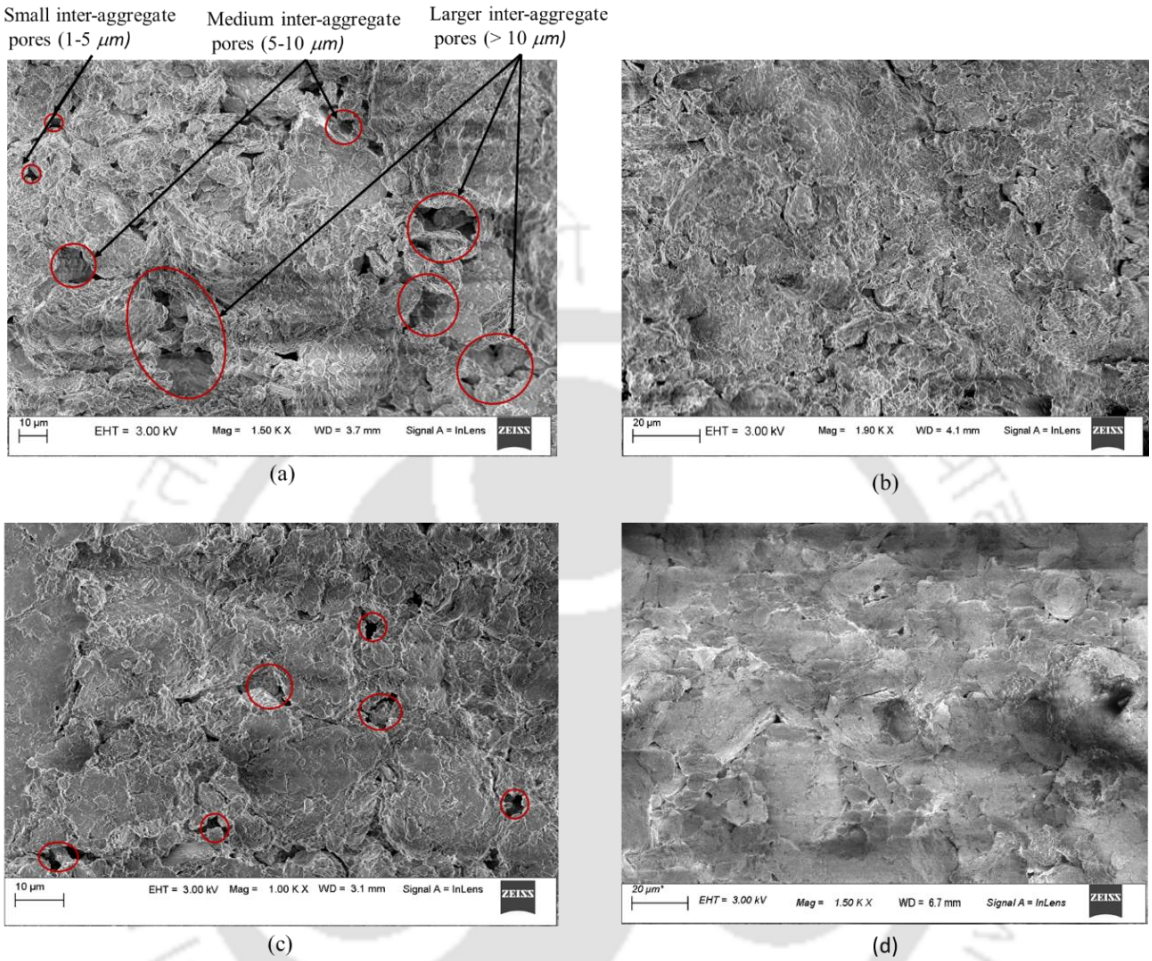

Fig. 8.9 FESEM images in as compacted condition for (a) B2 bentonite compacted at 1.45 Mg/m^3, (b) B2 bentonite compacted at 1.8 Mg/m^3, (c) B3 bentonite compacted at 1.45 Mg/m^3, (d) B3 bentonite compacted at 1.8 Mg/m^3.

Overall, the macropores of 1-50μm size were dominantly present in the *as-compacted* samples of both the bentonites at lower compaction density. The contributed porosity from the pore size class greater than 1 μm consistently reduced with compaction density for both the bentonites and subsequent increase in the finer pores (<1μm). This suggested that only the inter-aggregate (macro) pores were reduced while maintaining the finer intra-aggregate (micro) pores intact under the mechanical forces during the compaction at air-dry conditions.

A quantitative assessment of the evolution of microstructure during saturation along the two distinct SPECs is important to bring out the responsible micro-scale mechanisms behind the varied SPEC characteristics of the compacted bentonites. Thus the SPECs of bentonite B2 and B3 at compaction density of 1.45 Mg/m^3, which exhibited the two distinct behavior, were considered for understanding the micro-scale mechanisms during the water hydration. The bimodal SPEC (*b*-SPEC) behavior at *O*, *P*, *Q*, and *R* stages for B2 bentonite at lower compaction densities and monotonic SPEC (*m*-SPEC) behavior along *O'*, *P'*, *Q'* and *R'* stages for B3 as illustrated in Fig 8.6a & 8.6b, respectively, were studied in the following section.

8.3.2 Bimodal SPEC behavior

The PSD curve for B2 bentonite at 1.45 Mg/m^3 at different stages of *O*, *P*, *Q*, and *R* on the *b*-SPEC was presented in Fig. 8.10. Further, the contributed pore volume by eight different pore size classes was presented in the form of a bar diagram in Fig. 8.11. The PSDs at *O*, *P* and *Q* stages exhibited a bimodal behavior. The initial stage *O* corresponding to *as compacted* condition showed a dominant broad peak as explained earlier. Approximately 70% of the total intruded volume was contributed by the 1-50μm pore-sizes (stage *O* in Fig. 8.11). The peak consistently shifted towards the left with each hydration stage from *O* to *R* indicating a reduction in the larger inter-aggregate pore sizes until full saturation (Fig. 8.10). Water was drawn at a very fast rate in the initial stage of *b*-SPEC from *O* to *P* due to higher hydration energy (Tadikonda et al. 2021) at various pore size classes. The bar diagram at stage *P* (Fig. 8.11) showed that the finer macro-pore volume, indicated by the volume of the pore size classes of 1 – 5 μm and 5 – 10 μm, increased due to the initial hydration stage and which decreased the coarser macro-pore volume (10 – 50 μm) which transformed them into immediate smaller inter-aggregate pore sizes of 5-10 μm and 1-5 μm. The micro-pore (< 1 μm) volume was nearly unchanged during this stage indicating that the aggregate was intact and the hydration of micro-pores directly contributed to the swelling pressure development. The observation was in accordance with the PSD curves for *O* and *P* in Fig. 8.10. The FESEM image of the specimen at stage *P* showed swollen aggregates still holding the larger inter-aggregate pores (See stage *O* and *P* in Fig. 8.12a and 8.12b) suggesting that the overall aggregate structure remained intact during the initial hydration stage. Based on this observation, it can be deduced that the finer intra-aggregate (micro) pores remained unaffected during the initial hydration stage hence majorly contributing to the swelling pressure development whereas, the

coarser macro-pores slightly reduced into smaller size due to invasion of the swelling aggregate (see illustration in Fig. 8.11) thereby adversely affecting the swelling pressure development. Hence, from stage *O* to *P* on the SPEC of B1 bentonite at 1.45 Mg/m^3, the swelling pressure increased continuously to a temporary maximum value of 0.55 MPa.

Swelling of micro-pores and collapse of coarser macro-pores with further water uptake at stage *Q* destabilized the aggregate due to increased repulsive pressures between the clay platelets (Fig. 8.11). The collapse was identified by a significant decrease in the mercury intruded volume of the pore size classes 10-50μm and 5-10μm, which was accompanied by an increase in the intruded pore volume of all the pore size classes finer than 1μm including the UDP volume (Fig. 8.11). Further, the PSD curve is characterized by a considerable leftward shift of the peak as well as a significant reduction in the peak intensity. A very high-intensity narrow peak was observed near the 0.007 μm size (Fig. 8.10) indicating the evolution of a significant number of pores of that size range due to the collapse of the coarser macro-pores. The closure of larger inter-aggregate pores due to the estimated collapse was evident from the FESEM images at *P* and *Q* (Fig. 8.12b – 8.12c). The collapse of coarse macro-pores into finer pores was also well reflected on the SPEC, showing a reduction of ~14% of the swelling pressure from P to Q (Fig. 8.1a).

The structural collapse was followed by redistribution of water into the soil pores and into the inter-lamellar space of the clay particles at stage *Q*-*R*. A significant repulsive pressure was developed, at this stage, due to water diffusion into the inter-lamellar space at a relatively slow rate. This led to the expansion of finer micro-pores and thus decreased the UDP volume as seen in Fig. 8.11. The larger macro-pores further got compressed due to the re-adjustment of clay fabric resulting due to a high swelling pressure development. Thus the PSD curve was nearly uniformly throughout the size range.

In summary, during the gradual invasion of the swelling aggregates into the coarser macro-pores (> 5μm), which was observed in the initial water uptake stage (Fig. 8.4a), these pore size classes transformed into the immediate finer macro-pore size classes (Fig. 8.11). On the other hand, the collapse of the coarser macro-pores led to the formation of various finer pore size classes (Figs. 8.10 – 8.11). These collapsible pore size classes thus were considered to be the meta-stable pores in the compacted bentonites whose significant presence led to the bimodal behavior on the SPEC.

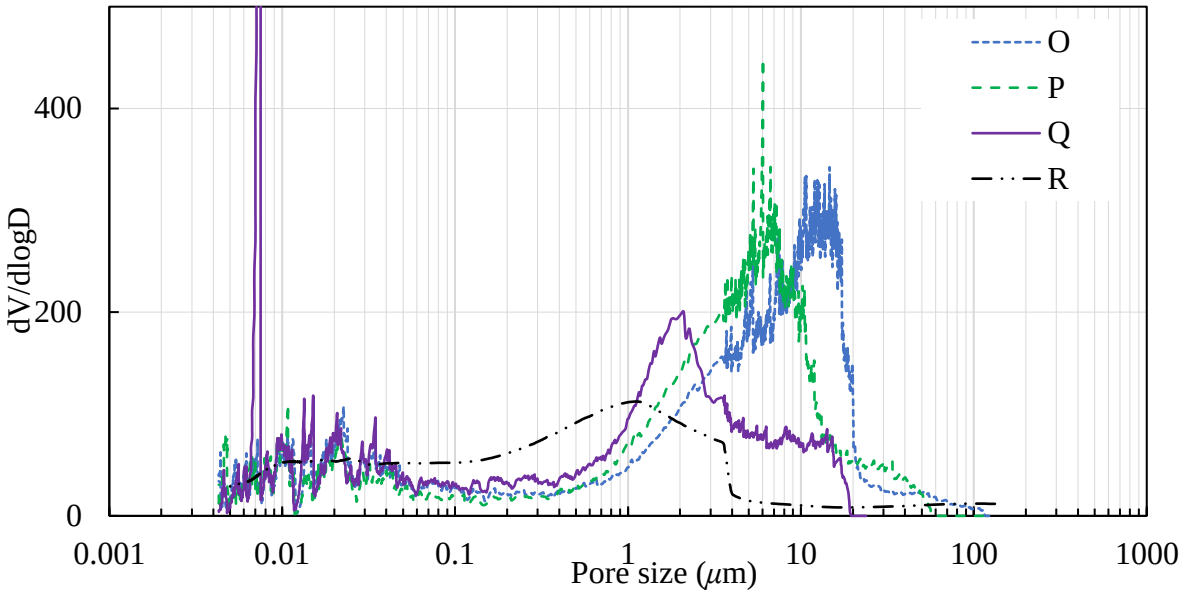

Fig. 8.9 MIP data at different stages of swell evolution for B2 bentonite compacted at 1.45 Mg/m^3 dry density.

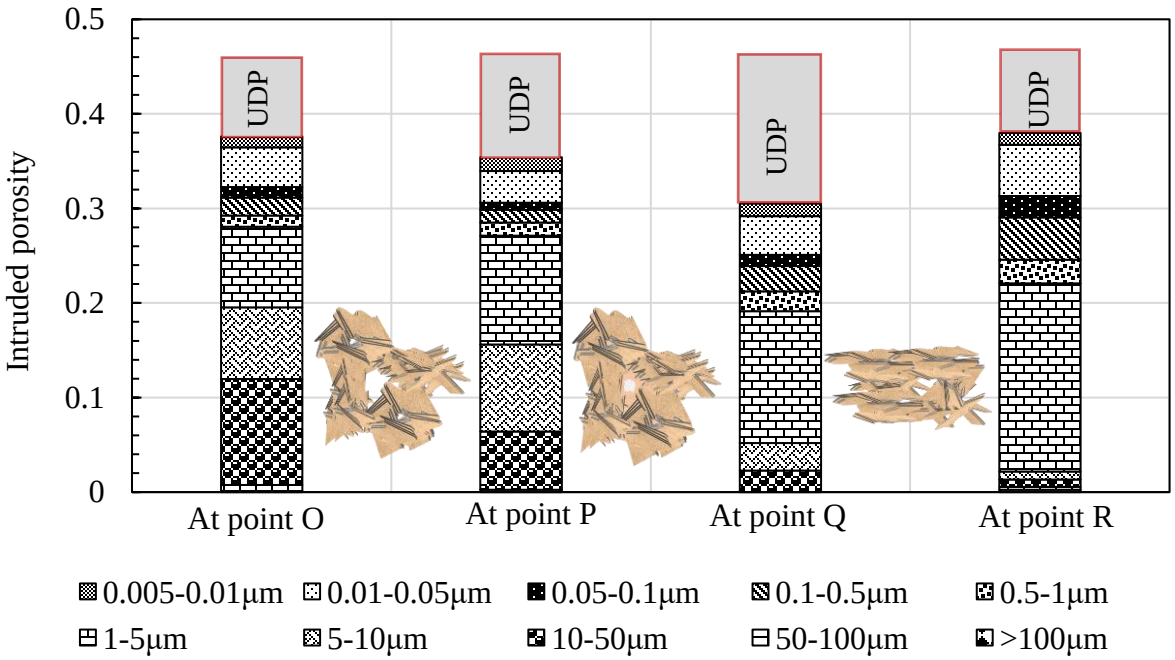

Fig. 8.10 Typical pore size distribution bar diagram of B1, ρ_d = 1.45 Mg/m^3

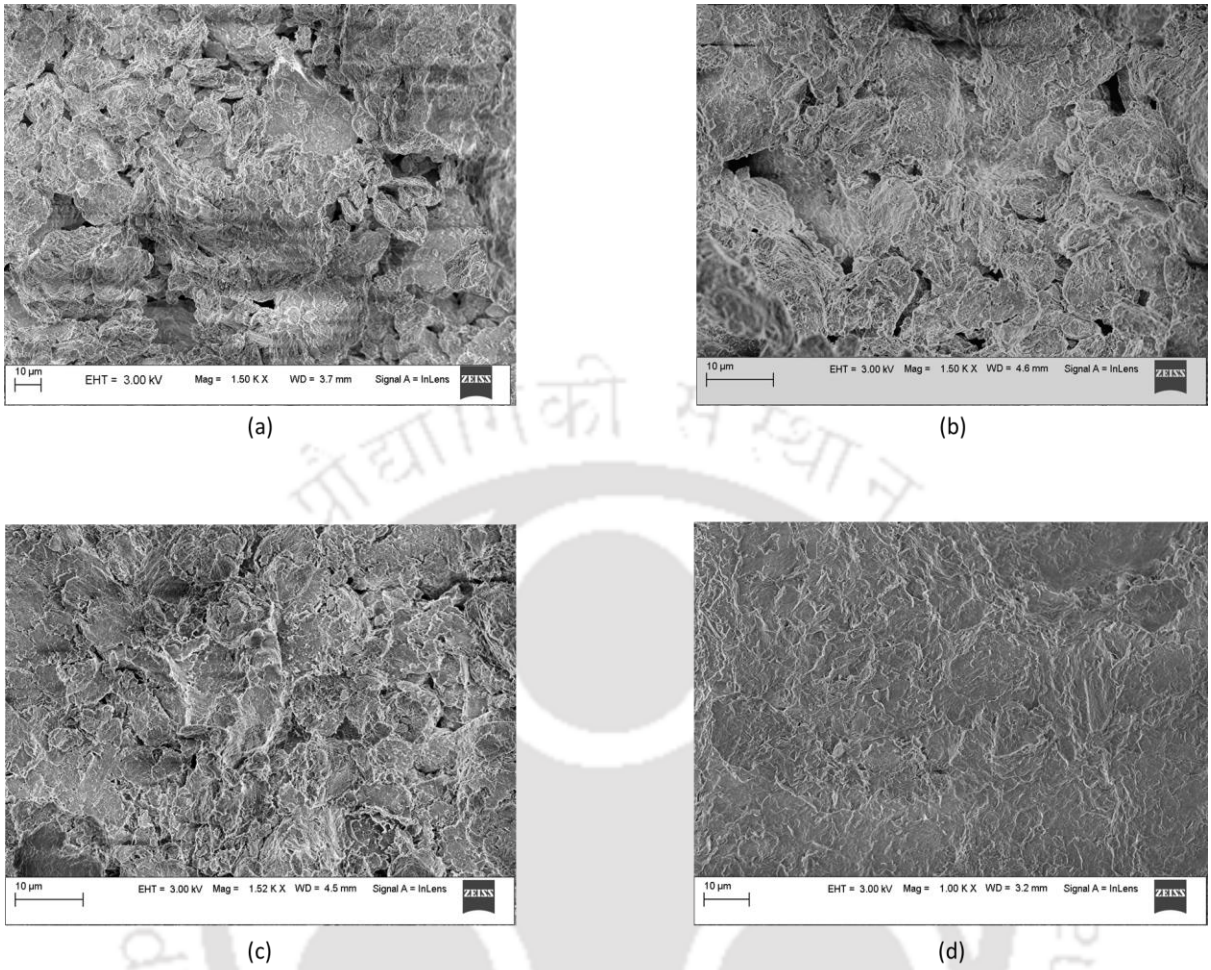

Fig. 8.11 FESEM images B2 bentonite compacted to dry density of 1.45 Mg/m^3 at three different stages on the SPEC (a) point 'O', (b) point 'P', (c) point 'Q', (d) point 'R'.

8.3.3 Monotonic SPEC behavior

The PSD curve for B3 bentonite at *O'*, *P'*, *Q'* and *R'* stages on the monotonic SPEC (Fig. 4b) was presented in Fig. 8.13. The initial stage *O'* corresponding to '*as-compacted'* condition at 1.45 Mg/m^3, which contains high density of micro-pores (with a sharp peak at 0.007 μm pore-size) as discussed earlier. The bar diagram showing the contribution of eight different pore size classes to total intruded porosity at *O'*, *P'*, *Q'* and *R'* were presented in Fig. 8.14. Similar to B2 bentonite at point *O'*, the dominance of the pores in the size range of 1-50μm was observed in the mercury intruded volume. About 72 % of total intruded volume was contributed by these macro-pores. However, the finer macro-pores of 1-5 μm size dominated the intruded pore volume due to increase in the plasticity (point *O'* in Fig. 8.14) unlike in B2 bentonite. The dominance of this pore-size was also evident in the FESEM image (Fig. 8.15a). The peak consistently shifted towards left (i.e.

finer pore sizes) from *O'* to *R'* indicating a reduction in the coarser macro-pore volume due to the hydration (Fig. 8.13). Fig. 8.14 showed a consistent decrease in the intruded porosity of 5-10μm and 10-50μm pore size classes, similar to B2 bentonite. The closure of the larger inter-aggregate pores (> 5μm) were apparent from the FESEM images at *O'*, *P'*, *Q'* and *R'* as shown in Fig. 8.15.

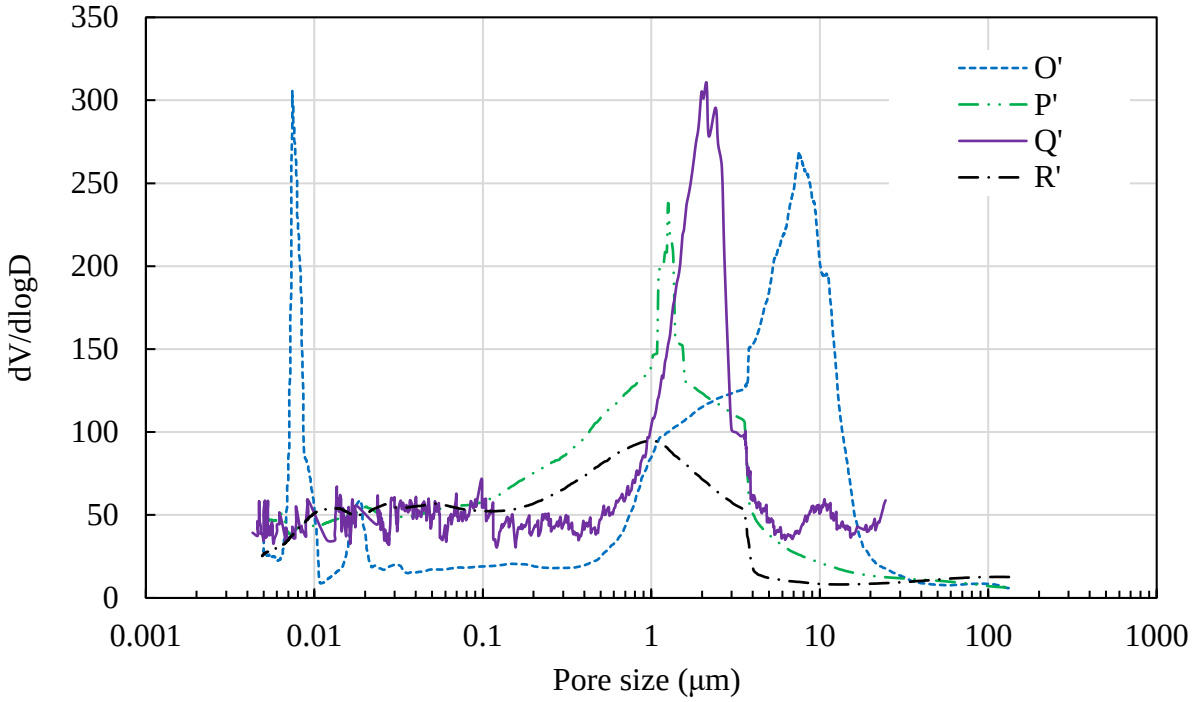

Fig. 8.12 MIP data at different stages of swell evolution for B3 bentonite compacted at 1.45 Mg/m^3 dry density.

The collapse of the coarser macro-pores (> 5μm) was observed during the initial hydration stage itself in case of B3 bentonite, which was observed at stage *P-Q* for B2 bentonite (see illustration in Fig 8.14). The decrease in the volume by 10 – 50 μm pore size class along with the immediate finer pore-size class and increase in the volume of finer micro-pore size classes (Fig. 8.14) indicated to be the collapse. The volume of the UDP also decreased at this stage indicating the expansion of the earlier inaccessible pores. A significant reduction in the larger macro-pores (>5μm) in FESEM image (Fig. 8.15b) and considerable leftward shift of the major peak in the PSD curve (Fig. 8.13) was observed. However, the structural collapse of coarser macro-pores did not reflect on the *m*-SPEC of B3 bentonite at 1.45 Mg/m^3 (Fig. 8.2a). A significant expansion of the micro-pores due to the generation of higher repulsive pressure during initial hydration with more number of finer pores (Fig. 8.14), owing to its high plasticity, dominated the collapse of the macro-pore volume and showed an increasing swelling pressure with time. A plateau behavior was

followed along P'Q' due to the readjustment of the collapsed pores before swelling of the micro-pores. During this second stage, the swelling pressure was constant from *P'* to *Q'* (between 200 – 400 min in Fig. 8.2a) due to collapse of very coarse macro-pores (50 – 100 μm) and increase in the volume of UDP. The hydration process further advanced into the inter-lamellar space of the clay particles beyond point *Q'* as discussed earlier. A similar trend to that of B2 bentonite was observed in the intruded porosity from *Q'* to *R'* for B3 bentonite as well (Fig. 8.14). The FESEM image showed a more compacted soil fabric at point *R'* suggesting a complete sealing/closure of the larger inter-aggregate pores (Fig. 8.15d) due to swelling of smaller aggregates. The differential intruded pore volume curve showed a more or less uniform distribution over a size range of 0.005 – 5μm (Fig. 8.13).

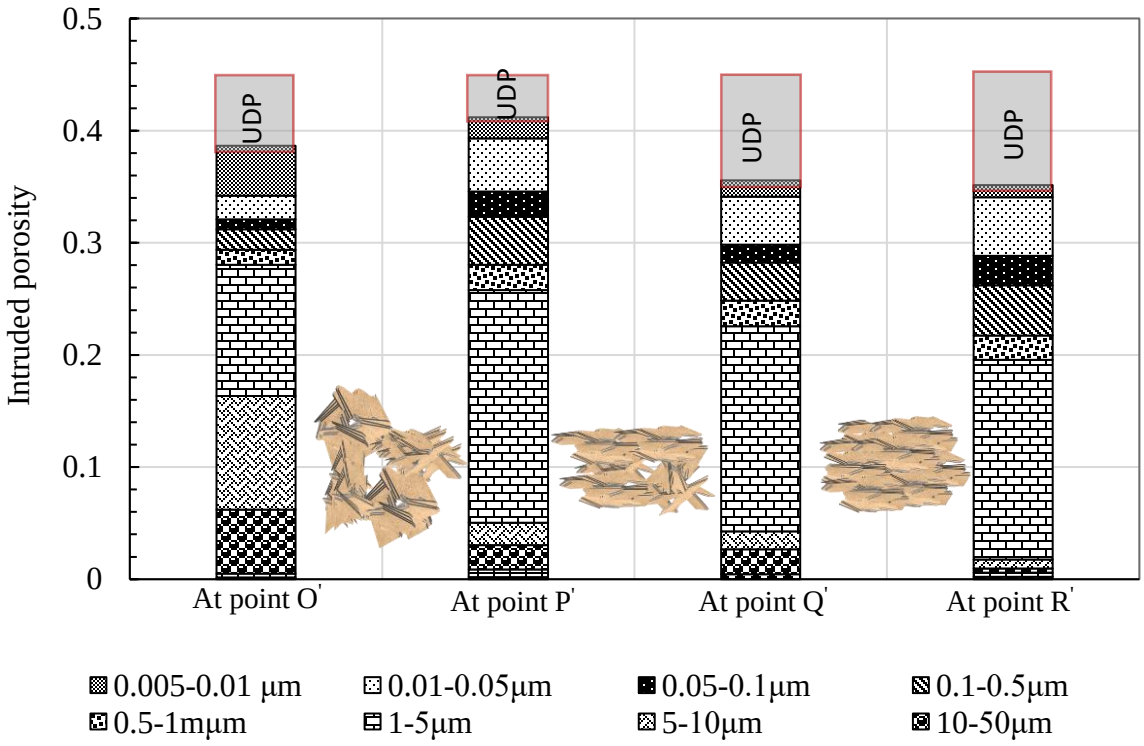

Fig. 8.13 Typical pore size distribution bar diagram of B3, ρ_d = 1.45 Mg/m^3

The intensity of different pore-size classes on the PSD curve decreased (Fig. 8.7) as mentioned earlier with further increase in compaction dry density. The decrease in the contribution of coarser macro-pores (>10 μm) to the total intruded porosity and significant increase in the micro-pores (<1 μm) influenced the shape of the SPEC and followed a monotonic behavior (Fig. 8.1b and 8.2a & b) for both the bentonites. The pore-size evolution of both the bentonites compacted at ρ_d = 2.0 Mg/m^3 was qualitatively similar due to similar nature of the SPEC and thus not presented here.

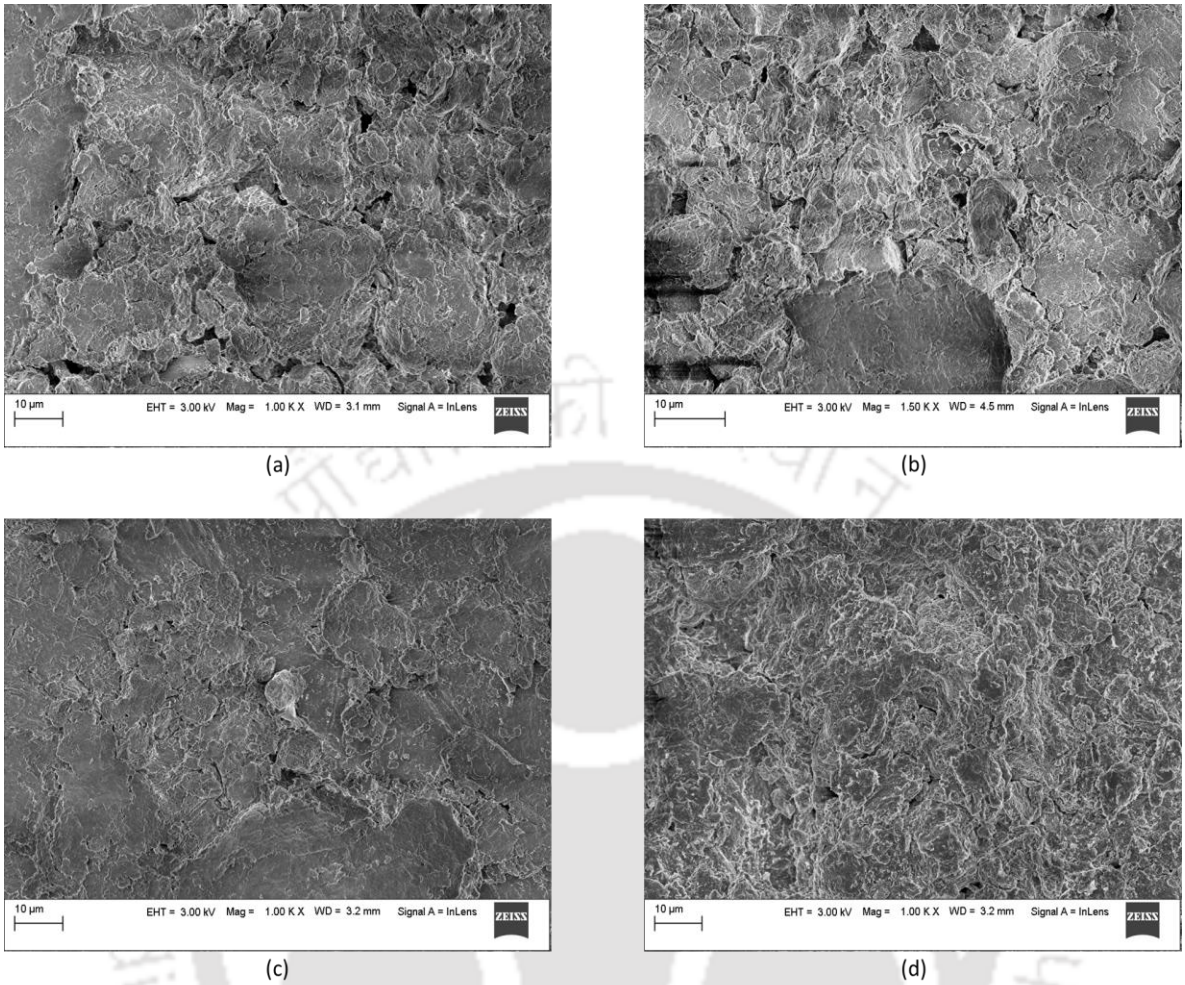

Fig. 8.14 FESEM images B3 bentonite compacted to dry density of 1.45 Mg/m^3 at four different stages on the SPEC. (a) point 'O' (b) point 'P'(c) point 'Q'(d) point 'R'.

In summary, both B2 and B3 bentonites showed a significant presence of macro-pores at 1.45 Mg/m^3 dry density. The coarser macro-pores were significant in B1 bentonite whereas finer macro-pores were dominant in B3 due to higher plasticity. During the initial hydration stage, a significant percentage of coarser macro-pores got affected, either by the invasion of swelling aggregates or structural collapse of the aggregates, depending on the bentonite plasticity. An illustration of the aggregate invasion and collapse mechanism at different stages of the hydration process is also presented in Fig. 4a-4b for both the SPEC behavior. The decrease in the swelling pressure on the SPEC is generally attributed, in the literature, to the loss of shear strength at the aggregate contacts due to a decrease in the suction under the hydration process. On contrary, the collapse of the macro-pores was observed for the bentonites at different stages on the SPEC that exhibited both bimodal and monotonic behaviors. Albeit, the decrease in the swelling pressure was not observed for B3

bentonite due to the dominating effect of different micro-pore size classes. The influence of the macro-pore collapse on the SPEC behavior was dependent on the relative contribution of the meta-stable macro-pore size classes to the total porosity, which in turn depends on the bentonite plasticity and compaction density.

8.3.4 Critical pore-size parameters

Various critical pore-size classes were quantified under the influencing factors of initial compaction density and bentonite plasticity for predicting the SPEC behavior. The relative contribution of various coarser macro-pore size classes namely, 5-10μm and 10-50μm; the micro-pore size classes (<1μm) to the total porosity has influenced the observed collapse on the SPEC. These observations were further validated on the available PSDs and swelling pressure data of the bentonites from the literature studies. Two parameters based on the contributed porosity from these critical pore size classes were introduced and the influence of each parameter on the SPEC behavior was discussed here.

- The parameter α represents the contributed micro-porosity which defines the ratio of micro-porosity (<1 μm) to macro-porosity (>1 μm).
- The parameter β represents the contributed coarser macro-porosity which defines the ratio of coarse macro-porosity (>5 μm) to the total macro-porosity (>1 μm).

The values of these two defined parameters along with the observed SPEC behavior for the studied bentonites were presented in Table 8.1. The α value increased from 0.33 to 1 for B2 bentonite and 0.37 to 1.44 for B3 bentonite with an increase in the dry density from 1.45 Mg/m^3 to 1.8 Mg/m^3 due to the reduction of macro-pores. Further, the α value was relatively smaller for B2 bentonite as compared to B3 bentonite, at a given density, due to the lower plasticity. The α value for both B2 and B3 bentonites at higher densities (ρ_d > 1.45 Mg/m^3) was ≥1 and the bentonites exhibited a monotonic behavior. The bimodal behavior was likely to be observed when α < 1 and further based on the limit of β. Thus the α value for both the bentonites at the lower density suggested a potential bimodal behavior on the SPEC.

The β value was smaller for B3 bentonite compared to B2 bentonite due to the higher clay content or lesser sand content. A β value of 0.69 was observed for B2 bentonite at ρ_d = 1.45 Mg/m^3, which

exhibited a 14% collapse on the SPEC. On the other hand, B3 bentonite exhibited a monotonic behavior with a marginal collapse with β of 0.6. Thus, a limiting criterion for $\beta <$ 0.6 was adopted for satisfying the monotonic SPEC behavior.

Thus, the limiting criteria were evolved based on the critical pore-size parameters for predicting the SPEC behavior of bentonite at a given compaction density. The SPEC exhibits a bimodal behavior with a distinct macroscopic collapse when $\alpha <$ 1 and $\beta \geq$ 0.6. On the other hand, monotonic behavior was observed when any one of the aforementioned criteria for bimodal behavior was not satisfied. The following steps may be followed for predicting the SPEC behavior:

- Determine α value and check the limiting criterion. A value of $\alpha \geq 1$ indicates monotonic behavior and no other criterion was required. Check the other criterion when $\alpha < 1$.
- Determine β value and check the limiting criterion. A value of $\beta < 0.6$ indicates monotonic behavior, otherwise a bimodal behavior.

Four different bentonites from the literature were identified that have both the measured PSDs and temporal variation of swelling pressure data at nearly the same compaction density to validate the proposed criteria. The PSD and swelling pressure data were obtained from different literature sources, independently, due to lack of data from the same study for many bentonites. Thus the efforts were taken to obtain the PSD data of the bentonites at nearly the same compaction density where the swelling pressure data are available as shown in the table. The SPEC behavior and critical pore size parameters (α & β) were identified from the reported PSDs and presented in Table 8.1.

The α value of the German (Bavaria) bentonite, which has 40% clay content and 60% silt content with zero sand content was 0.39, at a relatively low compaction density of 1.17 Mg/m^3 (Arifin 2010) indicating the dominance of the macro-pore size classes. The β = 0.65 suggested that the macro-pore size classes larger than 5μm had the major contribution to the total macro-porosity and indicated a bimodal SPEC behavior. The SPEC obtained at a comparable dry density of 1.26 Mg/m^3 (Arifin 2010) also showed a bimodal behavior.

The PSD parameters (Villar et al. 2012) for FEBEX bentonite at two different compaction densities were presented in Table 8.1. The α value for FEBEX bentonite at ρ_d = 1.8 Mg/m^3 was smaller as

compared to the lower density due to a very high undetected micro-porosity as observed from the mercury intruded pore volume data (Villar et al. 2012). The β parameter decreased with the compaction density for the FEBEX bentonite, similar to the Indian bentonites. The β value was higher for the FEBEX bentonite at 1.8 Mg/m^3 as compared to the Indian bentonites at the same compaction density due to higher percentage of sand content and lesser clay content. The β value for FEBEX bentonite was even higher at ρ_d = 1.6 Mg/m^3 compared to the Indian bentonites at a relatively lower density (ρ_d = 1.45 Mg/m^3). A bimodal SPEC behavior with a significant collapse was expected at 1.6 Mg/m^3 similar to B2 bentonite at ρ_d = 1.45 Mg/m^3. A monotonic SPEC behavior with a marginal collapse was expected at ρ_d = 1.7 Mg/m^3 as the β value at comparable density (ρ_d = 1.8 Mg/m^3) was about 0.6, similar to the B3 bentonite at ρ_d = 1.45 Mg/m^3. The observed SPEC behavior (Villar and Gómez-Espina 2009) was in good agreement with the predicted behavior as shown in the table 8.1.

The critical pore-size parameters of MX80 bentonite, which has a very high clay content and a small amount of sand, were obtained from the reported PSDs at 1.7 Mg/m^3 (Villar et al. 2012). The critical pore-size parameters showed the dominance of macro-porosity as well as the significant presence of critical macro-pore size classes (5-10 μm and 10-50 μm). This bentonite exhibited bimodal behavior as all the limiting criteria were satisfied. A bimodal SPEC behavior at the same density (Herbert et al. 2008) supported the proposed criteria.

The Chinese GMZ bentonite, with 60% clay content and zero sand content (Schanz and Al-Badran 2012), had majority of the macro-pores at 1.35 Mg/m^3 as indicated by the α (0.82). The presence of the coarser macro-pore classes were, however, negligible (i.e., β = 0.09) and thus exhibited a monotonic SPEC behavior. At 1.75 Mg/m^3, the value of α was very high (6.67) meaning complete dominance of the micro-pores and thus the exhibited the monotonic behavior.

Overall, the α parameter directly influenced by the presence of micro-pores and increases with the compaction density. The β parameter influences the magnitude of the collapse on the SPEC as the β value is related to the percentage of sand content in the bentonite. The collapse is significant at higher values of β. Bentonites containing higher non-clay content shows $\beta > 0.6$ due to higher porosity contribution by the coarser macro-pore size classes and thus exhibit bimodal behavior. The influence of fine sand content on the SPEC behavior was demonstrated based on the swelling

pressure tests on sand-bentonite (B3) mixtures at 1.45 Mg/m^3. The addition of fine sand content significantly changed the SPEC behavior as shown in Fig. 8.5. A significant collapse on SPEC was observed with the addition of 10% fine sand. With further increase in the sand content, the collapse magnitude and rate decreased. The collapse was marginal at 40% sand-bentonite mixture as excessive amount of sand results in the development of large amount of very-coarse macro-pore classes (>50 μm).

8.4 Summary

In this study, SPECs for two Indian bentonites were established in the presence of different electoytes as inundating fluid at various compaction densities. The SPECs exhibited bimodal (swelling pressure drop) as well as monotonously increasing (with a plateau) behavior depending on the bentonite plasticity, compaction densities and inundating fluids. Further, the influence of non-clay content on the SPECs was studied using bentonite-sand mixtures at four different mixing proportions. The addition of sand to the B3 bentonite at 1.45 Mg/m3 bentonite transformed the monotonous SPEC to the bimodal SPEC behavior. An increase in the sand content decreased the final swelling pressure and magnitude in the swelling pressure drop. With further increase in the sand content, however, the SPEC tends to exhibit the intermediate plateau behaviour. The evolution of PSDs and fabric during the water uptake process was analyzed for understanding the microstructural influence on the SPEC behavior. The available pore size range from the MIP study was divided into eight distinct pore-size classes and the pore volume contribution of each size class was analyzed for more detailed interpretation on various pore-size interactions during the hydration and the corresponding influence on the swelling pressure development. The critical pore-size classes contributing to the swelling pressure development in the compacted bentonite were identified. The influence of compaction density and bentonite plasticity on these pore-size classes were quantitatively analyzed to relate with observed SPEC behaviors. Two pore-size parameters were introduced based on the contributed porosity of the critical pore-size classes to identify the SPEC behavior with different plasticity and compaction densities. Further, the influence of non-clay content on the SPEC development was presented for bentonites from the present study and literature.

Table 8.1 Details of critical pore-size classes influencing the SPEC behavior for different bentonites

SL. No.	Bentonite	Density (Mg/m^3)	Particle size characteristics[1]		Pore size distribution Parameters[2]		SPEC mode[3]	Reference
			Clay (%)	Sand (%)	α	β		
1	Indian (B2)	1.45	69	4	0.33	0.69	Bimodal	Present study
2		1.8			1	0.08	Monotonic	
3	Indian (B3)	1.45	78	1.4	0.37	0.6	Monotonic (Marginal collapse)	
4		1.8			1.44	0.12	Monotonic	
5	German (Bavaria)	1.26	40	0	0.39*	0.65*	Bimodal	Arifin (2010)
6	Febex	1.6	65	7	0.89#	0.75#	Bimodal	Villar and Espina (2009)[3]; Mayor et al. (2005)[1]; Villar et al. (2012)[2]
7		1.7			0.49$	0.61$	Monotonic (Marginal collapse)	
8	MX-80	1.7	84	1	0.85	0.76	Bimodal	Herbert et al. (2008)[3]; Villar et al. (2012)[2] Wang et al. (2014)[1]
9	GMZ (China)	1.75	60	0	6.67	N/A	Monotonic	Schanz and Al-badran (2012)
10		1.35			0.82	0.09	Monotonic	

*based on PSD data at 1.17 Mg/m^3, #based on PSD data at 1.65 Mg/m^3; $based on PSD data at 1.8 Mg/m^3

[1,2]indicate the literature sources for the PSDs and swelling pressure data

9 Wetting-induced volume change behavior of air-dry kaolin

9.1 General

This chapter presents a detailed experimental investigation on the wetting-induced volume change characteristics of air-dry compacted kaolin. Volumetric response of the studied kaolin at six different initial compaction dry densities viz., 0.71, 0.9, 1.1, 1.25, 1.5, and 1.7 Mg/m^3, under different inundation pressures in the range of 5-1600 kPa were studied and presented here. Compressibility characteristics of the studied kaolin at the initial air-dry state and the saturated state were presented along with the wetting-induced volumetric path under different inundation pressures to assess the applicability of the existing BBM model. A quantitative analysis of the microstructural changes under different hydro-mechanical stress states was carried out based on the pore size distribution and the fabric images and presented next. A discussion on the relevant surface forces influencing the kaolin behavior based on the microstructural analysis was then presented followed by a summary in the end.

9.2 Wetting-induced volumetric response of kaolin

Fig. 9.1 presents the volumetric path of the studied kaolin subjected to different hydro-mechanical stress-paths at six different initial compaction densities viz., 0.71 Mg/m^3, 0.9 Mg/m^3, 1.1 Mg/m^3, 1.25 Mg/m^3, 1.5 Mg/m^3, and 1.7 Mg/m^3. The air-dry compressibility of kaolin was very minimal up to an inundation pressure of 20 kPa, at all the studied densities. Beyond 20 kPa inundation pressure, a considerable void ratio reduction was observed at the loosest compaction density of 0.71 Mg/m^3. The deformation increased significantly with a further increase in the applied pressure. A similar observation was also made at other compaction densities. The deformation was, however, significantly reduced with an increase in the compaction density under a given inundation pressure. The dotted line with an arrow represents the volumetric deformation path due to wetting under a given inundation pressure. Kaolin exhibited volumetric collapse at lower compaction densities ($\leq$ 1.25 Mg/m^3) consistently under all the inundation pressures (Fig. 9.1a-9.1d). The studied kaolin, however, exhibited swelling at 1.5 Mg/m^3, under smaller inundation pressures of up to 100 kPa and collapse under higher inundation pressures (Fig. 9.1e). Similarly, swelling under inundation pressures up to 400 kPa and a minimal collapse under 800 kPa was observed at 1.7 Mg/m^3 compaction density (Fig. 9.1f). The post-wetting equilibrium void ratio consistently decreased with the inundation pressure at all the compaction densities, except under

400 kPa inundation pressure at compaction densities of 0.9 Mg/m^3 and 1.1 Mg/m^3 (Fig. 9.1b & 9.1c). The variation of volumetric strain with inundation pressure was presented for all the six densities together in Fig. 9.2. A collapse strain of 16% was observed due to wetting under 5 kPa inundation pressure at the compaction density of 0.71 Mg/m^3.

The collapse magnitude consistently increased with an increase in the inundation pressure up to a peak value of 38% under 200 kPa. Under 400 kPa, the collapse magnitude was slightly reduced to 34%. Similar behavior was also observed at 0.9 Mg/m^3 density, with a peak collapse of 36% observed under 200 kPa pressure. The collapse magnitude at 0.9 Mg/m^3 was relatively smaller as compared to the smaller density (0.71 Mg/m^3), consistently under all the inundation pressures. At 1.1 Mg/m^3, a maximum collapse of 23% was observed under 400 kPa inundation pressure. At this density, the collapse magnitude under different inundation pressure was considerably reduced as compared to the smaller densities. With the increase in the initial density to 1.25 Mg/m^3, the collapse potential was further reduced under different inundation pressures.

A minimal collapse of 2% was observed under 10 kPa inundation pressure at this density. The collapse increased with an increase in the inundation pressure up to a peak value of 14% under 800 kPa inundation pressure. Under 1600 kPa, the collapse magnitude reduced to a value of 12%. Unlike the lower densities, the studied kaolin soil exhibited swelling under the inundation pressures up to 100 kPa at 1.5 g/cc. A maximum swelling of 10% was observed under 5 kPa inundation pressure. The swelling strain consistently decreased with increasing inundation pressure and achieved a minimal 2% swelling at 100 kPa inundation pressure. Kaolin exhibited collapse under 200 kPa and higher inundation pressures. Under 200 kPa, a maximum collapse of 4% was observed and the collapse was slightly decreased with further increase in the inundation load. A similar trend was also observed for 1.7 Mg/m^3 density. At 1.7 Mg/m^3, the swelling was observed up to the higher inundation pressure of 400 kPa. Under 800 kPa, a minimal collapse of 0.66% was observed at equilibrium.

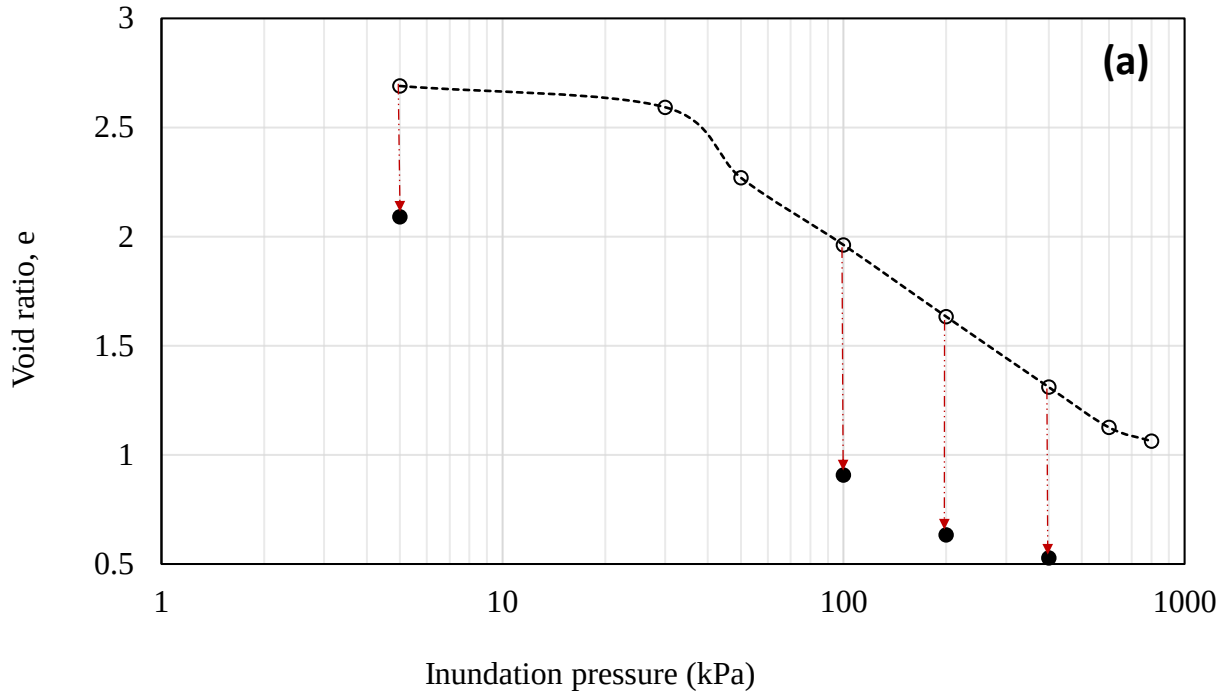

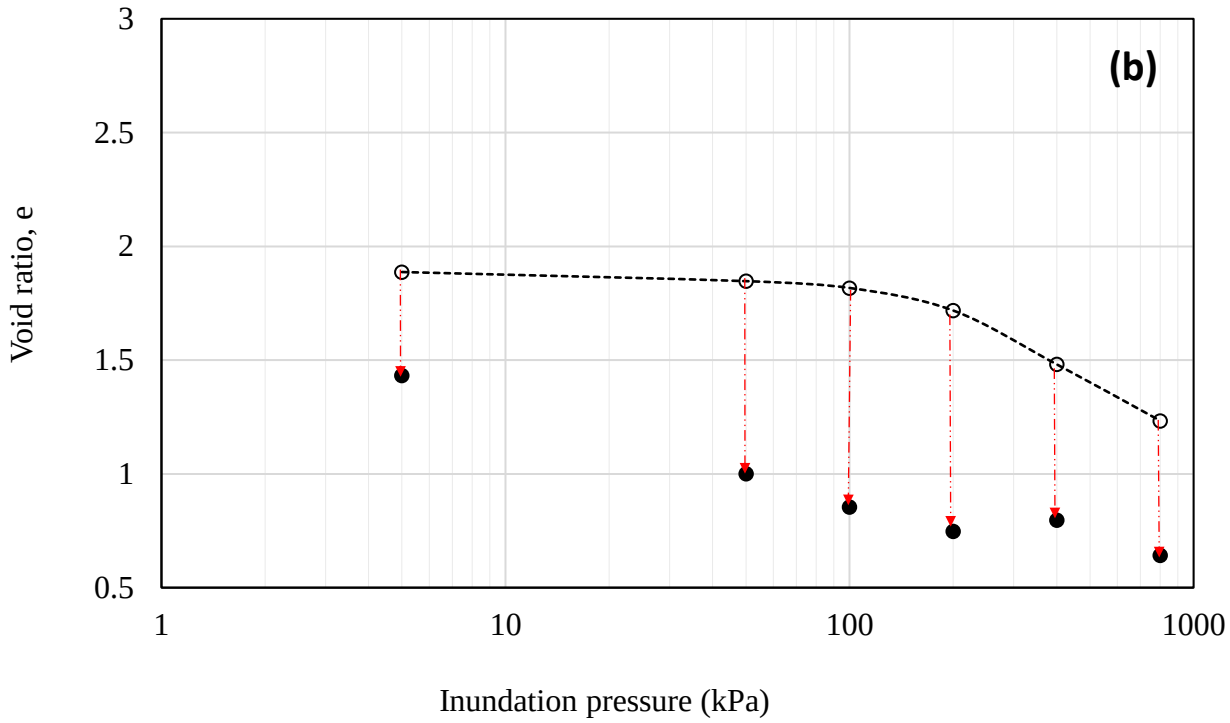

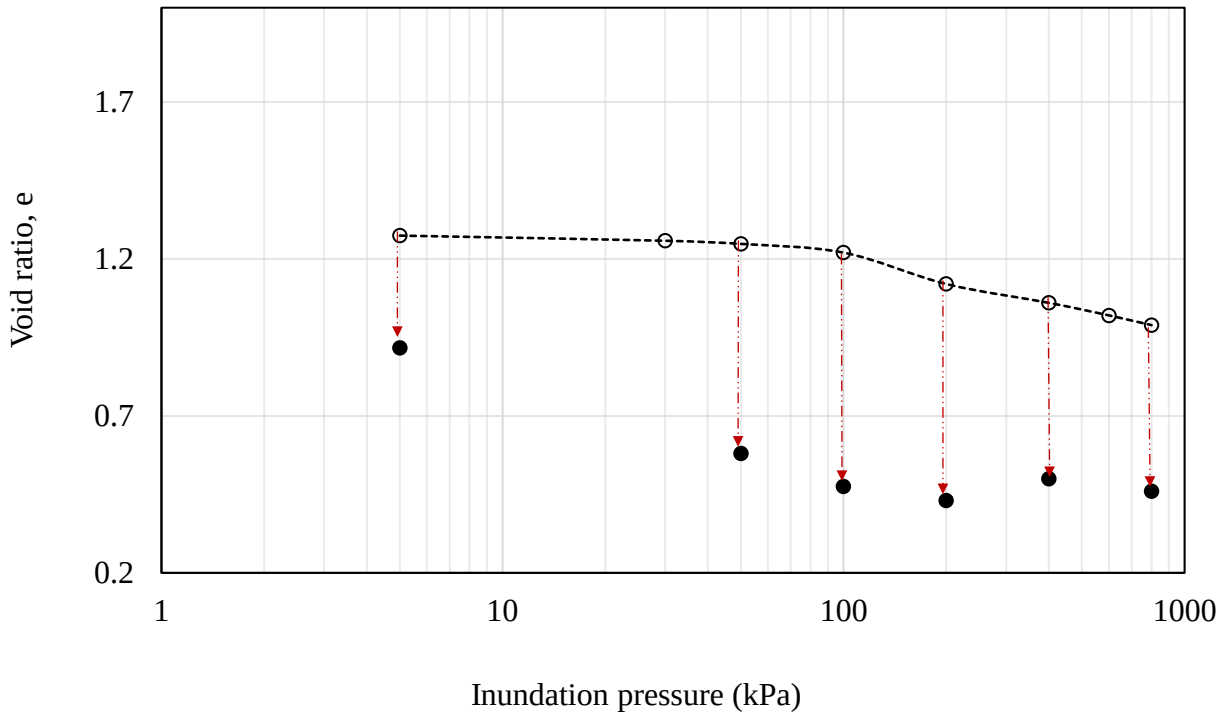

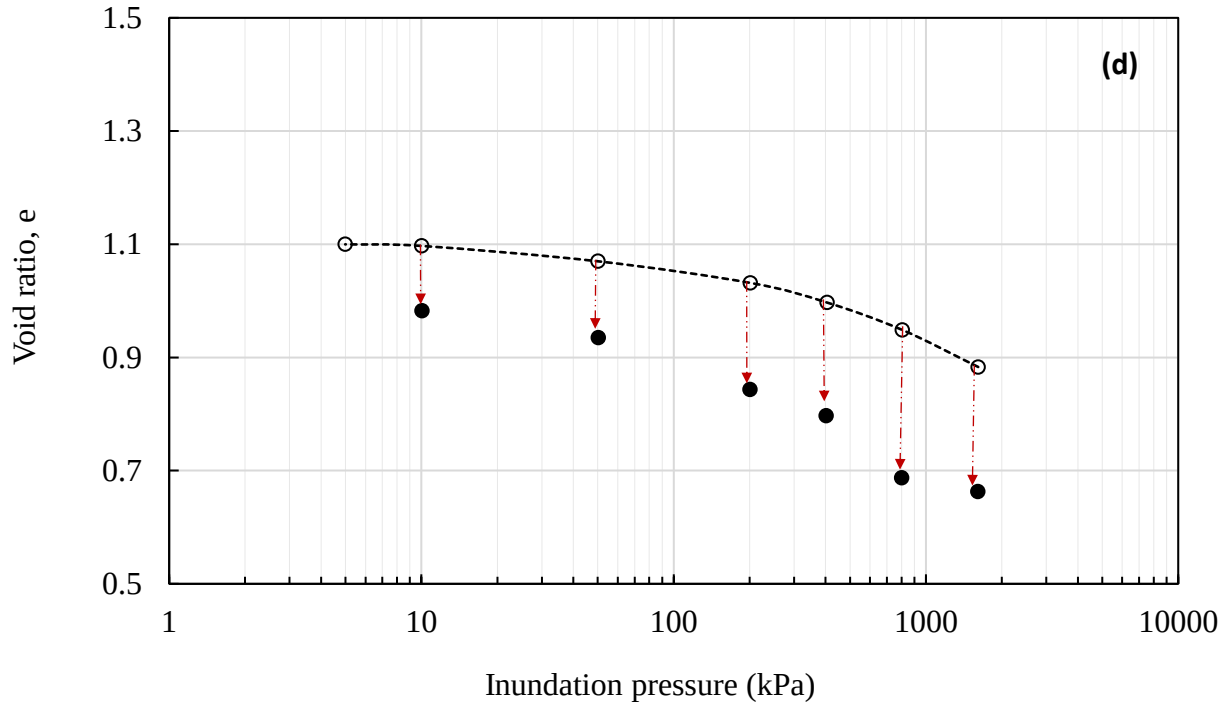

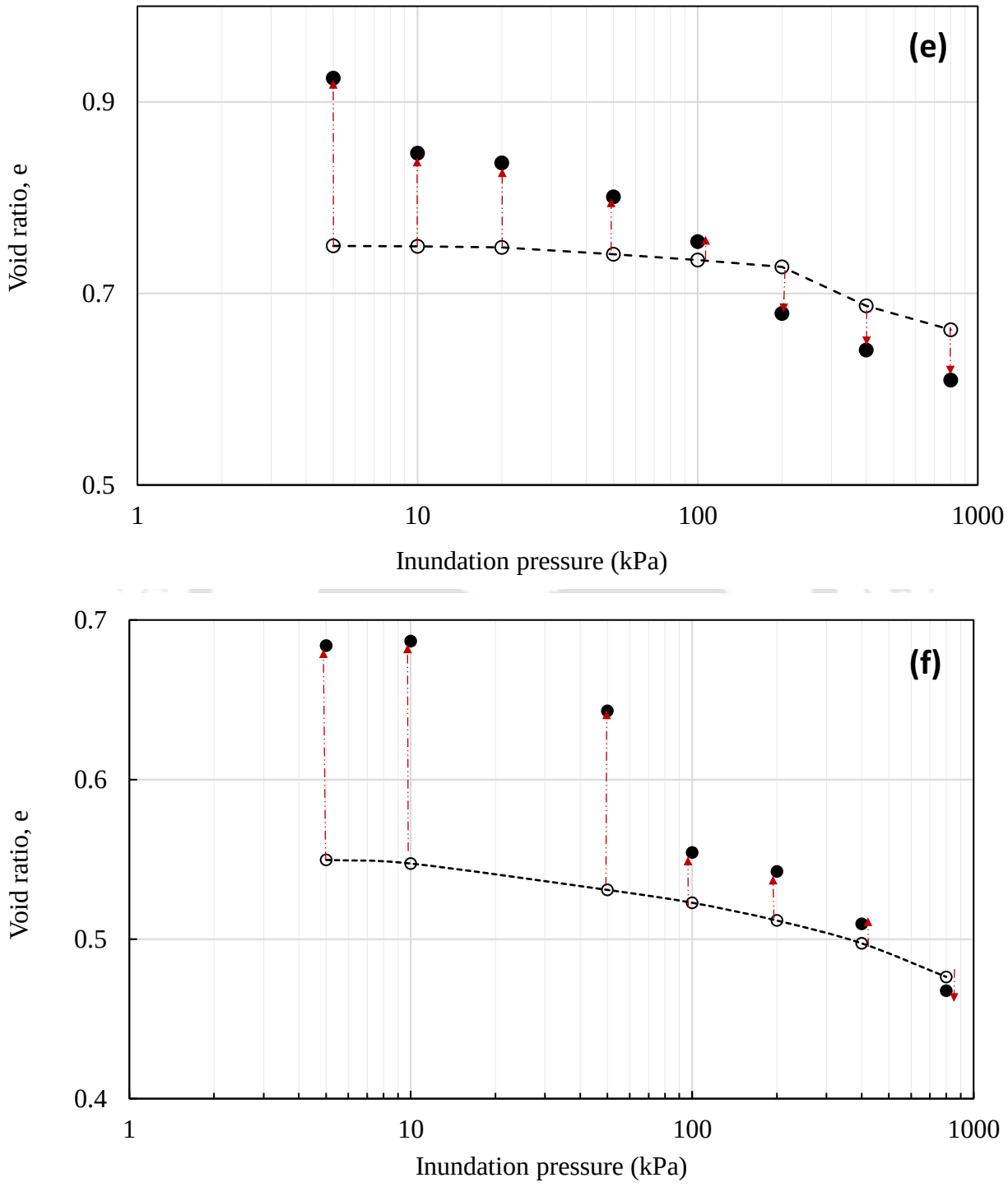

Fig. 9.1 Volumetric deformation of compacted kaolin subjected to wetting under different inundation pressure at (a) ***0.71 Mg/m³****, (b)* ***0.9 Mg/m³****, (c)* ***1.1 Mg/m³****, (d)* ***1.25 Mg/m³****, (e)* ***1.5 Mg/m³*** *and (f)* ***1.7 Mg/m³*** *dry density.*

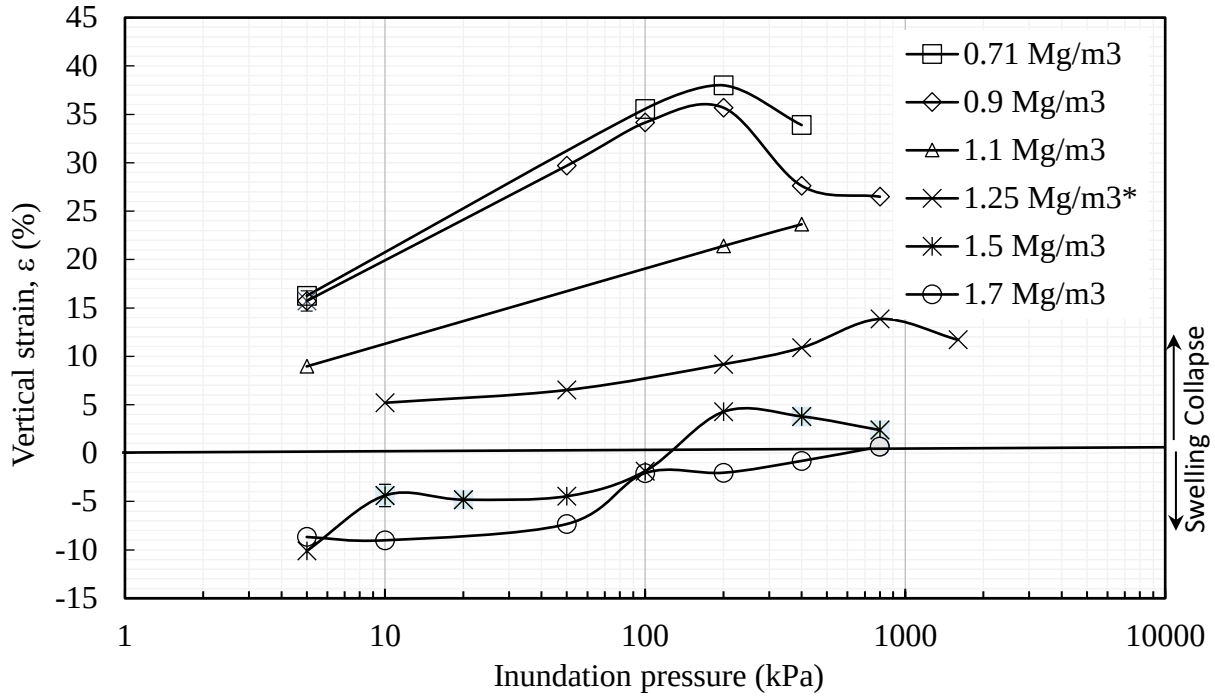

Fig. 9.2 The wetting-induced volumetric strain of compacted kaolin under different inundation pressure at six different dry densities.

In summary, the studied kaolin exhibited significant collapse potential at lower compaction densities (<= 1.25 Mg/m^3) (Fig. 9.2). The collapse magnitude increased with an increase in the inundation pressure up to a peak value and then decreased with a further increase in the inundation pressure at these densities. Similar behavior was reported for different residual soils in the past studies (Yudhbir, 1982; Booth, 1975). At higher densities, however, a swelling strain was observed under smaller inundation pressures (Fig. 9.2). The swelling strain decreased with the increase in the inundation pressure and exhibited collapse at very high inundation pressure. Overall, the collapse magnitude was significantly reduced with an increase in the density under a given inundation pressure.

The temporal volumetric deformation characteristics of the studied kaolin were recorded at all the six compaction densities. Results were, however, presented only at 1.5 Mg/m^3 for brevity and clarity, where both the volumetric swelling and collapse at equilibrium under different inundation pressure were observed (Fig. 9.3). A swelling strain of 5.5% was observed at equilibrium under 10 kPa inundation pressure. The swelling deformation started about four minutes from the time of

inundation under 10 kPa pressure at a very fast rate and reached the mechanical equilibrium within 20 minutes of inundation (Fig. 9.3a). A similar observation was also made at 20 kPa inundation pressure. A slight reduction (~0.05%) in the specimen height was observed, however, initially up to 3 min from the time of inundation, and then rapid swelling was observed until equilibrium at 100 kPa inundation pressure. A swelling strain of approximately 2% was observed at equilibrium, which was approximately 20 minutes from the time of inundation (Fig. 9.3b). The same compacted kaolin specimen, however, showed a consistent volumetric reduction at 200 kPa inundation pressure (Fig. 9.3c). The rate of volume change was relatively slower as compared to the former cases and the equilibrium was achieved approximately 1000 minutes from the time of inundation. The total reduction in the specimen height was found to be approximately 2.4% at equilibrium. A similar trend was also observed at higher inundation pressure values.

Overall, the temporal volume change behavior of the studied kaolin at 1.5 Mg/m^3 dry density shifted from swelling to volume reduction/collapse with increasing inundation pressure. The specimen exhibited a consistent and rapid swelling upon wetting at smaller inundation pressures of 10 kPa and 20 kPa. With the increase in the inundation pressure to a value of 100 kPa, the temporal volume change behavior shifted to a slight initial collapse then swelling for the same compacted kaolin specimen. At inundation pressure of 200 kPa or higher, the kaolin specimen exhibited a consistent collapse with time. Similar behavior was also observed for the higher density, 1.7 Mg/m^3. With the increase in the density, the initial collapse-then-swelling was observed even at higher inundation pressures of 200 kPa and 400 kPa. At all other studied densities smaller than 1.5 Mg/m^3, a consistent collapse with time was observed under various inundation pressures.

In summary, the studied kaolin exhibited three distinct volume change characteristics depending upon the compaction densities and the applied inundation pressures. In the first case, consistent swelling was observed due to inundation. Secondly, there was an initial collapse followed by swelling until the equilibrium. In the third case, a consistent collapse is due to inundation.

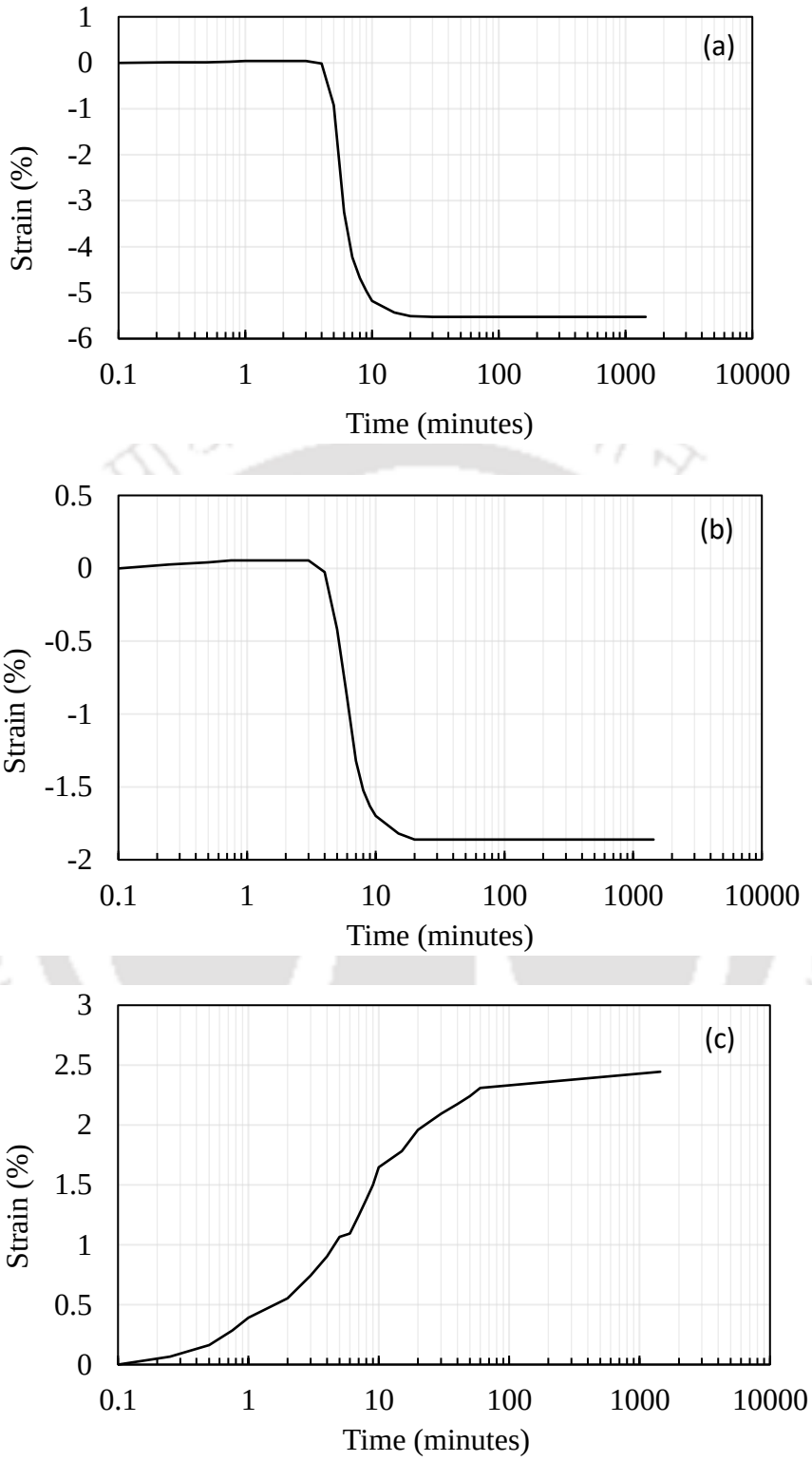

Fig. 9.3 Temporal variation of the wetting-induced volumetric strain of studied kaolin initially compacted to 1.5 Mg/m^3 under (a) 10 kPa (b) 100 kPa and (c) 200 kPa vertical pressure.

9.3 Assessment of kaolin behavior based on the BBM model

The existing critical state-based elastoplastic model for unsaturated soil behavior, commonly known as the Barcelona basic model (BBM) model (Alonso, 1990; Wheeler and Shivakumar, 1995) has been widely used to model the volume change behavior of unsaturated soil. The original model was developed based on the assumption that the volumetric path of an unsaturated soil reaches the saturated compression line upon wetting (suction decrease) under any given loading when represented in 'e-P' space (Alonso, 1990). The compressibility characteristics at the two suction stress states, the initial partially saturated case (suction = s) and the fully saturated case (suction = 0), are thus utilized to model the volumetric deformation of unsaturated soil. Many studies are carried out to utilize the BBM model to study the behavior of both collapsible soil and expansive soils (Josa et al., 1992; Wheeler and Shivakumar, 1995; Sun et al., 2003). The soil response considered in these studies was, however, either under the isotropic stress state or soils with a moderate initial suction value i.e., compacted at the near optimum moisture content (OMC) or maximum dry density (MDD). Modeling the wetting-induced volumetric response of air-dry compacted kaolin by using the BBM model is not attempted so far. This section presents a qualitative assessment of modeling the observed kaolin behavior based on the existing BBM model.

The compressibility characteristics of the studied kaolin at initial air-dry (s = 44 MPa) and saturated (s =0) state were presented along with the observed volumetric path during the wetting under constant loadings at the compaction densities of 1.25 $Mg/m^{3,}$ and 1.5 Mg/m^3 in Fig. 9.4a & 9.4b, respectively. Consolidation tests were carried out after saturating the compacted specimens of kaolin under a small seating load of 5 kPa at both the compaction densities. A minimal collapse (~1%) was recorded at the lower compaction density (1.25 Mg/m^3), and the saturated compression line was consistently below the air-dry compression in the considered range of inundation pressure (Fig. 9.4a). The two compression lines converged at a very small pressure (< 5 kPa) and started diverging with the increase in the inundation pressure. Except for 10 kPa, under all the inundation pressures, the volumetric path of the studied kaolin approached the saturated compression line in the 'e-log (P)' plot. However, the post-wetting equilibrium points never reached the saturated consolidation line under the inundation pressure of 200 kPa or higher, which was just after the observed yield point on the air-dry compression line (Fig. 9.4a). Under 10 kPa inundation

pressure, on the other hand, the volumetric path of the studied kaolin moved below the saturated compression line at this density.

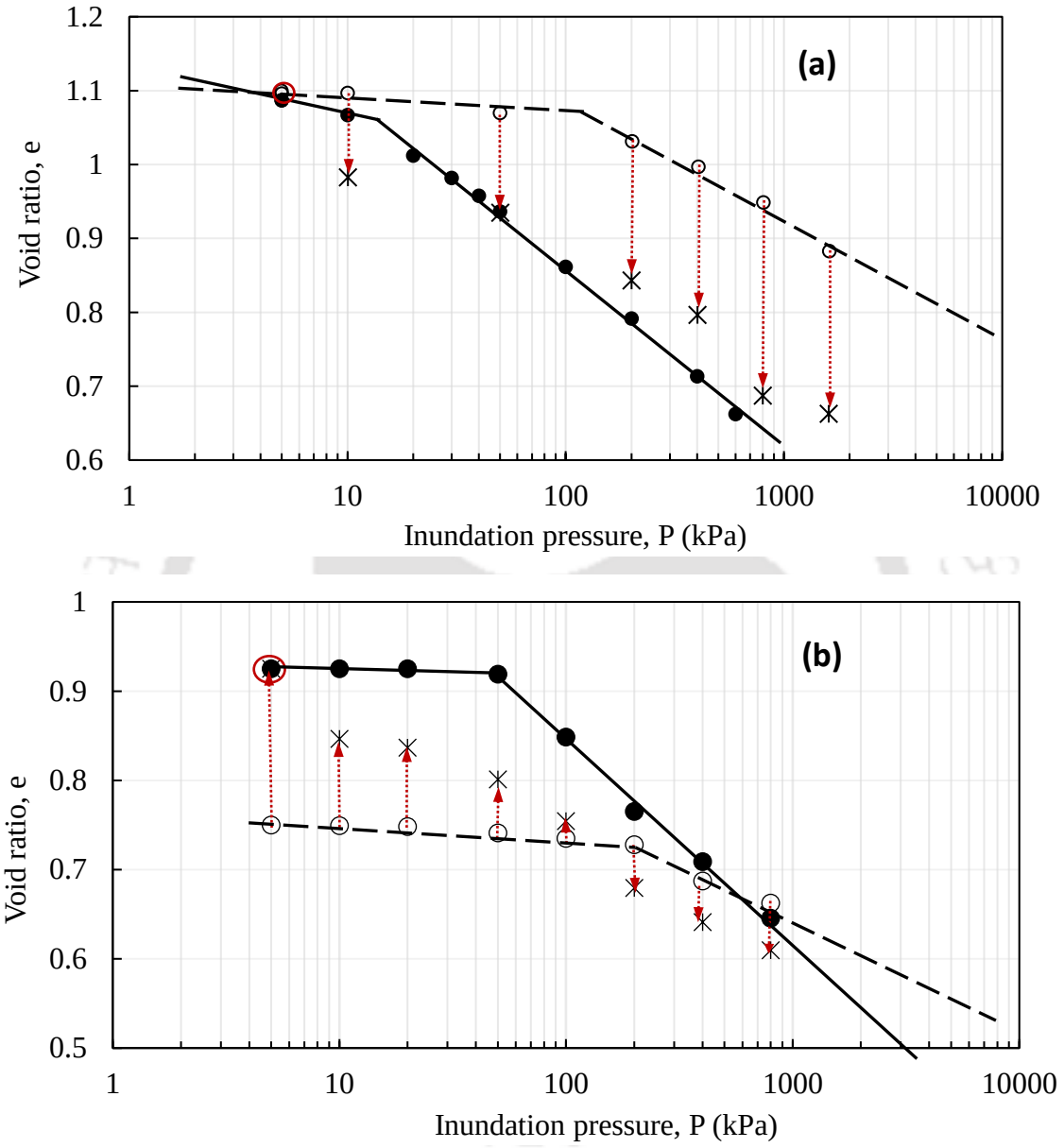

Fig. 9.4 Volumetric path of kaolin under different hydro-mechanical stress-state at (a) 1.25 Mg/m^3, and (b) at 1.5 Mg/m^3 dry density.

At the higher compaction density of 1.5 Mg/m^3, a considerable swelling strain (~10%) was observed during the saturation under 5 kPa. The saturated line was initially above the air-dry compression line and crisscrossed at around 600 kPa (Fig. 9.4b). The observed wetting-induced volumetric paths of kaolin at this compaction density were towards the saturated compression line

exhibiting swelling line under inundation pressures up to 100 kPa. However, the equilibrium points never reached the saturation line under all the inundation pressures. At 200 kPa or higher inundation pressure, on the other hand, the volumetric path did not follow the saturation line and exhibited collapse under the studied inundation pressures. Overall, the volumetric paths under different inundation pressures did not always reach the saturated compression line for the kaolin against the typical soil response considered in the BBM model. The transition from swell to collapse with an increase in the inundation pressure did not coincide with the crisscrossing pressure of the compression lines at the two suctions at 1.5 Mg/m^3 (Fig. 9.4b). This was rather related to the yield point on the air-dry compression line. The existing elastoplastic framework in the present form, therefore, is not applicable for the volumetric behavior of the studied air-compacted kaolin. A comprehensive understanding of the observed behavior of the kaolin is essential to identify the influencing parameters, which can be suitably incorporated in the model and can be extended to model the kaolin behavior. A detailed analysis based on the surface forces was presented in the next section to bring out the microstructural mechanisms involved during the wetting-induced volumetric process of the kaolin.

9.4 Microstructural investigations

A quantitative analysis on the microstructural changes in the compacted kaolin during the air-dry compaction, and wetting-induced volumetric collapse, and swelling was carried out based on the pore size distribution and the fabric changes. The PSD data were presented in terms of differential intrusion volume (dv/dlogD) vs pore entry diameter (D), and bar diagram showing pore volume contribution by various pore-size classes as well. The dual porosity concept by identifying micro-pores and macro-pores is often adopted in the available microstructural literature studies on kaolin behavior. However, delimitation between the two pore-size classes is not well-defined for the kaolin. For example, Shivakumar et al. (2010) considered 2 μm as the delimitation between the micro-pores and macro-pores for kaolin compacted at MDD-OMC. On the other hand, Pedrotti and Tarantino (2018, 2019) classified the micro-pores and macro-pores with an approximate delimitation in the ranges of 0.2-0.5 μm. Additionally, the wetting-induced volumetric deformation of kaolin is related to the changes in the mode of particle-particle association in the recent past studies (Choudhury and Bharat, 2018; Pedrotti and Tarantino, 2018). Kaolin exhibits a complex microstructure with different modes of particle-particle association due to the presence

of strong columbic forces in the air-dry state. Thus, classification of pore-size classes based on the mode of particle-particle association is necessary to provide a comprehensive understanding of the microstructural mechanisms behind the kaolin response under the hydro-mechanical stress state. In this analysis, four pore-size classes, viz., fine intra-aggregates (<0.05 μm), coarse intra-aggregate pores (0.05-0.1 μm), fine inter-aggregate pores (0.1-0.5 μm), and coarse inter-aggregate pores (>0.5 μm), were identified in the available pore size range based on the observed PSDs and fabric images of the studied kaolin.

9.4.1 Influence of compaction density

The pore-size distribution of the kaolin in the '*as-compacted'* condition at the different compaction densities of 1.25 and 1.5 Mg/m^3 were presented in Fig. 9.5a in terms of differential intrusion volume (dv/dlogD) vs pore entry diameter (D). A unimodal distribution was observed in the size range of 0.01- 1μm for both the compaction densities. The peak shifted towards the left with an increase in the compaction density indicating the reduction of the larger pores under the applied compression energy. Further, the changes in the microstructure were analyzed through the characterization of various pore size classes based on the fabric images from FESEM (Fig. 9.5c) and the contributed specific pore volume by various pore size classes (Fig. 9.5b). The dominant presence of the pore-size classes, >0.5 μm and 0.1–0.5 μm at the inter-aggregate pores was evident from the FESEM images at 1.25 Mg/m^3 (Fig.9.5c). Larger pores of ~ > 1 μm size that contribute to the open 'card house' structure were significantly present at this compaction density. The pores contributing to the open card-house structure are often referred to as the 'meta-stable' pores as their stability is significantly reduced upon wetting and contributes to the macroscopic collapse under the loading. These pore-sizes, however, were not reflected in the PSD curve from the MIP testing (Fig. 9.5a). This could be possibly due to the collapse of the meta-stable card-house structures during the mercury intrusion under the high applied pressures. Further, much larger pores remained undetected due to the limitations associated with the MIP testing (Koliji et al. 2012; Farulla & Rosone, 2012). The measured total specific pore volume at 1.25 Mg/m^3 was, thus, found to be smaller than the actual pore volume calculated based on the dry density as presented in the bar diagram (Fig. 9.5b). The undetected porosity (UDP) was illustrated by the shaded area on the top of the bar diagram. Overall, the pore-size class of >0.5 μm, mostly exists among the coarse aggregates with edge-face and edge-edge associations whereas the finer size class of 0.1–0.5μm,

was observed among the smaller aggregates with a more closed edge-face association. The much finer pore size classes of 0.05–0.1μm and <0.05μm exist in the intra-aggregate spaces of the compacted kaolin.

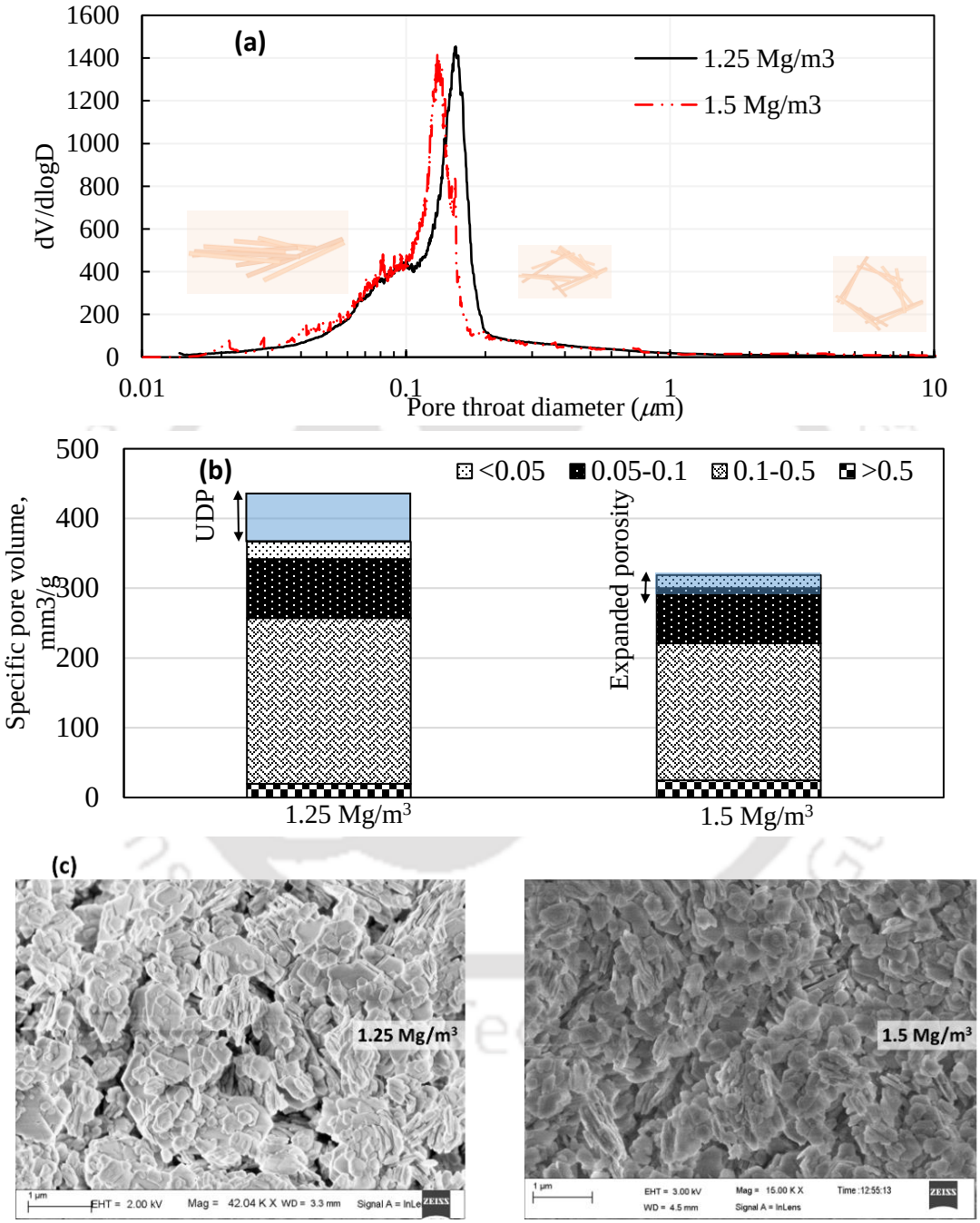

*Fig. 9.5 (a) Pore size density function, (b) intruded pore volume of different pore-size classes, and (c) fabric image of the studied kaolin at **1.25 Mg/m³** and **1.5 Mg/m³** in 'As-compacted' condition.*

The FESEM image at 1.5 Mg/m^3 suggested a considerable reduction in the inter-aggregate pores as the aggregates were spaced more closely at this density (Fig. 9.5c). The application of much higher uniaxial pressure (15 MPa) at this density lead to compression of the inter-aggregate pores that were earlier present in the relatively loose compacted state (1.25 Mg/m^3). A considerable reduction in the intruded pore volume of the fine inter-aggregate pore size class (0.1–0.5 μm) was observed from 1.25 Mg/m^3 to 1.5 Mg/m^3 (Fig. 9.5b), which was also reflected by the leftward shift in the differential intrusion volume curve in Figure 9.5a. The reduction of the much coarser inter-aggregate pore size class (>0.5μm) was not reflected in the bar diagram as the majority of the pores (the pores in the 'card house' structures) in this pore-size class remained undetected as explained earlier. At 1.5 Mg/m^3, however, the measured total specific pore volume was higher than the actual pore volume. The excess porosity was attributed to the expansion/rebound of the compacted specimen after the release of the compaction load. The increased porosity due to the rebound of the compacted specimen was termed as the expanded porosity and indicated by the shaded portion on the bar diagram in Fig. 9.5b. Overall, the pore size classes, 0.05–0.1 μm and 0.1–0.5 μm dominated the total porosity from the MIP analysis for both the compaction densities (Fig. 9.5b). Overall, the coarse inter-aggregate pores (>0.5 μm) with an open 'card-house' structure were significantly present at the lower compaction densities (<=1.25 Mg/m^3). Air-dry compaction resulted in compression of the inter-aggregate pore-size classes (>0.5 μm and 0.1–0.5μm) in the studied kaolin. The particle-particle association at the inter-aggregate pores shifted from edge-face to face-face manner under the applied mechanical pressure. At 1.5 Mg/m^3, these large pores were compressed to form a more closed pore-structure (0.1-0.5μm) with the edge-face association still existing at the inter-aggregate contacts.

9.4.2 Microstructural changes due to inundation

The PSDs and fabric of the kaolin specimen in '*as-compacted*' condition and 'post-collapse' under 400 *kPa* inundation pressure at 1.25 Mg/m^3 compaction density were compared in Fig. 9.6. The peak of the differential PSD curve shifted leftwards for the 'post-collapse specimen' indicating the transformation of the larger pores into smaller pore sizes during the collapse (Fig. 9.6a). The pore volume contributed by various pore size classes was presented in Fig. 9.6b in the form of a bar diagram. In the case of 'post-collapse' specimen under 400 kPa, the measured total pore volume was found to be approximately 5% in excess of the actual porosity, illustrated by the shaded portion

at the top of the bar. The actual porosity in the case of 'post-collapse' specimen was estimated based on the corrected dry density by considering the deformation due to wetting under the inundation pressure. The small amount of excess porosity could be due to the slight rebound observed after removing the load for extracting the kaolin specimen. A significant reduction in the intruded pore volume of the inter-aggregate pore size class of 0.1–0.5μm was observed in the 'post-collapse' specimen as compared to the 'as-compacted' specimen (Fig. 9.6b). The pore volume of the immediate finer pore-size class, 0.05–0.1μm, on the other hand, was higher in the 'post-collapse' specimen. Comparison between the FESEM images of the kaolin specimens at 'as-compacted' and 'post-collapse' conditions also suggested a significant reduction of the inter-aggregate pore size classes (>0.5μm and 0.1–0.5 μm) during the wetting-induced collapse under 400 kPa (Fig. 9.6c). The reduction of the coarse inter-aggregate pore-size class (>0.5μm) was not reflected in the bar diagram due to the UDP of 'as-compacted' specimen, explained earlier.

The kaolin particles were found to be shifted more towards a face-face manner after the wetting-induced collapse (Fig. 9.6c). A significant reduction in the intruded pore volume of the inter-aggregate pore-size classes of >0.5μm, and 0.1–0.5μm and consequent increase in the pore volume of the finer pore-size class, 0.05–0.1μm was an indication of the collapse of the inter-aggregate pores. Thus, the inundation of the studied kaolin compacted at 1.25 Mg/m^3 caused the collapse of the inter-aggregate structure under 400 kPa pressure, which lead to the macroscopic volume reduction.

The PSDs and fabric of kaolin specimen compacted at 1.5 Mg/m^3 and under three different hydro-mechanical stress-states of 'as-compacted', post-swelling under 10 kPa, and post-collapse under 400 kPa, were compared in Fig. 9.7. The peaks of the differential PSDs shifted towards the left with respect to the 'as-compacted' condition for both the 'post-swelling' and 'post-collapse' specimen (Fig. 9.7a). This suggested that the inter-aggregate pores decreased during the observed volumetric swelling as well as the collapse. The post-collapse specimen exhibited a much higher peak in the intra-aggregate pore-size range (< 0.1μm) as compared to the 'post-swelling' specimen indicating the possible collapse of the inter-aggregate pores.

Further, the broad peak in the post-swelling specimen suggested a gradual reduction of inter-aggregate pores in the post-swelling specimen. The porosity contribution of various pore size

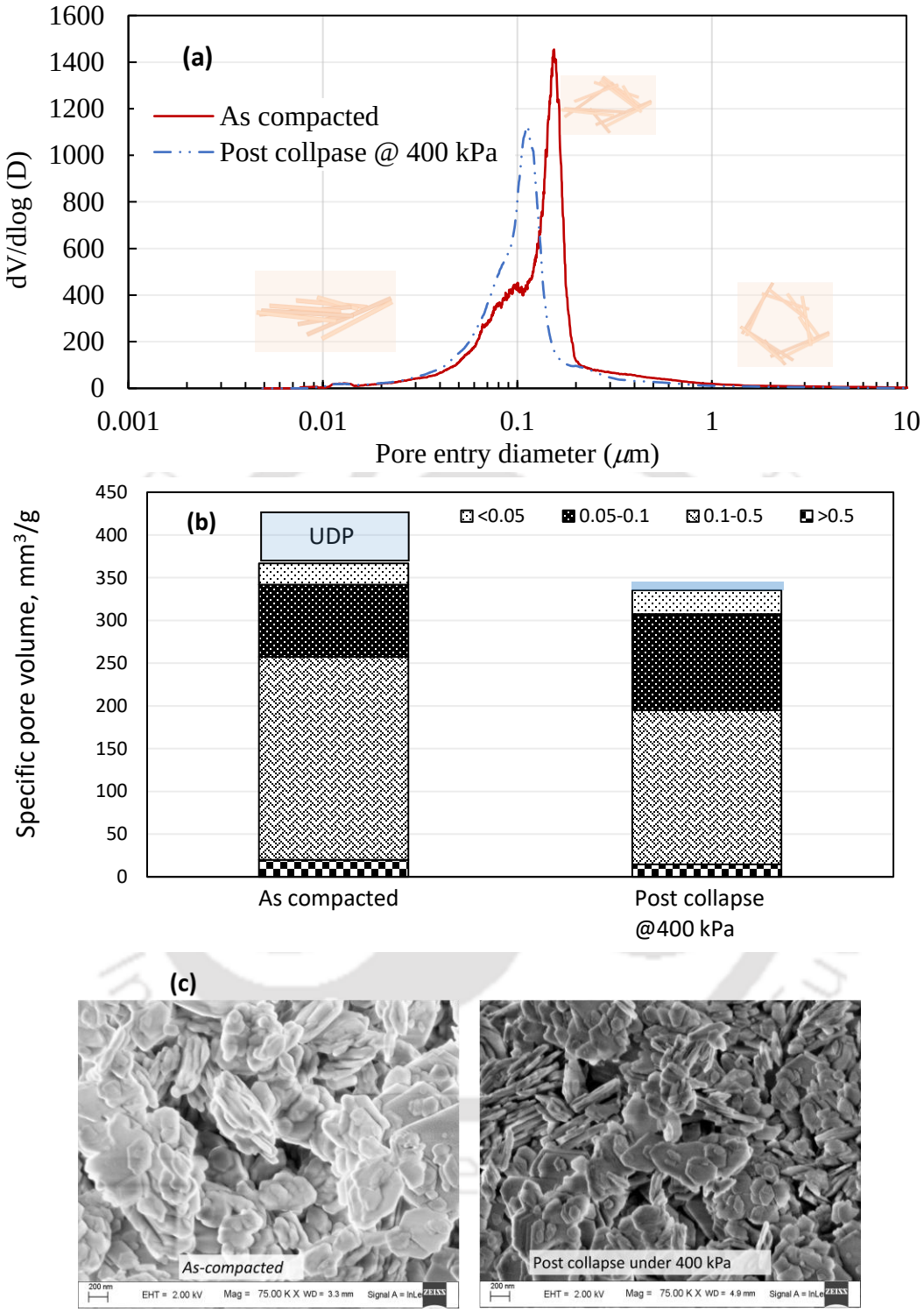

Fig. 9.6 (a) Pore size density function, (b) intruded pore volume of different pore-size classes, and (c) fabric image of the studied kaolin compacted to 1.25 Mg/m^3 in 'As-compacted' condition and after collapse under 400 kPa.

classes were presented as a bar diagram in Figure 9.7b. The pore volume of the coarse inter-aggregate pore size class (0.1–0.5 μm) was significantly reduced in the 'post-swelling' specimen under 10 kPa inundation pressure. The immediate fine intra-aggregate pore-size class (0.05–0.1 μm) and the coarse inter-aggregate pore size class (>0.5 μm), showed an increase in the intruded pore volume (Fig. 9.7b). The FESEM image of 'post-swelling' specimen exhibited a more open inter-aggregate structure as compared to the 'as-compacted' specimen (Fig. 9.7c). Due to the formation of large inter-aggregate pores, a considerable amount of UDP was observed for the 'post-swelling specimen (Fig. 9.7b). The overall inter-aggregate structure of the kaolin compacted at 1.5 Mg/m^3 remained intact during the wetting under 10 kPa inundation pressure. The repulsive pressure at the finer intra-aggregate pores leads to expansion of the pore-size class of <0.05 μm and increased pore volume of the immediate coarser intra-aggregate pore-size class (0.05–0.1μm). The developed repulsive pressure was further experienced at the inter-aggregate contacts leading to expansion of certain inter-aggregate pore-structures under the small inundation pressure of 10 kPa (Fig. 9.7c).

Meanwhile, the inter-aggregate pore size classes were also invaded by the swelling of hydrated kaolin particles as well as the aggregates. Overall, this led to a decrease in the pore volume of the fine inter-aggregate pore-size class of 0.1-0.5 μm and increased pore volume of the coarse inter-aggregate pore-size class (> 0.5 μm) (Fig. 9.7b). The 'post-collapse' specimen under 400 kPa at this density showed a significant reduction in the inter-aggregate pore-size classes (>0.5μm and 0.1–0.5μm) and an increase in the pore volume of the intra-aggregate pore-size class, 0.05–0.1 μm (Fig. 9.7b), similar to the 1.25 Mg/m^3 density. Similarly, the FESEM image also revealed shifting of the kaolin particles more towards the face-face manner following the collapse due to saturation (Fig. 9.7c).

In summary, wetting of the compacted kaolin resulted in collapse as well as swelling of the coarse inter-aggregate pores (>0.1μm) depending upon the compaction density and inundation pressure. The collapse and swelling of the coarse inter-aggregate pore-size class were directly related to the observed volumetric collapse and swelling of the studied kaolin. The variation in the surface force magnitude from the initial air-dry state to the full saturation controlled the pore evolution process. A detailed discussion on the surface forces influencing the kaolin behavior is presented in the next section.

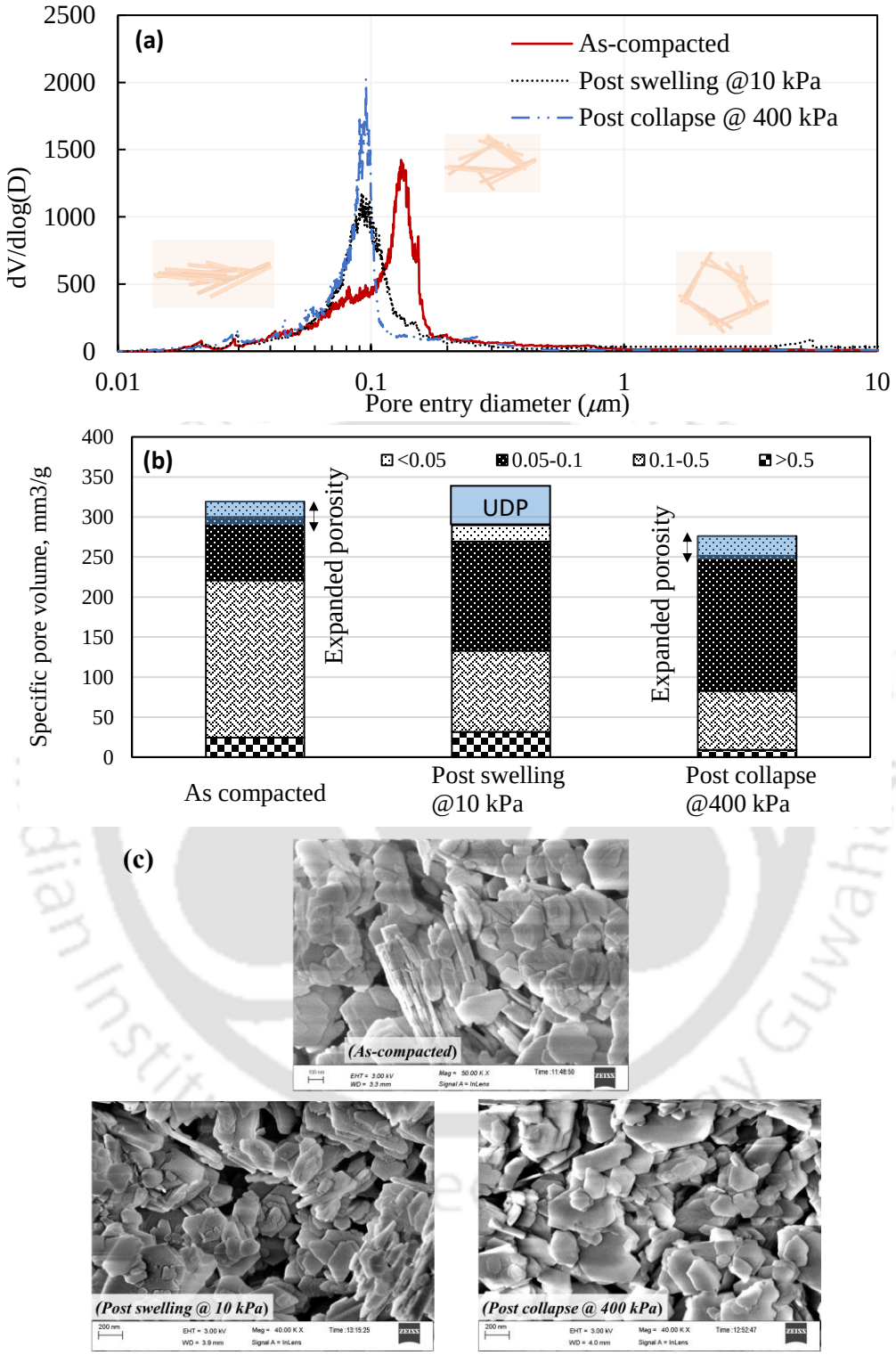

Fig. 9.7 (a) Pore size density function, (b) intruded pore volume of different pore-size classes, and (c) fabric image of the studied kaolin compacted to 1.5 Mg/m^3 under different hydro-mechanical stress-state.

9.5 Surface forces

Relevant surface forces at various pore scales of the studied kaolin were evaluated to understand the observed volume change behavior under the influence of compaction density and inundation pressure.

Columbic forces are significant in kaolin because of the complex charge characteristics on the surfaces of kaolinite particles (Celik, 2004; Choudhuri and Bharat, 2018; Delgado et al., 1986, Ramos-Tejada et al., 2001, 2002, Kelessidis et al., 2007; Gupta, 2010). The edge-face, edge-edge, and face-face particle-particle associations are commonly observed in compacted kaolin at various pore-scales (Carty, 1999; Santamarina et al., 2002; Palomino and Santamarina, 2005; Choudhury and Bharat, 2018; Pedrotti and Tarantino, 2018). 'Meta-stable' card-house structures are often observed in kaolin at air-dry states which are primarily attributed to the strong columbic attractions at the edge-face and edge-edge contacts of the inter-aggregate pores (Choudhury and Bharat, 2018; Pedrotti and Tarantino, 2018). The studied kaolin was dominated by the 'meta-stable' card–house structures at lower compaction densities (Fig. 9.8) The stability of these inter-aggregate pore structures primarily depends on the bond strength at the inter-aggregate contacts attributed by the surface forces. As the capillary forces and the DDL repulsion are absent in the air-dry state, the VdW and columbic attractive forces are the primary attributing forces. The columbic attraction, however, is lost at full saturation as the charges on the edges of the kaolin particles become negative (edge-IEP of the studied kaolin ~ 5.3). This significantly reduces the bond strength at the inter-aggregate contacts leading to alteration in the inter-aggregate pore structures under the applied stress. At full saturation, the VdW attractive forces and the long-range DDL repulsion primarily control the kaolin microstructure. The magnitude of these two types of forces in the studied kaolin in the air-dry state and fully saturated state was evaluated at various pore scales and presented below.

The DDL repulsive forces are absent at air-dry states. The inter-particle attractive pressure due to the VdW attraction at the inter-aggregate pores was estimated using Eq. 14. The parallel plate theory in Eq. 14 was valid at the intra-aggregate pores of the studied kaolin (Fig. 9.8). Hamaker's constant was taken as ~14*10-20 J for air and ~6.7*10-20 J for water as the intervening medium for the air-dry and saturated states, respectively (Israelachvili, 2011). The pressure due to the VDW attraction becomes significant when the separation distance between the parallel kaolin particles

is ⩽ 0.01 μm (Fig. 9.9). The attractive pressure at a given separation distance was relatively smaller in the fully saturated condition as compared to the air-dried state. At the inter-aggregate pores, however, the estimation of the pressure due to VdW forces becomes complex due to the edge-face association and variation in the aggregate sizes (Yang et al., 2015). A recent discrete element method (DEM) simulation study presented the variation of VdW attractive forces between non-parallel kaolin particles for the relative orientation (inclination angle) of kaolin particles (Jaradat and Abdelaziz, 2019). The estimated VdW forces at different inclination angles were used in this study to estimate the VdW attractive pressure acting on the kaolin particles at the inter-aggregate contacts of various pore-size classes. The variation of VdW attractive pressure with particle inclination was presented in Fig. 9.10. The particle inclination angle existing at pore configurations was approximately identified based on the fabric image and indicated on the plot. The VdW attractive pressure increases exponentially as the particle association shifts towards a face-face manner.

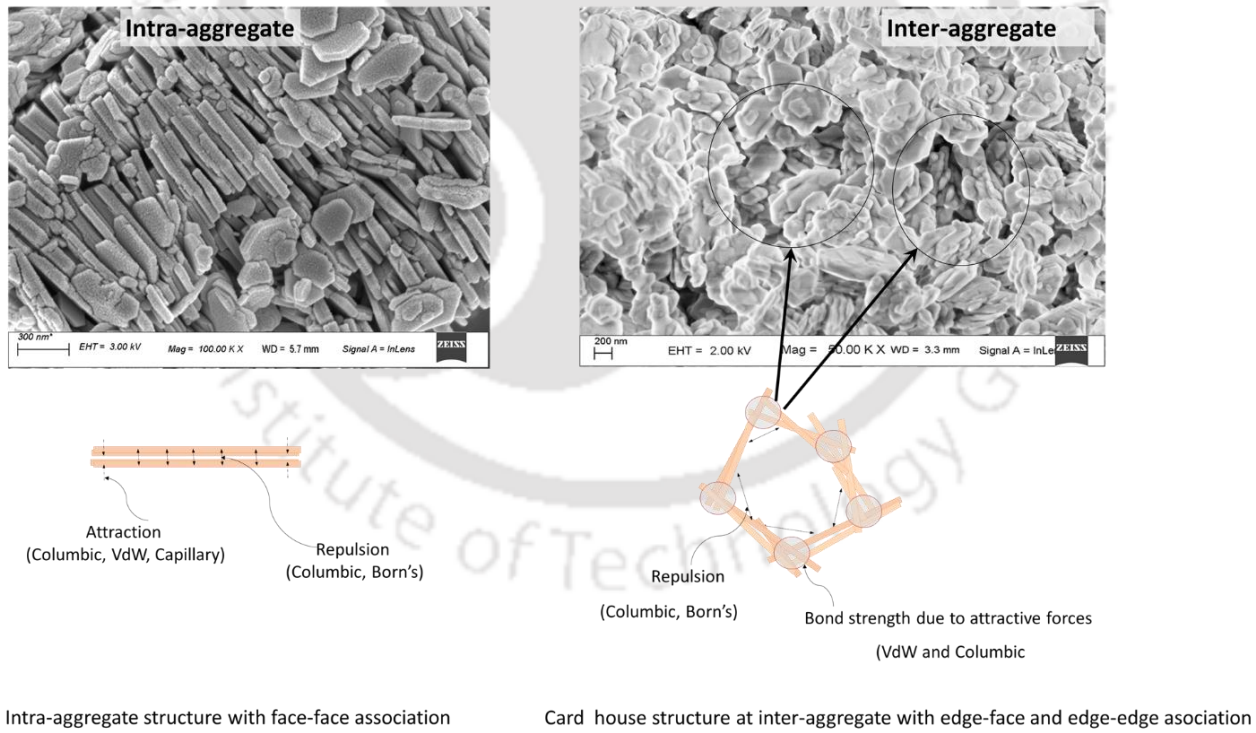

Fig. 9.8 Particle-particle association at the intra-aggregate and inter-aggregate pores of compacted kaolin.

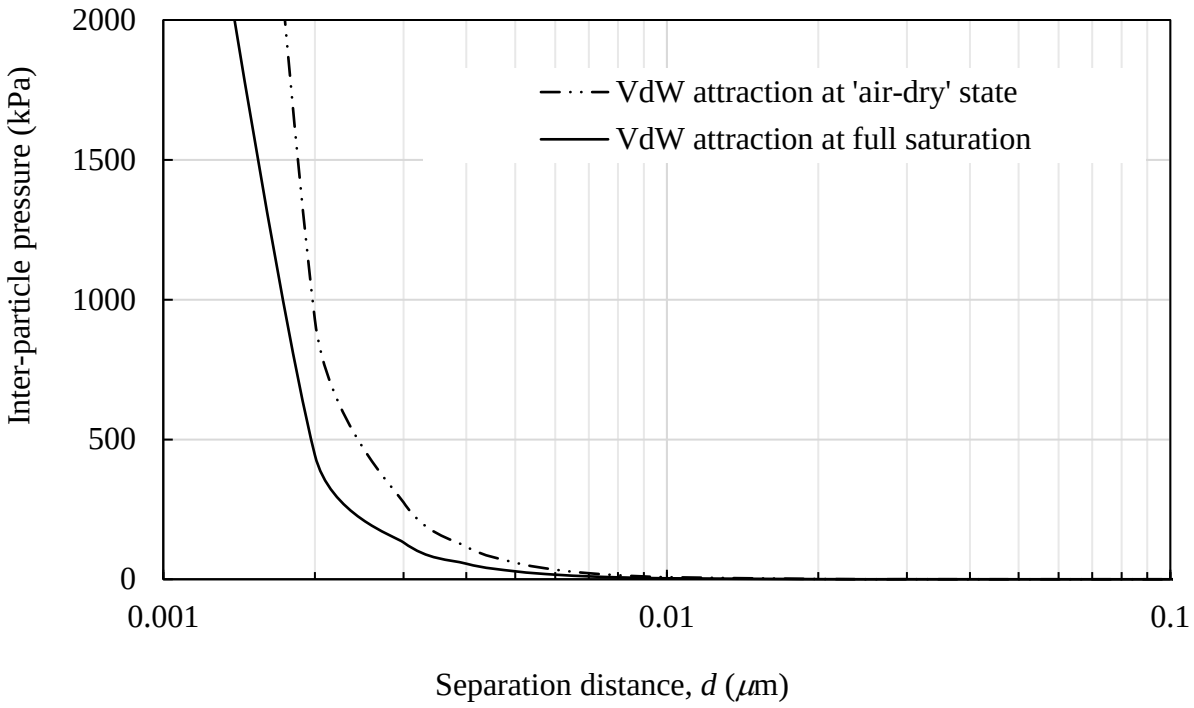

Fig. 9.9 Variation of van der Waal's attractive force with separation distance in air-dry and fully saturated kaolin

At full saturation, the VdW forces are reduced significantly (Fig. 9.9) and the long-range repulsive pressure develops at the finer pores. The variation of the magnitude of the repulsive and attractive forces with separation distance is presented in Fig. 9.11. The repulsive pressure was computed from the Gouy Chapman DDL theory assuming parallel plate arrangement, which is valid for the considered range of separation distance as observed within the intra-aggregate pore-size classes (< 0.1 μm). The repulsive pressure at a given separation distance was estimated by trial and error following the steps described in the flowchart presented in Fig. 2.13. A net repulsive pressure develops at full saturation in the pore-size range of 0.002μm– 0.05μm. At a separation distance of <0.002 μm, the VdW attraction becomes dominant which is counter-balanced by the passive Steric repulsion. A net repulsive pressure as high as ~100 kPa is generated at the intra-aggregate pores of the studied kaolin upon full saturation.

The kaolin particles-particle association shifted from the edge-face and edge-edge manner toward a face-face arrangement during the air-dry compression causing a significant reduction of the large-interaggregate pore-size classes. The shifting of the kaolin particle-particle association during the compression is illustrated in Fig. 9.12a. In an air-dry state, the capillary forces can be

neglected as the hygroscopic moisture is very small (~2%). The compaction energy was needed to work against the columbic repulsion at the edge-face joint, columbic repulsion between the faces of kaolin particles, and the VdW attractions which hold the inter-aggregate pore structures. As the particles are gradually brought towards parallel orientation under applied mechanical stress, the VdW forces among the kaolin particles at the inter-aggregate joints increases (Fig. 9.10).

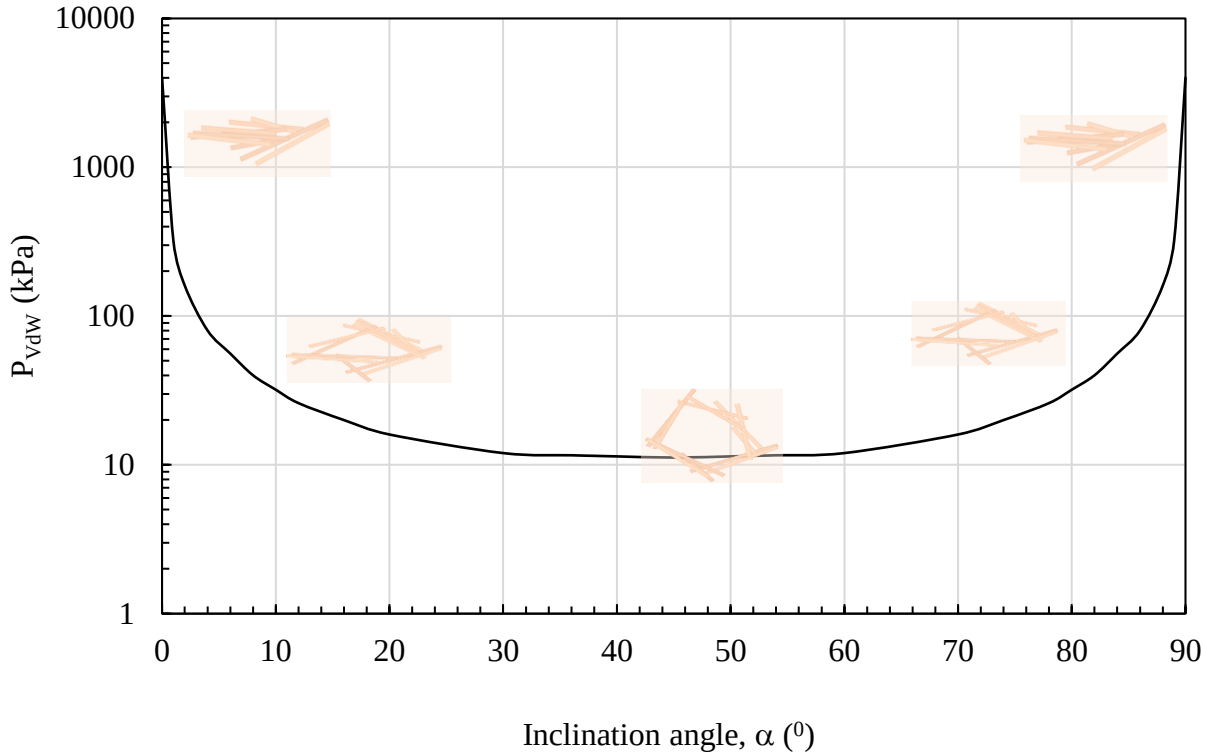

Fig. 9.10 Variation in the magnitude of VdW attraction at the inter-aggregate contacts with change in the particle inclination angle in air-dry kaolin (After Jaradat and Abdelaziz, 2019).

Meanwhile, the columbic repulsion among the faces of kaolin particles increased as the kaolin particles are brought closer and towards the face-face manner. Thus, a new stress equilibrium is established following the compaction, with an increased VdW attraction at the inter-aggregate pores. The increased VdW attraction prevents the rebound of the kaolin particles to the earlier configuration when the applied mechanical stress is released and maintains the newly established microstructure. Further compression requires a much higher amount of energy to overcome the strong columbic repulsion between the faces of the kaolin particles. At very high compaction densities, apart from the columbic repulsion, the born's repulsion is also mobilized at the intra-aggregate pores once the inter-aggregate pores were completely compressed. The intra-aggregate pores (<0.1 μm) remained unaffected during the air-dry compaction due to the strong columbic

and born repulsion acting against the applied stress. Thus, an exponential relationship between the applied mechanical pressure and the compaction density was observed for the studied kaolin (Fig. 9.13).

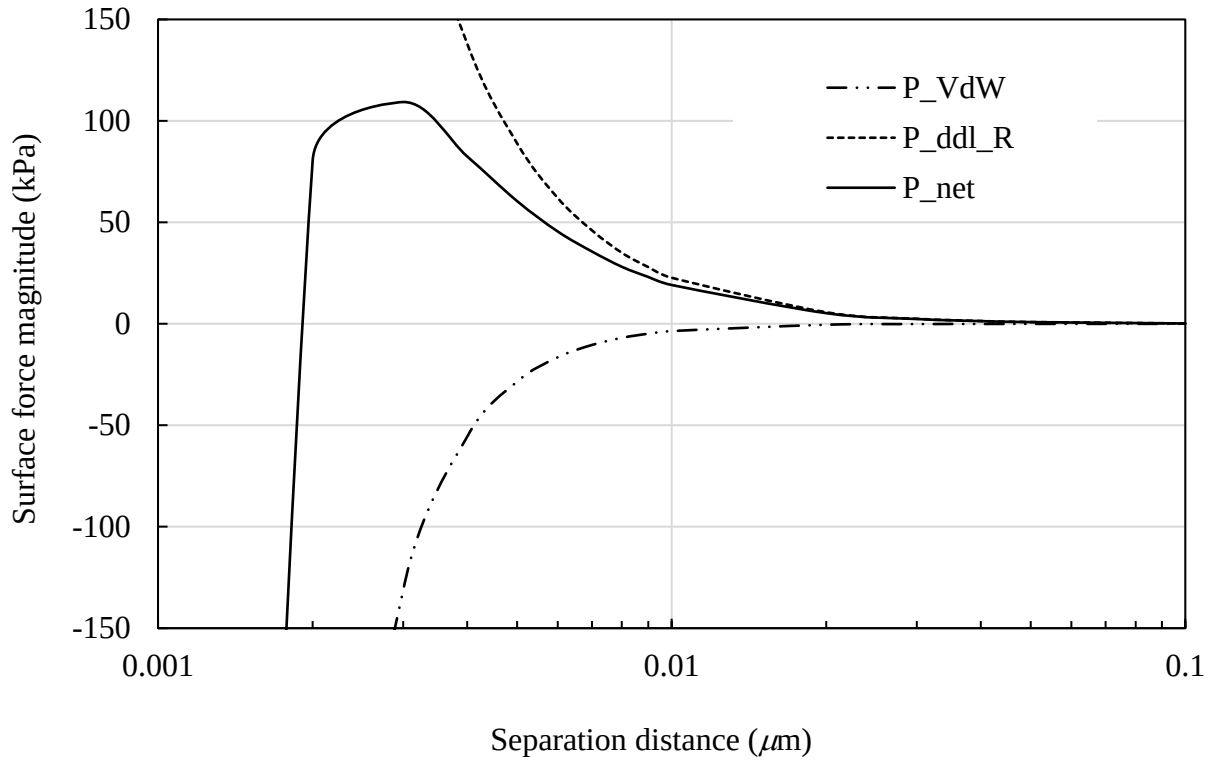

Fig. 9.11 Variation in surface force magnitude with distance in the saturated pores of kaolin with a face-face orientation (intra-aggregate pores).

The edge-face columbic attraction and capillary forces at the inter-aggregate contacts were completely lost and the VdW attraction was significantly reduced at full saturation (Fig. 9.9). Thus, bond strength at the inter-aggregate contacts which provides the resistance against the mechanical loading reduced considerably following the inundation. The inter-aggregate structure collapses when the applied mechanical stress exceeds the bond strength at the inter-aggregate contacts contributed by the VdW attraction at full saturation. The inter-aggregate bond strength increased from coarse pore-size to finer pore-size classes as the VdW attraction increased with the shift in the particle-particle orientation (Fig. 9.9). The microstructural evolution during the wetting under two different inundation stresses at lower and higher compaction densities is illustrated in Fig. 9.12b and 9.12c. The coarse inter-aggregate pores (> 0.5 μm) were significantly present in the studied kaolin at lower compaction densities (≤ 1.25 Mg/m^3). The VdW attraction at the coarse

inter-aggregate pores (> 0.5 μm) is approximately 10 kPa in the air-dry state (Fig. 9.9) which is significantly reduced at full saturation. This coarse inter-aggregate pore-size class, therefore, collapsed following the wetting under 10 kPa inundation pressure and thus exhibited volumetric collapse under 10 kPa inundation pressure. The volumetric collapse was higher for lower compaction density as the number of the coarse pores (> 0.5 μm) was more. At a given density, the magnitude of the volumetric collapse increased with an increase in the inundation pressures as more pore-size classes i.e., the finer inter-aggregate pores were collapsed under the increased mechanical stress. However, the coarse inter-aggregate pores were significantly compressed during the air-dry compression at higher inundation pressure before the wetting. This significantly reduced the collapsible inter-aggregate pores and increased the bond strength at the inter-aggregate pore structures. Due to this, the collapse magnitude initially increased to a peak value under an intermediate inundation pressure and decreased with a further increase in the inundation pressure.

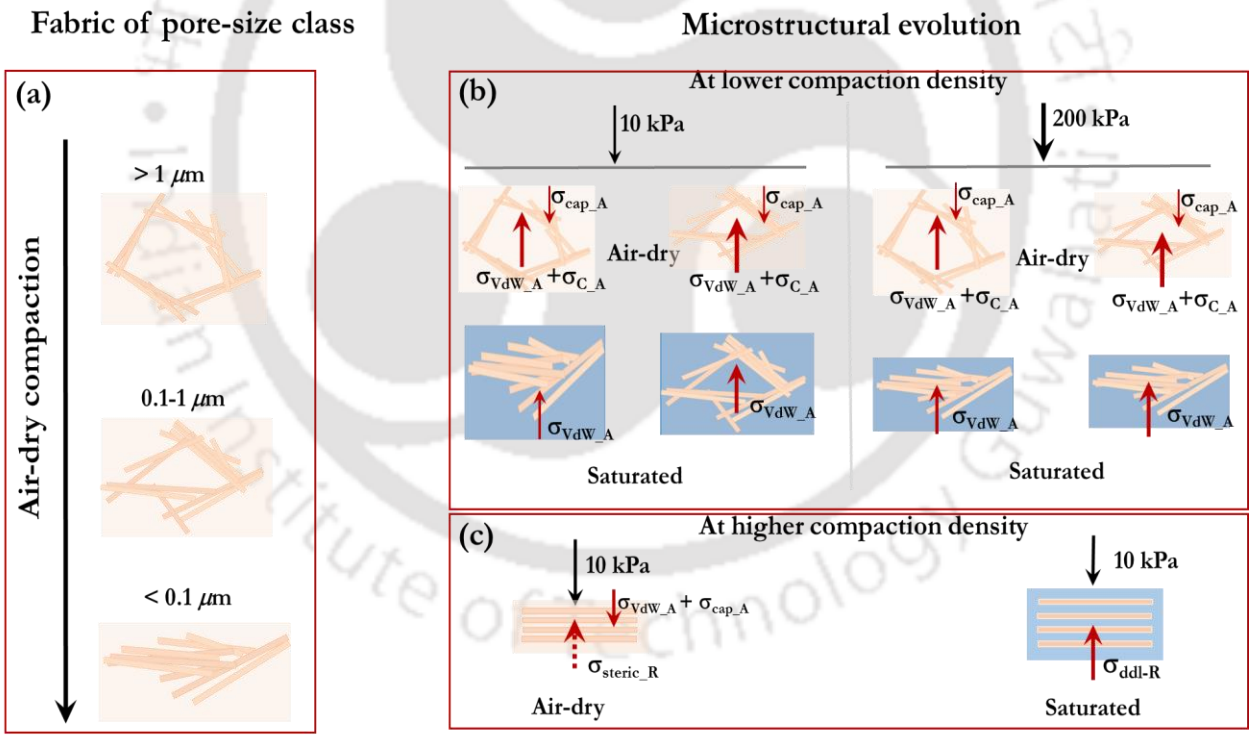

Fig. 9.12 Illustration showing (a) fabric changes in air-dry kaolin during uniaxial compression, (b) wetting–induced deformation of meta-stable card-house structure at lower compaction density, and (c) swelling of intra-aggregate finer pores at higher compaction density.

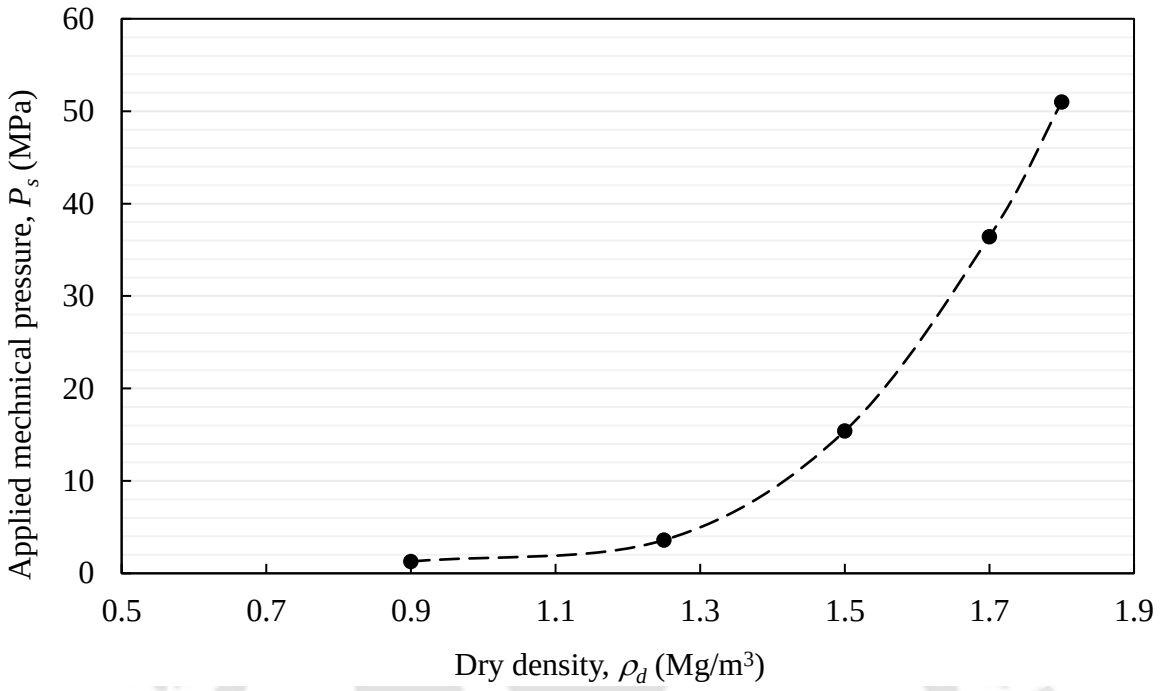

Fig. 9.13 'Compaction energy-dry density' relationship of the kaolin soil from the uniaxial static compression test in the air-dry state.

At 1.5 Mg/m^3, the meta-stable 'card house' structures are absent at the inter-aggregate pore-size class (>0.5μm). A small percentage (~7.5%) of the coarse inter-aggregate pore-size class (>0.5μm) with the edge-face association at a relatively smaller inclination angle were present at this density. The VdW attraction at these pores is in the range of 10–157 kPa. The VdW attraction at the finer inter-aggregate pore-size class (0.1–0.5 μm), which had a 61.5% contribution to the total porosity, is in the range of 157–394 kPa. The overall inter-aggregate pore structure remained intact during saturation under inundation pressures value of up to 100 kPa. Under this condition, the overall aggregates swelled due to the surface and cation hydration and DDL repulsive pressure at the finer intra-aggregate pores. An overall swelling was observed when the net repulsive pressure exceeds the applied mechanical stress. Similarly, at 1.7 Mg/m^3, volumetric swelling was observed at a lower inundation pressure up to 400 kPa, beyond which a minimal volumetric collapse was recorded. The inter-aggregate bond strength increased at this high compaction density as the inter-aggregate pores were compressed significantly.

The volume change behavior of kaolin was further studied in the presence of three different pore fluids viz., water, ethanol, and kerosene that exhibit different di-electric properties to further confirm the influence of repulsive pressure and VdW pressure on the volumetric behavior. In the

presence of the two pore-fluids other than water, which has a dielectric constant of 1 and 10 respectively, kaolin did not exhibit any significant collapse up to 800 kPa inundation pressure (Fig. 9.14). This was due to the much higher VdW attraction in the presence of the low di-electric pore fluids as compared to water. Thus, the inter-aggregate pores remained intact during the wetting under all the inundation pressure considered in this study. The repulsive pressure, however, decreased with the dielectric constant thus lower swelling was observed for the lower dielectric pore fluid under any given inundation pressure (Fig. 9.14).

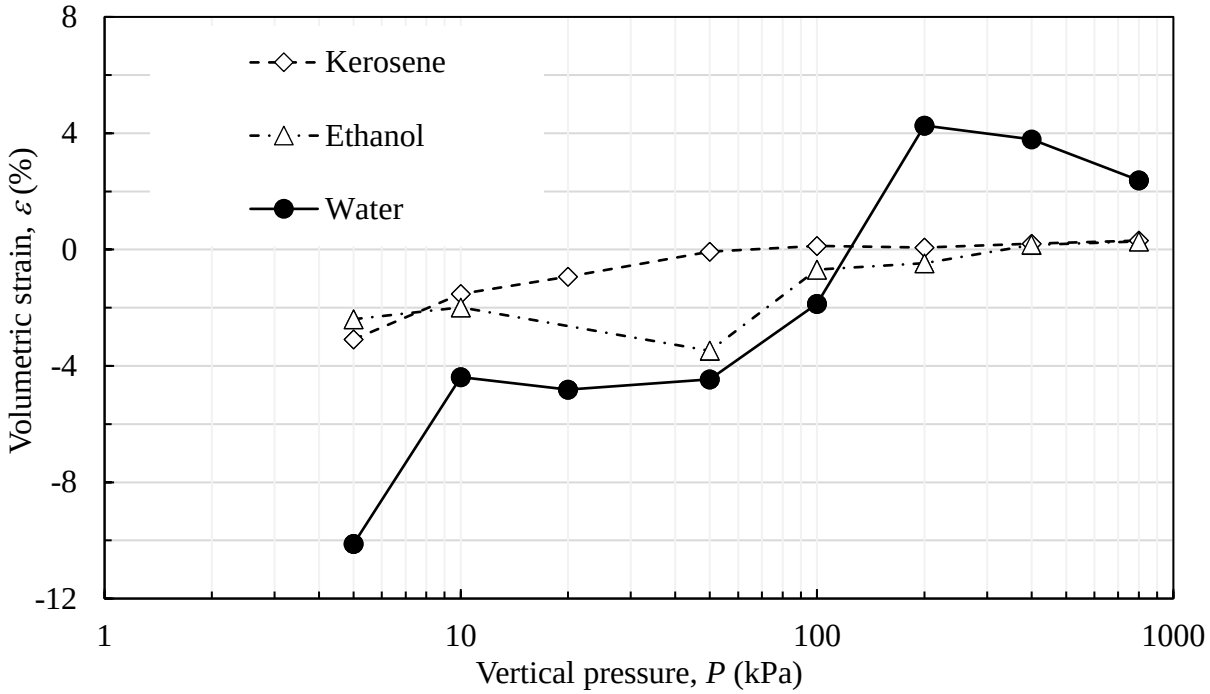

Fig. 9.14 Volumetric deformation of the studied kaolin compacted to 1.5 Mg/m^3 dry density, when inundated with four different pore fluids under various applied vertical pressure.

9.6 Summary

The wetting-induced volume change behavior of air-dry kaolin was studied at six different initial compaction densities under various inundation pressures in the range of 10-1600 kPa. At lower compaction densities (<1.25 Mg/m3), kaolin exhibited significant collapse. The collapse magnitude increased with the inundation pressure to a peak value and decreased thereafter. With the increase in the compaction density, the collapse was reduced at any given inundation pressure. At higher compaction densities (> 1.5 Mg/m3), kaolin exhibited volumetric swelling under low inundation pressure. The swelling decreased with the increase in the inundation pressure and a

marginal collapse was observed at a sufficiently high inundation pressure. A qualitative assessment was carried out to understand the applicability of the existing BBM model to model the kaolin behavior. The observed kaolin behavior deviated from the typical soil response in the BBM model. A detailed microstructural analysis was carried out to understand the influence of compaction density on the initial microstructure of the studied kaolin. Inter-aggregate pores were mainly affected during the air-dry compaction while the intra-aggregate pores remained unaffected. Further, the influence of the initial microstructure on the microstructural evolution during the wetting under different inundation pressures was brought out to understand the influence of compaction density and inundation pressure. At lower compaction densities, the collapse of the coarse inter-aggregate pores caused the volumetric collapse. At higher compaction densities, on the other hand, the coarse inter-aggregate pores were absent. The finer inter-aggregate pores with a small particle inclination dominated at this density. These inter-aggregate structures remained intact during the saturation under small inundation pressure and exhibited an overall expansion caused by the aggregate swelling. These inter-aggregate pores, however, collapsed and exhibited volumetric collapse under a sufficiently high inundation pressure. The surface forces were evaluated at various pore scales in the air-dry and fully saturated state to explain the observed microstructural mechanisms at different densities and inundation pressures. The reduction in the bond strength at the inter-aggregate contacts due to the loss of columbic attraction and significant reduction of VdW attraction at full saturation caused the collapse of the inter-aggregate pores. In the absence of the coarse inter-aggregate pores, repulsive pressure at the intra-aggregate pores contributed to the volumetric swelling.

10 Conclusions and future scope

10.1Conclusions

Equilibrium sediment volume

The proposed analytical model for predicting the equilibrium sediment volume provided useful insights into the influencing parameters and improved the quantitative understanding. Equilibrium sediment volume was found to be directly related to the specific surface area, normalized surface potential, and characteristic length. The cation exchange capacity of the bentonites, on the other hand, did not influence ESV. The presence of different exchangeable cations, however, influenced the sediment volume at low electrolyte concentrations. On the other hand, the volume of the non-clay content was significant at high electrolyte concentrations.

The proposed analytical model based on the parallel plate assumption provides a very good estimation of ESV in the concentration range of 0.01 M < c_0 < 1 M in NaCl solution. In the presence of $CaCl_2$ and a higher concentration of NaCl, the parallel-plate assumption breaks down and the clay changes to flocculated fabric due to the dominance of van der Waals forces.

Further, the proposed theoretical prediction provided an indirect assessment of SSA laboratory measurement techniques. The influence of different SSA measurement techniques for bentonites containing various mineral constituents can be assessed using the developed model in this work.

The proposed work significantly contributes to understanding the engineering behavior of different bentonites, qualitatively, for the application in nuclear waste repositories due to the fact the SSA directly influences the swelling and hydraulic properties of the bentonites. As the measured ESV data was significantly affected by the presence of different non-dominant exchangeable cations at low electrolyte concentrations (especially, for Kutch bentonite), the influence of these cations on the mechanical behavior of natural bentonites can't be ignored.

Surface area estimation

A new method for the estimation of surface area was proposed using the measured equilibrium sediment volume of the plastic clays, in the presence of a common electrolyte solution. The following conclusions were drawn from this study:

Thick water film around the clay platelets was developed, and the parallel orientation of the platelets was prevalent in the sediment volume tests in the presence of 0.1 N NaCl solution. Further, the free Na^+ ions in the pore-fluid effectively replaced the exchangeable cations on the clay surface at this concentration for most of the clays. This was evident from the highest predicted S_a values by the proposed method for most of the studied clays.

The proposed method showed qualitatively good agreement with the EGME and MB methods. However, the proposed method showed greater agreement with the MB method, especially in Na-dominant clays. The predicted S_a values by the proposed method were higher than both the existing methods for the highly plastic clays, such as bentonites, due to the greater inter-layer accessibility of water molecules.

The proposed method was in good agreement with the estimated S_a values by the MB method for the organic clays. The EGME method, however, was found to be sensitive for these clays and estimated higher values due to over-accumulation of EGME molecules in excess of the monolayer formation in the presence of organic matter.

The EGME and the proposed method were influenced by the added fine-sand content and underestimated the theoretical S_a values for the bentonite-sand mixtures. The MB method, on the other hand, showed a good agreement with the theoretically S_a values for all the bentonite-sand mixtures.

The MB method is influenced by the divalent exchangeable cations and the method estimated smaller S_a values for such clays. The influence of the exchangeable cations is very minimal by the proposed method as all the surface cations are replaced with the free Na^+ ions. Similarly, the exchangeable cations do not influence the EGME method, significantly.

The proposed method is simple and quick for a good estimation of the surface area of the plastic clays with a commonly available electrolyte solution. The method is not sensitive to the ambient conditions, unlike the EGME method, and is not sensitive to the pH environment, unlike the MB method. The proposed technique for the S_a estimation should be readily adopted in the standard practice as an additional method.

Compressibility behavior at very high pressure

The compressibility behavior of natural bentonites and clayey soils is influenced by many factors such as the presence of multiple exchangeable cations, anion exclusion, the presence of non-clay content, and higher electrolyte concentrations. The measured compressibility data, for different bentonites and clayey soils, severely deviated from the ideal compressibility behavior predicted by the DDL theory due to these influencing factors. Further, accurate measurement of bulk solution concentration in the soil was not possible for theoretical simulation of clay–pore–fluid interaction under mechanical loads. The normalization and the linearization procedures applied earlier for highly plastic clays were not applicable for many bentonites and natural clayey soils studied in this work.

A general theoretical model was proposed in this work by relating normalized void ratio with P^{-a} for predicting the compressibility data up to very high consolidation pressures for clayey soils with different plasticity. The model required the compressibility data at a low consolidation pressure range, just beyond the preconsolidation pressure, for estimating the intrinsic parameter, a. As the intrinsic parameter was found to be related to the plasticity of the clayey soil, the parameter captured the intrinsic properties and compressibility nature of the given clayey soil for predicting the compressibility data at high consolidation pressures. The intrinsic parameter varied between 0.71 to 0.1 for different clayey soils and with different salt interactions. The estimated intrinsic parameter for highly plastic bentonites ($w_L \geq 14$) was found to be approaching $a = 0.5$ but decreased with the decreasing plasticity.

The proposed model satisfactorily predicted over 110 sets of compressibility data from higher pressures to maximum consolidation pressures ranging between 800 kPa – 42000 kPa for 88 clays studied in this work. The advantage of the proposed method is that the model does not require the knowledge of the clay surface and pore-fluid characteristics; the computation of midplane potentials to relate with clay-platelet distances; or the knowledge of the plasticity of the clays, unlike previous predictive models.

The intrinsic parameter not only predicted the compressibility data at higher consolidation pressures accurately but provided qualitative information on the bentonite plasticity and changes to the bentonite quality with the exposure to different electrolytes, presence of different mineral

content, non-clay content, etc. The parameter will be very useful for the classification of clayey soil.

The proposed model is useful in the design of solid waste landfills for choosing ideal bentonite with limited available compressibility data. The proposed model, further, cuts down the cost of specialized high-pressure load frames using a double-arm lever system for estimating the compressibility data to high consolidation pressures for in-situ settlement estimations. In future work, an interrelationship between the estimated intrinsic parameter with different index parameters will be studied more rigorously for establishing interdependency.

Compressibility behavior by Stern theory

A mathematical model was developed for the first time to establish the potential-distance relation for the interacting Stern model at constant charge condition. The compressibility of the Stern layer was further incorporated in the theory for the first time to provide a more realistic prediction of the compressibility behavior of bentonites in the high-pressure range. Based on the detailed analysis of the compressibility data of different bentonites from the literature using the proposed Stern theory, the following conclusions were drawn.

Under the application of load, the diffused Gouy layer initially undergoes significant compression, while the Stern layer remains unaffected. The compression of the Stern layer starts in the pressure range of 0.5–1 MPa for different bentonites once the thickness of the Gouy layer is significantly reduced. The thickness of the Stern layer reaches a minimum value of equivalent to the water molecule size at a pressure of ~40 MPa. The siloxane cavities on the surface of the clay platelets accommodate the cations at such high pressure to facilitate the Stern layer compression. The void ratio corresponding to the minimum Stern layer thickness at such high pressure is ~0.4.

The ratio of the midplane to Stern potential, which represents the degree of interaction in the clay-water system, influenced the compression behavior of the Stern layer under the loading. The

potential ratio of the clay-water electrolyte system at any given pressure is dependent on the type and composition of the exchangeable cations on the clay surface. The Stern layer compression starts when the potential ratio is in the range of 0.65-0.75 for bentonites with different surface cations characteristics.

Swelling pressure of compacted bentonites

The two distinct SPEC behaviors exhibited by the studied bentonites at different compaction densities were analyzed through the microstructural characterization based on the PSD data and fabric images from FESEM. Based on the quantitative analysis of the evolution of various pore size classes during the hydration of the bentonite at different initial stress states, the following conclusion was drawn.

Aggregate invasion and collapse are two distinct mechanisms occurring during the water uptake process in the compacted bentonites that control the SPEC behavior. The aggregate invasion is due to the swelling of aggregates following the hydration at various pore size classes. During the aggregate invasion, the inter-aggregate pores are gradually reduced by increasing the volume of the immediate finer pore-size classes, but the overall inter-aggregate geometry remains intact. On the other hand, collapse refers to the failure of the aggregate pore geometry/structure due to the developed repulsive pressure within the compacted clay matrix. This leads to the increase in the volume of very fine micro-size classes.

The observed bimodal SPEC behavior is primarily attributed to the collapse of the aggregate structure. However, the aggregate collapse is not always reflected in the SPEC behavior. An early collapse of aggregate during the hydration process is often observed which didn't show any reduction in the swelling pressure on the SPEC due to domination of the micro-pore size classes. A bimodal behavior is observed in very high-quality MX80 bentonite at a high density of 1.7 Mg/m^3, but a monotonic SPEC behavior is observed in GMZ and Indian (B2) bentonites at much lower densities (i.e., 1.35 – 1.45 Mg/m^3). The overall SPEC behavior is thus dependent on the relative presence of the micro-pores and various critical macro-pore size classes.

The influence of density and bentonite plasticity on the PSDs of compacted bentonite is well captured by the proposed critical pore-size parameters. The proposed parameters successfully predicted the SPEC behavior of bentonite at any given density. The α parameter influenced the

overall SPEC behavior and the β parameter is related to the magnitude of swelling pressure reduction on the SPEC.

The addition of sand to the bentonite changes the monotonic SPEC behavior of compacted bentonite to a bimodal one due to the increase in the macro-porosity. With a further increase in the sand content, the SPEC becomes monotonic as the very-coarse macro-pore size classes become dominant. Thus SPEC behavior is another important criterion for understanding the optimal sand content in the bentonite-sand mixtures in many Geo-environmental engineering applications to obtain the knowledge of stress state.

Wetting-induced volume change behavior of kaolin

Edge-face and edge-edge interactions are significantly present at the inter-aggregate pores (>0.1 μm) of kaolin in the air-dry state due to the strong columbic attractions. The columbic attraction is completely lost at full saturation resulting in collapse or compression of the inter-aggregate pores under the mechanical stress leading to the volume change. The bond strength at the inter-aggregate contacts attributed by the VdW forces at full saturation determines the collapsibility of a given pore-size class under mechanical stress. The bond strength is higher for the smaller inter-aggregate pores due to the stronger VdW attractions at the inter-aggregate contacts as the separation distance is smaller and the kaolin particles shift towards the face-face manner. The bond strength of open card-house structures at the coarse inter-aggregate pores (>0.5 μm) is very minimal at full saturation. The collapse of these pores can take place when wetted under mechanical stress of as small as 10 kPa.

The magnitude of volumetric collapse is directly related to the amount and size of the pores which undergo collapse/compression under a given mechanical stress. At lower compaction densities, kaolin exhibits significant volumetric collapse even under lower mechanical stress, because of the predominant presence of the metastable card-house structures. The collapse magnitude decreases at higher compaction densities as the card-house structures are significantly reduced during the air-dry compaction. Collapse magnitude increases with an increase in the mechanical stress as more pore-size classes collapse during the wetting. In the case of wetting under very high mechanical stress, the inter-aggregate pores get compressed significantly due to the loading before

the inundation. Thus, a peak collapse is often observed at certain mechanical stress, beyond which the collapse magnitude decreases with an increase in mechanical stress.

At very high compaction density, where the metastable pores are absent, the DDL repulsive pressure at the intra-aggregate pores becomes significant and influences the volume change behavior. Kaolin exhibits volumetric swelling under given mechanical stress when the following two conditions prevail. Firstly, the bond strength at the inter-aggregate is sufficient to withstand the mechanical stress, and secondly, the repulsive pressure exceeds the mechanical stress.

10.2 Future scope

The theoretical study in this work can be improved by addressing the following limitations of the DDL theory:

The theory assumed the presence of a single exchangeable cation at the clay surface. The limitations in the proposed theory can be addressed by considering the models for mixed ions at low electrolyte concentrations ($c_0 \leq 0.01$ M). Further, kinetic models can be adapted to account for the cation exchange process while the electrolyte concentration was increased.

Nevertheless, the parallel-plate assumption in DDL theory is valid over a wide range of NaCl concentrations, the assumption is not valid in the presence of $CaCl_2$ solution. Therefore, non-parallel plate models (Anandarajah and Lu, 1991) may be explored in the presence of higher valence cations.

A comprehensive model which also considers the size of the cations can be developed by extending the current study as the influence of K^+ (a monovalent cation similar to Na^+, but contains a smaller hydrated radius) and Mg^{2+} ions could not be assessed even though they were present in the studied bentonites.

The Stern model can be further explored at a weak particle interaction to study the ESV behavior of clays under the specific influence of the size of the cations.

More studies on kaolin behavior at different hydro-mechanical stress-state are required to develop a comprehensive understanding of the influence of the surface forces on the kaolin behaviour and improve the BBM model.

Appendices

Appendix 1

A 2 g of clay sample was mixed with 100 mL NaCl solution having a concentration (c_0) of 0.001 M in a 100 mL cylindrical glass jar for measuring the equilibrium sediment volume. The clay surface properties are: C_{EC} = 100 meq/100 g and S_{SA} = 800 m^2/g; pore-fluid parameters are: T = 298 K and ε = 80.4. The specific gravity of the clay is 2.7. The procedure for computing the theoretical *ESV* is given in the following steps

1. Scaled surface potential from Eq. 37,

$$z = \cosh^{-1}\left(1+0.5\left[\frac{CEC}{SSA}\times\frac{2513.6}{\sqrt{\varepsilon nT}}\right]^2\right) = 8.324, \quad n = \frac{c_0\times 6.022\times 10^{23}}{1000} \text{ ions/cm}^3$$

2. Characteristic length is

$$\frac{1}{\kappa} = \sqrt{\frac{\varepsilon k_B T}{8\pi e'^2 n}} = 97.37 \text{ Å}$$

1st iteration:

3a. The osmotic pressure in the system due to body forces can be written as $P = \left(t_p G_s + 2t_{DDL}\right)\gamma_w$ (Eq. 33). The DDL thickness was assumed to be equal to the characteristic length, 1/κ, as a first approximation for the calculation of osmotic pressure. After substituting the value for the clay plate thickness t_p = 10 Å,

$P = 2.182\times10^{-7}$ kPa.

3b. The mid-plane potential can now be computed using Eq. 23,

$$u = \cosh^{-1}\left(1+P/2nRT\right) = 2.97\times10^{-4}$$

3c. The DDL thickness is (Eq. 36)

$t_{DDL} = \frac{1}{\kappa} \times \left[\ln\left(\tanh\left(z/4\right)\right) - \ln\left(\tanh\left(u/4\right)\right) \right]$ = 922.811 Å when initial t_{DDL} was assumed to be equal to 97.37 Å.

2nd iteration:

The computed t_{DDL} can be used to estimate the osmotic pressure and compute the DDL thickness.

4a. The osmotic pressure, $P = \left(t_p G_s + 2t_{DDL}\right)\gamma_w$ = 1.84×10^{-6} kPa.

4b. The mid-plane potential can now be computed using Eq. 23,

$u = \cosh^{-1}\left(1 + P/2nRT\right) = 8.61\times10^{-4}$

4c. The DDL thickness is (Eq. 36)

$t_{DDL} = \frac{1}{\kappa} \times \left[\ln\left(\tanh\left(z/4\right)\right) - \ln\left(\tanh\left(u/4\right)\right) \right]$ = 819.07 Å when initial t_{DDL} was assumed to be equal to 922.81 Å.

3rd iteration:

Assume t_{DDL} = 819.07 Å.

5a. The osmotic pressure, $P = \left(t_p G_s + 2t_{DDL}\right)\gamma_w$ = 1.634×10^{-6} kPa.

5b. The mid-plane potential can now be computed using Eq. 23,

$u = \cosh^{-1}\left(1 + P/2nRT\right) = 8.122\times10^{-4}$

5c. The DDL thickness is (Eq. 36)

$t_{DDL} = \frac{1}{\kappa} \times \left[\ln\left(\tanh\left(z/4\right)\right) - \ln\left(\tanh\left(u/4\right)\right) \right]$ = 824.79 Å when initial t_{DDL} was assumed to be equal to 819.07 Å.

4th iteration:

Assume t_{DDL} = 824.79 Å.

6a. The osmotic pressure, $P = \left(t_p G_s + 2t_{DDL}\right)\gamma_w$ = 1.645×10^{-6} kPa.

6b. The mid-plane potential can now be computed using Eq. 23,

$u = \cosh^{-1}\left(1 + P/2n\mathrm{R}T\right)$ = 8.149×10^{-4}

6c. The DDL thickness is (Eq. 14)

$t_{DDL} = \frac{1}{\kappa} \times \left[\ln\left(\tanh\left(z/4\right)\right) - \ln\left(\tanh\left(u/4\right)\right)\right]$ = **824.456 Å** when initial t_{DDL} was assumed to be equal to 824.79 Å. The difference between assumed and computed is marginal.

7. Equilibrium sediment volume can now be estimated theoretically as (Eq. 30)

$E_{SV} = \frac{\left(1 + S_{SA} t_{DDL} \rho_w G_s\right) M_s}{G_s \rho_w}$ = 66.32 cm^3 per one gram of dry soil mass.

Appendix 2

A 2 g of dry clay sample was mixed with 100 ml NaCl solution having a concentration (c_0) of 0.1 M in a glass cylinder for measuring the equilibrium sediment volume. The final sediment volume was measured as 10 cm^3. The procedure for the specific surface area estimation was given in the following steps by assuming T = 298 K, ε = 80.4, and the specific gravity of solids as 2.7.

1. Characteristic length is

$$\frac{1}{\kappa} = \sqrt{\frac{\varepsilon k_B T}{8\pi e'^2 \nu^2 c_0 N_A 1000}} = 9.74 \text{ Å}$$

where ε (~80.4) is the dielectric constant of water, k_B (= 1.38×10^{-16} erg K^{-1}) is the Boltzmann constant, T is the temperature (K), e' (= 4.8 × 10^{-10} esu) is the elementary electric charge, ν is the cation valence in the diffuse double layer and N_A *(=6.02×10^{23})* is the Avogadro's number.

2. The water film thickness was computed iteratively using the following equation (Eq. 39), as shown below:

$$t_f = \frac{1}{\kappa} \ln\left[1 \Big/ \tanh\left(\frac{1}{4}\cosh^{-1}\left(1 + \gamma_w\left(\frac{t_p G_s + 2t_f}{2n\mathrm{R}T}\right)\right)\right)\right]$$

where the thickness of clay platelet, t_p is assumed as 10 Å and R (=8.314 J/mol-K) is the universal gas constant.

1st iteration:

The DDL thickness was assumed to be equal to the characteristic length, 1/κ, as a first approximation for the calculation of osmotic pressure. Solving Eq 39, the water film thickness was obtained as,

$t_f = 113.725$ Å

2nd iteration:

The new t_f value was used as the initial value on the right-hand side of Eq 39. Hence the computed t_f = 111.089 Å when initial t_f was assumed to be equal to 113.725 Å.

3rd iteration:

Assume initial t_f = 111.089 Å.

Calculated t_f =111.14 Å when initial t_f was assumed to be equal to 111.089 Å.

4th iteration:

Assuming t_f = 111.14 Å, the calculated t_f was found to be 111.14 Å. Hence the optimized value t_f was **111.14 Å**.

3. The specific surface area was estimated from the measured ESV, using the following equation,

$$S_a = \frac{1}{t_f} \times \left(\frac{ESV}{M_s} - \frac{1}{\rho_w G_s} \right) = 416.55 \text{ m}^2 \text{ per one gram of dry soil mass.}$$

where M_s is the mass of the oven-dried soil sample used in the sediment volume test.

List of Publications

Journal Articles

1. Bharat, T.V. and **Das, D.S.**, (2017). "Physicochemical approach for analyzing equilibrium volume of clay sediments in salt solutions," Applied Clay Science, 136, pp.164-175. https://doi.org/10.1016/j.clay.2016.11.021

2. Bharat, T. V., **Das, D. S.** and Sahu, R. K., (2020). "Prediction of compressibility behavior of clayey soils of different plasticity for containment applications at large consolidation pressures," Journal of Hazardous, Toxic, and Radioactive Waste (ASCE), 24(1), 04019036. https://doi.org/10.1061/(ASCE)HZ.2153-5515.0000479

3. **D. Das** and B. Venkata Tadikonda, (2021). "Specific Surface Area of Plastic Clays from Equilibrium Sediment Volume under Salt Environment," *Geotechnical Testing Journal* 44, no. 5 (2021): 1484-1500. https://doi.org/10.1520/GTJ20200190

Book Chapters

1. **Das, D. S**., & Bharat, T. V. (2021) "Theoretical Study on Equilibrium Volume of Clay Sediments in Salt Solutions," In Problematic Soils and Geoenvironmental Concerns. Springer, Singapore, Vol. 88, Chapter 26, pp. 307-317. https://link.springer.com/chapter/10.1007/978-981-15-6237-2_26

Manuscript submitted/under preparation for publication in refereed Journal

1. **Das, D.S**., Choudhury, C., and Bharat, T. V., "Swelling pressure evolution curves of compacted bentonites: microstructural analysis."

2. **Das, D. S.**, Suresh, R., and Bharat, T.V., "Stern diffuse double layer model for compressibility behavior of clays at higher mechanical loadings."

3. **Das, D.S.,** Pegu, S., and Bharat, T. V., "Wetting-induced volume change behavior of air-dry kaolin using pore-scale forces."

Patent filed

1. **Das, D.S**., Bharat, T.V., "A Method for Determining Surface Area of Plastic Clays Through Equilibrium Sediment Volume," India (*Application No*- **202231015588**).

References

Alonso, E. E., (1998). "Modelling expansive soil behavior." In Proceedings of the 2nd International Conference on Unsaturated Soils, Beijing, China, Vol. 2, pp. 37-70.

Alonso, E.E., Gens, A. and Josa, A., (1990). "A constitutive model for partially saturated soils." Géotechnique, 40(3): 405-430.

Alonso, M. C., Calvo, J. L. G., Cuevas, J., Turrero, M. J., Fernández, R., Torres, E., & Ruiz, A. I., (2017). "Interaction processes at the concrete-bentonite interface after 13 years of FEBEX-Plug operation. Part I: Concrete alteration." Physics and Chemistry of the Earth, Parts A/B/C, 99, 38-48.

Al-Rawas, A.A., (2000). "State-of-the-art review of collapsible soils." Science and Technology, 115-135.

Altschaeffl, A. G. (1960). "Compressibility of artificially sedimented clays." PhD thesis, Purdue University.

Amarasinghe, P. M., Anandarajah, A., and Ghosh, P., (2014). "Molecular dynamic study of capillary forces on clay particles." Applied clay science, 88, 170-177.

American Colloid Co., (1945). "Laboratory methods for evaluating the physical properties of bentonites." Data Sheet 251.4 p.

Anandarajah, A. and Chen, J., (1997). "Van der waals attractive force between clay particles in water and contaminants." Soils and Foundations 37(2), 27–37.

Anandarajah, A. and Lu, N., (1991). "Numerical study of the electrical double-layer repulsion between non-parallel clay particles of finite length." International Jl. Num. Anal. Meth. Geom., 15, 683-703.

Arifin, Y. F., (2008). "Thermo-hydro-mechanical behavior of compacted bentonite-sand mixtures: an experimental study." PhD thesis.

ASTM D4318-10e1., (2010). "Standard Test Methods for Liquid Limit, Plastic Limit, and Plasticity Index of Soils." ASTM International, West Conshohocken, PA.

ASTM D5890, (2003). "Standard test method for swell index of clay mineral component of geosynthetic clay liners." ASTM International, West Conshohocken, PA.

ASTM D854-14., (2014). "Standard Test Methods for Specific Gravity of Soil Solids by Water Pycnometer." ASTM International, West Conshohocken, PA.

ASTM, D., 2014. 4546-14: Standard test methods for one-dimensional swell or collapse of soils. West Conshohocken, PA, USA.

Atabek, R. B., Felix, B., Robinet, J. C., and Lahlou, R., (1991). "Rheological behavior of saturated expansive clay materials." Proceedings of the Workshop on Stress Partitioning in Engineered Clay Barriers, Duke University, Durham, N.C, 29-31.

Baille, W., Tripathy, S., and Schanz, T., (2010). "Swelling pressures and one-dimensional compressibility behavior of bentonite at large pressures." Applied Clay Science, 48(3), 324-333.

Barnaji, M.J., Pourafshary, P. and Rasaie, M.R., (2016). "Visual investigation of the effects of clay minerals on enhancement of oil recovery by low salinity water flooding." Fuel, 184: 826-835.

Bennet, R. H., and Hulbert, M. H., (1986). Clay Microstructure, Int. Human Res. Oevelopm. Corp. Boston/Houston/London.

Benson, C. H., Zhai, H., Wang, X., (1994). "Estimating hydraulic conductivity of compacted clay liners." J. Geotech. Eng. 120, 366-387.

Bergaya, F. & Lagaly, G., (2013). Basics, Vol. 1 of Handbook of Clay Science, Elsevier Ltd., chapter 1.

Bharat T. V., and Das D. S., (2017). "Physicochemical approach for analyzing equilibrium volume of clay sediments in salt solutions." Applied Clay Science, 136: 164-75.

Bharat T. V., and Gapak Y., (2018). "Hydration kinetics of bentonite buffer material: Influence of vapor pressure, bentonite plasticity, and compaction density." Applied Clay Science, 157: 41-50.

Bharat, T. V., and Gapak, Y. (2021). "Soil-water characteristic curves of bentonites in isochoric conditions during wetting: measurement and prediction." Canadian Geotechnical Journal, 58(5), 711-721.

Bharat, T.V. and Sridharan, A. (2015a). "Prediction of compressibility data for highly plastic clays using diffuse double-layer theory." Clay. Clay. Miner., 63, 30-42.

Bharat, T.V. and Sridharan, A. (2015b). "A Critical Appraisal of Debye Length in Clay-Electrolyte Systems. Clay." Clay. Miner., 63, 43-50.

Bharat, T.V., (2004). "Simplified methods of evaluation of diffuse double layer parameters employed in geotechnical engineering." MSc (Eng) thesis, Indian Institute of Science, Bangalore, India, 102 pp.

Bharat, T.V., Sivapullaiah, P.V., and Allam, M.M. (2009). "Swarm intelligence-based solver for parameter estimation of laboratory through-diffusion transport of contaminants." Comput. Geotech., 36, 984-992

Bharat, T.V., Sivapullaiah, P.V., and Allam, M.M. (2013). "Novel procedure for the estimation of swelling pressures of compacted bentonites based on diffuse double layer theory." Environ. Earth Sci., 70, 303-314.

Bishop, A. W., (1959). The principle of effective stress. Teknisk ukeblad, 39: 859-863.

Blümling, P., Adams, J., (2008). "Borehole Sealing. Nagra Technical Report." NTB 07-01. Nagra, Wettingen, Switzerland.

Bolt, G. H. (1956). "Physico-chemical analysis of compressibility of pure clays." Geotechnique, 46, 291–311.

Brackley J. J. A., (1973). "Swell pressure and free swell in compacted clay." In Proceedings of 3rd International Conference on Expansive soils, Haifa, 1, 169-176.

Bradbury M. H., and Baeyens B., (2003). "Porewater chemistry in compacted re-saturated MX-80 bentonite." Journal of Contaminant Hydrology, 61(1-4): 329-38.

Bresler, E. (1970). "Numerical solution of the equation for interacting diffuse layers in mixed ionic systems with nonsymmetrical electrolytes." J. Col. Intf. Sci., 33, 278-283.

Bresler, E. (1972). "Interacting diffuse layers in mixed mono-divalent ionic systems." Soil Sci. Soc. Amer. Proc., 36, 891-896.

Burland, J. B. (1990). "On the compressibility and shear strength of natural clays." Geotechnique, 40, 329–378.

Campbell, G. S., Smith, D. M., & Teare, B. L. (2007). "Application of a dew point method to obtain the soil water characteristic." In *Experimental unsaturated soil mechanics* (pp. 71-77). Springer, Berlin, Heidelberg.

Carlson, L. (2004). "Bentonite mineralogy. Part I: Methods of investigation – a literature review. Part II: Mineralogical research of selected bentonites." Working Report 2004-2, Posiva Oy, Olkiluoto, Finland.

Castellanos, E., Villar, M. V., Romero, E., Lloret, A., & Gens, A. (2008). "Chemical impact on the hydro-mechanical behaviour of high-density FEBEX bentonite." Physics and Chemistry of the Earth, Parts A/B/C, 33, S516-S526.

Celik, M.S., (2004). "Electrokinetic behaviour of clay surfaces. Clay surfaces: fundamentals and applications." Elsevier Ltd., London.

Cerato AB and Lutenegger A. J., (2002). "Determination of surface area of fine-grained soils by the ethylene glycol monoethyl ether (EGME) method." Geotechnical Test. J. 25: 315–321.

Chapman D. L., (1913). "A contribution to the theory of electrocapillarity." The London, Edinburgh, and Dublin Philosophical Magazine and J. of Sci. 25, 475-481.

Chapman H. D., (1965). "Cation-exchange capacity. In: Black, C.A. (Ed.), Methods of Soil Analysis - Chemical and Microbiological Properties." Agronomy. vol. 9, pp. 891–901.

Chen, Y. G., Dong, X. X., Zhang, X. D., Ye, W. M., and Cui Y. J., (2018). "Combined thermal and saline effects on the swelling pressure of densely compacted GMZ bentonite." Applied Clay Science, 166: 318-326.

Chen, Y. G., Sun, Z., Cui, Y. J., Ye, W. M., & Liu, Q. H. (2019). "Effect of cement solutions on the swelling pressure of compacted GMZ bentonite at different temperatures." Construction and Building Materials, 229, 116872.

Chen, Y. G., Zhu, C. M., Ye, W. M., Cui, Y. J., Chen, B., (2016). "Effects of solution concentration and vertical stress on the swelling behavior of compacted GMZ01 bentonite." Appl. Clay Sci. 124, 11-20.

Choudhury C and Bharat TV (2018). "Wetting-induced collapse behavior of kaolinite: influence of fabric and inundation pressure." Canadian Geotechnical Journal, 55(7): 956-67.

Choudhury, C., (2019). "Effective stress development in kaolin and bentonite clays during the hydro-mechanical loading," PhD thesis, Indian Institute of Technology, Guwahati, India.

Clemence, S. P., & Finbarr, A. O. (1981). "Design considerations for collapsible soils." Journal of Geotechnical and Geoenvironmental Engineering, 107(ASCE 16106).

Collis-George, N. and Bozeman, J. M. (1970). "A double layer theory for mixed ion systems as applied to the moisture content of clays under restraint." Aust. J. Soil Res., 8, 239-258.

Conley, R. F., & Althoff, A. C. (1971). "Surface acidity in kaolinites." Journal of Colloid and Interface Science, 37(1): 186-195.

Cotecchia, F. and Chandler, R. J. (2000). "A general framework for the mechanical behaviour of clays." Géotechnique, 50, 431-448.

Cui YJ, Loiseau C, and Delage P (2002a). "Microstructure changes of a confined swelling soil due to suction controlled hydration." In Proceedings of 3rd International Conference on Unsaturated Soils, UNSAT Recife, Brazil, Balkema vol. 2, pp. 593-598.

Das, D. S., and Tadikonda, B. V. (2021) "Specific Surface Area of Plastic Clays from Equilibrium Sediment Volume under Salt Environment," Geotech. Test. J. 44, (5): 1484-1500. https://doi.org/10.1520/GTJ20200190

Das, P., (2021). "Influence of Ionic Characteristics of inorganic salt solutions and Chemo-mechanical Loading on Attenuation and Self-sealing Ability of Compacted Bentonites." PhD thesis, Indian Institute of Technology, Guwahati, India.

Das, P., and Bharat, T. V., (2021). "Kaolin based protective barrier in municipal landfills against adverse chemo-mechanical loadings." Scientific reports, 11(1), 1-12.

Das, S.K. and Basudhar, P.K. (2006). "Comparison study of parameter estimation techniques for rock failure criterion models." Canadian Geotech. J., 43(7), pp. 764-771.

Delage, P., Cui, Y.J. and Antoine, P.,)2008). "Geotechnical problems related with loess deposits in Northern France." arXiv preprint arXiv:0803.1435.

Delgado, A., Gonzalez-Caballero, F. and Bruque, J.M.,)1986). "On the zeta potential and surface charge density of montmorillonite in aqueous electrolyte solutions." Journal of colloid and interface science, 113(1): 203-211.

Deng, Y. F., Cui, Y. J., Tang, A. M., Nguyen, X. P., Li, X. L., Geet M. v., (2011). "Investigating the pore-water chemistry effects on the volume change behavior of Boom clay." Phys. Chem. Earth. 36, 1905–1912.

Derbyshire, E., (2001). "Geological hazards in loess terrain, with particular reference to the loess regions of China." Earth-Science Reviews, 54(1-3): 231-260.,

Dhandapani Y and Santhanam M (2017). "Assessment of pore structure evolution in the limestone calcined clay cementitious system and its implications for performance." Cement and Concrete Composites. 2017, 84: 36-47.

Di Maio, C., Santoli, L., and Schiavone, P. (2004). "Volume change behaviour of clays: the influence of mineral composition, pore fluid composition and stress state." Mech. Materials, 36, 435-451.

Dixon, D. A., and Gray, M. N., (1985). "The engineering properties of buffer material." Technical Report TR-350, Fuel Waste Technology Branch, Whiteshell Laboratories, Pinawa, Man.

Djeran-Maigre, I., Tessier, D., Grunberger, D., Velde, B., and Vasseur, G. (1998). "Evolution of microstructures and of macroscopic properties of some clays during experimental compaction." Marine Petrol. Geol., 15, 109-128.

Dolinar, B., Miŝiĉ, M., & Trauner, L., (2007). "Correlation between surface area and Atterberg limits of fine-grained soils." Clays and Clay Minerals, 55(5), 519-523.

ENRESA, (2000). FEBEX project - full scale engineered barriers experiments for a deep geological respiratory for high level radioactive waste in crystalline host rock. Final report, Publicación téechnica 1/2000, Empresa Nacional de Residuos Radiactivos SA (ENRESA), Madrid, Spain.

Fall, M., Célestin, J. C., & Han, F. S. (2009). "Suitability of bentonite-paste tailings mixtures as engineering barrier material for mine waste containment facilities." Minerals Engineering, 22(9-10), 840-848.

Faucon, P., Adenot, F., Jacquinot, J. F., Petit, J. C., Cabrillac, R., & Jorda, M. (1998). "Long-term behaviour of cement pastes used for nuclear waste disposal: review of physico-chemical mechanisms of water degradation." Cement and Concrete Research, 28(6), 847-857.

Gaaver, K. E. (2012). "Geotechnical properties of Egyptian collapsible soils." Alexandria Engineering Journal, 51(3): 205-210.Houston et al., 2001.

Gapak, Y., Das, G., Yerramshetty, U., and Bharat, T. V. (2017). "Laboratory determination of volumetric shrinkage behavior of bentonites: A critical appraisal." Appl. Clay Sci., 135: 554-566. http://dx.doi.org/10.1016/j.clay.2016.10.038.

Gens A. and Alonso E. E., (1992). "A framework for the behavior of unsaturated expansive clays." Canadian Geotechnical Journal, 29: 1013-1032.

Gens A., Guimaraes L. D., Garcia-Molina A., and Alonso E. E., (2002). "Factors controlling rock–clay buffer interaction in a radioactive waste repository." Engineering geology, 64(2-3): 297-308.

Gens, A. (1982). "Stress-strain and strength characteristics of a low plasticity clay." PhD thesis, University of London.

Glatstein, D. A., Francisca, F. M., (2015). "Influence of pH and ionic strength on Cd, Cu and Pb removal from water by adsorption in Na-bentonite." Appl. Clay Sci. 118, 61-67.

Gouy G. (1910). "Electrical charge on the surface of an electrolyte." J Phys 4:457–468

Gray M. N., Cheung S. C. H., and Dixon D. A., (1984). "The influence of sand content on swelling pressures and structure developed in statically compacted Na-bentonite." Report 7825, Atomic Energy of Canada Limited, Mississauga, Ont. pp. 1-24.

Grim R. E., (1968). Clay mineralogy, 2nd edn. McGraw-Hill, New York

Grindrod P., Peletier M. and Takase H., (1999). "Mechanical interaction between swelling compacted clay and fractured rock, and the leaching of clay colloids." Engineering Geology, 54(1-2): 159-65.

Gupta, V., (2011). Surface charge features of kaolinite particles and their interactions. The University of Utah.

Gurtug, Y. (2011). "Prediction of compressibility behavior of highly plastic clays under high stresses." Appl. Clay Sci., 51, 295-299.

Guven, N., and Pollastro, R.M. (Editors). (1992). "Clay-water interface and its rheological implications." CMS workshop lectures, Vol. 4. The Clay Minerals Society, Boulder, Colo.

He Y., Ye W. M., Chen Y. G. & Cui Y. J., (2019). "Effects of K+ solutions on swelling behavior of compacted GMZ bentonite." Engineering Geology, 249: 241-248.

Heller, H., Keren, R., (2001). "Rheology of Na-rich montmorillonite suspension as affected by electrolyte concentration and shear rate." Clays Clay Miner. 49, 286-291.

Herbert H. J., and Moog H. C., (2002). "Untersuchungen zur Quellung von Bentonit in hochsalinaren Lösungen." Report GRS-179, Gesellschaft für Anlagen und Reaktorsicherheit (GRS) mbH, Berlin.

Herbert H. J., Kasbohm J., Sprenger H., Fernández A. M. and Reichelt C., (2008), "Swelling pressures of MX-80 bentonite in solutions of different ionic strength." Physics and Chemistry of the Earth, Parts A/B/C, 33: S327-42.

Holtz, W. G., Gibbs, H. J., (1956). "Engineering Properties of Expansive Clays." Transactions of the American Society of Civil Engineers. 121, 641-677.

Hong, Z., Yin, J. and Cui, Y. (2010). "Compression behaviour of reconstituted soils at high initial water contents." Géotechnique, 60, 691-700.

Horpibulsuk, S., Yangsukaseam, N., Chinkulkijniwat, A. and Du, Y.J. (2011). "Compressibility and permeability of Bangkok clay compared with kaolinite and bentonite." Appl. Clay Sci., 52, 150-159.

Houston, S.L., Houston, W.N., Zapata, C.E. and Lawrence, C., (2001). "Geotechnical engineering practice for collapsible soils." In Unsaturated soil concepts and their application in geotechnical practice (pp. 333-355). Springer, Dordrecht.

Hunter R. J. (1981). Zeta potential in colloid science. Academic press Inc., London

Hvorslev, J. M. (1937). "Physical properties of remoulded cohesive soils." Translation 69-5, USAEWES, Vicksburg.

Hvorslev, M. J. (1960). "Physical components of shear strength of saturated clays." Proc. Conf. Shear Strength of Cohesive Soils, Colorado, AXE, 169-273.

Imbert C. and Villar M. V. (2006). "Hydro-mechanical response of a bentonite pellets-powder mixture upon infiltration." Applied Clay Science, 32 (3-4): 197-209.

Ingles, O., (1968). Soil chemistry relevant to the engineering behaviour of soils, Chapter I, Soil Mechanics, Selected Topics, Elsevier, New York.

IS 2720-4, (1985). Methods of test for soils, Part 4: Grain size analysis. BIS, New Delhi.

IS 2720-40, (1977). Methods of test for soils, Part 40: Determination of free swell index of soils. (CED 43: Soil and Foundation Eng.)

Israelachvili, J. and Pashley, R., (1983). "Molecular layering of water at surfaces and origin of repulsive hydration forces." Nature. 306, 249–250.

Israelachvili, J., (1992). Intermolecular and Surface Forces, 2nd edn, Academic Press, London-San Diego.

Israelachvili, J.N., (2011). Intermolecular and surface forces. Academic press.

Iwata S., Tabuchi T., and Warkentin B. P., (1995). "Soil-Water Interactions: Mechanisms and Applications." 2nd ed., Marcel Dekker, New York.

Japan Nuclear Cycle Development Institute (1999). H12: project to establish the scientific and technical basis for HLW disposal in Japan: supporting report 2 (respiratory design and engineering Technology). Japan Nuclear Cycle Development Institute, Tokyo.

Jaradat, K. A., and Abdelaziz, S. L., (2019). "On the use of discrete element method for multi scale assessment of clay behavior." Computers and Geotechnics, 112, 329-341.

Jardine, R. J. (1985). "Investigation of pile-soil behaoiour with special reference to the foundations of offshore structures." PhD thesis, University of London.

Jennings, J. E. B. and Burland, J. B. (1962). "Limitations to the use of effective stresses in partly saturated soils." Geotechnique, 12, 125-145.

Jennings, J.E., and Knight, K. (1957). "The additional settlement of foundations due to a collapse of structure of sandy sub soils on wetting." Proceedings of the 4th International Congress on Soil Mechanics and Foundation Engineering, London, 1: 316-319.

Jiang, X., Zhou, J., Zhu, M., He, W., & Yu, G. (2001). "Charge characteristics on the clay surface with interacting electric double layers." Soil science, 166(4), 249-254.

Kanno T, and Wakamatsu H., (1992), "Water uptake and swelling properties of unsaturated bentonite buffer materials." Canadian Geotechnical Journal, 29: 1102-1107.

Kariuki, P. C., Meer, F. V. D., (2004). "A unified swelling potential index for expansive soils." Eng. Geol. 72, 1 –8.

Karnland, O. (2010). "Chemical and mineralogical characterization of the bentonite buffer for the acceptance control procedure in a KBS-3 repository (No. SKB-TR--10-60)." Swedish Nuclear Fuel and Waste Management Co.

Katti, D.R., Matar, M.I., Katti, K.S. and Amarasinghe, P.M., (2009). "Multiscale modeling of swelling clays: A computational and experimental approach." KSCE Journal of Civil Engineering, 13(4): 243-255.

Kaufhold, S., Baille, W., Schanz, T., Dohrmann, R., (2015). "About differences of swelling pressure—dry density relations of compacted bentonites." Appl. Clay Sci. 107, 52-61.

Kelessidis, V.C., Tsamantaki, C. and Dalamarinis, P., (2007). "Effect of pH and electrolyte on the rheology of aqueous Wyoming bentonite dispersions." Applied Clay Science, 38(1-2): 86-96.

Khasraghi et al., 2015

Khorshidi, M., & Lu, N., (2017). "Intrinsic relation between soil water retention and cation exchange capacity." Journal of Geotechnical and Geoenvironmental Engineering, 143(4), 04016119.

Khorshidi, M., Lu, N., & Khorshidi, A., (2016). "Intrinsic relationship between matric potential and cation hydration." Vadose Zone Journal, 15(11), 1-12.

Kitazumi, Y., Shirai, O., Yamamoto, M., and Kano, K., (2013). "Numerical simulation of diffuse double layer around microporous electrodes based on the Poisson–Boltzmann equation." Electro. Acta, 112(1), 171-175.

Koda, E., Osinski, P., (2016). "Bentonite cut-off walls: solution for landfill remedial works." Env. Geotechnics. doi: 10.1680/jenge.14.00022.

Komine H, and Ogata N, (1996). "Prediction for swelling characteristics of compacted bentonite." Canadian Geotechnical Journal, 33: 11-22.

Komine H, and Ogata N., (1994)., "Experimental Study on Swelling Characteristics of Compacted Bentonite." Canadian Geotechnical Journal, 31:478-490.

Komine H. and Ogata N., (2003). "New equations for swelling characteristics of bentonite-based buffer materials." Canadian Geotechnical Journal, 40: 460-475, doi: 10.1139/T02-115.

Komine, H. (2004). "Simplified evaluation on hydraulic conductivities of sand–bentonite mixture backfill." Appl. Clay Sci., 26, 13-19.

Komine, H. and Ogata, N., (2004). "Predicting swelling characteristics of bentonites." Journal of Geotechnical and Geoenvironmental engineering, 130, 818-829.

Komine, H., (2008). "Theoretical equations on hydraulic conductivities of bentonite-based buffer and backfill for underground disposal of radioactive wastes." Jl. Geot. Geoenv. Eng., 134, 497-508.

Lambe, T. W. (1960). "A mechanistic picture of the shear strength of clay." Proc., Research Conf. on the Shear Strength of Cohesive Soils, ASCE, New York, 437.

Lambe, T. W. (1964). "Methods of estimating settlement." Proc., ASCE Conf. Design of Foundations for Control of Settlements, North Western University, 47-72.

Lambe, T. W., and Whitman, R. V. (1969). Soil mechanics, Wiley, New York.

Langmuir, I. (1938). "The role of attractive and repulsive forces in the formation of tactoids, thixotropic gels, protein crystals, and coacervates." The Journal of Chemical Physics, 6(12), 873-896.

Lee, J.O., Cho, W.J., and Chun, K.S., (1999). "Swelling Pressures of a Potential Buffer Material for High-Level Waste Repository." J. Korean Nucl. Society. 31, 139–150.

Leong, E. C., Tripathy, S., and Rahardjo, H. (2003). "Total suction measurement of unsaturated soils with a device using the chilled-mirror dew-point technique." Geotechnique, 53(2), 173-182.

Li, P., Vanapalli, S. and Li, T., (2016). "Review of collapse triggering mechanism of collapsible soils due to wetting." Journal of Rock Mechanics and Geotechnical Engineering, 8(2): 256-274.

Lloret A., Villar M. V., Sanchez M., Gens A., Pintado X., (2003). "Mechanical behaviour of heavily compacted bentonite under high suction changes." Geotechnique, 53 (1): 27-40.

Lovera, P., Le Bescop, P., Adenot, F., Li, G., Tanaka, Y., & Owaki, E., (1997). "Physico-chemical transformations of sulphated compounds during the leaching of highly sulphated cemented wastes." Cement and concrete research, 27(10), 1523-1532.

Low, P., (1959). "Viscosity of water in clay systems." Clays and Clay Minerals 8(1), 170–182.

Low, P.F. (1980). "The swelling of clay, II Montmorillonites." J. Soil Sci. Soc. America, 4, 667–676.

Lu, N. and Likos, W.J., (2006). "Suction stress characteristic curve for unsaturated soil." Journal of geotechnical and geoenvironmental engineering, 132(2): 131-142.

Ma, C., & Eggleton, R. A., (1999). "Cation exchange capacity of kaolinite." Clays and Clay minerals, 47(2): 174-180.

Manca D., Ferrari A. and Laloui L., (2016). "Fabric evolution and the related swelling behaviour of a sand/bentonite mixture upon hydro-chemo-mechanical loadings." Géotechnique, 66(1): 41-57.

Marcial D., Delage P., & Cui Y.J., (2002). "On the high-stress compression of bentonites." Can Geotech J 39:812–820

Martin, R., (1960). Adsorbed water on clay: a review, in A. Swineford & P. Franks, eds, 'Proceedings of the Ninth National Conference on Clays and Clay Minerals 1960', International Series of Monographs on Earth Sciences, Pergamon Press, Symposium Publ. Division, 1962, Lafayette, Indiana, pp. 28–70.

Massat L., Cuisinier O., Bihannic I., Claret F., Masrouri F., et al., (2016). "Swelling pressure development and inter-aggregate porosity evolution upon hydration of a compacted swelling clay." Applied Clay Science, Elsevier, 124-125: 197-210.

Mayor J. C., García-Siñeriz J. L., Alonso E., Alheid H. J., and Blumbling P., (2005). "Engineered barrier emplacement experiment in Opalinus Clay for the disposal of radioactive waste in underground repositories." Empresa Nacional de Residuos.

McBride, M. B., (1997). "A critique of diffuse double layer models applied to colloid and surface chemistry." Clays Clay mine, 45(4), 598-608.

Mesri, G. and Funk, J. R., (2014). "Settlement of the Kansai International Airport Islands." J. Geotech. Geoenviron. Engg., 141, 04014102.

Mesri, G. and Olsen, R.E., (1971). "Consolidation characteristics of Montmorillonite." Géotechnique, 21, 341–352.

MINES, Indian Bureau of, (2018). Indian Minerals Yearbook 2016. Government of India, Ministry of Mines, Nagpur13: 1-17.

Mitchell, J. K., & Soga, K., (2005). Fundamentals of soil behavior (Vol. 3). New York: John Wiley & Sons.

Monroy R., Zdravkovic L., Ridley A., (2010). "Evolution of microstructure in compacted London Clay during wetting and loading." Géotechnique, 60(2): 105-19.

Mooney, M. A., Grasmick, J., Kenneally, B., Fang, Y., (2016). "The role of slurry TBM parameters on ground deformation: Field results and computational modelling." Tunnelling and Underground Space Tech. 57, 257-264.

Muhunthan, B., (1991). "Liquid limit and surface area of clays." Geotechnique, 41(1), 135-138.

Muller-Vonmoos M and Kahr G (1982). "Bereitstellung von Bentonit für Laboruntersuchungen." Nagra Technischer Bericht: 82-04.

Nadeau, P. H., (1985). "The physical dimensions of fundamental clay particles." Clay Miner., 20, 499-514.

Nagaraj, T. S., and Srinivasa Murthy, B. R. (1986). "A critical reappraisal of compression index equations." Geotechnique, 36, 27-32.

Nakagawa, M., Santosh, M., Yoshikura, S., Miura, M., Fukuda, T. and Harada, A., (2006). "Kaolin deposits at Melthonnakkal and Pallipuram within Trivandrum block, southern India." Gondwana Research, 9(4): 530-538.

Nakayama, S., Sakamoto, Y., Yamaguchi, T., Akai, M., Tanaka, T., Sato, T., & Iida, Y. J. A. C. S. (2004). "Dissolution of montmorillonite in compacted bentonite by highly alkaline aqueous solutions and diffusivity of hydroxide ions." Applied clay science, 27(1-2), 53-65.

Nelson, J., Miller, J. M., (1997). "Expansive Soils: Problems and Practice in Foundation and Pavement Engineering." John Wiley & Sons, New York.

Newland, P. L. and Allely, B. H. (1957). "A study of the sensitivity resulting from consolidation of a remoulded clay." Proc., 4th Inr. Conf. Soil Mech., Budapest, 1, 83-86.

Ng, A. M., A. T. Yeung, P. K. Lee, and L. G. Tham., (2006). "Design, fabrication, and assembly of a large oedometer." Geotech. Test. J. 29 (4): 298–305.

Nouaouria, M.S., Guenfoud, M. and Lafifi, B., (2008). "Engineering properties of loess in Algeria." Engineering Geology, 99(1-2): 85-90.

Oren, A. H., (2014). "Estimating compaction parameters of clayey soils from sediment volume test." Appl. Clay Sci. 101, 68–72.

Palomino, A. & Santamarina, J., (2005). "Fabric map for kaolinite: Effects of ph and ionic concentration on behaviour." Clays and Clay Minerals 53(3), 209–222.

Palomino, A. M. and Santamarina, J. C., (2015). "Fabric map for kaolinite: effects of pH and ionic concentration on behavior." Clays Clay mine. 53, 211-223.

Peirce, J. J., Sallfors, G., and Murray, L. (1986). "Overburden pressures exerted on clay liners." J. Environ. Engg., 112, 280-291.

Peng JB, Sun P and Li X., (2006). "Ground fissure: the major geological and environmental problem in the development of Xi'an City, China." Environmental Science and Technology, 2: 469e74.

Petersen, L. W., Moldrup, P., Jacobsen, O. H., & Rolston, D. E., (1996). "Relations between specific surface area and soil physical and chemical properties." Soil Science, 161(1), 9-21.

Petersen, L. W., Moldrup, P., Jacobsen, O. H., Rolston, D. E., (1996). "Relations between specific surface area and soil physical and chemical properties." Soil Sci. 161, 9-21.

Phien-Wej, N., Pientong, T. and Balasubramaniam, A.S., (1992). "Collapse and strength characteristics of loess in Thailand." Engineering Geology, 32(1-2): 59-72.

Prakash, K., Sridharan, A., (2002). "Determination of liquid limit from equilibrium sediment volume." Geotechnique. 52, 693–696.

Prakash, K., Sridharan, A., (2004). "Free swell ratio and clay mineralogy of fine-grained soils." Geotech. Test. J. 27, 220-225.

Přikryl, R. and Weishauptová, Z., (2010). "Hierarchical porosity of bentonite-based buffer and its modification due to increased temperature and hydration." Applied clay science, 47(1-2): 163-70.

Pusch, R. (1982). "Chemical interaction of clay buffer materials and concrete (No. SKBF-KBS-SFR--82-01)." Swedish Nuclear Fuel Supply Co.

Pusch, R. and Yong, R., (2006). "Microstructure of smectite clays and engineering performance." Taylor and Fracis, New York.

Pusch, R., (1982). "Mineral-water interactions and their influence on the physical behaviour of highly compacted Na bentonite." Canadian Geotechnical Journal, 19: 381-387.

Pusch, R., (1992). "Use of bentonite for isolation of radioactive waste products." Clay Miner. 27, 353-361.

Pusch, R., (2015). "Bentonite Clay: Environmental Properties and Applications." Taylor & Francis,

Pusch, R., Yong, R., and Nakano, M., (2011). "High Level Radioactive Waste (HLW) Disposal: A Global Challenge." WIT Press.

Ramos-Tejada, M.M., De Vicente, J., Ontiveros, A. and Duran, J.D.G., (2001). "Effect of humic acid adsorption on the rheological properties of sodium montmorillonite suspensions." Journal of rheology, 45(5): 1159-1172.

Revil, A., & Lu, N., (2013). "Unified water isotherms for clayey porous materials." Water Resources Research, 49(9), 5685-5699.

Rogers, C. D. F., Dijkstra, T. A., & Smalley, I. J., (1994). "Hydroconsolidation and subsidence of loess: studies from China, Russia, North America and Europe: in memory of Jan Sajgalik." Engineering Geology, 37(2): 83-113.

Rollins, M. B., (1969). "Sealing properties of bentonite suspensions." Clays Clay Miner. 16, 415-423.

Romero, E., Gens, A. and Lloret, A., (1999). "Water permeability, water retention and microstructure of unsaturated compacted Boom clay." Elsevier 54 (1-2): 117-127.

Ross, D., (1995). "Recommended soil tests for determining soil cation exchange capacity." In J.T. Sims, A. Wolf (ed.) Recommended soil testing procedures for the Northeastern United States. Northeast Regional Bull. 493. Agric. Exp. Stn., Univ. of Delaware Newark, DE. 62–69.

Saikia, B.J. and Parthasarathy, G., (2010). "Fourier transform infrared spectroscopic characterization of kaolinite from Assam and Meghalaya, Northeastern India." J. Mod. Phys, 1(4): 206-210.

Saikia, N.J., Bharali, D.J., Sengupta, P., Bordoloi, D., Goswamee, R.L., Saikia, P.C. and Borthakur, P.C., (2003). "Characterization, beneficiation and utilization of a kaolinite clay from Assam, India." Applied clay science, 24(1-2): 93-103.

Savage, D. (1997). "Review of the potential effects of alkaline plume migration from a cementitious repository for radioactive waste."

Savage, D., (2005). "The effects of high salinity groundwater on the performance of clay barriers." SKI Report 54.

Schanz, T. and Tripathy, S., (2009). "Swelling pressure of a divalent-rich bentonite: Diffuse double-layer theory revisited." Water Resources Research, 45, 1-9.

Schanz, T., Al-Badran, Y., (2014). "Swelling pressure characteristics of compacted Chinese Gaomiaozi bentonite GMZ01." Soils and Foundations, 54(4): 748-59.

Schanz, T., Khan, M. I., and Al-Badran, Y., (2013). "An alternative approach for the use of DDL theory to estimate the swelling pressure of bentonites." Applied Clay Science, 83, 383-390.

Sengupta, P., Saikia, P.C. and Borthakur, P.C., (2008). "SEM-EDX characterization of an iron-rich kaolinite clay."

Shackelford, C. D., Sample-Lord, K. M., (2014). "Hydraulic conductivity and compatibility of bentonite for hydraulic containment barriers." In From Soil Behavior Fundamentals to Innovations in Geotechnical Engineering: Honoring Roy E. Olson. ASCE. 370-387.

Shang, J. Q., Lo, K. Y., & Quigley, R. M., (1994). "Quantitative determination of potential distribution in Stern-Gouy double-layer model." Canadian Geotechnical Journal, 31(5), 624–636. https://doi.org/10.1139/t94-075

Sivakumar, V. and Wheeler, S.J., (2000). "Influence of compaction procedure on the mechanical behaviour of an unsaturated compacted clay. Part 1: Wetting and isotropic compression." Géotechnique, 50(4): 359-368.

Sivakumar, V., Sivakumar, R., Murray, E.J., Mackinnon, P. and Boyd, J., (2010). "Mechanical behaviour of unsaturated kaolin (with isotropic and anisotropic stress history). Part 1: wetting and compression behaviour." Géotechnique, 60(8): 581-594.

Sivapullaiah, P. V., Sitharam, T. G., Rao, K. S., (1987). "Modified Free Swell Index for Clays." Geotech. Test. J. 10, 80-85.

Sjoblom, K.J., (2016). "Coarse-grained molecular dynamics approach to simulating clay behavior." Journal of Geotechnical and Geoenvironmental Engineering, 142(2): 06015013.

Skempton, A. W. (1944). "Notes on the compressibility of clays." Q. J. Geol. Sot. Lond. 100, 119-135.

Skempton, A. W., (1953). "The colloidal activity of clays." Selected papers on soil mechanics, 106-118.

Skempton, A.W., 1960. "The pore-pressure coefficient in saturated soils." Geotechnique, 10(4): 186-187.

Smith, P. R., Jardine, R. J., and Hight, D. W. (1992). "The yielding of Bothkennar clay." Géotechnique, 42, 257-274.

Som, N. N., (1968). "The effects of stress path on the deformation and consolidation of London Clay." PhD thesis, University of London.

Sowers, G. F. (1964). "Fill settlement despite vertical sand drains." Proc., Am. Sot. Cit. Engrs Con J. Design of Foundations for Control of Settlements, North Western University, pp. 363-376.

Sparks, D. L., (1999). Soil Physical Chemistry. 2nd edition, Boca Raton: CRC Press.

Sposito G., (2008). The chemistry of soils, 2nd edn. Oxford University press, New York

Sposito, G., (1984). The surface chemistry of soils. Oxford university press.

Sridharan A (1968). "Some studies on the strength of partly saturated clays." PhD thesis, Purdue University, West Lafayette

Sridharan, A. and Prakash, K., (2000). "Percussion and cone methods of determining the liquid limit of soils: controlling mechanisms." Geotech. Test. j., 23, 242–250.

Sridharan, A., (1968). Some studies on the strength of partly saturated clays, PhD thesis, Purdue University.

Sridharan, A., and Satyamurty, P. V., (1996). "Potential-distance relationships of clay-water systems considering the stern theory." Clays and Clay Minerals, 44(4), 479–484. https://doi.org/10.1346/CCMN.1996.0440405

Sridharan, A., Prakash, K., (1999). "Influence of clay mineralogy and pore-medium chemistry on clay sediment formation." Can. Geotech. J. 36, 961-966.

Sridharan, A., Prakash, K., (2000). "Classification procedures for expansive soils." ICE Proceedings Geotech.Eng. 143, 235-240.

Sridharan, A., Rao, G. V., (1973). "Mechanisms controlling volume change of saturated clays and the role of the effective stress concept." Geotechnique. 23, 359-382.

Sridharan, A., Rao, S. M., Murthy N. S., (1986b). "Compressibility behavior of homoionized bentonites." Geotechnique. 36, 551-564.

Sridharan, A., Rao, S.M., Murthy, N. S., (1986a). "A rapid method to identify clay type in soils by the free-swell technique." Geotech. Test. J. 9, 198-203.

Stern O., (1924). "Zur Theorie der elektolytischen doppelschicht." Z Elektrochem 30:508–516

Sun H, Mašín D., Najser J., Neděla V. and Navrátilová E., (2019). "Bentonite microstructure and saturation evolution in wetting–drying cycles evaluated using ESEM, MIP and WRC measurements." Géotechnique, 69(8): 713-26.

Sun PP, Zhang MS, Zhu LF., (2013). "Typical case study of loess collapse and discussion on related problems." Geological Bulletin of China, 32(6): 847e51 (in Chinese).

Sun, D. A., Sheng, D., & Xu, Y., (2007). "Collapse behavior of unsaturated compacted soil with different initial densities." Canadian Geotechnical Journal, 44(6): 673-686.

Swedish Nuclear Fuel and Waste Management Company, (1983). Final storage of spent nuclear fuel-KBS-3, III barriers. Swedish Nuclear Fuel Supply Company, Division KBS Technical Report, pp. 9:1-16:12.

Tadikonda, V. B, Srivastava, A, and Y. Gapak. "Forthcoming. Prediction of wetting hydraulic characteristics of compacted bentonites in isochoric conditions." Journal of Geotechnical and Geoenvironmental Engineering (ASCE). https://doi.org/10.1061/(ASCE)GT.1943-5606.0002584.

Tanaka, H. and Locat, J. (1999). "A microstructural investigation of Osaka Bay clay: the impact of microfossils on its mechanical behaviour." Can. Geotech. J., 36, 493-508.

Tavenas, F., Jean, P., Leblond, P., and Leroueil, S. (1983). "The permeability of natural soft clays. Part II: Permeability characteristics." Can. Geotech. J., 20, 645-660.

Taylor, D. W. (1942). "Research on consolidation of clays." Dept. Civil Engg. Pub., Sr. 82. Massachusetts: Massachusetts Institute of Technology.

Taylor, D. W. (1948). Fundamentals of soil mechanics. J. Wiley.

Tessier, (1990a). "Soil Colloids and Their Associations in Aggregates." Plenum Press, New York, chapter 14 Behaviour and Microstructure of Clay Minerals, pp. 387–415.

Tessier, D. and Pedro, G., (1976). "Les modalités de l'organisation des particules dans les matériaux argileux." Science du Sol 2, 85–99.

Theng, B. K. G., Ristori, G. G., Santi, C. A., and Percival, H. J., (1999). "An improved method for determining the specific surface areas of topsoils with varied organic matter content, texture and clay mineral composition." Euro. Jl. Soil Sci., 50, 309-316.

Tiller, K. G. and Smith, L. H., (1990). "Limitations of EGME retention to estimate the surface area of soils." Soil Resea., 28, 1-26.

Timmons, J., Cho, Y. M., Townsend, T., Berge, N., and Reinhart, D. (2012). "Total earth pressure cells for measuring loads in a municipal solid waste landfill." Geotech. Geol. Engg., 30, 95-105.

Tripathy et al., 2004;

Tripathy S., Bag R. and Thomas H. R., (2014). "Effects of post-compaction residual lateral stress and electrolyte concentration on swelling pressures of a compacted bentonite." Geotechnical and Geological Engineering, 32(4): 749-63.

Tripathy, S. and Schanz, T. (2007). "Compressibility behaviour of clays at large pressures." Can. Geotech. J., 44, 355–362.

Tripathy, S., Bag, R., & Thomas, H. R., (2014). "Effect of Stern-layer on the compressibility behavior of bentonites." Acta Geotechnica, 9(6), 1097–1109. https://doi.org/10.1007/s11440-013-0222-y

Tripathy, S., Sridharan, A., and Schanz, T. (2004). "Swelling pressures of compacted bentonites from diffuse double layer theory." Can. Geotech. J., 41, 437-450.

Tripathy, S., Tadza, M.Y.M., Thomas, H.R. (2014). "Soil-water characteristic curves of clays." Can. Geotech. J., 51, 869-883

van Olphen, (1963). An introduction to clay colloid chemistry. Inter science Publishers, Div. of John Wiley & Sons, 605 Third Ave., New York 16.

van Olphen, H. (1977). "An introduction to clay colloid chemistry." Interscience, New York.

van Olphen, H., (1963). An introduction to clay colloid chemistry, 1st edn, John Wiley & Sons, New York London Sydney Toronto.

van Olphen, H., (1964). "Internal mutual flocculation in clay suspensions." Journal of Colloid Science, 19(4), 313–322. https://doi.org/10.1016/0095-8522(64)90033-9

van Olphen, H., (1977). An introduction to clay colloid chemistry, 2nd edn, John Wiley & Sons, New York London Sydney Toronto.

Vaunat J. and Gens A., (2005). "Analysis of the hydration of a bentonite seal in a deep radioactive waste repository." Engineering geology, 81(3): 317-28.

Verwey E. J. W. and Overbeek J. T. G., (1948). Theory of the Stability of Lyophobic Colloids: The Interaction of Soil Particles Having an Electric Double Layer. Elsevier, Amsterdam.

Verwey, E. J. W., and Overbeek, J. T. G., (1955). "Theory of the stability of lyophobic colloids." In Journal of Colloid Science (Vol. 10, Issue 2, pp. 224–225). https://doi.org/10.1016/0095-8522(55)90030-1

Villar M. V. and Gómez-Espina R., (2009). "Report on thermo-hydro-mechanical laboratory tests performed by CIEMAT on FEBEX bentonite 2004-2008." Centro de Investigaciones Energeticas Medioambientales y Tecnologicas (CIEMAT).

Villar M. V., Gómez-Espina R., Campos R., Barrios I. and Gutiérrez L., (2012), "Porosity changes due to hydration of compacted bentonite." In Unsaturated soils: research and applications, Springer, Berlin, Heidelberg, pp. 137-144.

Villar M. V., Gomez-Espina R., Campos R., Gutierrez-Nebot L. and Barrios I., (2014). "Retention curves of bentonite under a microstructural perspective." In Unsaturated soils (eds Khalili A, Russell R and Khashghalb A), Leiden, the Netherlands: CRC Press/Balkema, vol. 2, pp. 989–994.

Wahls, H. E. and Godoy, N. S., (1964). "Discussion on Interpretation of consolidation test." Proc., ASCE Conf. Design of Foundations for Control of Settlements, North Western University, 116-121.

Wang Q., Cui Y. J., Tang A. M., Xiang-Ling L. and Wei-Min Y., (2014). "Time-and density-dependent microstructure features of compacted bentonite." Soils and Foundations, 54(4): 657-66.

Wang, J., (2014). "On area-specific underground research laboratory for geological disposal of high-level radioactive waste in China." Journal of Rock Mechanics and Geotechnical Engineering, 6(2), 99-104.

Wang, Y.-H. & Siu, W.-K., (2006a). "Structure characteristics and mechanical properties of kaolinite soils. i. surface charges and structural characterizations." Can. Geotech. J., 43, 587–600.

Wang, Y.-H. & Siu, W.-K., (2006b). "Structure characteristics and mechanical properties of kaolinite soils. ii. effects of structure on mechanical properties." Can. Geotech. J., 43, 601–617.

Warkentin B. P. and Schofield R. K., (1958) "Swelling pressures of dilute Na-montmorillonite pastes." Clays and Clay Minerals, 7: 343-349.

Washburn, E. W. (1921). "Note on a method of determining the distribution of pore sizes in a porous material." Proc. Nat. Acad. Sci. 7, 115–116

Wiklander, L., and Andersson, E. K., (1955). "Floc Volume of Clays." Acta Agriculturae Scandinavica. 5, 215-223.

Ye W. M., Chen Y. G., Chen B., Wang Q. and Wang J., (2010). "Advances on the knowledge of the buffer/backfill properties of heavily-compacted GMZ bentonite." Engineering Geology, 116(1-2): 12-20.

Ye, W. M., Zhang, F., Chen, B., Chen, Y. G., Wang, Q., and Cui, Y. J. (2014). "Effects of salt solutions on the hydro-mechanical behavior of compacted GMZ01 Bentonite." Environ. Earth Sci., 72, 2621-2630.

Ye, W. M., Zheng, Z. J., Chen, B., Chen, Y. G., Cui, Y. J., & Wang, J. (2014). "Effects of pH and temperature on the swelling pressure and hydraulic conductivity of compacted GMZ01 bentonite." Applied Clay Science, 101, 192-198.

Ye, W. M., Zhu, C. M., Chen, Y. G., Chen, B., Cui, Y. J., & Wang, J. (2015). 'Influence of salt solutions on the swelling behavior of the compacted GMZ01 bentonite." Environmental Earth Sciences, 74(1), 793-802.

Yong R. N., (1999). "Soil suction and soil–water potentials in swelling clays in engineered clay barriers." Engineering Geology, 54: 3–13.

Yong, R. N., Nakano, M., and Pusch, R. (2012). "Environmental Soil Properties and Behaviour." CRC Press, Taylor & Francis.

Zaoui, A., Sekkal, W., (2015). "Can clays ensure nuclear waste repositories?." Scientific reports, 5.

Zheng L., Samper J., Montenegro L., (2011). "A coupled THC model of the FEBEX in situ test with bentonite swelling and chemical and thermal osmosis." Journal of contaminant hydrology, 126(1-2): 45-60.

Zhu C. M., Ye W. M., Chen Y. G., Chen B. & Cui Y. J., (2013). "Influence of salt solutions on the swelling pressure and hydraulic conductivity of compacted GMZ01 bentonite." Engineering Geology, 166: 74-80.

Zhu, C. M., Ye, W. M., Chen, Y. G., Chen, B., & Cui, Y. J. (2013). "Influence of salt solutions on the swelling pressure and hydraulic conductivity of compacted GMZ01 bentonite." Engineering Geology, 166, 74-80.